Impact of innovative sphere-pac fuels on safety performances of sodium cooled fast reactors

Lena Andriolo

▶ **To cite this version:**

HAL Id: tel-01257910

https://tel.archives-ouvertes.fr/tel-01257910

Submitted on 18 Jan 2016

UNIVERSITÉ GRENOBLE ALPES

THÈSE

Pour obtenir le grade de

DOCTEUR DE L'UNIVERSITÉ GRENOBLE ALPES

Spécialité : **Mécanique des fluides, Énergétique, Procédés**

Arrêté ministériel : 7 août 2006

Présentée par

Lena ANDRIOLO

Thèse dirigée par **Elsa MERLE-LUCOTTE** et
codirigée par **Andrei RINEISKI**

préparée au sein du **Laboratoire KIT/IKET/TRANS**
dans **l'École Doctorale IMEP-2 : Ingénierie – Matériaux, Mécanique, Énergétique, Environnement, Procédés, Production**

Impact des combustibles sphere-pac innovants sur les performances de sûreté des réacteurs à neutrons rapides refroidis au sodium

Thèse soutenue publiquement le **19 août 2015**, devant le jury composé de :

M. Piero RAVETTO
Professeur, Polytechnic University of Turin, Rapporteur
M. Rudy KONINGS
Professeur, Delft University of Technology, Rapporteur
Mme Elsa MERLE-LUCOTTE
Professeur, Grenoble-INP PHELMA, Directrice de thèse
M. Andrei RINEISKI
Professeur, Karlsruhe Institute of Technology, Co-directeur de thèse
Mme Fabienne DELAGE
Ingénieur-chercheur, CEA de Cadarache, Co-encadrante de thèse
Mme Sandra POUMEROULY
Ingénieur-chercheur, Electricité de France, Examinatrice
M. Janne WALLENIUS
Professeur, KTH Royal Institute of Technology, Examinateur
M. Werner MASCHEK
Professeur, Karlsruhe Institute of Technology, Examinateur

Acknowledgments

This work would not have been possible without the support and motivation of many people and I would like to take the opportunity to thank them.

First of all, I would like to thank Prof. Schulenberg for giving me the opportunity to perform my doctoral research at the Institute of Nuclear and Energy Technologies.

I thank Prof. Janne Wallenius for having agreed to be the chair of my doctoral committee as well as Prof. Piero Ravetto and Prof. Rudy Konings for having carefully read my manuscript and for their advice on my PhD. I thank also Dr. Sandra Poumerouly and Dr. Werner Maschek for having kindly accepted to be part of my PhD committee.

Je tiens à remercier tout particulièrement ma directrice de thèse Prof. Elsa Merle-Lucotte pour son soutien et sa sollicitude tout au long de ces trois années, ce qui n'était pas chose facile avec la distance géographique.

I would like to thank my co-professor and group leader Dr. Andrei Rineiski for the trust he placed in me to fulfill this work and for the guidance and support he continuously provided me and which made this work a success. De même, je souhaite remercier vivement ma co-encadrante Dr. Fabienne Delage pour toute l'aide, l'enthousiasme et les discussions que nous avons pu avoir au long de ces trois années.

Mein besonderer Dank gilt Herrn Dr. Werner Maschek für die stets professionelle Betreuung und wertvolle Unterstützung und die anregenden Diskussionen. Mit seinen zahlreichen konstruktiven Ideen/Gedanken hat er maßgeblich zum Gelingen der Arbeit beigetrag. Es war und ist ein Privileg für mich, mit ihm arbeiten zu dürfen.

Weiterhin möchte ich mich bei Frau Claudia Matzerath Boccaccini herzlich für ihre engagierte und warmherzige Begleitung bedanken. Es hat mich immer wieder gefreut mit dir und Werner auf PELGRIMM Dienstreise zu fahren, wo uns immer die unwahrscheinlichsten Geschichten passierten.

Diese Arbeit wäre in dieser Form nicht ohne Dr. Edgar Kiefhaber und seine glücksbringenden „4-blättrigen Kleeblätter" möglich gewesen: Herzlichen Dank Edgar für deine unermüdliche Unterstützung deine große Fachkunde und äußerst hilfreichen Ratschläge zum wissenschaftlichen Arbeiten. Ein großes Dankeschön auch für deine akribische Korrektur der Doktorarbeit.

I also would like to thank my friends and colleagues Dr. Barbara Vezzoni and Dr. Fabrizio Gabrielli, for their unlimited support, their invaluable technical advices and the numerous laughters we had. Whenever I felt the need to discuss some issues, you took the time to discuss them with me and gave me precious support to go on with my work. I am very greatful for this (and for the nice coffee breaks!).

AKCNOWLEDGMENTS

The future belongs to those

who believe in the beauty of their dreams

- E. Roosevelt

Abstract

Future sodium cooled fast reactors (SFRs) have to fulfill the GEN-IV requirements of enhanced safety, minimal waste production, increased proliferation resistance and high economical potential. This PhD project is dedicated to the evaluation of the impact of innovative fuels (especially minor actinides bearing oxide sphere-pac fuels) on the safety performance of advanced SFRs with transmutation option.

The SIMMER-III code, originally tailored to mechanistically analyze later phases of core disruptive accidents, is employed for accident simulations. During the PhD project, the code has been extended for a better simulation of the early accident phase introducing the treatment of thermal expansion reactivity effects and for taking into account the specifics of sphere-pac fuels (thermal conductivity and gap conditions). The entire transients (from the initiating event to later accident phases) have been modeled with this extended SIMMER version.

Within this PhD work, first the thermo-physical properties of sphere-pac fuel have been modeled and casted into SIMMER-III. Then, a new computational method to account for thermal expansion feedbacks has been developed to improve the initiation phase modeling of the code. The technique has the potential to evaluate these reactivity feedbacks for a fixed Eulerian mesh and in a spatial kinetics framework. At each time step, cell-wise expanded dimensions and densities are calculated based on temperature variations. Density factors are applied to the expanded densities to get an equivalent configuration (in reactivity) with original dimensions and modified densities. New cross sections are calculated with these densities and the reactivity of the equivalent configuration is computed. The developed methods show promising results for uniform and non-uniform expansions. For non-uniform expansions, model improvement needs have been identified and neutronics simulations have been carried out to support future SIMMER extensions. Preliminary results are encouraging.

In the third part of the PhD, two core designs with conventional and sphere pac fuels are compared with respect to their transient behavior. These designs were established in the former CP-ESFR project: the working horse core and the optimized CONF2 core (with a large sodium plenum above the core for coolant void worth reduction). The two fuel design options are compared for steady state and transient conditions (unprotected loss of flow accident, ULOF) either at beginning of life (BOL) or under irradiated conditions. Analyses for sphere-pac fuel reveal two main phases to consider at BOL. At start-up, the non-restructured sphere-pac fuel shows a low thermal conductivity compared to pellet fuel of same density. However, the fuel restructures quickly (in a few hours) due to the high thermal gradients and its thermal conductivity recovers. The fuel then shows a behavior close to the pellet one. The study also shows that the CONF2 core leads to a very mild transient for a ULOF accident at BOL. The large upper sodium plenum seems to effectively prevent large positive reactivity insertions. However, stronger reactivity and power peaks are observed under irradiated conditions or when americium is loaded in the core and lower axial blanket.

This PhD work demonstrates, under current simulation conditions, that sphere-pac fuels do not seem to cause specific safety issues compared to standard pellet fuels, when loaded in SFRs. The accurate simulation of core thermal expansion reactivity feedbacks by means of the extended SIMMER version

plays an important role in the accident timing (simulations confirm the expected delay in the first power peak) and on the energetic potential compared to the case where these feedbacks are omitted. The analyses also confirm the mitigating impact of a large sodium plenum on transients with voiding potential. The behavior of sphere-pac fuel in these conditions opens a perspective to its practical application in SFRs.

Key-Words: Sodium cooled Fast Reactors, severe accidents, safety, innovative sphere-pac fuels, SIMMER.

Résumé

Les futurs réacteurs à neutrons rapides refroidis au sodium (RNR-Na) doivent remplir les critères GEN-IV à savoir présenter des qualités d'économie, de sûreté améliorée, de résistance à la prolifération et de minimisation des déchets. Ce projet de thèse est dédié à l'étude de l'impact des combustibles innovants (spécialement le combustible oxyde sphere-pac chargé en actinides mineurs) sur les performances de sûreté des RNR-Na dédiés à la transmutation.

Le code de calcul SIMMER-III, développé à l'origine pour les phases avancées d'un accident grave, est utilisé pour les simulations. Ce code a été étendu dans le cadre de cette thèse afin d'améliorer la simulation de la phase primaire de l'accident, en introduisant le traitement des effets en réactivité liés à la dilatation du cœur et les spécificités du combustible sphere-pac (conductivité thermique, gap). Les transitoires complets (de la phase d'initiation aux phases avancées) sont simulés avec cette version étendue du code.

Dans le cadre de cette thèse, les propriétés thermiques du combustible sphere-pac ont été modélisées et adaptées à SIMMER. Une méthodologie innovante tenant compte des effets en réactivité liés à la dilation thermique du cœur dans un maillage Eulérien et dans le cadre de la cinétique spatiale a ensuite été développée. A chaque pas de temps, les dimensions et densités dilatées sont calculées pour chaque cellule suite aux variations de températures. Des facteurs correctifs sont appliqués aux densités dilatées pour obtenir une configuration équivalente (en réactivité) ayant les dimensions non-dilatées et des densités modifiées. De nouvelles sections efficaces sont calculées à partir de ces densités et l'effet en réactivité lié à la dilatation est calculé. Les résultats sont prometteurs pour des dilatations uniformes et non-uniformes. Des limitations dans le cas de dilatations non-uniformes ont été identifiées et des calculs neutroniques ont été effectués en vue de futurs développements SIMMER. Les résultats préliminaires sont encourageants.

Enfin, deux cœurs RNR-Na, issus du précédent projet CP-ESFR, ont été modélisés avec des combustibles sphere-pac : le Working Horse et le CONF2 (présentant un plénum sodium élargi pour une diminution de l'effet de vide sodium). Des analyses de sûreté ont été effectuées afin de fournir une première évaluation du comportement du combustible sphere-pac comparé au combustible pastille. Les deux options sont analysées en situation nominale et accidentelle (accident de perte de débit primaire) en début de vie du cœur et après irradiation. Les analyses révèlent deux phases à considérer en début de vie pour le combustible sphere-pac. Au démarrage du réacteur, ce combustible n'est pas restructuré et sa conductivité thermique est très inférieure à celle du combustible pastille. Après quelques heures sous irradiation, il se restructure suite aux importants gradients de température, ce qui améliore sa conductivité. Il se comporte alors de façon similaire au combustible pastille. Ce travail a également permis d'évaluer le comportement accidentel du cœur CONF2 qui subit un transitoire doux, prouvant que le large plénum sodium prévient efficacement de larges insertions de réactivité positive. Cependant, avec l'ajout d'américium ou suite à l'irradiation, des excursions de puissance et de réactivité plus prononcées sont observées.

Ce travail a permis de démontrer que le combustible sphere-pac ne semble pas causer de problèmes de sûreté spécifiques comparé au combustible pastille, dans les conditions de simulations actuelles.

RESUME

La prise en compte des effets en réactivité liés à la dilatation du cœur avec cette version étendue de SIMMER retarde et réduit le potentiel énergétique lors d'un accident. Les analyses confirment également l'action atténuante du plénum sodium sur les transitoires conduisant à la vidange du sodium du cœur. Le comportement du combustible sphere-pac dans ces conditions ouvre une perspective à son utilisation en RNR-Na.

Mots clés : Sûreté, Combustible sphere-pac innovant, Réacteurs à neutrons rapides refroidis au sodium, SIMMER, Accidents graves

List of figures

LIST OF FIGURES

List of tables

List of abbreviations

ALARA	as low as reasonably achievable
BOL	beginning of life
BU	burnup
CDA	core disruptive accident
CP-ESFR	collaborative project on European sodium fast reactor
CSD	control and shutdown device
DBA	design basis accident
DBC	design basis condition
DEC	design extension condition
DENSF	density factor
DPA	deterministic and phenomenological analysis
DPIN	detailed pin model
DSD	diverse shutdown device
efpd	equivalent full power days
EFR	European fast reactor
EOC3	end of cycle 3
EOS	equation of state
ESFR	European sodium cooled fast reactor
FCCI	fuel-cladding chemical interaction
FCI	fuel coolant interaction
FCMI	fuel-cladding mechanical interaction
FOP	first order perturbation theory
FP	fission product
FR	fast reactor
GEN-IV	generation IV
GFR	gas cooled fast reactor
GIF	Generation IV international forum
HCDA	hypothetical core disruptive accident
HTGR	high temperature gas reactor
IFR	Integral fast reactor
IMF	inert matrix fuel
INES	international nuclear and radiological event scale
INPRO	international project on innovative nuclear reactors and fuel cycles
IQM	improved quasistatic method
ISAM	integrated safety assessment methodology
LAB	lower axial blanket
LBE	lead-bismuth eutectic
LFR	lead cooled fast reactor
LGP	lower gas plenum
MA	minor actinide
MOX	mixed oxide
MSR	molten salt reactor

O/M	oxygen over metal ratio
ODS steel	oxide dispersion strengthened steel
OPT	objective provision tree
P&T	partitioning and transmutation
PIRT	phenomena identification and ranking table
PK	point kinetic
PSA	probabilistic safety assessment
PT	perturbation theory
PWR	pressurized water reactor
QSR	qualitative safety feature review
RR	residual risk
SCWR	supercritical water reactor
SFR	sodium cooled fast reactor
SNF	spent nuclear fuel
SPIN	simplified pin model
TD	theoretical density
TIB	total instantaneous blockage
TOP	transient over power
TRU	transuranic
UAB	upper axial blanket
UBA	unprotected blockage accident
UGP	upper gas plenum
ULOF	unprotected loss of flow
ULOHS	unprotected loss of heat sink
USS	upper steel structure
UTOP	unprotected transient over power
VHTR	very high temperature reactor
WENRA	western European nuclear regulators association
WEO	world energy outlook
WH	working horse

Table of contents

TABLE OF CONTENTS

Chapter 1

INTRODUCTION

1.1. General context of the PhD

The world energy demand has been constantly increasing over the last decades and drives the need for a reliable and affordable energy supply. The International Energy Agency predicts a growth of 0.9% per year in the world population over the period 2012-2040 bringing it from 7 billion to 9 billion [1].

Accordingly, and with the increasing digitalization of the world economy, the world electricity demand will rise by 2.1% per year in average over the same time period, leading to an increase of 80% in the installed capacity (going from 5 952 GW in 2013 to slightly more than 10 700 GW in 2040 in the new policy scenario). According to the World Energy Outlook (WEO) "broad policy commitments and plans have been announced by countries, including national pledges to reduce greenhouse-gas emissions and plans to phase out fossil-energy subsidies, even if the measures to implement these commitments have yet to be identified or announced" [1].

To cope with this trend, a new energy mix between oil, gas, coal and low-carbon sources has to be found (Figure 1-1), while being in accordance with the concerns on climate change. Thus, in the new energy scenarios, the share of fossil fuels – whose resources are abundant (Figure 1-2) – as coal and oil, producing large amounts of greenhouse gases (GHG) as CO_2 main responsible for the earth warming, is dropping. On the contrary, the share of nuclear and gas is increasing, the share of renewables seeing the largest growth [1].

Not only the supply but as well the sustainability of electricity are a matter of increasing concern. Indeed, the effects of different conflicts on oil prices and availability and the potential threats to oil and gas supplies have stressed the importance of being energetically independent [1].

Nuclear energy provides a safe, almost CO_2 free energy source and can be used for electricity base load.
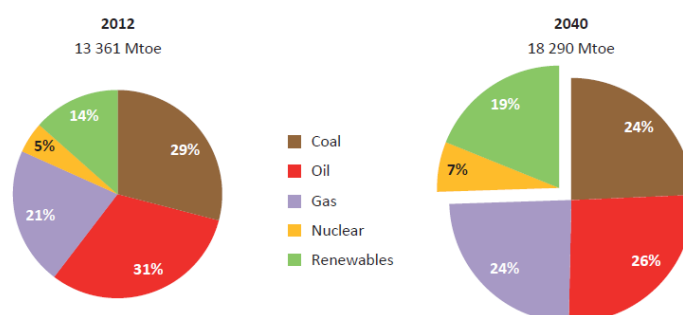
Figure 1-1. Current and future energy mix in the world according to the new policies scenario: fuel shares [1].
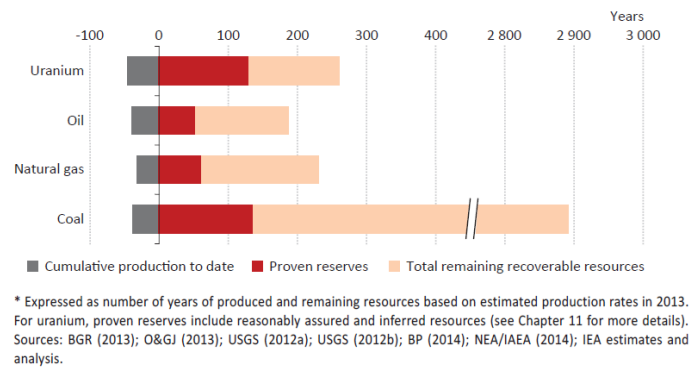
Figure 1-2. Lifetime of fuel resources [1].

However, strong public concern is perceived with regard to safety, especially after the 2011 Fukushima Daiichi accident in Japan, as well as waste management and proliferation issues. Nowadays, 434 nuclear reactors are operating worldwide and represent 332 GW installed capacity providing more than 11% of the world electricity. 76 new reactors are currently under construction in the world. Nearly all these reactors are thermal reactors, mainly from 2nd and 3rd generation (Figure 1-3). They mostly use uranium fuel ^{238}U enriched to about 5% ^{235}U. However, as ^{238}U is a fertile isotope and considering that only 0.7% of the natural uranium ore is ^{235}U, a significant amount of ^{238}U is not efficiently used with these concepts. Even if the global uranium resources are currently estimated to last for the next 150 years [2] when utilizing the currently operating type of Light Water cooled Reactors (LWRs), a better use of resources is sought to ensure the sustainability of nuclear power for the next generations. Worldwide, new reactors are investigated, the so-called Generation IV (GEN-IV) reactors, promising concepts for a better fuel efficiency and able to reduce the amount of nuclear waste.
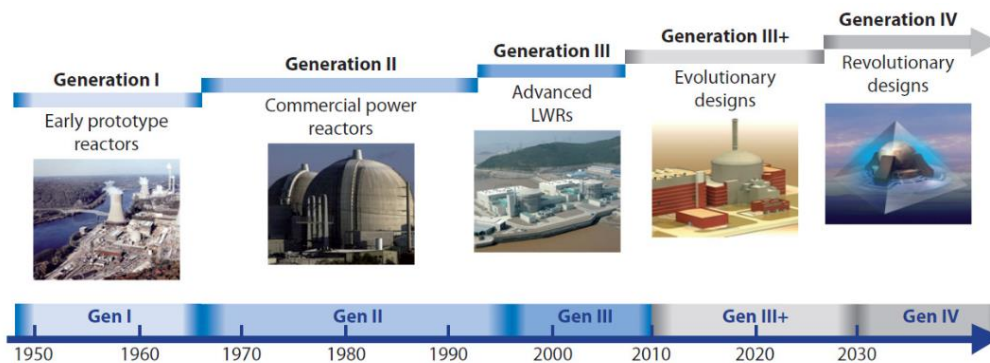
Figure 1-3. Generations of nuclear reactors over time [3].

This research is performed within the Generation IV forum [3], where 6 reactor concepts are currently investigated: the sodium cooled Fast Reactor (SFR), the gas cooled fast reactor (GFR), the lead cooled fast reactor (LFR), the supercritical water cooled reactor (SCWR), the very high temperature reactor (VHTR) and the molten salt reactor (MSR) [3].

These reactors have to prove their sustainability, their improved safety and reliability, their proliferation resistance and physical protection in addition to their economic competitiveness [3].

Among these 6 concepts, the reactors with fast spectrum fulfill the sustainability requirement, where the SFR concept is the most advanced and mature one. For this concept, key objectives for the next ten years have been defined, two of which are:

- improved safety and operation, especially core inherent safety, inspection and control, prevention and mitigation of severe accidents with high energetic potential

- advanced fuel developments especially innovative fuels containing minor actinides

Especially in France, the SFR concept is given strong attention. This is due to experience feedback from former reactors. Indeed, France has a long experience with SFR construction and operation. The first one was the RAPSODIE reactor [4], a 20 MWth experimental reactor built in 1957, which is currently under decommissioning. In 1974, the PHENIX reactor was started [4]. It was a 250 MWth reactor, connected to the electrical grid and used for transmutation purposes of high level waste. It has been shut down in 2009. In 1985 the SUPERPHENIX reactor was operated for the first time, producing 3000 MWth. It stopped in 1997 due to political reasons [4]. The following European Fast Reactor (EFR) was extensively analyzed and ready to be built. However the project was abandoned [5]. Recently, the CP-ESFR project was conducted [6] and gave rise to the ESNII+ project [7], with the objective of the construction of the Advanced Sodium Technological Reactor (ASTRID) in France [8]. Within the CP-ESFR project, an optimization of a 3600 MWth sodium cooled reactor was carried out. Optimization and safety studies particularly aimed at a low sodium void effect for this core. Additional studies on the introduction of minor actinides into the core and blankets were carried out [9].

The use of minor actinide bearing fuels gets more and more attention from the scientific community and specific fuel forms and materials are investigated worldwide [10]. Additional technological conditions, as the high dose due to neutron emissions both at fabrication and reprocessing steps led to the development of innovative processes. Here the specific sol-gel methods can be cited in which all fabrications are done in a wet route, thus avoiding the handling of powders and a possible contamination of facilities.

The current PhD work is embedded within this framework of improved safety and waste reduction.

1.2. Objectives of the PhD

The objective of the PhD is to contribute to the safety studies on SFRs loaded with innovative minor actinide bearing fuels. It targets the analyses of the impact of innovative sphere-pac fuels on the safety behavior of SFRs both in nominal and accidental transient conditions.

Sphere-pac pins are composed of small fuel microspheres vibrationally compacted into a cladding tube. The pins are usually helium filled. The specific macrostructure of these fuels is assumed to enhance the fission gas accommodation, thus reducing the pressure load on the cladding, which makes them interesting candidates to add minor actinides to the fuel. In addition, their fabrication can be performed immediately after the spent fuel reprocessing step as a wet route is used. However, the fresh sphere-pac fuels possess a very low thermal conductivity due to the narrow and few contact points among the spheres. This issue is alleviated some hours after the reactor start-up. Indeed, the high temperature gradients in the fuel lead to extensive restructuring: the fuel shows rapidly a pellet-like structure, possessing the same properties as a pellet fuel of same density, surrounded by a layer of spheres.

The PhD work is embedded in the European FP-7 project PELGRIMM (2012-2016) [11] standing for Pellets versus Granulates, Irradiation, Manufacturing and Modeling which addresses the development of minor-actinide bearing oxide fuel for SFRs. As options, minor actinide homogeneous

recycling, where minor actinides are put into the driver fuel, and heterogeneous recycling of minor actinides, where UO_2 blankets are loaded with minor actinides, are investigated. A first safety assessment is performed within this PhD thesis for the homogeneous recycling route, which is in continuity with the former FP-7 CP-ESFR project [6] , aimed at designing and analyzing a 3600 MWth sodium cooled fast reactor, assessing its safety behavior and its transmutation capabilities. Thanks to a large pin diameter and a high smear density, the so-called Working Horse (WH) core [12; 6] allowed to strongly reduce the burnup reactivity swing. Despite a reduced sodium fraction, the sodium void worth remained relatively high (~1500 pcm at beginning of life) being a major cause for significant reactivity insertion during an unprotected loss of flow accident (ULOF) leading to void reactivity driven core disruption and a whole core melt [13]. An optimized core with reduced sodium void worth was hence designed. This core is the so-called CONF2 core design. It presents a large sodium plenum which provides a reduced positive void worth [14; 9] and was therefore chosen for the safety analyses within the PELGRIMM project. Within the CP-ESFR project no extended safety analyses have been performed for this core design and they have hence been assessed during this PhD work.

Core designs with a low void effect like the CONF2 core are expected to undergo much milder transients than core designs with high void effect. However these cores show a delicate balance of their reactivity effects. It becomes hence of high importance to enhance the modeling of the initiation phase of the accident. In order to address this point, a new methodology for taking into account core thermal expansion feedbacks has therefore been developed within this PhD project for space-time kinetic codes with a Eulerian mesh.

In order to perform a safety assessment and an evaluation of the CONF2 core loaded with sphere-pac driver fuel, the SIMMER-III code had to be adapted to the specifics of the sphere-pac fuel, as much as possible within its framework; in particular to take into account the thermal conductivity of this innovative fuel. Important differences to the standard pellet fuel are as well the existence of spheres (particles), the non-existence of a gap and the fuel "one column" structure. The specifics of the sphere-pac fuel reveal additional phenomena to the ones observed with pellet fuel under pin failure conditions, as one could experience the release of particles at the column rim in a dispersive fashion. Other important issues are the release of fission gases and helium, which is expected to be different in case of sphere-pac fuel in quantity and timing, especially during transient conditions. These issues have not been investigated in detail during the PhD project because of the lack of suitable experimental transient data.

For accidental transients and especially for high temperature conditions, typical for severe accident conditions, a limited experimental knowledge base is available for sphere-pac fuels. Understanding the behavior of fuel pins under transient operating and accidental conditions is important to evaluate the overpower margins of fuel and to assess the influence of temporary abnormal conditions. It has to be mentioned at this point that the goal of this PhD work has been to provide a preliminary safety assessment of sphere-pac fuels i.e. to determine if sphere-pac fuels could be loaded in a sodium cooled fast reactor without major design modifications and whether or not these fuels would lead to an unacceptable safety behavior. Hence, no uncertainty analysis is performed at this stage of research and within this PhD thesis. To remember is that hypothetical core disruptive scenarios and phenomena have a very small occurrence probability and full scale simulations represent extrapolations. A full assessment of epistemic uncertainties (due to gaps in knowledge), which are the dominant uncertainties in severe accident safety analyses, are usually addressed in the

framework of licensing procedures since it requires an extensive and complex work which is out of the scope of this thesis (and of the FP-7 PELGRIMM project)

To understand the context of the PhD project, an introductory explanation on GEN-IV systems and their benefits in waste reduction and fuel utilization is given in Chapter 2.

The safety approach, its main principles as well as the main families of accidents, are detailed in Chapter 3.

The specific core designs used for the study are described in Chapter 4. Two core designs, main outcome of the former CP-ESFR project, are investigated: the so called Working Horse (WH) core as well as its optimized version, the so-called CONF2 core.

Since the current PhD work investigates the safety behavior of innovative sphere-pac fuels, the main fuel families are detailed in Chapter 5. Main focus is put on the oxide fuels in two specific fuel forms: the pellet and the sphere-pac form. Fabrication, operational behavior as well as reprocessing are considered.

Chapter 6 deals with a new neutronic feature for SIMMER-III: the ability to take into account core thermal expansion feedbacks. These feedbacks are particularly important in the initiation phase of the transient. Since the SIMMER codes were originally developed for already disrupted cores i.e. for investigating so-called core disruptive accidents (CDAs), these feedbacks had no or less importance at this stage of the accident. For consistency reasons SIMMER should be used from the very start of the accident. This new route needs model developments such as the consideration of core thermal expansion feedbacks. The first part of the chapter describes the neutron transport equation and the different numerical methods employed to solve it. Special focus is concentrated on the improved quasi-static method since SIMMER is based on this method. In a second part, the theory and methodology of the different expansion models is presented. The particularity here is that the methodologies should fit into the space-time kinetic framework of SIMMER and cope with its Eulerian mesh. Two main methods based on first order perturbation theory and a third one based on the direct method are presented. The last part of the chapter aims at validating the hypothesis as well as the overall procedure through simple test cases. Finally, benefits of the core expansion feedbacks on the transient calculation are presented.

In Chapter 7 sphere-pac fuels properties are adapted to the SIMMER framework. In this chapter, especially the specific thermal conductivity is investigated since it undergoes large variations during the first hours of irradiation due to extensive restructuring processes. A literature review of the different theoretical models available for modeling their thermal conductivity is given. These models are too detailed for the SIMMER framework, where a more simple fuel model is used and where thermal conductivity is calculated through temperature based correlations. Correlations are thus developed both for beginning of life and three cycle irradiated sphere-pac fuels. Comparison to pellet fuel conductivity is also performed in this chapter as well as a study on thermal penetration lengths.

In Chapter 8 the results of the modifications described in Chapters 6 and 7 are analyzed. Simulations for a ULOF are performed for the CP-ESFR WH MOX fueled core as well as for the CONF2 MOX fueled core, both at beginning of life and at equilibrium configurations, with and without core thermal expansion feedbacks. The analyses at beginning of life are performed to highlight the strong difference in thermal conductivity between pellet and sphere-pac fuels. However, a representative core would be a core in equilibrium conditions, and in this case the sphere-pac fuels would have had time to restructure. Additional analyses are performed for americium contents of 2wt% and 4wt%.

Finally, Chapter 9 summarizes the conclusions and presents future outlooks of the work.

Chapter 2

FAST REACTOR DESIGNS AND MISSIONS

In the world energy outlook 2014 [15], the OECD International Energy Agency [16] predicts a growth of the world electricity demand by almost 80% over the period 2012-2040. To cope with this increasing demand, an energy mix between fossil fuels, renewables and nuclear energies has to be found. Several studies are carried out by international organizations to investigate the impact of the future energy mix. Among the different sources, nuclear power provides reliable base load electricity and enhances energy security of supply. In addition, it is one of the few options with almost no CO_2 emissions. However, the long-term durability and sustainability of nuclear energy mainly depends on an adequate uranium resource and waste management. In the Generation-IV (GEN-IV) framework [17], the objectives for future reactor systems have been defined and target sustainability, cost-effectiveness, safety and reliability. To meet these objectives, six reactor designs are currently investigated with either thermal ($\lesssim 1$ eV) or fast energy neutron spectra. Among the thermal systems the thermal supercritical water cooled reactors (SCWRs) and the very high temperature reactors (VHTRs) are investigated. The fast molten salt, sodium cooled, gas cooled, and lead cooled reactors (MSRs, SFRs, GFRs, and LFRs respectively) are ranged in the category of fast systems. Subcritical fast systems can also be used to transmute minor actinides (i.e. americium, curium and neptunium isotopes). Subcritical LFRs and GFRs ensure an enhanced safety and allow a high content of minor actinides to be loaded in the core. In addition, they can use uranium free fuels, thus avoiding the buildup of higher transuranic (TRUs) elements. However, they are usually not thought to produce electricity and their development is still at a very early stage. Critical systems are thus generally preferred for electricity production and could also contribute to the waste management.

2.1. Uranium resources and waste stocks

Only a very small amount of natural uranium is fissile (^{235}U, $\sim 0.7\%$); the rest is essentially non fissile ^{238}U. Current pressurized water reactors (PWRs) are using uranium oxide fuels enriched up to 5% with fissile ^{235}U.
Spent nuclear fuel (SNF) coming from current PWRs consists of 95% uranium, $\sim 1\%$ plutonium, $\sim 4\%$ fission products and $\sim 0.1\%$ minor actinides (americium, curium, neptunium) for a burnup of ca. 40 GWd/t [18; 10]. Hence only a few percent of the natural uranium is actually used in current light water reactors (LWRs). A better use of uranium is therefore essential to cope with increasing uranium resources consumption. Fast reactors (FRs) are one of the suitable solutions. In addition,

since FR fuel is mainly composed of plutonium recovered from SNF and of depleted or recycled uranium, their fuel cost would be less sensitive to the natural uranium ore price than for PWRs.

The IAEA evaluated the worldwide production of nuclear waste to 10,500 MTHM/year (metric tons of heavy metal) [19]. In the open cycle strategy (as it is the case in the USA) no SNF reprocessing and plutonium recycling are foreseen. In France the open cycle is slightly modified considering the SNF reprocessing and plutonium loading in LWRs.

Nuclear waste is classified according to half-life, energy and decay type in addition to physical and chemical properties including migration in the environment. Six categories of nuclear waste can be distinguished according to the IAEA [20]:

1. Exempt waste (EW) - waste with a very low radioactivity. No control by the regulatory authority is required.

2. Very short-lived waste (VSLW) - waste that can be stored for a limited time period of up to some years in order to decrease by radioactive decay. It includes radionuclides with very short half-lives often used for research and medical purposes.

3. Very low level waste (VLLW) - waste with a radioactivity content higher than EW which, however, does not require high level containment and isolation. Near-surface facilities with limited regulatory control are considered for VLLW. This waste includes soil and rubble with low levels of radioactivity from sites formerly contaminated by radioactivity. Quantities of longer-lived isotopes are usually very limited.

4. Low level waste (LLW) - high radioactivity content waste with a limited amount of long-lived radionuclides. High level isolation and containment is compulsory over periods of up to a few hundred years. Disposal is done in engineered near surface facilities. This waste includes short-lived radionuclides with higher levels of activity and long-lived radionuclides with relatively low levels of activity.

5. Intermediate level waste (ILW) - waste that necessitates a higher degree of containment and isolation than that provided by near surface disposal. However, for ILW no or limited provision for heat dissipation during storage and disposal is required. ILW may contain long-lived radionuclides whose decay will not bring the activity level below the one required for near-surface storage during the time for which institutional controls can be relied upon. ILW thus requires disposal at greater depths (tens of meters to a few hundred meters).

6. High level waste (HLW) - waste with high levels of activity concentration producing significant heat through radioactive decay processes. It also includes waste with large quantities of long-lived radioisotopes that needs to be considered in the design of a disposal facility for such waste. Disposal is done in deep stable geological formations (several hundred meters below the surface).

Three options are considered for HLW management: deep-storage, long-term interim storage and separation/transmutation. Separation (partitioning) refers to special processing adapted to each specific case and transmutation is defined as any transformation of a long half-life radionuclide to stable or short half-life ones, through nuclear reactions [21]. Partitioning and transmutation (P&T) strategies are largely investigated by the international community.

Figure 2-1 depicts the impact of transmutation on long-term SNF radiotoxicity. Radiotoxicity is defined as the noxiousness of a radionuclide taking into account the characteristics of radiation and metabolism in case of ingestion or inhalation by a person [21]. It can be seen that if no recycling is performed, it would take about 400.000 years for the nuclear waste radiotoxicity to decrease to the level of radiotoxicity comparable to that of natural uranium. If, however, multiple plutonium and minor actinide recycling is performed in FRs, the time could be decreased to less than a thousand years. [10]
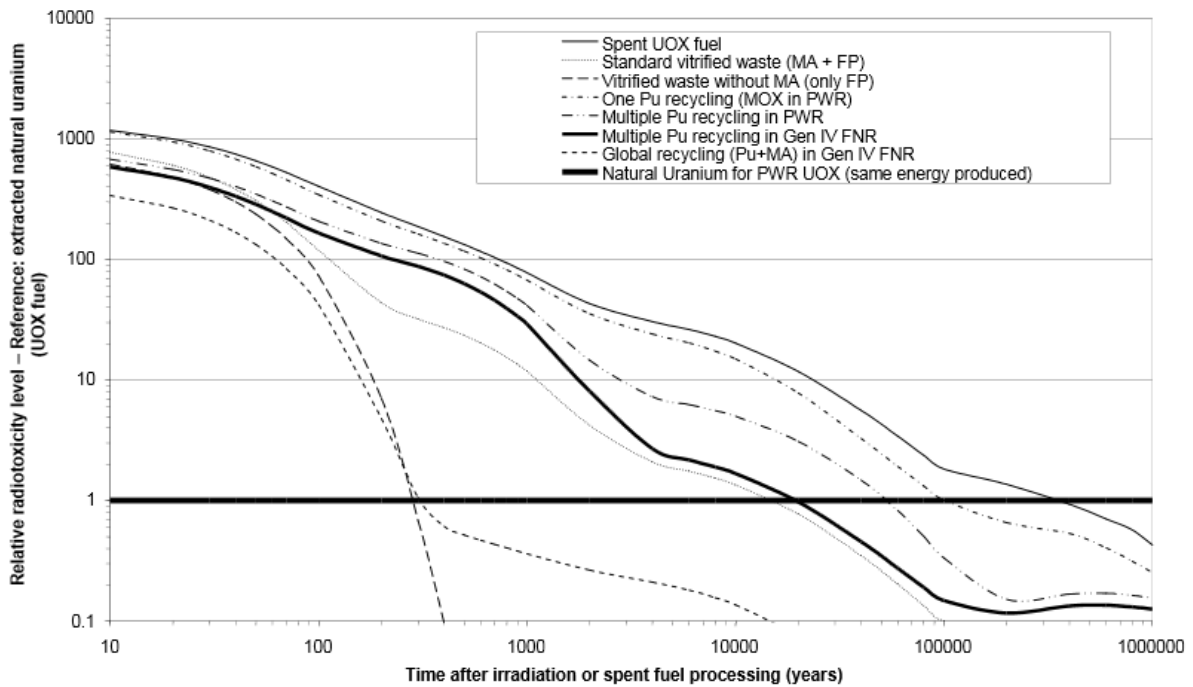
Figure 2-1. Relative radiotoxicity versus time for different recycling options [22].

Table 2-1 shows the annual inventory balance of a 900 MWe PWR (uranium and mixed-oxide fuel (MOX) options are compared). About 200 kg of plutonium are produced per year in a PWR reactor. Even if plutonium represents about 1% of the SNF, it is responsible for 90% of the radiotoxicity of the SNF. Hence, transmuting plutonium will not only provide a better fuel efficiency but also decrease the radiotoxic inventory of the SNF [21].

Table 2-1. Isotopic inventory in kg/year for fresh and spent nuclear fuel of a 900 MWe pressurized water reactor [21].

Nuclide	Period (years)	Uranium fuel		MOX fuel	
		Inlet mass (kg)	Outlet mass (kg)	Inlet mass (kg)	Outlet mass (kg)
^{235}U	7.08E+08	751	221	11.1	5.8
^{236}U	2.34E+07	/	88	/	1.2
^{238}U	4.47E+09	20734	20204	4478	4261
^{238}Pu	8.80E+01	/	3.3	11.3	12.4
^{239}Pu	2.41E+04	/	123.1	209	105.2
^{240}Pu	6.57E+03	/	47.5	98.5	87.4
^{241}Pu	1.40E+01	/	25.4	44.5	40.7
^{242}Pu	3.70E+04	/	10.5	31	35.8
^{237}Np	2.14E+06	/	8.8	/	0.8
^{241}Am	4.32E+02	/	4.4	/	14.4
^{243}Am	7.38E+03	/	2.2	/	9.0
^{244}Cm	1.80E+01	/	0.5	/	4.0
^{245}Cm	8.50E+03	/	0.1	/	0.5
^{93}Zr	1.50E+06	/	15.5	/	3.0
^{99}Tc	2.10E+05	/	17.7	/	4.8
^{107}Pd	6.50E+06	/	4.4	/	3.2
^{126}Sn	1.00E+05	/	0.4	/	0.2
^{129}I	1.57E+07	/	3.9	/	1.3
^{135}Cs	2.00E+06	/	7.7	/	4.8

Uranium and plutonium constitute the major part of SNF and are hence called major actinides. Neptunium, americium and curium are called minor actinides (MAs). They are mainly alpha emitters. In order to determine which isotopes should be transmuted, radiotoxicity, heat load and neutron emissions are compared.

Figure 2-2 compares the radiotoxicity of the different elements. It can be noticed that the SNF radiotoxicity level is dominated by ^{137}Cs, ^{90}Sr and plutonium for about 200 years after discharge; plutonium and MAs for one hundred thousand of years; and uranium, plutonium and MAs in the very long term. The heat load follows the same trend. In the short term it is dominated by fission products mainly ^{137}Cs and ^{90}Sr (about 2000 W/TWhe) while for medium and long term, plutonium (about 100 W/TWhe), americium and curium are the dominating elements. The main contributor to the neutron source for the first 200 years in storage is ^{244}Cm with a neutron source of about 10^7 n·s^{-1}·g^{-1} [10].
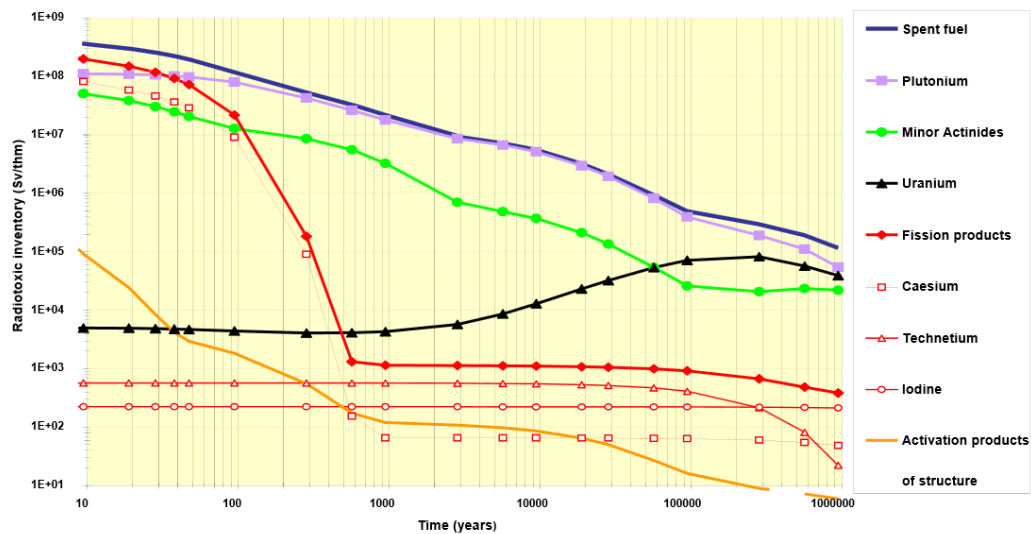
Figure 2-2. Radiotoxic inventory of UO$_x$ nuclear fuel [10].

Recycling TRUs allows a decrease in the TRU mass as well as in the radiotoxicity and heat load of the nuclear waste. However, not only the fuel cycle back-end but also its front-end (i.e. fabrication) and the core performance characteristics are impacted by a possible recycling of TRUs.

When transmuting TRUs, two main consequences are observed. First, the neutron balance in a FR contributes to a surplus of neutrons, which is balanced by the higher neutron leakage. This is due to the higher fission over capture ratios of the actinides. From the core neutronics point of view, the reactivity coefficients and kinetic parameters are also impacted: a worsening of all feedback coefficients as well as a decrease in the delayed neutron fraction is observed [23].

Second, the fuel cycle is impacted. In fact, even though the transmutation of actinides through capture is less probable in a FR than in a thermal reactor and thus the buildup of higher isotopes is limited, buildup of curium isotopes like ^{246}Cm and ^{248}Cm (after multiple recycling) through successive captures on americium isotopes, as well as higher elements like berkelium and californium (^{252}Cf) produced through successive captures in ^{244}Cm, may have an impact on the fuel cycle as these isotopes are strong neutron emitters through spontaneous fissions [10].

2.2. Breeders and iso-generators

As mentioned earlier, an interesting feature of FRs is their efficient use of fuel. The primary target of FRs was to breed fissile material through fertile material (mainly ^{238}U in the U/Pu cycle) in order to save, at that time underestimated, available and reasonably assured uranium resources [24; 25].
In order to breed, a fertile isotope (e.g. ^{232}Th, ^{238}U) should be converted into a fissile isotope (^{233}U, ^{239}Pu) through neutron capture. The conversion chain for uranium is shown in Figure 2-3 (the one of thorium being omitted for our current purposes).
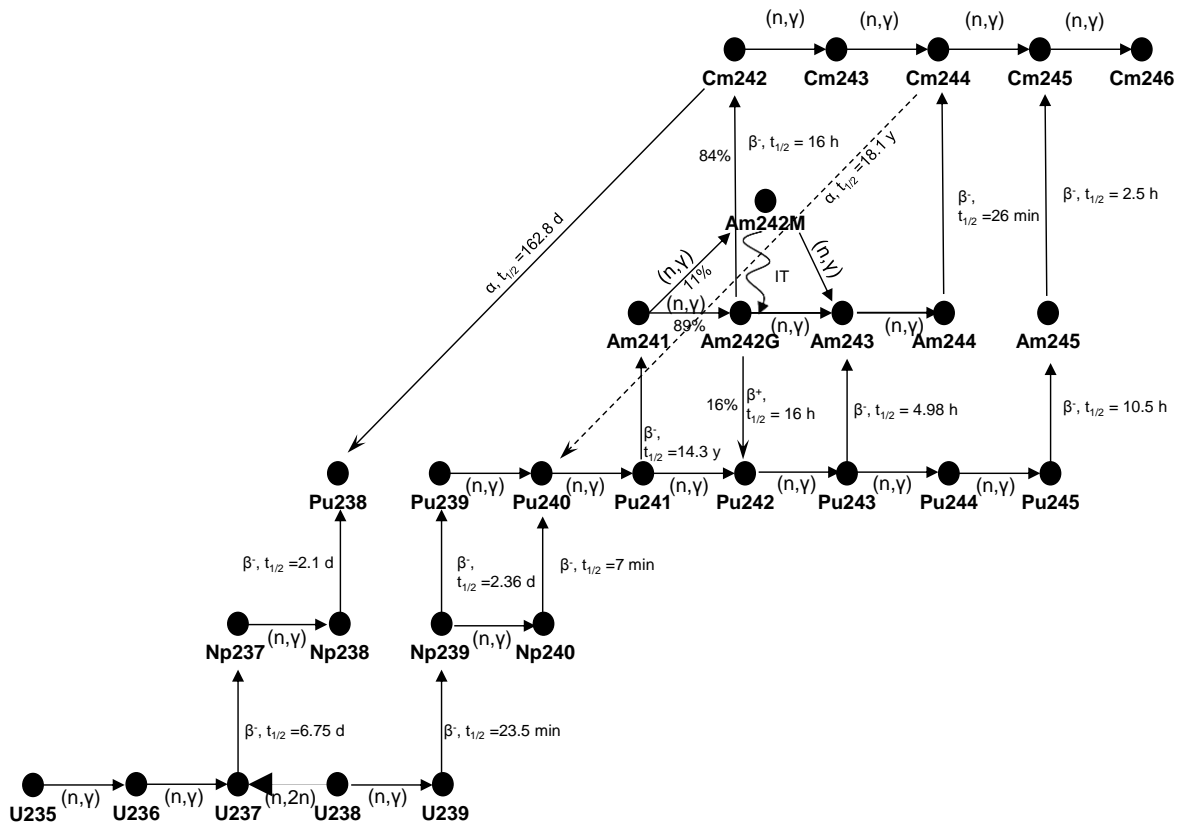
Figure 2-3. Uranium conversion chain (several α-decay processes have been omitted for simplification).

The degree of conversion in a nuclear reactor reflects the breeding potential of a core and is defined as the conversion ratio. It is the ratio of fissile material produced to fissile material destroyed (both through capture and fission) – Eq. 2-1 [21].

$$CR = \frac{number \quad of \quad fissile \quad nuclei \quad produced}{number \quad of \quad fissile \quad nuclei \quad destroyed} = \frac{P}{A} \qquad \textbf{2-1}$$

If CR>1, the reactor is called a breeder i.e. it produces more fissile material than it consumes. In practice, fast neutron reactors with MOX fuel can become breeders only if a fertile blanket is placed at the periphery of the core. Neutrons escaping from the fissile core are then absorbed in the blanket. Blankets are efficient in FRs as neutrons have a higher probability to leak (compared to thermal reactors) from the fissile core due to the high neutron energies (and their long neutron mean free path).

If CR=1, the reactor is an iso-generator which means that it consumes as much fissile material as it produces.

In order to be actually able to breed, enough surplus neutrons have to be available. This is usually measured through the reproduction factor η defined as the number of neutrons produced through fission per absorption, see Eq. 2-2 (where Σ_f^{fuel} and Σ_a^{fuel} are the macroscopic fission and absorption cross-sections in the fuel, respectively, and ν is the number of neutrons emitted per fission)

$$\eta = v \frac{\Sigma_f^{fuel}}{\Sigma_a^{fuel}}$$

2-2

One neutron has to be saved for the reaction chain. In order to breed, at least one additional neutron has to be used for replacing the destroyed fissile isotope by a neutron capture reaction in a fertile isotope. Considering that some neutrons might be lost through leakage from the reactor or through parasitic absorption e.g. in the structures (denoted L) Eq. 2-3 has to be satisfied in order to achieve breeding.

$$\eta \geq 2 + L$$

2-3

The loss term is always greater than zero, but lower than one. Hence Eq. 2-3 can be simplified to Eq. 2-4.

$$\eta > 2$$

2-4

Looking at the main fissile isotope in a FR i.e. the ^{239}Pu, η increases (although not monotonously) from 2.04 in a thermal spectrum ($\sim$25 meV) to 2.45 in a fast spectrum [25].

In addition, the better fuel efficiency in FRs is related to the energy spectra of neutrons. In a thermal reactor interactions are mainly taking place at neutron energies of around 0.1 eV as can be deduced from Figure 2-4 [26]. This is due to the fact that a moderator (water and/or graphite) is present in the reactor, thus slowing down the neutrons from their emission energy ($\sim$2 MeV in average for neutrons coming from prompt fissions) to the thermal energy below 1 eV. In a fast spectrum, however, only a small amount of moderation occurs (mainly due to inelastic scattering in heavy metal, iron and sodium isotopes as well elastic scattering in oxygen and sodium isotopes) and the neutrons remain rather fast. Interactions hence occur at neutron energies of about 100 keV. Figure 2-4 displays the neutron energy spectra of several reactor concepts.
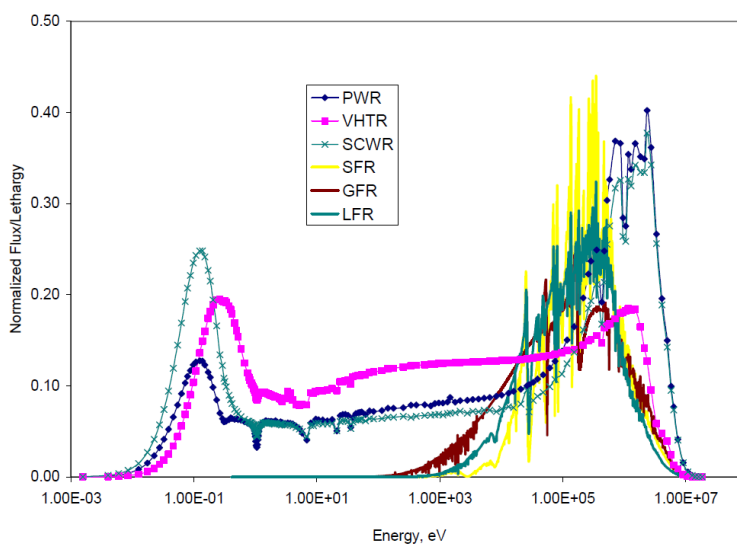
Figure 2-4. Normalized neutron spectra for different reactor systems [26].

The physics of the major actinides (i.e. uranium and plutonium isotopes) is very different in the thermal (<1 eV) and fast energy ranges. The fissile isotopes ^{233}U, ^{235}U, ^{239}Pu, ^{241}Pu are fissioning both when hit with neutrons in the low and intermediate to fast energy ranges. Fertile isotopes, however, as ^{238}U are essentially fissioning when bombarded with neutrons of higher energies i.e. of about 1 MeV or more.

2.3. Actinide transmutation

As mentioned earlier, plutonium can either be seen as fuel, as a material that has to be transmuted in order to reduce the long-term radiotoxicity of the SNF or as nuclear waste that will be sent to the geological repository. In addition to plutonium, MAs also have to be transmuted if reduction of radiotoxicity and mass of SNF is intended.

When looking at the fission over absorption ratios of all considered isotopes - Figure 2-5 - an increase in the fast energy range is observed: from 60-80% in thermal reactors to 80% in fast reactors for the fissile isotopes (essentially ^{235}U, ^{239}Pu, ^{241}Pu) while the fertile isotopes increase from <5% in thermal reactors to almost 50% in fast reactors. This implies that FRs are efficiently destroying MAs through fission hence avoiding or at least reducing the production of heavier actinides (through capture).
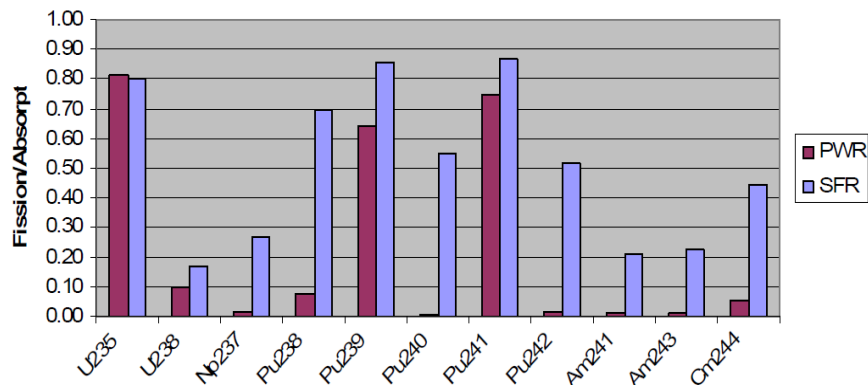
Figure 2-5. Fission over absorption ratios in thermal and fast spectra of the main actinides [26].

In order to reach high transmutation rates, usually multi-recycling has to be envisaged. The transmutation performances and the transmutation rate are usually the adequate quantities to compare the transmutation capabilities and capacities of different types of reactors. The transmutation performance, TR, is defined in Eq. 2-5 (where m is the mass) and is expressed in kg/TWhe. The transmutation rate, Y, is defined in Eq. 2-6 (efpd stands for equivalent full power days, N for the minor actinide inventory) and is expressed in percent.

$$TR = \frac{m_{heavy\ atoms\ of\ MA\ in\ fresh\ fuel} - m_{heavy\ atoms\ of\ MA\ at\ end\ of\ irradiation}}{E_{irradiation\ lifetime}} \qquad \textbf{2-5}$$

With

$$E_{irradiation\ lifetime} = efpd * ElectricPower * 24$$

$$Y = \frac{\Delta N_{MA}}{N_{MA}}$$

2-6

Two transmutation modes are envisaged for burning minor actinides in solid fueled reactors: the homogeneous and the heterogeneous modes. In the former one, minor actinides are mixed to the standard FR MOX fuel. In the latter one, MAs are transmuted in dedicated targets (blankets) usually placed at the periphery of the core. It is worth mentioning that in this case the MAs can be inserted in an inert matrix [27; 28] or in a depleted uranium matrix.

Depending on the chosen option for transmutation, the fuel cycle will be more or less impacted and the efficiency of the transmutation will be more or less high. Figure 2-6 recalls the different cycles when considering one option or the other.
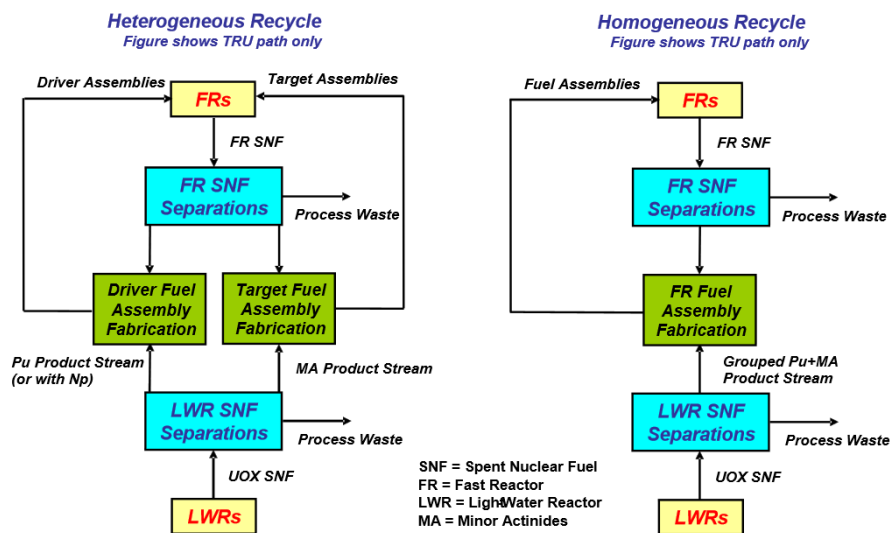
Figure 2-6. Fuel cycle in the heterogeneous and homogeneous recycling options [10].

2.4. Sodium cooled fast reactors

As mentioned earlier, several concepts of GEN-IV reactors are developed throughout the world. However, the sodium cooled fast reactor is the most advanced technology of the GEN-IV concepts since several reactors were already built and operated worldwide. To be cited are the PHENIX [4] and SUPERPHENIX [4] reactors in France, JOYO [4] and MONJU [4] in Japan, BN-600 [4] in Russia or EBR-I and EBR-II in the USA [4; 29].

Sodium cooled fast reactors usually display a near cylindrical arrangement of hexagonal fuel elements. Two to three enrichment zones are considered in SFRs in order to obtain a flat radial power profile. As mentioned in the previous section, the neutron energy spectrum is peaked at around 100 keV.

2.4.1. Sodium as a coolant

From the neutronics point of view sodium is almost transparent for neutrons [30; 31]. Its capture cross section is low, thus allowing a better neutron economy – more neutrons are available to the reaction chain - though [23]Na has a rather high resonance at about 2.8 keV. The capture resonance integral is, however, fairly low compared for example to its scattering one and is comparable to the one of structure material components as iron ([56]Fe) [32; 33]. Furthermore, the small ratio of capture to scattering processes in this resonance is illustrated by the ratio of the associated radiative width to neutron width for that resonance [33]. In addition, moderation in sodium is rather low (compared to hydrogen or helium for example) which keeps the neutrons at higher energy [34].

Sodium is characterized by a very high thermal conductivity in comparison with other coolants – Table 2-2. The heat transfer will thus be very efficient. However its heat capacity is moderate. As its density and viscosity are quite low, the mass flow rate can, however, be increased to limit the increase in sodium temperature at nominal conditions with a limited increase in the pump power. In addition, due to its high thermal conductivity and other good thermal properties, sodium supports a good natural convection. This is of high advantage in case of an unexpected pump coast down since the cooling of the core will be assured naturally [34].

Sodium has a large thermal inertia, and a large temperature difference between its melting and boiling temperature at atmospheric pressure (delta of 785 K – see Table 2-2) thus inducing some flexibility in choosing the operating temperatures at atmospheric pressure (no pressurization has to be applied). As a consequence, the thermal efficiency of the whole plant can reach 40% [34]. In the European Sodium Fast Reactor (ESFR) core [35] (chapter 3) sodium enters the core at 668 K and exits it at 818 K leaving a margin to boiling of 338 K. This increases the grace time in case of an accident.

Table 2-2. Main properties of liquid metal coolants [36].

Properties		Units	Na	Pb	Bi	Pb-Bi
Atomic number		—	11	82	83	—
Atomic mass		—	22.99	207.2	208.98	—
Melting temperature	°C		98	327.4	271.4	125
	K		371	600.85	544	398
Boiling temperature	°C		883	1 745	1 552	1670
	K		1 156	2 018	1825	1943
Heat of melting	kJ/kg		114.8	24.7	54.7	38.8
	kJ/mole		2.6	5.1	11.4	8.07
Heat of vaporization	kJ/kg		3871	856.8	852	852
	kJ/mole		89.04	178	178	178
Density	sol. 20°C	kg/m^3	966	11 340	9 780	10 474
	liq. 450°C		845	10 520	9 854	10 150
Heat capacity	sol. 20°C	kJ/kgK	1.23	0.127	0.129	0.128
	liq. 450°C		1.269	147.3	150	146
Thermal conductivity	sol. 20°C	W/mK	130	35	8.4	12.6
	liq. 450°C		68.8	17.1	14.2	14.2
Kinematic viscosity (450°C)		m^2/s	3×10^{-7}	1.9×10^{-7}	1.3×10^{-7}	1.4×10^{-7}
Prandtl number (450°C)		—	0.0048	0.0174	0.0135	0.0147
Surface tension (450°C)		mN/m	163	480	370	392
Volume change with melting		%	+2.6500	+3.6	−3.3	~ +0.5

From the chemical point of view, sodium is not corrosive as long as the impurity concentration of oxygen and carbon is kept low. As example, O_2 has to be limited to 5-10 ppm while C has to be kept below 50 ppm [34]. A high corrosion implies that radioactive products will be eroded from the clad and wrapper and transported all the way to the intermediate heat exchangers thus making maintenance and repair activities more difficult. In existing FRs, a continuous purification avoiding corrosion is hence performed.

The main issue related to the use of sodium is its exothermic reaction with air and water. Sodium fires due to oxidation of sodium through contact with air were already experienced in the MONJU reactor for example [37]. They can be avoided in the radioactive primary system by enclosing it in cells or double walled piping filled with nitrogen or argon. Leak tightness of the cooling system is ensured through detection systems. Fire extinction systems are also present [34].
Non-radioactive sodium from the secondary system can interact with water in the steam-generators in case of a tube failure. A high pressure water steam jet would be injected into the sodium inducing a violent reaction with temperatures around 1300 ˚C. An exothermic reaction (Eq. 2-7) would occur producing sodium hydroxide and hydrogen with pressures of 9-13 MPa in the reaction zone [34].

$$2Na + H_2O \rightarrow Na_2O + H_2 \qquad \textbf{2-7}$$

In order to avoid a pressure buildup, steam generators are equipped with a pressure relief system: a rupture disk breaks on the sodium side, pushing the sodium, hydrogen, and sodium hydroxide into a reaction tank. Hydrogen is then separated from the other components and vented to the air where it burns. Detectors closely monitor such type of accident, immediately shutting down the steam generator.

Another drawback of sodium compared to e.g. water is its opacity. In fact, inspection maintenance and supervision of e.g. refueling or repairs have to be performed with ultrasonic devices.

2.4.2. Kinetic parameters and feedback effects

The control of the power of a nuclear reactor is a key parameter for operational reactor safety. The power is closely linked to the neutron population. The variation in the neutron population can be expressed as Eq. 2-8[1] (time-dependent). In this equation, β is the delayed neutron fraction i.e. the ratio of the amount of delayed neutrons to the total amount of neutrons, l is the neutron lifetime, ρ is the reactivity, $\sum_k \lambda_k c_k$ is the amount of delayed neutrons (produced by radioactive decay of all precursors, c_k being the neutron precursor concentration) and S is an external source. In case there is no external neutron source, as long as the positive reactivity insertion ρ is lower than the delayed neutron fraction β the neutron population increase can be controlled. However, if ρ is higher than the delayed neutron fraction, the neutron population will increase exponentially. Thus, the higher the value of the delayed neutron fraction β, the easier it will be to control the reactor [21].

---

[1] This equation will be detailed in chapter 6.

$$\begin{cases} \dfrac{dn}{dt} = \dfrac{\rho - \beta}{l} n + \sum_k \lambda_k c_k + S \\ \dfrac{dc_k}{dt} = \dfrac{\beta_i}{l} n - \lambda_k c_k \end{cases}$$

<div align="right">**2-8**</div>

Depending on the fuel type, the amount of delayed neutrons in the reactor varies. The delayed neutron fraction of ^{238}U for example is of 1580 pcm while the one of ^{235}U and ^{239}Pu are of 680 pcm and 215 pcm, respectively [38]. In a typical PWR, the delayed neutron fraction will hence be of 730 pcm considering that 93% of the fission comes from ^{235}U and 7% come from ^{238}U. In a FR however, where MOX fuel is used as standard fuel, the average delayed neutron fraction is of only 350 pcm. This already indicates that fast reactors will tolerate lower reactivity insertions as a PWR. However, the reactivity insertions during an excursion in a LWR are larger than in a FR [39].

Any reactivity variation brings along associated reactivity effects. These feedbacks play an important role in the control of the reactor [40]. Three categories of feedback effects can be distinguished: the Doppler effect due to the temperature driven broadening of fission and capture resonance cross-sections, the effect of material densities (coolant in nominal conditions and e.g. fuel or steel in a molten configuration) and the effect of thermal expansion of materials.

The Doppler effect

The Doppler effect is related to the thermal motion of nuclei. In fact, if this motion of the nuclei of the various reactor components becomes more intense (due to temperature increase) it modifies the relative velocity of an incident neutron in relation to the nucleus thus inducing a broadening of the capture and fission cross-sections. The effect is mainly for ^{238}U, as for fissile isotopes the influences of fission and capture resonances practically compensate. In a reactor the resonance escape probability which is the fraction of fission neutrons that manage to slow down from fission to lower energies without being absorbed in the resonances decreases with increasing temperature and the Doppler effect is negative. This effect varies with the spectrum of the reactor since it occurs at resonances [34].
The Doppler effect is quasi-instantaneous[2], unlike e.g. coolant density effects. In order to correlate the reactivity change due to the Doppler effect with the fuel temperature change, the Doppler constant approximation is used (Eq. 2-9). Eq. 2-9 should not be considered as a rigorous law but it can be applied to most FRs as a reasonably good approximation [34; 25]. The Doppler constant K_d is defined in Eq. 2-10 where T_0 and T are two different fuel temperatures. Even for the same type of FRs it depends on the coolant volume fraction and density.

$$d\rho = K_d \frac{dT}{T}$$

<div align="right">**2-9**</div>

---

[2] Experiments specifically dedicated to the Doppler effect were carried out at the Southwest Experimental Fast Oxide Reactor (SEFOR) [34; 41].

$$K_d = \frac{\rho - \rho_0}{\ln\left(\dfrac{T}{T0}\right)}$$

<div align="right">**2-10**</div>

Material density effects

- Sodium density effect

The expansion effect of sodium induces a decrease in the sodium density. This affects the neutron reactions in three ways: it simultaneously decreases the amount of scattering collisions and of absorptions between neutrons and the coolant, and increases the neutron leakage. The reduced scattering induces a positive reactivity insertion due to the hardening of the neutron spectrum (i.e. the average energy of neutrons is increased compared to before). Similarly the decrease of absorptions on sodium leaves more neutrons available to the reaction chain hence provoking a positive although small reactivity increase. The lower collision scattering probability additionally increases the neutron mean free path, defined as the average distance a neutron travels after a collision with a nucleus before interacting with another nucleus, thus increasing the neutron leakage (more neutrons will escape from the core, especially in the outer core zones) and introducing a negative reactivity effect. The overall effect of sodium expansion is usually positive, especially in large sodium cores. When during an accident the reactor is voided, the coolant void effect is, thus, in general positive unless special designs are considered [42]. Most accidents to be considered in sodium fast reactor safety analyses are impacted by the sodium void reactivity effect. In small cores the sodium expansion effect for the whole core can be negative if the core is designed to enhance the neutron leakage [34].

When accidental conditions are analyzed, it also becomes important to consider the density effect of moving fuel and steel.

Thermal expansion reactivity effects

The thermal expansion effects concern the fuel, the structures, the diagrid, the control rod drivelines and the vessel.

- Fuel expansion effect

The thermally driven expansion of fuel is split into an axial and a radial component.
The axial fuel expansion has a threefold effect. It locally reduces the fuel density thus causing the reactivity to decrease, it increases the total fissile height causing the reactivity to increase and finally it increases the sodium mass in the core due to the increase in the fissile core height (this effect corresponds to an increase in the sodium density). The axial fuel expansion effect is globally negative. The radial fuel expansion (within the pins) has no effect on the reactivity as it does not decrease the sodium density in the core (unless there is a sodium gap as in metal fuel pins; the minor relocation of sodium in such pins has nonetheless a minor impact on reactivity). In fact, the radial fuel expansion is restrained by the cladding expansion. However, cladding expansion will have an effect on reactivity.

- Thermal expansion effect of structures

The thermal effect of structures includes the dilatation of cladding and hexagonal wrappers. It occurs both in axial and radial direction. An axial dilatation of structures induces a local decrease of steel density, thus decreasing the absorption probability in steel. The reactivity is consequently increased. Furthermore, a radial dilatation of the pins (or the hexagonal wrapper tubes) causes the sodium fraction to decrease in the unit cell. The amount of sodium in the core is hence reduced and the neutron spectra hardens, leading both to an increase of fissions and neutron leakage. The overall reactivity effect of this structure dilatation is positive in a not "flowering" core design.

- Fuel bowing

Fuel bowing depends on the temperature distribution and its time-dependent variation across the core. It is induced by temperature gradients, swelling gradients or temperature creep through the fuel pin or fuel assembly [43]. The related strain causes a pin or assembly displacement (leading the pin or assembly to bow), thus moving the fuel into an area with lower or higher neutron importance, causing a reactivity change [44]. This reactivity feedback is highly complex and depends on the core design and, in particular on the core clamping system. Modern FR fuel pins are assembled in such a way that no fuel bowing occurs in the pins themselves, making the non-uniform temperatures across the fuel assemblies the main driver for fuel bowing [44; 43]. The way the assemblies are supported by the diagrid and within the core barrel highly contributes to this reactivity effect. For example, the core restraint system – if present – can consist of one or several restraint points at the assembly nozzle and several load pads on the wrapper tubes [45]. Depending on the core clamping system, the displacement of assemblies may differ appreciably as will the related reactivity effect (it can be positive or negative).

- Diagrid expansion effect

The diagrid expansion is caused by fluctuations in the temperature of the incoming sodium. This might happen e.g. when the electricity demand decreases and the tertiary system consequently imposes a smaller power production from the core. The diagrid onto which the assemblies are plugged will then expand, pushing the assemblies further from one another. More sodium will flow into the core and the relative volume of sodium to fuel will increase. However, the core radius will also increase while the fuel mass remains constant: neutron leakage will thus be enhanced. The overall effect of diagrid expansion remains negative. During fast transients, the diagrid expansion will however not play an important role due to the thermal inertia of the diagrid (tens of seconds).

- Control rod driveline and vessel differential expansion

Another expansion feedback effect is coming from the differential expansion of core, vessel and control rods - Figure 2-7. This feedback effect is composed of three different effects: an increase in fuel temperature, an increase in the coolant outlet temperature, and an increase of sodium temperature in the cold pool[3]. The first effect will cause the fuel to expand axially, thus making the

---

[3] Cold sodium from the primary pumps enters the core at its bottom and heats up. The hot sodium then flows upwards into a large sodium pool (hot pool). It then passes usually through the intermediate heat exchangers

control rods to be inserted in the core if they are hanged from the top. This will lead to a decrease in the reactivity. The second effect will induce an axial expansion of the control rod causing again an insertion of the controls rods into the core. This second effect has a negative effect on the reactivity. The third effect will cause an axial expansion of the vessel towards the lower part of the core. The control rods will thus have a lower relative removal/insertion. All three effects depend on different time constants.

The total differential effect relies on the changes of sodium inlet and outlet temperature and on the expansion coefficients of fuel, vessel and control rods.
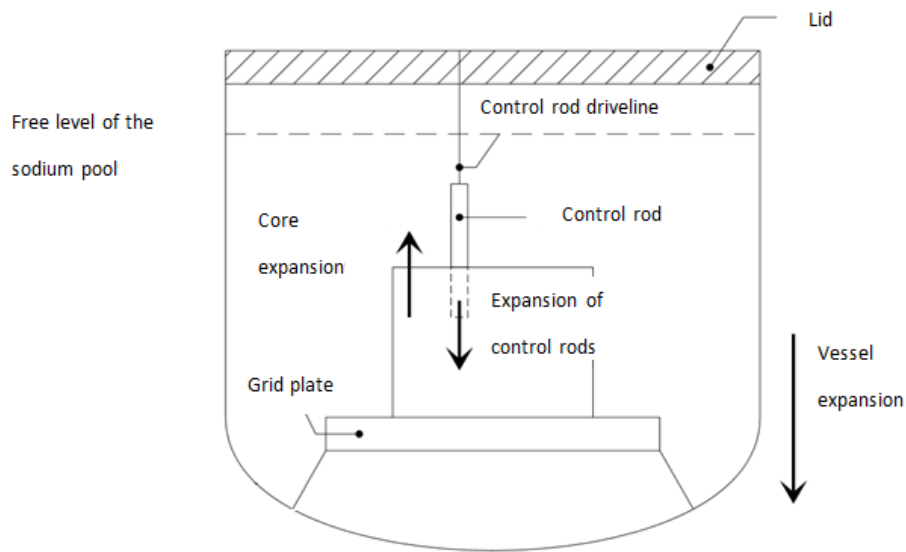
Figure 2-7. Schematics of the control rod driveline and vessel differential expansion [46].

Typical values of reactivity feedbacks [47] are presented in Table 2-3 for the 3000 MWth sodium cooled fast reactor SUPERPHENIX [4].

Table 2-3. Typical values of reactivity feedbacks in the SUPERPHENIX reactor [47].

Type of effect	Effect	Related To	Value pcm/°C
Intrinsic	Doppler	T fuel	-0.08
Local	Sodium density	T sodium	+0.33
	Cladding radial	T cladding	+0.08
	Cladding axial	T cladding	+0.07
	Wrapper tube radial	T wrapper tube	+0.01
	Wrapper tube axial	T wrapper tube	+0.04
	Fuel axial (linked)	T cladding	-0.31
	Fuel axial (free)	T fuel	-0.22
Global	Diagrid radial	T diagrid	-1.01
	Relative expansion core/ vessel /control rods	T core, T control rods, T vessel	Dz = 12 mm/°C

(from top to bottom) where it is cooled down. The sodium then flows into a large sodium pool (cold pool) where it is taken from the pumps and forced back into the core [34].

The diagrid, clad axial, and fuel axial expansion feedback modeling under transient conditions is closely investigated in this PhD thesis. They are referred to core thermal expansion feedbacks throughout the thesis.

2.5. Impact of minor actinide transmutation on SFR core performances and fuel cycle

As described earlier, two main transmutation modes are considered for reducing the nuclear waste mass and radiotoxicity: the homogeneous and heterogeneous modes.

The homogeneous mode is based on reprocessing of the spent nuclear fuel to recover actinides (Pu, Am, Cm, Np). The actinides are then mixed homogeneously with ^{238}U for fabrication of fresh fuel, and loaded in the core. In the heterogeneous recycling option, minor actinides (Am, Cm, Np) are put into dedicated assemblies that are placed at the periphery of the core (radially and/or axially). The fuel is a binary mixture of uranium and minor actinides (in some designs the addition of moderating material such as ZrH$_x$ is considered for increasing the capture reaction probability).

Both options present advantages and drawbacks. The homogeneous mode does not allow a high content of MAs in the fresh fuel. This is mainly related to safety, since feedback coefficients are worsened with the introduction of MAs in the driver fuel [10; 48]. In addition, the whole fuel cycle is impacted by the homogeneous mode as there is no separation of the standard driver fuel (MOX) and MAs. The existing fabrication and reprocessing facilities as well as the transportation and handling have hence to be adapted (e.g. considering remote operations). In addition, the very high content of MAs in the fuel leads to an increase of the helium production under irradiation thus impacting the sub-assembly design. The heterogeneous mode on the other hand allows charging a higher content of MAs (up to 20%) than in the driver fuel since this option has a very small impact on safety feedbacks. A considerable advantage of this option is that the management of the dedicated assemblies is decoupled from the standard fuel, hence leaving the existing facilities of the LWR MOX fuel cycle unperturbed [10]. However, dedicated facilities have to be built.

In the next sections, the main impacts of one and the other modes on core performance and fuel cycle are displayed for a 3550 MWth sodium cooled fast reactor [49].

2.5.1. Transmutation performance

For an initial mass of minor actinides of 2.4 tons, the heterogeneous option with radial blankets and the homogeneous option are compared. This mass corresponds to a 3.2% volume content of MAs in the homogeneous mode and 20% in volume in the heterogeneous mode. For the homogeneous mode, only the transmutation of americium was considered, while for the heterogeneous one a case with americium only and a case with all minor actinides (i.e. Am, Cm and Np) were considered [49].

The heterogeneous options show transmutation performances close to the homogeneous mode. This is due to the fact that the residence time of sub-assemblies in the radial blankets is twice as long as the one of driver fuels since the neutron flux and the corresponding displacement per atom (dpa)

values of structure materials at the periphery of the core are lower than in the core. The same trend could be obtained by adding some moderator material to soften the spectrum and reach a better transmutation rate in the blankets.

Transmutation rates as high as -28% are observed. As concerns the transmutation performance (kg/TWhe), the homogeneous mode shows the highest value (Table 2-4) [49].

Table 2-4. Characteristic transmutation rates and transmutation performances in a 3550 MWth sodium cooled fast reactor for different transmutation strategies [49].

	Homogeneous	Heterogeneous	
	3.2% Am	20%Am	20%MA
Charged mass (kg)			
Np	0	0	411
Am	2429	2438	1866
Cm	0	0	160
MA	2429	2438	2437
Discharged mass (kg)			
Np	43	20	265
Am	1435	1493	1101
Cm	390	242	223
MA	1867	1589	1755
Transmutation rate at end of life (2050 efpds) (%)			
Np	-	-	-35.5
Am	-40.9	-38.7	-41
Cm	-		+39
MA	-23.1	-28	-34.8
Mass balance at end of life (2050 efpds) (kg/TWhe)			
Np	+0.60	+0.14	-1.02
Am	-13.93	-6.62	-5.36
Cm	+5.46	+1.7	+0.44
MA	-7.87	-4.79	-5.94

2.5.2. Impact on core performances

Although high transmutation rates are desired, the introduction of MAs in the reactor should, however, not deteriorate too much the neutronics parameters and reactivity feedbacks. Adding MAs into a critical core has the following effects:
- Hardening of the spectrum
- Decrease in the fuel temperature coefficients i.e. the Doppler effect. This is related to the substitution of ^{238}U (main contributor to Doppler effect) by minor actinides.
- Increase in the coolant void reactivity effect. This is due to the increased fissile nature of minor actinides in a fast spectrum.
- Decrease of the delayed neutron fraction;
- Decrease of the prompt neutron lifetime;
- Less pronounced reactivity swing (MAs acting as burnable poisons);
- Decrease in the axial expansion coefficient;
- Decrease in the radial expansion coefficient;

- Decrease in the fuel density coefficient;
- Decrease in the structure density coefficient

In [10] analyses of a large 1500 MWe sodium cooled fast reactor are presented. The MA content in the homogeneous recycling fuel was increased from 0 to 10%. In this case, the coolant void reactivity effect increased by almost 20%, the Doppler constant decreased by almost 50%, the effective delayed neutron fraction decreased by about 15%, and the burnup reactivity swing by about 40%.

As mentioned previously, the delayed neutron fraction allows controlling the power of a reactor and a lower value is associated to a more "nervous" reactor, since the power control is more sensitive to reactivity changes.

It has already been mentioned that the deterioration of the reactivity feedbacks is much less pronounced if MAs are transmuted in specific assemblies surrounding the fissile core (heterogeneous transmutation strategy). This is confirmed as well in [49] for lower amounts of MAs (Table 2-5). This is due to the fact that at the periphery of the core, the neutron flux and especially the neutron importance are already rather low.

Table 2-5. Main neutronic parameters and reactivity feedbacks in homogeneous and heterogeneous recycling [49].

	Reference core	Homogeneous	Heterogeneous	
	0.1%Am	3.2% Am	20%Am	20%MA
Δρ cycle (pcm)	-450	300	-250	-270
βeff	369	346	365	365
Void effect ($)	4.9	5.4	4.9	4.9
K_D (pcm)	-888	-723	-886	-885

However, not only the core performances but also the front-end and back-end of the nuclear fuel cycle are impacted by the introduction of MAs.

2.5.3. Impact on fuel cycle

Front-end of the fuel cycle

The MAs present in the fresh fuel challenge the fabrication, storage and handling steps.

In the heterogeneous mode, the very high amount of minor actinides in the fresh fuel causes the thermal power, the neutron source and the dose rate to be significantly higher than in standard MOX driver fuel. The homogeneous mode where minor actinides are put within the standard driver fuel is advantageous from the handling point. In fact, at the fabrication stage only few percent of MAs are added to the driver fuels (due to safety reasons as mentioned previously) hence limiting the neutron emissions and the thermal power of fresh fuels – Table 2-6 [49].

It can be noticed from Table 2-6 that as soon as other minor actinides are added in the core in addition to americium, the heat release is increased by a factor 3 and the neutron source is increased by more than one order of magnitude compared to the reference.

Table 2-6. Thermal power and neutron source per fuel assembly for fresh fuel with and without considering transmutation [49].

	Reference	Homogeneous	Heterogeneous	
	0.1% Am	3.2%Am	20%Am	20%MA
Thermal power (kW)	0.75	1.17	2.35	7.19
Neutron source (10^7 n/s)	3.8	4.8	6.8	190

Back-end of the fuel cycle

The same tendency as in the pre-irradiation phase is seen in the post-irradiation phase [10].

The heat level is mainly driven by curium. Curium is produced under irradiation through captures in ^{241}Am. In the heterogeneous modes, the current limit of 40 kW to handle assemblies is reached after 10 days – during this time, the fission products drive the decay heat. The limit value of 7.5 kW to clean the assemblies is reached after 1000 days in comparison to 2 and ~100 days for the standard MOX fuel – Figure 2-8. For the homogeneous mode, the decay heat of the homogeneous recycling fuel follows the same tendency as the standard MOX fuel. In comparison with the heterogeneous recycling option, the fuel can be handled and cleaned much earlier (3 and 200 days respectively) – Figure 2-8.

The neutron emissions are increased by more than one order of magnitude in all recycling options compared to the reference case (1.10^9 n/s).
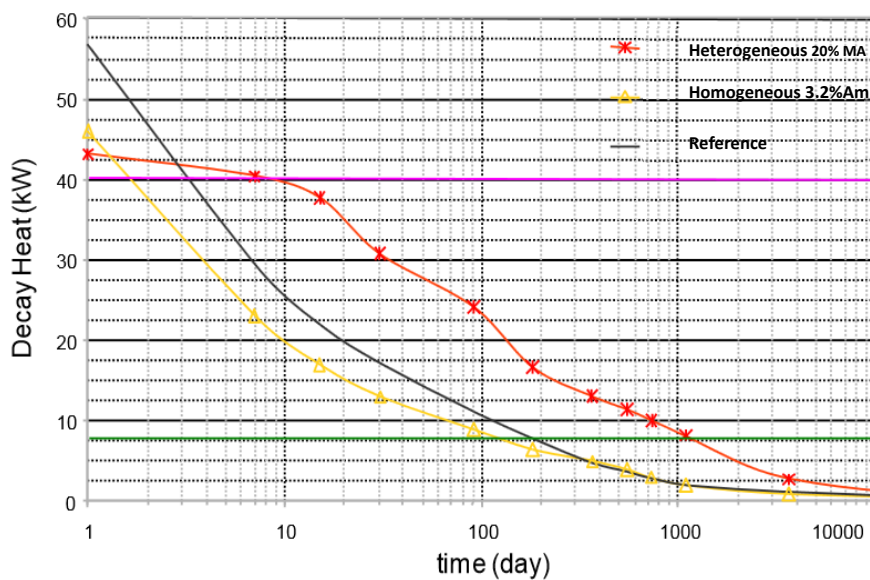
Figure 2-8. Decay heat temporal evolution for irradiated fuel in the heterogeneous, homogeneous and reference (no transmutation) strategies [10].

In conclusion, both the heterogeneous and the homogeneous transmutation mode are feasible, each of them presenting some advantages and drawbacks, the main ones being recalled hereafter.
With the homogeneous mode, fuel fabrication is easier compared to the heterogeneous mode but impacts the whole fuel fabrication chain. The fuel behavior under irradiation is close to the standard

one. The homogeneous mode impacts the core reactivity coefficients, limiting the MAs content to about a few percent of the total heavy isotopes within the fuel. A higher content would require a redefinition and optimization of the core design (compared to the standard one) [10].

With the heterogeneous mode, the fuel fabrication is more complex than in the homogeneous route but it is concentrated on a limited number of sub-assemblies and does not impact the standard fuel cycle since dedicated facilities have to be built. The fuel behavior under irradiation differs from the standard one due to a large production of curium and a large helium release, thus requiring validated target designs. The heterogeneous mode shows no impact on the main reactor core parameters. However, a higher thermal load of SNF compared to the standard one limits the minor actinide content within targets and requires a new handling process at reactor stage [10].

2.6. Conclusion

In this chapter, the nuclear waste issue has been addressed. The new generation of reactors and especially the fast reactors are a suitable solution to cope with this issue. Several options to reduce the radiotoxicity of nuclear waste are currently investigated. Each of them implies advantages and drawbacks in the core performances and in the fuel cycle. A compromise between high transmutation rates and acceptable impacts on the fuel cycle and its economics has to be found. For the present PhD work, focus is put on the homogeneous recycling strategy. In the previously mentioned PELGRIMM project (Chapter 1), the safety behavior of two different fuel forms (pellet and sphere-pac), with and without minor actinides is analyzed. Especially the sphere-pac fuels are of high interest when it comes to recycling of minor actinides since the helium production from minor actinide decay can be accommodated more easily in those pins. Analyses are performed under nominal and accidental conditions and consequently an overview of the safety approach of sodium cooled-fast reactors is proposed in the next chapter.

Chapter 3

SAFETY APPROACH FOR SODIUM COOLED FAST REACTORS

Fast reactors (FRs) constitute an unprecedented technology towards a sustainable energy source. Among all FR systems, the Sodium cooled Fast Reactors (SFRs) present currently the most comprehensive technological knowhow due to a large experience gained with several operating systems. However, SFRs, as FRs in general, are not in their most reactive neutronic configuration (i.e. they can become more reactive in case of a perturbation) thus requiring the investigation of particular transients (e.g. seismic ones) and Hypothetical Core Disruptive Accidents (HCDAs).

Indeed in case of an accident, where e.g. the coolant is lost or fuel compacts, SFRs become neutronically more reactive quite to the contrary of thermal reactors. This is mainly caused by their high enrichment of 15 – 30 % fissile material to compensate for the higher leakage.

In thermal reactors currently in operation, where the average neutron energy is about 25 meV, if the coolant boils neutrons are no longer moderated and the chain reaction ceases itself[4]. On the contrary, in SFRs, where the average neutron energy is about 0.1 MeV, if the coolant boils or its density is significantly reduced in central regions of the core, the already modest moderation coming from sodium is reduced, neutrons become faster and the spectrum hardens. Due to the fuel composition used in SFRs and to the energy dependence of the reproduction factor η of e.g. plutonium – increasing with energy – the reaction chain is enhanced. The neutrons become thus more important to the reaction chain when the energy increases. This can be seen by the adjoint flux i.e. the neutron importance. However, the coolant void is not the only feedback causing a reactivity change. Any material (fuel, steel, absorber) mobilized by melting or pin disruption causes reactivity changes. Other feedback effects as Doppler might partially counterbalance the positive coolant void. Nevertheless, a sequence of events – called scenario – might induce a degradation of the core which might lead to some reactivity increases due to e.g. material relocation or in-pool material motions.

Consequently, the study of sequences of severe accidents in SFRs becomes essential and possible recriticalities should be limited at any stage of the accidental scenario. The objectives of the study of HCDAs are thus twofold: it aims for prevention and mitigation of the accident. The former one is aiming at the conception of the reactor design such that the likelihood of an accident becomes low. The latter one focuses on the minimization of the consequences of an accident [50].

---

[4] However, even when the chain reaction has been terminated the fuel may melt due to the still prevailing decay heat and the interruption of coolant circulation (as was experienced e.g. in the Fukushima Daiichi accident in Japan in 2011).

3.1. The safety approach

The safety approach provides a methodology whose application allows to construct the safety architecture and to demonstrate that a nuclear power plant presents tolerable risks [51].

A risk can be defined as the product of the occurrence probability of a considered accident/incident with its associated consequences. The Farmer diagram - Figure 3-1 - describes a method to categorize accidents depending on their frequency[5] and their related consequences on the environment [52].

The key issue of the "Farmer diagram" is to assure extremely low consequences for frequent events and extremely low frequencies for highly destructive plant conditions. With the system architecture defined, it has to be proven that for all the conditions which the plant may experience the corresponding risk can be kept within the tolerable domain.
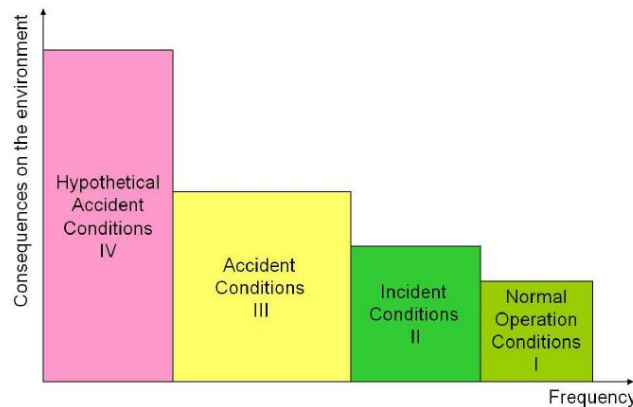
Figure 3-1. The Farmer diagram: categorization of incidental/accidental conditions according to their likelihood and their consequences [53].

For guaranteeing safety, **fundamental safety objectives** have been formulated by the International Atomic Energy Agency (IAEA) as follows [54]:

- **General safety objective**: "protect the public health by limiting the risk of radiological releases to tolerable levels".

- **Radiation protection objective**: "To ensure that in all operational states, radiation exposure within the installation or due to any planned release of radioactive material from the installation is kept below prescribed limits and as low as reasonably achievable (ALARA principle), and to ensure mitigation of the radiological consequences of any accident."

- **Technical safety objective**: "To take all reasonably practicable measures to prevent accidents in nuclear installations and to mitigate their consequences should they occur; to ensure with a high level of confidence that, for all possible accidents taken into account in the design of the installation, including those with a very low probability, any radiological consequences would be minor and below prescribed limits; and to ensure that the likelihood of accidents with serious radiological consequences is very low."

---

[5] Frequency is defined as events/(reactor · year)

A set of more practical safety targets completes the general safety objectives and leads to the following main guidelines for SFRs:

- **-** The safety objectives defined in the European safety framework for new nuclear plants and in particular the technical guidelines of the French EPR [55; 56] constitute the basis for SFR guidelines.

- **-** The fulfillment of the objectives is cumbersome and must be demonstrated in a robust way.

The safety objectives are achieved through **fundamental safety functions**:

- Reactivity control at any time from every state and condition

- Removal of heat and decay heat

- Confinement of radioactive material

The safety objectives and safety functions should be guaranteed via

- The Multi-barrier principle

- The Defence-in-Depth principle

3.1.1. The Multi-barrier principle

The multi-barrier principle provides the prevention and limitation of contamination outside the power plant in case an accident occurs. Several physical barriers are present between the fuel and the environment – Figure 3-2. Their number varies with the risk and aims at the implementation of progressive defence architecture [25]. One can cite four main barriers:

1. **The fuel matrix**. The fuel matrix retains most of the fission products.

2. **The cladding tube**. It prevents both fuel and fission gas release to the coolant.

3. **The primary circuit**. Depending on the reactor design it includes both the intermediate containment (e.g. main vessel) and the primary containment (e.g. security containment).

4. **The secondary containment** i.e. the reactor building.
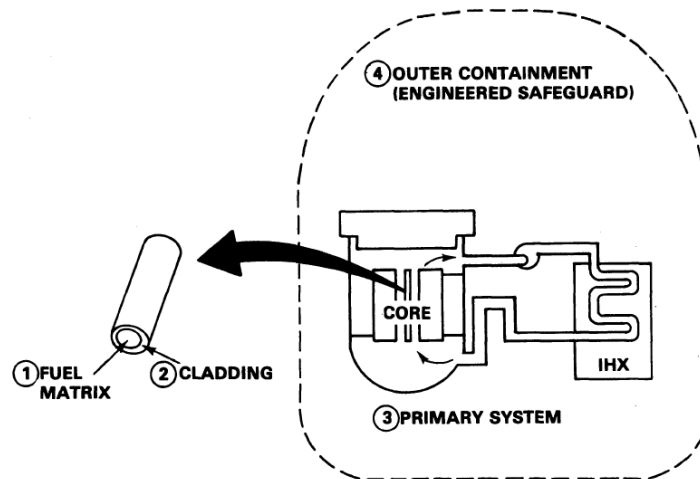
Figure 3-2. The multi-barrier approach [25].

3.1.2. Defence-in-Depth safety strategy

The Defence-in-Depth strategy helps to structure and implement the safety architecture, thus guaranteeing the efficiency of the barriers while keeping the risk of an accident acceptable. This principle consists "in the implementation of an appropriate set of successive provisions to ensure the protection against harms and in particular radiological ones in case of human error or equipment failure" [51]. Several strategies with respect to SFR risks aiming at the protection of the previously mentioned barriers are developed. They aim at controlling the reactivity level, removing the decay heat and confining the radioactive products [51] and target both the prevention and the limitation of potential consequences of an accident. The interrelation between the multi-barrier approach and the levels of Defence-in-Depth can be seen in Figure 3-3.
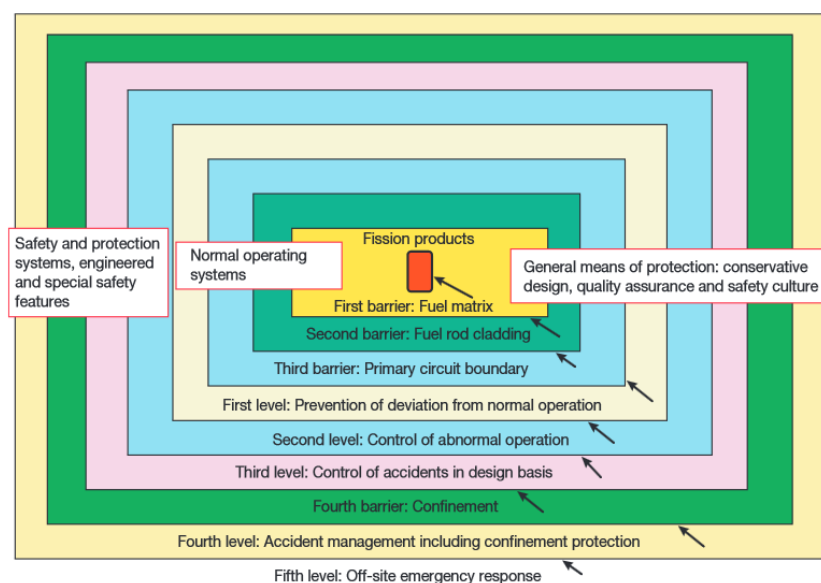
Figure 3-3. Interrelation between the multi-barrier approach and the levels of Defence-in-Depth [57]

According to the definition of IAEA safety standards, five levels of Defence-in-Depth have to be considered [54]:

1st level: Prevention of abnormal operation and failure: quality in design and achievement, prevention of nonconformity are mandatory.

2nd level: Surveillance, detection and control of operation and failure, quality of operation. The state of the facility must be kept within authorized limits.

3rd level: Control the accident to limit radiological release and prevent a development to core damage and whole core accidents. Thus safety systems and protection systems are designed for all plausible postulated incidents and accidents to limit their consequences within tolerable levels.

4th level: Control of whole core accident: accident management and containment protection to limit its consequences.

5th level: Limitation of significant radiological release and its consequences outside the site.

The different levels of Defence-in-Depth, objectives and associated plant conditions are displayed in detail in Table 3-1.

Table 3-1. Defence-in-Depth principle [58].

Levels of Defence-in-Depth		Objective	Essential means	Radiological consequences	Associated plant conditions
Level 1		Prevention of abnormal operation and failures	Conservative design and high quality in construction and operation, control of main plant parameters inside defined limits	No off-site radiological impact (bounded by regulatory operating limits for discharge)	Normal operation
Level 2		Control of abnormal operation and failures	Control and limiting systems and other surveillance features		Anticipated operational occurences
Level 3	3a	Control of accident to limit radiological releases and prevent escalation to core melt conditions	Reactor protection system, safety systems, accident procedures	No off-site radiological impact or only minor radiological impact	Postulated single initiating event
	3b		Additional safety features, accident procedures		Postulated multiple failure events
Level 4		Control of accident with core melt to limit off-site releases	Complementary safety features to mitigate core melt, management of accidents with core melt (severe accidents)	Off-site radiological impact may imply limited protective measures in area and time	Postulated core melt accidents (short and long term)
Level 5		Mitigation of radiological consequences of significant releases of radioactive material	Off-site emergency response. Intervention levels.	Off-site radiological impact necessitating protective measure	

The Defence-in-Depth Safety Strategy is elaborated in the following way:

- Initiating events of internal incidents and/or accidents are allocated to different categories which are associated to a range of occurrence frequencies.
- Higher radiological consequences must be connected with lower estimated frequencies.
- The occurrence frequency is generally assessed by safety analyses, engineering judgment and probabilistic studies. Normal and abnormal core/plant states evolving during anticipated transients are grouped into four categories which represent Design Basis Conditions (DBCs).
- Accidents belonging to Design Extension Conditions (DECs) are low frequency events considered in the design with respect to the application of the Defence-in-Depth principle and normally correspond to multiple failures of safety barriers.

The IAEA [59] defines the Design Basis Condition (DBC) as a sequence of events "causing accident conditions for which a facility is designed in accordance with established design criteria and conservative methodology, and for which releases of radioactive material are kept within acceptable limits". The DBC – formerly called Design Basis Accident (DBA) – is analyzed with a deterministic approach which will be presented in section 3.1.4. The accident starts with a postulated initiating event which leads the reactor to deviate from its initial state. All initial states of the plant have to be defined by the plant designers (steady state and operational transients). For each DBC the plant response has to be analyzed to verify that the acceptance criteria associated to each DBC are respected. The safety assessment of the plant is performed by analysis of these DBCs.

In the Defence-in-Depth concept, as described before, not only the DBCs but also the DECs up to severe accidents have to be prevented, controlled and their consequences to be mitigated and limited. The IAEA definition of a DEC is "accident conditions that are not considered for design basis accidents, but that are considered in the design process of the facility in accordance with best estimate methodology, and for which releases of radioactive material are kept within acceptable limits. Design extension conditions could include severe accident conditions" [59]. DECs have a very low occurrence frequency and usually correspond to multiple failures.

In detail the DBC and DEC conditions are grouped as follows:

Design Basis Conditions:
Category 1 (DBC 1): Normal operating conditions as steady state power operation, start-up and shut-down, load following operation etc.
Category 2 (DBC 2): Incidents and anticipated occurrences which might happen several times during plant life time.
Category 3 (DBC 3): Accidents considered in this category are not expected to occur during the life of the plant. Nevertheless, consequences are analyzed to demonstrate that these remain tolerable and radiological consequences stay below limits. The plant should be able to return to normal operation after inspection and repair.
Category 4 (DBC 4): Low probability events evaluated to demonstrate that safety systems are sufficient to prevent large radioactivity releases and protect the environment.

Design Extension Conditions (DEC)

Complex sequences: Accident sequences with failures of mitigating systems or components beyond those considered for DBC analysis. Consequences of these sequences are evaluated to demonstrate the efficiency of preventive measures against core damage.

Limiting events: Bounding accidents evaluated for investigating generic core and/or plant behavior. These postulated sequences should bound consequences related to specific technology issues and to common mode failure sequences. Demonstration that there are no cliff-edge effects especially concerning severe core damage has to be provided.

Severe accidents: Postulated accidents leading to severe core degradation. Simulations of these accidents should demonstrate that there are no cliff-edge effects to be expected and serve as support on possible mitigation measures to guarantee integrity of the primary system enclosure and the confinement/containment structures.

3.1.3.   Events and initiators

The demonstration of the suitability of a nuclear plant design with regard to the safety objectives is performed by considering two types of events: the "dealt-with events" and "the practically eliminated" events. The first category of accident corresponds to transients whose consequences are taken into account in the design of the plant. The second category of accident comprises a limited number of initiators, for which a robust demonstration is given and through the implementation of specific provisions it is shown that the corresponding risk is made acceptable and event initiators can be rejected within the Residual Risk (RR) [51].

Possible initiators:

Two approaches might be employed for identifying the possible initiating events of an accident. These events can either challenge confinement barriers themselves or initiate transients likely to challenge them. A first way to proceed with the identifications is to list pertinent initiating events based on engineering judgment using information from previous risk assessments, operating experience and plant specific design data. A second way is to employ top-down or bottom-up analysis techniques looking for risks that could challenge confinement barriers [51; 60].

All situations leading to core melting must be considered. A phase of identification of those situations for which the consequences cannot be minimized has to take place and provisions should be taken to practically eliminate their occurrence. The remaining situations must be examined and representative cases are selected for each family of accidents as not all accidents can be treated in full detail. The representative case has to be the most conservative one in the respective group.

While in the past a best estimate calculation was satisfactory enough for the safety demonstration, nowadays all hypotheses and uncertainties have to be carefully examined and/or proven to be representative of the worst situation in order for all situations to be within this envelope case [53].

The "Dealt-with events":

The previously mentioned Design Basis Conditions (DBCs) and Design Extension Conditions (DECs) are the two main considered categories of "Dealt-with events". Each category has its own frequency of occurrence [51].

The "Practically-eliminated events":

These situations are either of extremely low probability (beyond technical imagination) or have otherwise to be practically eliminated by design and prevention systems so that their occurrence is regarded as negligible. As a consequence, they do not need to be taken into account in the design of the plant. The choice whether or not these situations are excluded has to be firmly justified.

The initiating "Dealt-with events" of internal incidents and/or accidents which appear likely to occur and challenge the plants' safety are allocated to different categories which are associated to a range of occurrence frequencies (Table 3-2). Evaluation of the adequacy of a detailed design is made through consideration of these events. In addition, temperature criteria for e.g. clad and fuel have to be fulfilled: clad (respectively fuel) temperatures should not exceed 550 ˚C (respectively 2000 ˚C) in normal operation conditions and 650 ˚C (respectively 2250 ˚C) in incidental conditions [61].

Table 3-2. Categorization of initiating faults and related design targets [61].

Category	Safety target	Fuel limits	Fuel pin clad limit
1	Radiological release ALARA < 10 μSv/year	No fuel melting.	No open clad failure.
2 $f>10^{-2}$/year	Radiological release < 10 μSv/event	No fuel melting.	No open clad failure except random effects.
3 $f>10^{-4}$/year	Radiological release < 1 mSv/event	No fuel melting.	No systematic (i.e. large number of) pin failures.
4 $f>10^{-6}$/year	Maintaining core coolability. Radiological release < 50 mSv/event	Any predicted localized melting to be shown to be acceptable.	No systematic clad melting. No simultaneous and coincident clad failure and fuel melting.
Complex sequences and limiting events	Maintaining core coolability. Radiological release < 150 mSv/event	No extended core melting.	No systematic clad melting.
Severe accidents	Radiological release < 150 mSv/event	Coolability of the damaged core. No recriticality of the damaged core.	

3.1.4. Deterministic and probabilistic safety analyses

With the basic safety approach structured and defined, the effectiveness of the different principles has to be proven. This is performed with the help of detailed safety analyses.

Safety analyses involve deterministic and probabilistic analyses in support of the siting, design, licensing, operation and finally decommissioning of a nuclear facility. The analyses are performed to confirm that fundamental safety criteria and goals are met and to demonstrate the effectiveness of measures for preventing accidents, and mitigating potential radiological consequences under accidental conditions.

Traditionally the safety of nuclear power plants is based on the classical deterministic and phenomenological analyses. These safety analyses are used to understand and classify the range of safety issues and their consequences. They provide guidance for the reactor design and safety systems evaluation and represent the principal means for demonstrating that safety goals are met with a high degree of confidence for all accidents within the design basis. The deterministic analyses also provide input for probabilistic analyses that complement the safety assessment.

Probabilistic safety analyses (PSAs) integrate the concept of probability into the safety assessment and they are the principal means of demonstrating that the safety goals are met for potential accidents both within and beyond the design basis. It identifies vulnerabilities not necessarily accessible through deterministic safety analysis alone. The analyses focus on evaluating the risk arising from various events providing an assessment whether safety goals are met or not. They serve as means to identify weak points in the design and prove an assessment of the effectiveness of the safety provisions. To be mentioned are e.g. the event-tree and fault-tree methods [34]. For performing a PSA, the design of a plant must have reached a sufficient level of maturity and detail.

In the last years besides the "Defence-in-Depth" concept, the "Risk-Informed Design" concept is proposed which merges risk-methodologies with Defence-in-Depth methodologies and tries to combine deterministic and probabilistic success criteria. As elaborated in [62] DBAs and the general design criteria, which were established before probabilistic safety assessments were developed, are still central to current regulations. These regulations implement a structuralized approach to safety through traditional Defence-in-Depth and large safety margins. In a rationalistic approach to safety, accident frequencies are quantified and protective measures are introduced to make these frequencies acceptably low. Both approaches have advantages and disadvantages and future reactor design and licensing processes will probably have to implement a hybrid approach [62].

3.1.5. The Integrated Safety Assessment Methodology (ISAM)

Several guidelines exist for the safety assessment (e.g. from the International Project on Innovative Nuclear Reactors and Fuel Cycles INPRO [63] or from the Western European Nuclear Regulators association WENRA [58]). For GEN-IV systems in particular the Generation IV International Forum (GIF) Risk and Safety Working Group (RSWG) proposed a new methodology, called the Integrated Safety Assessment Methodology (ISAM).

The ISAM consists of five distinct analytical tools [64] which are intended to promote an improved safety from the earliest design stages on. A key issue of the concept are "built-in" rather than "added on" safety provisions (for former reactor designs, the safety analyses were performed once the

design of the reactor was fixed while nowadays the safety analyses have to be performed as a part of the design process). This reflects the ideas of integrating into the design increased inherent and passive safety systems.

The ISAM tools are the following ones:

- Qualitative Safety features Review (QSR)

- Phenomena Identification and Ranking Table (PIRT)

- Objective Provision Tree (OPT)

- Deterministic and Phenomenological Analyses (DPAs)

- Probabilistic Safety Analysis (PSA)

Figure 3-4 shows the overall task flow of the ISAM and indicates which tools are intended for use in each phase of Generation IV system technology development.
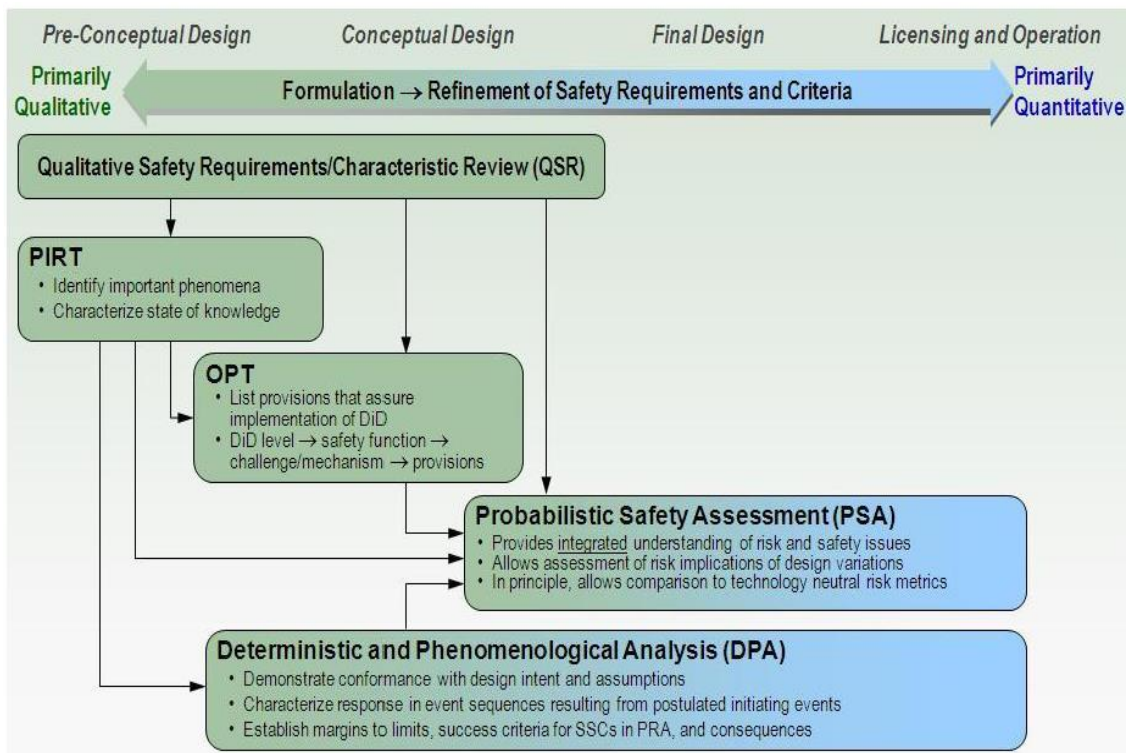
Figure 3-4. Schematics of the Integrated Safety Assessment Methodology (SSCs stands for Systems, Structures and Components while PRA stands for Probabilistic Risk Assessment) [64].

The Qualitative Safety Review (QSR) is a new tool that provides a systematic means of ensuring and documenting that the evolving Generation IV system concept of design incorporates the desirable safety-related attributes and characteristics that are identified and discussed in the RSWG's documents.

The Phenomena Identification and Ranking Technique (PIRT) is used to identify the spectrum of safety-related phenomena or scenarios that could affect systems, and to rank the phenomena or

scenarios on the basis of their importance and consequences and the state of knowledge related to associated phenomena. It relies on expert opinion and engineering judgment. It provides input for PSA and guides needed research.

The Objective Provision Tree (OPT) is applied from late pre-conceptual design stage through conceptual design and focuses on ensuring and documenting "lines of protection" in response to safety-significant phenomena identified in PIRT. While PIRT identifies phenomena, OPT identifies provisions intended to prevent, control, or mitigate the consequences of those phenomena.

The Probabilistic Safety Assessment (PSA) is a tool for identifying potential accident scenarios, and to quantitatively estimate their probabilities of occurrence and to estimate the consequences associated with these postulated accidents. It was usually used for already existing designs. Nowadays PSA is used as an important contributor for the design process.

Deterministic and Phenomenological Analyses (DPA) are classical deterministic and phenomenological analyses used from the pre-conceptual design phase through ultimate licensing and regulation of the Generation IV systems

3.1.6.   The IAEA INES scale

In order to communicate and standardize the report of nuclear incidents/accidents the International Nuclear and Radiological Event Scale (INES) was developed [65]. INES allows a characterization of the severity of events associated with sources of ionizing radiation. Seven levels exist in the INES scale (Figure 3-5) and consider 3 areas of impact: people and environment, radiological barriers as well as control. Levels 1–3 are referred as "incidents" and levels 4–7 as "accidents" (among the most known ones are the Chernobyl and Fukushima Daiichi accidents both classified level 7 and the Three Mile Island accident classified level 5 [66]). In this scale an accident is defined as "Deviations from normal operation that are less frequent and more severe than anticipated operational occurrences, and which include design basis accidents and design extension conditions" [59]. With each new level in the scale, the severity of an event is about 10 times greater than the previous level. Only events with a safety relevance to radiation or nuclear safety are rated in the scale. Levels with no safety significance are classified level 0.
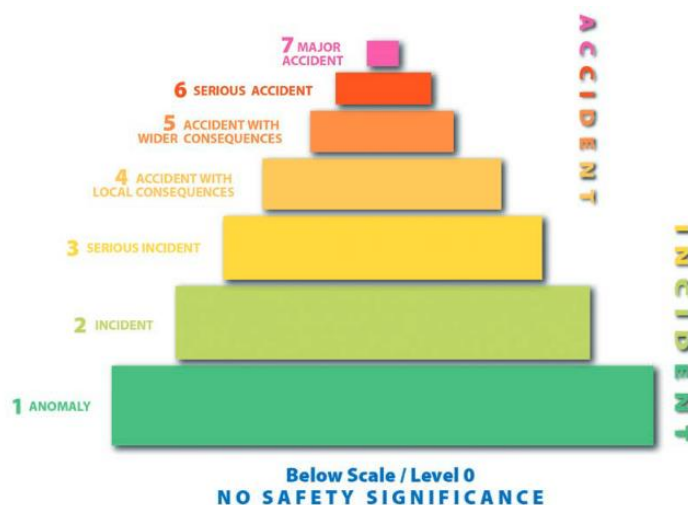
Figure 3-5. The INES scale [65].

3.2. SFR related accidents and hypothetical core disruptive accidents

For the next generation of nuclear plants, the prevention of an accident progression has to be considered systematically in the wide range of preventive strategies for accident management. Means to control accidents resulting in severe core damage have to be included in the design [67]. As the focus of this PhD thesis lies on severe accidents, it is important to give an overview of such accidents and their initiators.

For an SFR in normal operation conditions the key perturbing events can be related to the following initiators [38]:

- A variation in the coolant flow rate. This initiating event leads to a protected or unprotected loss of flow accident (P/ULOF). In the unprotected accident, both the reactor coolant pumps and the primary and backup shutdown systems are assumed to fail. The transient represents a global initiator, as it has an impact on the whole core.

- A variation in the inlet temperature of coolant is initiated by a protected or unprotected loss of heat sink (P/ULOHS) accident. In the unprotected accident, the heat removal capability is not assured anymore and the primary and backup shutdown systems are assumed to fail. The transient represents a global initiator.

- A change in reactivity. This leads to the protected or unprotected transient over power (P/UTOP). In this accident a positive reactivity amount is inserted e.g. due to a removal of one or several control rods and in the unprotected case it is accompanied by the failure of the primary and backup systems. The transient represents a global initiator.

- A local blockage of the flow in a sub-assembly caused either by an internal or external blockage, protected or unprotected leading to an accident (P/UBA). A specific accident is the Total Instantaneous Blockage (TIB). The transient represents a local initiator and the key issue is the time of reactor-shut down and further accident propagation.

From these perturbing events, HCDAs are those accidents where a general melting and disruption of the core occur. The analysis of HCDAs is intrinsic to SFRs since the core is not in its most reactive configuration. Therefore, a core melting might occur, inducing large changes in the core material distribution, possibly triggering large reactivity insertions. HCDA provides a deep insight into the generic behavior of a certain type of reactor based on a particular design concept and supports design considerations for improved inherent and passive safety (feedback effects, natural circulation).

The safety demonstration has to ensure that the accident consequences are tolerable from the point of view of radiological release to the environment. The study of the consequences of the HCDAs thus addresses several items:

1. The quantification of the importance of the occurring phenomena following the PIRT. This helps to identify and optimize the key impacting parameters. In addition, it allows inferring means to introduce systems attenuating the consequences of the phenomena and its

uncertainties. Last, an estimation of the value of mechanical energy release and the determination of its consequences on confinement structures and heat removal systems can be given.

2. The stability of corium[6] and core structures in the long-term.

3. The estimation of the accident consequences. This is based on radiological release to the environment as well as on consequences inside the reactor (e.g. sodium fire) or problems of confinement.

As mentioned earlier, representative cases are chosen for the safety assessment (UTOP, ULOF, UBA, ULOHS), and studies are performed for these cases solely. However, only the unprotected loss of flow (ULOF) accident will be detailed in this thesis as it is representative of the worst situation.

The unprotected loss of flow accident

This accident is usually investigated for the SFR safety assessment since it represents a global transient affecting the whole core and covers the most important phenomena which might occur in case of core disruption. It usually shows the highest energetic potential. In addition it is an accident on short time scale: core disruption is a matter of seconds or minutes.
It can be divided in the following phases for the analyses:

- the initiation phase;

- the transition phase;

- the last part either is a post-accident heat removal phase if a non-energetic route is followed or the disassembly, core expansion and mechanical load phase in case of an energetic development (Figure 3-6 (a)).

When the accident starts, the sodium flow rate is drastically reduced. The core temperatures increase and induce positive or negative effects on the reactivity, depending on the type of the feedbacks. Among the positive reactivity effects, the sodium expansion and the core structure materials expansion (cladding and hexcan) can be cited. On the contrary, fuel and diagrid expansion (i.e. core expansion) provide a negative effect on reactivity as does the Doppler effect and the control rod driveline and vessel differential expansion. If the negative feedbacks sufficiently counterbalance the positive effects, sodium boiling will be avoided. However, sodium boiling onset is usually reached in reactor designs of the past.

The sodium boiling might stabilize in some particular case (e.g. if a large sodium plenum is present at the top of the fissile core). If this is not the case, sodium boiling will extend to the whole core and general sodium boiling will be observed. This sodium voiding induces a high positive reactivity insertion and a related power increase - Figure 3-6 (b) - since neutrons become faster, thus making fission processes more probable. In addition, the cladding temperature increases eventually reaching its melting temperature as heat cannot be sufficiently removed anymore (the cladding loses its

---

[6] Corium is the molten mixture of core materials (fuel, steels etc.) formed during the core meltdown.

mechanical properties even earlier). Cladding relocation inserts additional positive reactivity. Fuel is then predicted to disrupt and fills all voided zones (sodium channels). The fuel is then driven away from the disrupted area by fission gas and sodium vapor pressures inducing a negative reactivity insertion [25].

The subsequent phases of the scenario largely depend on the magnitude of the primary excursion:

- If the primary excursion is low energetic, the fuel expansion might make the core sub-critical, and no secondary power excursion will be observed in the short term. This possible behavior is shown later in the thesis (see chapter 8) for the specific CONF2 core design [35].

- If the primary excursion is moderately energetic, part of the fuel is ejected in the upper parts of the core, outside of the fissile core zone. The core configuration is thermal-hydraulically and neutronically unstable and the amount of ejected fuel is too small to avoid a secondary power excursion by the mobilized fuel. The secondary excursion could load the vessel structures in case of a severe recriticality.

- If the primary excursion is highly energetic, enough fuel is ejected from the fissile core zone out of the core region and any further recriticality is avoided. However the integrity of the vessel structures is endangered since they are mechanically loaded.
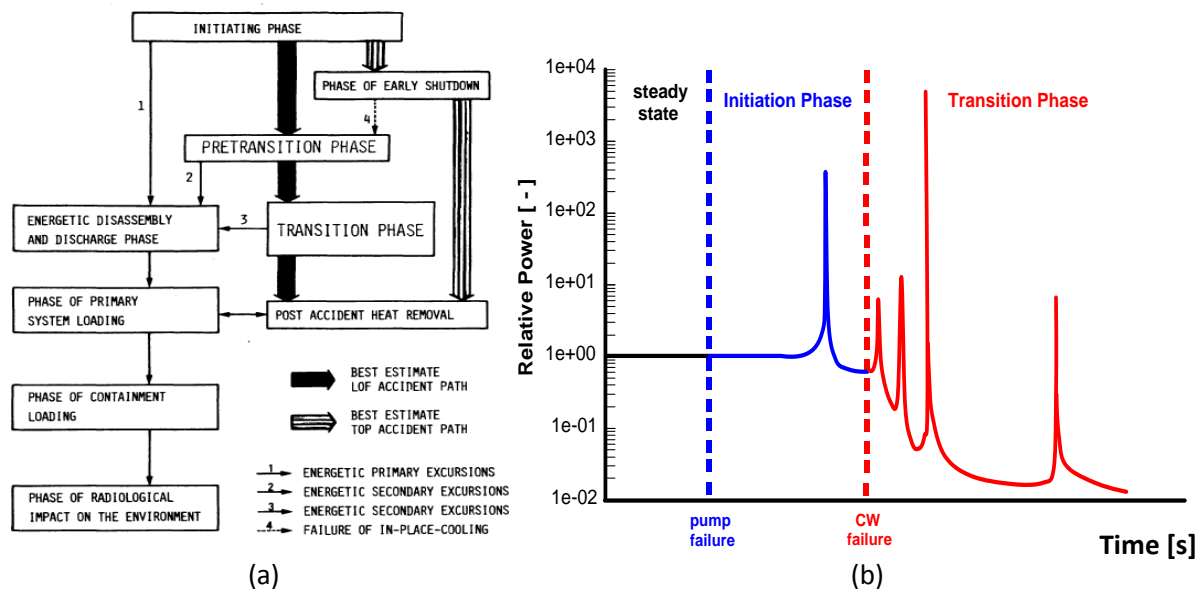
Figure 3-6. Potential paths of a severe accident (a) Relative power versus time in case of a ULOF in the ESFR WH core (b) [13; 68].

The later accident development is strongly influenced by blockages in and at the exits of the sub-assemblies, and the following two situations might occur:

- No complete blockage forms. This allows the discharge of molten and particulate fuel leading to a fuel dispersion and termination of the accident.

- A significant blockage forms. The accident enters a transition phase where hexcans are progressively melting, allowing large scale material motions with fuel sloshing possibly

leading to recriticalities and excursions. The accident usually finishes with a high pressure buildup in the core and core disassembly dispersing the fuel into the upper sodium plenum.

For recent core designs the goal is to eliminate the route into severe accident development, thus avoiding mechanical loading on the reactor structures. Hence, preventive and mitigating measures are introduced. The initiation phase can be prevented or at least mitigated if the impact of sodium voiding on reactivity is decreased, and if the void/Doppler ratio and structural feedbacks are optimized. The transition phase can be mitigated by implementing systems which help the fuel to be ejected out of the core region. The FAIDUS sub-assembly is one important example of such systems [69]. In past FR designs the introduction and fall-down of blanket material (including absorber) helped to reduce the reactivity levels in the fuel pools.

Thus, the transition phase can be mitigated by sufficient and definite fuel ejection from the core for recriticality prevention.

3.3. Simulation needs, tools and methods

Studies of severe accidents constitute a major part of the safety analyses for SFRs. HCDAs studies have been carried out in the past for almost all reactors in Europe and in the US [38].

In the early stages of the safety analysis, the question of core compaction was of high concern as it potentially triggers the power excursions. The focus was mainly directed to the quantification of the maximum work. The original analyses were based on the Bethe-Tait model [70]. A simple geometry as well as simplifying approximations to allow a hand calculation solution were chosen for the studies [25]. It was assumed that the reactor could be modeled in R-Z geometry, and that the starting phase of the accident was represented by a molten core having lost all its coolant (sodium). Core collapse due to the force of gravity was then assumed and the reactivity ramp rate induced by fuel compaction leading to prompt critically induced an energetic disassembly of the core. Bethe and Tait assumed a totally coherent collapse, a spherical geometry for the core disassembly phase as well as an absence of delayed neutrons and Doppler feedback. The neglect of delayed neutrons was justified due to the fact that the core dynamic response was analyzed during the prompt critical domain only in the original model. In addition, the use of metal fuels in the early cores in the United States justifies the neglect of the Doppler effect [25]. The analysis predicted increasing values for maximum HCDA work with increasing core size. However, when considering fuel vapor buildup as a disassembly force, the mitigating role of Doppler feedback and a more mechanistic approach, the maximum work significantly decreases.

The Bethe-Tait analysis was the impetus of significant improvements in severe accident analysis [25] and several codes have been developed since the 1970's to analyze the different phases of a severe accident. The initiation phase analysis is performed with codes like SAS4A [71]. These codes allow calculating the accident up to the loss of assembly geometry. In SAS4A, assemblies of same power, mass flow and irradiation history are grouped into channels each of which contains one representative fuel pin, its cladding, the associated coolant, and a fraction of the sub-assembly duct wall. The coolant flow is assumed to be axially one-dimensional and the axial height of a channel covers the whole sub-assembly length. The code contains mechanics and neutronics modules. Coolant boiling, clad failure, fuel melting and relocation can be modeled in one dimension until the sub-assembly geometry is lost. Further modeling of the accident evolution is no longer valid and

meaningful as only representative channels in 1D, independent from each other, are considered (no radial propagation of the accident can be simulated).

The code evaluates the reactivity insertion, the related power excursion as well as the energy release during the initiation phase of an accident. As neutronic model, SAS4A employs point kinetics i.e. neutron flux and power shape have to be specified as input data and do not vary during the transient, only the amplitude of the flux changes. A reactivity variation is evaluated via feedback coefficients given by input and temperature variations. This approach is valid as long as only little dimensional changes occur and integrity of the core and its components remains almost intact [72].

From the point in time on where the assembly geometry is lost the SIMMER codes take over [13; 73; 74]. SIMMER-III is a two-dimensional (2D), SIMMER-IV a three-dimensional (3D), multi-velocity-field, multi-phase, multi-component, Eulerian, fluid-dynamics code system coupled with a structure model for fuel-pins, hexcans and general structures, and a space-, time- and energy-dependent transport theory neutron dynamics model (Figure 3-7). An elaborate analytical equation-of-state (EOS) closes the fluid-dynamics conservation equations [75]. The fluid-dynamics portion is interfaced with the structure model through heat and mass transfer at structure surfaces. The neutronics part provides nuclear heat sources based on time-dependent neutron flux distributions consistent with the mass and energy distributions (Figure 3-8).

The code models the five basic SFR core materials: fuel, steel, sodium, control and fission gas. A material can exist in different physical states, e.g. fuel can exist as fabricated solid fuel pellet column, liquid fuel, a crust refrozen on structure, solid particles, broken fuel pellets (called chunks) and fuel vapor. The structure field components, which consist of fuel/control pins and can walls, are immobile. For the mobile components the number of velocity fields is usually eight plus a gas field. Phenomena as the relative motion of the fuel-liquid/particle mixture and chunk fuel in the penetration of molten core materials into pin bundle or fall-down of fuel chunk into molten pools can be modeled [75].

From the neutronics point of view, SIMMER is a deterministic code with separated cell and flux calculations [76]. In each cell the self-shielded macroscopic cross-sections are calculated inside the code from a set of infinite diluted cross sections and self-shielding factors tabulated in temperature and so-called background cross-sections, and updated at every time step of reactivity calculation because of the changes in material number densities and temperatures [77]. Since SIMMER is primarily tailored for fast reactors, usually homogeneous cell calculations are performed. With the set of self-shielded macroscopic cross sections, the core calculation is carried out. Neutron flux calculations are performed by an S_N transport code using a synthetic diffusion acceleration scheme [76].
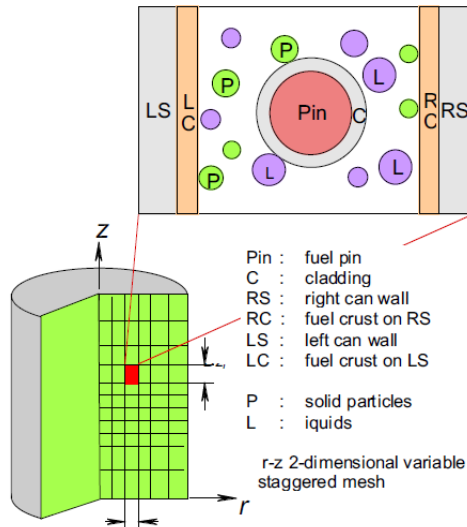
Figure 3-7. SIMMER-III, multi-phase, multi-component fluid-dynamics model [78].
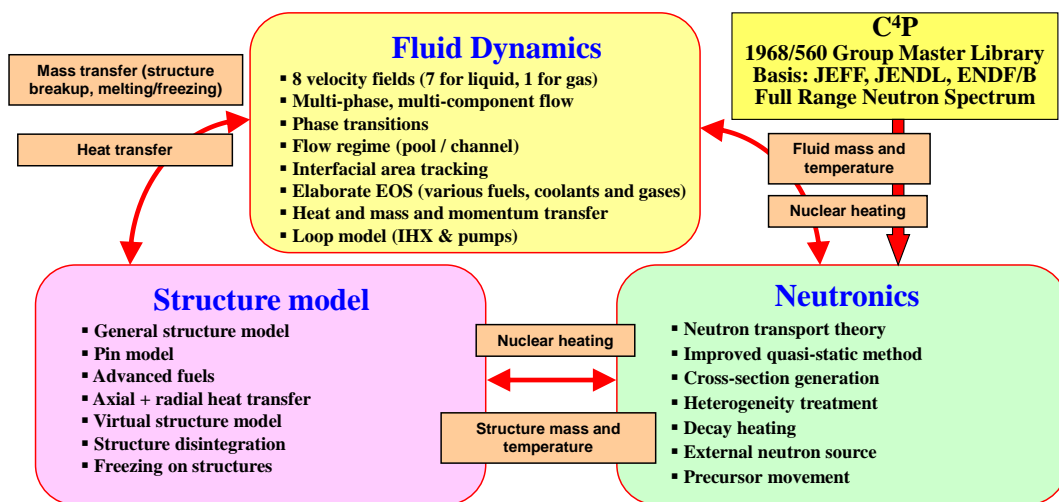
Figure 3-8. SIMMER overall code structure [73]

Given the differences between the SAS4A (a channel-wise reactor model and a neutron point kinetics model are employed) and SIMMER codes (system code with space-time kinetics model) certain approximations may have to be done in connection to the data transfer between the two codes. Hence, focus is currently put on the extension of the application range of the SIMMER family codes to the initial phase of core disruptive accidents. Having this in mind, the SIMMER code has to be extended in particular to take into account the core thermal expansion feedbacks (more details on this extension will be provided in chapter 6). In the next chapter the different reactor designs under study in this PhD thesis are described.

Chapter 4

SPECIFIC SODIUM COOLED FAST REACTOR DESIGNS UNDER STUDY

The design of sodium cooled fast reactors has continuously evolved during the last decades. A primary target of design studies is an improved prevention/mitigation of a possible accident. This is mainly achieved through a decrease in the positive sodium void worth, since the reactivity induced by sodium voiding drives the initiation phase of a severe accident. This chapter aims at providing a short overview of former European concepts[7] and examines in some detail two core designs with improved mitigation capabilities developed within the former Collaborative Project on a European Sodium Fast Reactor (CP-ESFR).

4.1. Previous sodium cooled fast reactor designs: PHENIX, SUPERPHENIX and the European Fast Reactor

The PHENIX and SUPERPHENIX reactors, built in France on the basis of the experience gained from the experimental fast reactor RAPSODIE, both used mixed oxide (MOX) fuel [4]. The former one operated from 1973 to 2009. Extensive feedback experience is available from this reactor [81] which allowed demonstrating the feasibility of in-service inspection, maintenance, reparability and transmutation in addition to electricity production. Based on this experience, the SUPERPHENIX reactor was built and operated from 1985 to 1998. It was shut down mainly due to political reasons.

With the European Fast Reactor (EFR) project [5], a 3600 MWth reactor design was extensively studied and reached a degree of optimization considered to be the reference for the pool type sodium cooled fast reactors (SFRs) using MOX fuel. This study supported the conclusions of the PHENIX and SUPERPHENIX projects that SFRs present a strong potential both for the creation of fissile material and for actinide transmutation apart from their main purpose of producing electricity.

The reactor is a breeder, thanks to axial and radial fertile blankets. From the safety standpoint, the EFR demonstrates a very strong reduction in the severe accident probability as well as a strong mitigating capacity and is considered as a reference for new SFR designs. However, its economic competitiveness was not confirmed since an additional cost (compared to light water reactors

---

[7] SFRs have been built worldwide: to mention are e.g. the Experimental Breeder Reactor No. 2 (EBR-II) in the USA [29], the JOYO reactor in Japan [4] or the Fast Breeder Test Reactor (FBTR) in India [79]. These reactors are, however, not addressed in this chapter, the focus being on European ones, but details can be found in [80].

(LWRs)) of about 20% on the capital cost and about 10% on the cost per kWh was expected and the reactor was, hence, never built [82]. In Table 4-1 the characteristics of these three reactor designs are presented.

Table 4-1. Characteristics of the PHENIX, SUPERPHENIX and EFR reactors [47].

Reactor	PHENIX	SUPERPHENIX	EFR
Thermal power (MW)	563	2990	3600
Pellet diameter (mm)	5.50	7.14 (central hole 2mm)	6.94 (central hole 2 mm)
Cladding diameter (mm)	5.65	8.50	8.20
Pins per subassembly (SA)	217	271	331
Fissile height (cm)	85	100	100
Blanket zone height (radial/upper/lower) (cm)	52/22/30	60/30/30	40/15/25
SA width across flats (cm)	12.37	17.3	18.3
SA pitch (cm)	12.72	17.9	18.8
Equivalent core fissile radius (cm)	68	179	194
Core fissile volume (m3)	1.2	10	12
Number of fuel Sas	104	364	387
Zone Enrichment 1	50	193	207
Zone Enrichment 2	54	191	108
Zone Enrichment 3	-	-	72
Number of control rods	6	21	24
Number of safety control rods	1	6	9
Number of blanket SAs	78 (2 rings)	237 (3 rings)	78 (1 ring)

The former fast reactors as PHENIX, SUPERPHENIX and the EFR were analyzed with regard to safety once the design was fixed. The new reactor designs, however, have to take into account the safety from the conception on. In this context, the CP-ESFR project (2009-2012) was launched [35].

4.2. New reactor designs: the CP-ESFR project

The CP-ESFR project (2009-2012) is part of the EURATOM 7th Framework Program [35]. Its aim was to investigate and optimize concepts for large innovative sodium cooled fast reactors, addressing key viability and performance issues to support the development of a European sodium cooled fast reactor (ESFR). At the beginning, two core designs were analyzed (one oxide and one carbide core). These cores were referred to as "Working Horse" cores (WH).

Once analyses were performed on the WH cores, necessary modifications were identified in order to improve the safety behavior of these cores in nominal and accidental conditions (focus is hereafter on the oxide version only). Especially the reduction of the sodium void worth was addressed to decrease the energetic potential in case of a severe accident. In fact, the sodium void reactivity effect governs the initiation phase of hypothetical transients e.g. unprotected loss of coolant flow (ULOF) or Total Instantaneous Blockage (TIB) potentially leading to a core disruption. Special assembly designs were also analyzed within the project to enhance melt relocation. In addition, transmutation capabilities of the optimized configurations of the oxide WH core (called CONF2) were investigated [14].

4.2.1. The oxide fueled Working Horse core (WH)

The oxide WH is a core proposed by CEA. Its design is based on optimization studies for a low sodium void effect and on the previously mentioned PHENIX, SUPERPHENIX and EFR projects [6]. This core is an iso-generator (no fertile blanket) which limits the reactivity loss during the irradiation cycles: enough fissile material is constantly produced in the core to counterbalance the disappearance of fissile material [6].

The WH core is a 3600 MWth core containing 453 sub-assemblies. These sub-assemblies are divided into two fuel zones i.e. an inner and an outer one differing in plutonium enrichment: 14.5 wt% and 16.9 wt%, respectively, in average. The provision of two core enrichment zones allows a flattening of the radial power profile at equilibrium – Figure 4-1. The design is similar to another SFR design developed by CEA, EdF and AREVA [83].

The average core burnup at end of life (5 cycles of 410 days i.e. 2050 equivalent full power days or efpds) is of 100 GWd/tHM. The core contains 24 control and shutdown devices (CSDs) containing natural B_4C and 9 diverse shutdown devices (DSDs) composed of B_4C with 90% ^{10}B [14].

To obtain a low sodium void effect compared to previous designs, the WH core uses "fat pins" – Figure 4-2 – this means the fuel pellet diameter is larger in the WH core than in previous core designs. The fuel volume fraction is hence maximized while the sodium volume fraction is reduced. This can be envisaged if Oxide Dispersion Strengthened (ODS) steels are used for the pin cladding [83] as they are known to have a considerable resistance to neutron-irradiation induced swelling as well as to high-temperature creep [84; 85]. Another effect of these "fat pins" is a reduction of the power density (206 W/cm^3 average) and of the maximum fuel temperature. The WH oxide core sub-assembly characteristics are presented in Table 4-2.
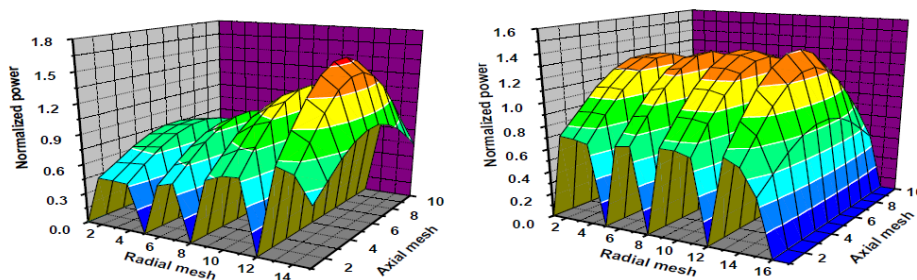
Figure 4-1. Normalized power in the beginning of life (BOL) and end of equilibrium cycle (EOEC) Working Horse core [13].
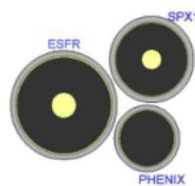
Figure 4-2. Pin dimensions in the PHENIX, SUPERPHENIX (SPX1) and ESFR cores [14]

Table 4-2. Characteristics of the ESFR sub-assembly [6].

	"Oxide fuel core"
Sub-assemblies pitch (mm)	210.8
Sodium gap width inter assembly (mm)	4.5
Wrapper tube outer flat-flat width (mm)	206.3
Wrapper tube thickness (mm)	4.5
Wrapper tube material	FM steel (EM10)
Wire wrap spacer diameter (mm)	1.0
Wire wrap helical pitch (mm)	225
Wire wrap spacer material	ODS steel
Number of fuel pins per sub-assembly	271
Outer clad diameter (mm)	10.73
Inner clad diameter (mm)	9.73
Cladding material	ODS steel
Fuel pellet diameter (mm)	9.43
Fuel pellet material	$(U,Pu)O_2$
Fuel average density	88.8% TD
O/M	1.98

The WH core is considered as the reference core in the CP-ESFR project. Axially, it presents the following structure from bottom to top: a sub-assembly foot of steel, a 91.3 cm lower gas plenum (LGP), a lower steel axial blanket of 30 cm (LAB), a fissile zone of 100 cm, an upper steel axial blanket of 7.6 cm (UAB), an upper gas plenum of 15 cm (UGP), plugs, a 15 cm sodium plenum, an Upper Steel Structure (USS) and sub-assembly head of steel [35]. Its axial and radial layouts are presented in Figure 4-3.
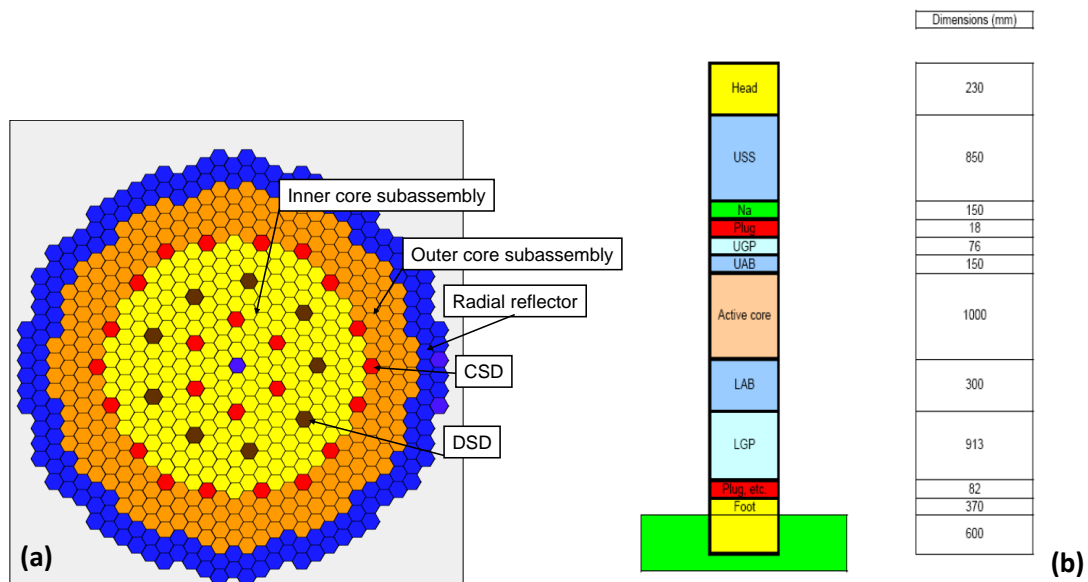
Figure 4-3. Radial (a) and axial (b) layout of the CP-ESFR Working Horse oxide core [6].

The sodium void effect due to fissile core voiding is of +1532 pcm at beginning of life (BOL). If additionally the upper gas plenum, the upper axial blanket, plugs and sodium plenum regions are voided, the effect (called extended sodium void reactivity effect) reduces to +1211 pcm at BOL. Voiding is assumed only inside the wrapper tubes since it constitutes the primary effect[8] (sodium

---

[8] This has been demonstrated in the CP-ESFR project [6].

between sub-assemblies is not removed). These positive values drive the reactivity excursion at the beginning of a transient, as shown later on by the SIMMER study, even if partially compensated by other negative feedbacks like the Doppler effect (Doppler constant *ca.* −1239 pcm) and axial and radial thermal expansion (*ca.* −200 pcm) [9].

4.2.2. The CONF2 core

As mentioned earlier, the rationale of the CP-ESFR project (2009-2012) was to reduce the sodium void reactivity effect as a part of the prevention and mitigating safety strategy. Hence the focus lies on a geometry optimization even if other options like special devices for fuel relocation (e.g. the FAIDUS devices [86]) can help to achieve the same goal (they were however not investigated).

Based on previous studies [87–89], possible options for reducing the extended sodium void reactivity effect, i.e. when core and sodium plenum are voided, were identified. However, these optimizations might lead to a worsening of other core characteristics like the reactivity variation per cycle [14]. Therefore a parametric study has been performed in the CP-ESFR project to identify the most promising options. Two routes can be followed to reduce the sodium void effect [87; 89]. The first one relies on an enhanced neutron leakage in voided conditions by the introduction of a large sodium plenum [87]. This route is usually the most effective one. The second one relies on a softening of the neutron spectra through e.g. the addition of moderating material.

After an extensive study of the geometrical changes [35] the most effective ones were identified and applied to the WH core leading to the so-called CONF2 design. Consequently, the sodium plenum height was increased from 15 cm to 60 cm (close to the asymptotic value) and an absorber layer of 30 cm composed of natural B_4C was placed above it. In addition the upper axial blanket present in the WH core was removed and the upper gas plenum was decreased (to 5 cm). The sodium plenum is thus much closer to the fissile core in the CONF2 design. Below the core, a fertile material (depleted uranium) was introduced into the lower blanket to enhance the neutron capture there under voided conditions (neutron reflection back to the core is reduced) - Figure 4-4. Furthermore, this fertile blanket reduces the reactivity swing per cycle as additional plutonium is bred (from BOL to the end of the 3rd irradiation cycle, i.e. 1230 efpds, the WH has a reactivity swing of 0.68 pcm/efpd while CONF2 yields 0.59 pcm/efpd i.e. 13% relative discrepancy). In addition, by introducing minor actinides (MAs) into this fertile blanket, a beneficial impact on proliferation resistance can be obtained [9]. Other measures (special sub-assemblies, internal fertile layer, modifications of the Height over Diameter ratio) were investigated as well, as mentioned in [14].
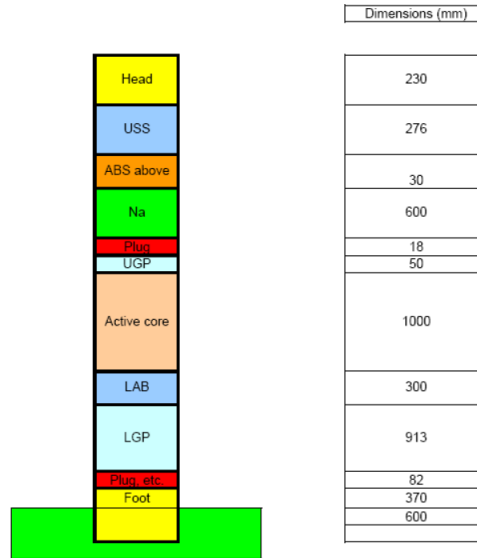
Figure 4-4. Axial layout of the CONF2 core [9].

To keep the criticality level of the BOL WH configuration, the plutonium content has been homogeneously increased in the inner and outer core zones of the CONF2 core (14.76 wt% in the inner and 17.15 wt% in the outer core).

The improvements performed on the Working Horse design lead to a reduced sodium void effect of ca. +1432 pcm and a reduced "extended void reactivity effect" of +496 pcm thanks to the increased sodium plenum and the axial fertile blanket. The values can be found in Table 4-3. It can also be noticed from Table 4-3 that the void worth and Doppler constant are worsened with burnup: after 1230 efpd i.e. at End of Cycle 3 (EOC3[9]) the sodium void reactivity effect is increased by 600 pcm and the extended sodium void reactivity effect by 750 pcm, becoming very close to the sodium void reactivity effect of the BOL Working Horse core.

Table 4-3. Values of void and Doppler reactivity effects in the CP-ESFR Working Horse and CONF2 cores [9].

	Working Horse	CONF2	
	BOL	BOL	EOC3
Sodium void reactivity effect (pcm)	+1532	+1423	+1952
Extended Sodium void reactivity effect (pcm)	+1211	+496	+1170
Doppler constant, K_D (pcm)	-1239	-1158	-843
β_{eff} (pcm)	392	393	

It has to be mentioned that the considered measures do not affect the power distribution. Figure 4-5 displays the radial power distributions of the CONF2 core both at BOL and EOC3. They do not differ appreciably from the corresponding ones of the WH core (which were imposed by the project).

---

[9] EOC3 compositions are considered in order to quantify the deterioration of safety coefficients for the equilibrium composition. Indeed, EOC3 is a representative composition for a beginning of equilibrium cycle condition [9].

As mentioned previously, the lower fertile blanket in the CONF2 design leads to a less pronounced reactivity swing than in the WH core (0.59 pcm/efpd versus 0.68 pcm/efpd from BOL to EOC3 as mentioned previously) - Figure 4-6.
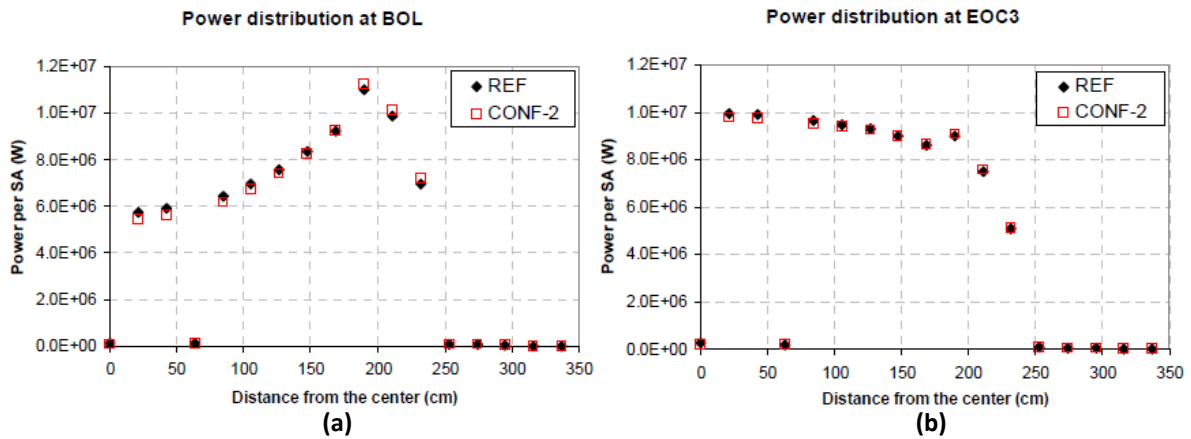
Figure 4-5. Radial power profile in the CP-ESFR Working Horse core (REF) and the CONF2 core both at beginning of life (a) and end of cycle 3 (b) [9].
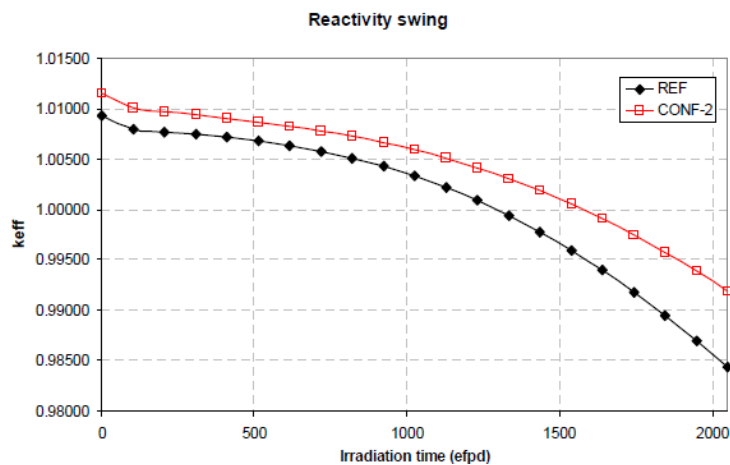
Figure 4-6. Reactivity swing in the CP-ESFR Working Horse (REF) and CONF2 cores versus burnup [9].

Since the modifications that lead to the CONF2 configuration were primarily intended at achieving a better behavior of the core under transient and accidental conditions, preliminary analyses of an unprotected loss of flow (ULOF) transient both for the WH and for the CONF2 configurations have been performed with the SIMMER-III code [73]. The ULOF transient coolant mass flow is gradually reduced with a halving time constant of 10 seconds. The results show that the reactivity drops when the sodium starts to boil in the CONF2 core (*ca.* 31 s after pump failure) while a reactivity excursion is observed in the WH design[10] – Figure 4-7. The oscillations observed in case of the CONF2 core are related to the consecutive voiding of plenum (negative effect) and fissile core region (positive effect) in the different rings (starting in the hottest one) leading to a competition between positive and negative effects.

---

[10] The thermal expansion contribution has not been simulated in SIMMER for these calculations in the CP-ESFR project.

However, no extended safety analyses of this core have been performed within the CP-ESFR project and additional investigations are necessary to demonstrate and confirm the effectiveness of the applied modifications (detailed in Chapter 8).
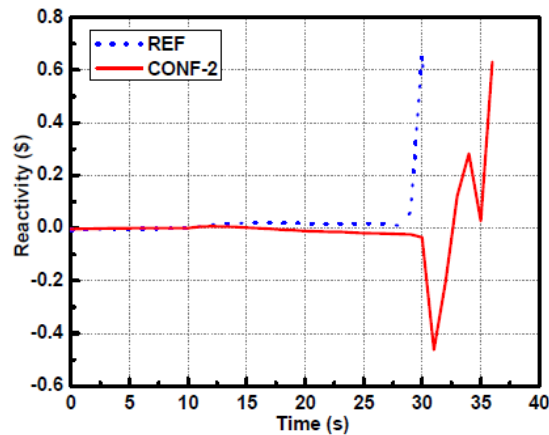
Figure 4-7. Reactivity evolution in the CP-ESFR Working Horse (REF) and CONF2 cores under ULOF conditions [9].

It can be taken advantage of the fact that the extended sodium void reactivity effect in the CONF2 core at BOL is low in order to introduce and burn MAs in the system. Several cases were studied in the CP-ESFR project, but only two are considered here [9]:

- 2 wt% Am (^{241}Am:^{243}Am, 76%:24%) are put in the lower axial blanket and ~1.9 wt% Am are inserted homogeneously in the fissile core. This configuration allows transmuting the minor actinides produced by the core.
- 4 wt% Am (^{241}Am:^{243}Am, 76%:24%) are put in the lower axial blanket and ~3.8 wt% Am are inserted homogeneously in the fissile core. This configuration is capable of burning not only the americium coming from the CP-ESFR core itself but as well additional americium coming from thermal reactors.

As detailed in Chapter 2, the insertion of MAs into a core worsens the reactivity feedbacks and the neutronic parameters. For comparison, the CONF2 with and without MAs is considered. The reference CONF2 core presents an effective neutron fraction (i.e. weighted by the importance function of the flux, see Chapter 6 for more details) of 393 pcm which decreases to 377 pcm when introducing the 2 wt% Am and to 361 pcm when introducing 4 wt% Am. Indeed the ^{241}Am and ^{243}Am isotopes have delayed neutron fractions of 122 pcm and 224 pcm, respectively [90].

In Table 4-4 the sodium void reactivity effect, the extended sodium void reactivity effect and the Doppler constant are displayed. It can be noticed that at BOL, all reactivity effects are worsened upon addition of MAs to the fuel. The same tendency is observed when comparing the BOL core with the EOC3 core where MAs have built up during irradiation and the uranium content has been reduced.

Table 4-4. Values of the sodium void worth and the Doppler effect in the CONF2 core with different contents of americium [9].

	CONF2		CONF2 with 2%Am		CONF2 with 4%Am	
	BOL	EOC3	BOL	EOC3	BOL	EOC3
Sodium void reactivity effect (pcm)	+1423	+1951	+1636	+2029	+1821	+2104
Extended Sodium void reactivity effect (pcm)	+496	+1170	+781	+1290	+1031	+1407
Doppler constant, K_D (pcm)	-1158	-843	-904	-785	−712	−600
β_{eff} (pcm)	393		377		361	

On the other hand, loading americium in the core reduces the reactivity swing as indicated in Figure 4-8. The CONF2 with 2 wt% Am shows an almost constant reactivity during the irradiation due to the ^{241}Am transmutation. For the CONF2 (4%) configuration, an increase in reactivity *versus* burnup is observed due to the fact that ^{241}Am is burnt (strong capture cross-section leading to a negative contribution to the reactivity). In addition, fissile material is generated.
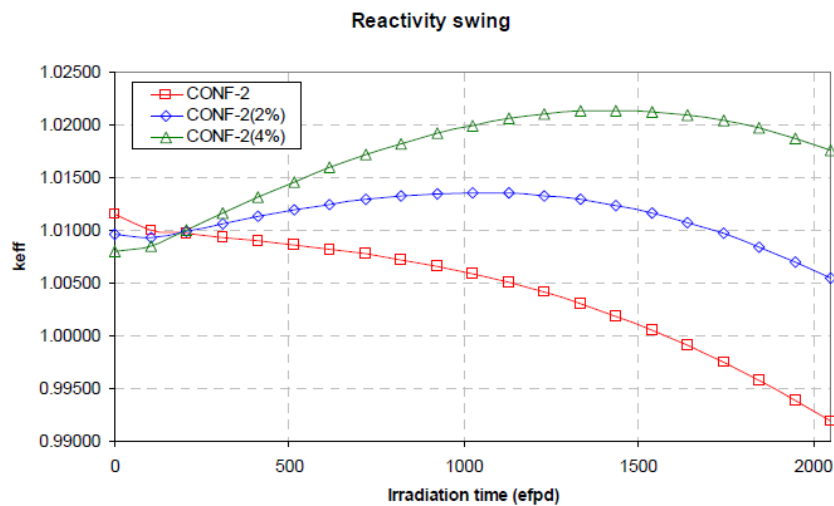
Figure 4-8. Reactivity swing versus burnup in the CONF2 core with different contents of americium [9].

4.3. Conclusions

SFR designs have steadily evolved since the PHENIX design. One pursued objective of reactor designers is the decrease of positive reactivity feedbacks related to a temperature increase. Especially the reduction of the sodium expansion feedback is sought. Within this framework of prevention and mitigation of severe accidents, the Working Horse core was developed in the CP-ESFR project (2009-2012). An increased sodium plenum, shifted close to the core, as well as the addition of an absorber layer above the sodium plenum, and of a lower fertile blanket further decreases the positive void worth (about 2$ to 3$ decrease) and leads to the optimized CONF2 design.

To guarantee the sustainability of nuclear power in the long term, the option of a closed fuel cycle with minor actinide transmutation is envisaged. The low value of the extended sodium void reactivity effect at beginning of life allows the introduction and burning of MAs in the CONF2 core. However,

when minor actinide transmutation is intended, other fuel types might result in an improved safety behavior of the core. Thus, the Working Horse and CONF2 cores are loaded with so-called sphere-pac fuels and associated safety analyses are performed within the framework of this PhD project.

Chapter 5

NUCLEAR FUELS

Fast Reactors (FRs) are suitable nuclear reactors for managing the existing plutonium and minor actinide (MA) stocks as they can serve as breeders, iso-generators and burners. Breeding is the key issue of sustainability of these GEN-IV systems to cope with future declining uranium resources. To ensure a maximum saving of the uranium resources, spent nuclear fuel is recycled. A recycling in thermal reactors would however not be sustainable as these reactors do not make efficient use of the fuel and multirecycling becomes impossible due to a worsening of the safety coefficients caused by the influence of "dirty" plutonium with high contents of even isotopes like ^{238}Pu [91]. On the contrary, fast breeder reactors based on fast neutrons have the ability to efficiently transform fertile in fissile isotopes, therefore exploiting well the energy potential of the fuel [92].

As detailed in Chapter 2, the other key feature of fast reactors is their ability to burn MAs. Reducing the MA masses and radiotoxicity of spent fuel would help considerably to alleviate the loads on final repositories.

Using fast neutrons requires specific constraints on reactor and fuel designs. At high neutron energies, cross sections are rather low compared to the ones at lower energies. This ought to be counterbalanced by a high concentration in fissile isotopes in the fuel. Fast reactor cores have therefore to be designed to be compact and irradiation damage have to be anticipated in core structures due to the high neutron flux and fluence [93].

From a technological and economical point of view, fuel fabrication and reprocessing costs have to be recovered. This leads to aiming at high burnups: high specific powers and high fuel utilization as well as an optimized fuel cycle with a reduced out-of-pile time are required.

Any solid fuel development has to ensure improvements not only with respect to nominal but also transient and accidental conditions. In particular no fuel melting should occur in nominal and off-nominal events. This first requirement is the main limiting factor for the linear heat generation rate. Secondly, the cladding integrity and pin tightness have to be ensured, as the cladding is the first containment barrier after the fuel matrix. Since the principal cause of failure has been identified to be cladding deformation due to swelling, the in-core lifetime and burnup of fuel has to be limited. A third safety requirement concerns the ability of cooling the fuel pin bundle in all operating conditions. In addition to the previous requirements, the capability of loading and unloading of assemblies has to be ensured, one of the limiting phenomena being the deformation of the hexagonal wrapper tubes [94].

A deep understanding of physical and chemical processes taking place in the fuel during its life-time is necessary to design fuels meeting all previously mentioned criteria. Numerous experiments are performed and experimentally validated fuel performance and safety codes are hence developed based on this knowledge to help in the designing process.

Within the GEN-IV framework, reactor systems able to recycle part of their own waste or even waste coming from previous reactor generations are investigated. For the solid reactors a large variety of fuels for transmutation is under development worldwide. Depending on the chosen recycling strategy (mixing of small quantities of MAs in standard driver fuels of critical cores or introducing large MA loads in dedicated areas of critical cores or in fuels of transmutation machines as ADS) one can distinguish uranium based or uranium free fuels. Europe has a large experience with oxide fuels. However, for GEN-IV reactors with different missions and coolants other advanced fuel types are considered too. While oxide fuels are still investigated due to their robustness and the large experience gained with LWRs and some FRs [95], other fuel types are of interest. This also includes the investigation of special accident resistant fuels. For GEN-IV reactors, besides oxide, denser materials exhibiting also a higher thermal conductivity as e.g. the carbide, nitride or metal fuels are under consideration. The operating temperatures of these "cold" fuels are lower and in general the power to melt ratio is high. However, these fuels reveal specifics in their safety behavior which have to be taken care of in the reactor design. In the case of uranium free fuels for ADS, ceramic-ceramic (CERCER) or ceramic-metal (CERMET) fuels are studied. These fuels are developed for ADS systems but still need major developments. In conclusion, these fuels present some advantages compared to oxide fuels, but they also involve drawbacks. Likewise, structural materials have to be developed to cope with the requirements but are out of the scope of this chapter. Moreover, molten salt reactors (MSRs) will not be discussed here.

Besides the fuel type itself, the mechanical fuel form is of high interest. Thus, alternatively to pellets, particle fuels are investigated. The FP7-PELGRIMM [11] project dedicated to fuels for MA transmutation considers two particular fuel forms: the standard pellet and the sphere-pac fuel.

In this chapter, specificities of driver fuels for FRs are briefly described. The focus at the end of the chapter is devoted to oxide fuels in their pellet and sphere-pac forms, related to the above mentioned PELGRIMM project.

5.1. Metal fuels

The first FRs developed in the 1950's in the US and the UK used metal fuels. This choice was based on the ease of fabrication of these fuels, their high thermal conductivity and their high heavy metal density allowing a high breeding ratio [96]. Nonetheless, these fuels were found to present a dimensional instability ascribed to swelling and growth during irradiation and the desired high burnup could not be achieved [94].

Metal fuels are easy to manufacture remotely and can be produced in two ways. The most common fabrication process consists of an injection casting of alloy. The alloy is heated in a furnace up to its melting temperature and then poured into a quartz mold where it quickly solidifies. This method is

compatible with remote handling and automation which is crucial when minor actinides are present in the fuel. When adding americium to the alloy, problems might appear due to the volatility of Am and therefore a trapping system has to be used. Once the fuel slugs are produced, they are inserted into the cladding tube. An appropriate amount of sodium is then added to enhance the heat transfer (to stay below the very low melting temperature of the metal fuel). The pins are then heated to liquefy the sodium and an end cap is welded on the cladding. A second option for fabricating metal fuels is via powder metallurgy. The alloy can be obtained either by pyrochemical processing or by co-melting of components. It is then converted into powder of small particles size [97].

Metallic fuel in association with injection casting and pyro-electric reprocessing is a promising fuel for FRs. (U,Pu) fuel was extensively irradiated in the US fast breeder program [4] and the Integral Fast Reactor (IFR) of Argonne [98]. Metal fuels show good compatibility with Na coolant and a good performance under nominal conditions, reaching high breeding ratios. However, during off-normal conditions the fuel expands considerably and a reaction between fuel and cladding occurs [97]. Nevertheless, metal fuel has excellent transient capabilities. The eutectic formation temperature between fuel and cladding is an important parameter for the metal fuel pin design. Depending on the fuel alloy and cladding type, fuel-cladding eutectic formation starts at ~ 700 °C. Eutectic penetration into cladding becomes rapid and massive around 1000 °C. The inherent passive safety characteristics under anticipated transients without scram, such as ULOF, UTOP or ULOHS are especially mentioned as advantages of metal fuels [99]. The reason is a combination of the temperature margin to sodium boiling, the fuel expansion effect and the small stored Doppler reactivity. Significant experience of transient behavior has been gained during the Experimental Breeder Reactor No. 2 (EBR-II) shut-down [29].

In conclusion, metallic fuel has proven to have a very high thermal conductivity but its low melting temperature leads to a pin design with a sodium bond. This bond enhances the heat transfer to the coolant and allows a higher margin to melt. Swelling of the fuel occurs already at very low burnup, therefore limiting the allowable fissile density. Using Zr alloy (as used e.g. in EBR-II metal fuel) can alleviate this problem. At higher burnups, fission gases produced during irradiation enhance the swelling [97].

5.2. Nitride fuels

Nitride fuels were initially investigated for space power applications. They are considered attractive for use in FRs due to their high heavy metal atom density (interesting for core neutronics, especially when it comes to breeding) and their high thermal conductivity [94]. Since only one moderating atom (i.e. nitride atom) is present per heavy atom instead of two (i.e. oxygen atoms) the spectrum of nitride fuels is harder than in oxide fuels (though softer than in metal fuels) leading to better breeding ratios. An additional advantage of nitride fuels is their compatibility with sodium. As concerns the safety coefficients, nitride fueled sodium cooled fast reactor cores have a more negative Doppler coefficient than metal fueled cores due to the softer spectra and higher uranium density [100].

Nitride fuels can be fabricated directly after the PUREX (Plutonium-Uranium-Reduction-EXtraction) reprocessing process [101; 102] as they do not interact with water, used during washing or storage steps of the reprocessing process [97]. While in the past nitride fuels were fabricated by nitriding the metal with N_2 or NH_3 gas or by nitriding the actinide hydride, nowadays carbo-thermic reduction is used (Eq. 5-1 [101]). In this process oxide powders are mixed with carbon, compacted and heated in a stream of nitrogen. The product is then milled to produce a fine powder, pressed into pellets and sintered. Pressing can as well be applied directly, thus avoiding the milling step.

Alternatively, the sol-gel method can be used for fabricating nitride fuels. This method is detailed in section 5.5.2. The nitride fuel pins are usually helium- or sodium-bonded [97].

A major drawback of nitride fuels is the formation of ^{14}C by (n,p) reactions with ^{14}N. This is problematic with regard to the limitations for radiological impact on the environment. This problem can be avoided by using ^{15}N instead (in [103] a scenario based on 820 MWth ADS reactors fueled with nitride fuel has been considered, and a production of 6.7 grams of ^{14}C /yr/ADS could be reached, making it comparable to the release coming from the oxide reprocessing), increasing however fuel fabrication costs [97]. ^{15}N recovery during reprocessing is considered as a possible means for cost reduction.

$$(U,Pu)O_2 + 2C + \frac{1}{2}N_2 \rightarrow (U,Pu)N + 2CO \qquad \textbf{5-1}$$
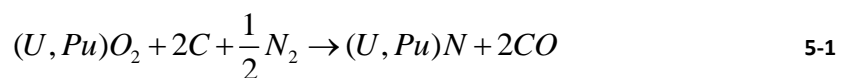
Irradiation programs for nitride fuels were mainly conducted in Russia, Europe and Japan. Experiments showed that these fuels are chemically compatible with stainless steel clad. Their thermal conductivity is higher than the oxide one while their melting temperatures are similar. This leads to a lower central fuel temperature and allows increasing the initial MA content in the fuel. A major drawback of nitride fuels is their behavior in case of core disruptive accidents. Nitrides thermally decompose in metal, producing nitrogen. Depending on the fissile enrichment of the fuel this leads to a recriticality concern [104] and pressure buildup could challenge the reactor vessel. Different to metal fuels with their low eutectic formation temperature, nitride fuels could be heated up under hypothetical severe accident conditions. Reaction of the decomposed metal with sodium might then lead to FCI (Fuel Coolant Interaction) events. Different to carbide fuels this issue has not been considered. In general, however, the good thermal conductivity leads to reduced average fuel temperatures and high power to melt ratios.

Furthermore, a violent reaction of mixed nitrides with sodium has been observed in some experiments. In fact, the high thermal conductivity of these fuels induces an explosive heat exchange between fuel and coolant in its gaseous state [97].

The sodium bond present in nitride fuels reacts with aqueous solutions and a pyrochemical reprocessing is needed. Therefore the helium bond design is usually chosen. This choice impacts the thermal exchange between fuel and cladding, leading to higher temperatures and therefore a higher swelling rate. Fuel Clad Mechanical Interaction (FCMI) will occur and could limit the burnup (BU). A limit on smear density has therefore to be set (up to 85% theoretical density - TD) and the cladding material has to be optimized [97].

5.3. Carbide fuels

Research on carbide fuels has been performed since the 1960's. These fuels are of special interest as they display a high thermal conductivity, less restructuring than metal or oxide fuels at same operating conditions and allow a higher fissile density [105]. In addition, the presence of only one moderating atom instead of two (contrary to oxide fuels) leads to harder neutron spectrum and better breeding ratios [38]. This induces as well a more negative Doppler [106]. A major drawback of carbide fuels is that they cannot be reprocessed directly by aqueous reprocessing. Moreover, they are pyrophoric at room temperature and react with nitrogen [94].

Carbide fuels are produced in the same way as nitride fuels via carbo-thermic reduction of oxides. Pre-compacted mixtures of oxides and carbon are heated in vacuum above 1300 ˚C. The mixture is crushed, milled, pressed into pellets and sintered. Carbide fuels are pyrophoric, which implies they have to be fabricated under an inert gas atmosphere – specifically argon – and in a low oxygen containing environment (less than 10 ppm).

Carbide fuels benefit from an extensive irradiation history, especially in the EBR-II reactor [29] in the US, at Los Alamos, as well as in India (BARC) and in Europe. Experiments have shown that a low fuel smear density i.e. a high amount of porosity is needed to avoid FCMI due to swelling (increasing with burnup) [97].

Concerning safety for carbide fuels the FCI potential is a concern under severe accident conditions with higher fuel temperatures. Melting temperatures are in the range of ca. ~ 2570 °C. At SANDIA national laboratories in the USA specifically the so-called PBE (Prompt Burst Experiments) have been performed to investigate the FCI issue. They revealed the expected behavior of an increased FCI energetics compared to the UO_2/Na system [107]. Again, the good thermal conductivity leads to reduced average fuel temperatures and high power to melt ratios.

5.4. Inert matrix fuels

In the 1990's focus was dedicated on the reduction of the actinide stockpile through transmutation. To enhance the actinides transmutation rates, the ^{238}U matrix was replaced by an inert one (with regards to neutronics). These kinds of new fuels which avoid production of new transuranic (TRU) elements are therefore named Inert Matrix Fuels (IMF).
The actinide oxides are usually diluted in the matrix leading generally to solid-solution Ceramic-Ceramic (CERCER) in case of a ceramic or Ceramic-Metal (CERMET) configurations. MA oxides in general have lower thermal conductivities requiring a matrix which compensates for it. This allows reaching acceptable power levels and temperatures in the fuel during operation and irradiation. Several materials were considered for the matrix, among them oxides, zirconium and titanium nitrides, SiC and metals. In addition to be neutronically inert, the thermal conductivity of the matrix should be as high as the one of the UO_2. If possible, mechanical properties should not be degraded compared to the UO_2. Compatibility of the matrix with coolant and cladding has to be ensured as well

as good compatibility with fissile isotopes (formation of eutectic with low melting temperature should be avoided) [108].

For transmutation of MAs, CERCER or CERMET fuels have especially been investigated for accelerator driven-systems as the EFIT reactor [109].

Assessing the fuels against a number of criteria, ranging from fabrication, reprocessing via economics to safety, the composite CERMET fuel $(Pu0.5,Am0.5)O_{2-x}$ – ^{92}Mo (93% enriched) and the composite CERCER fuel $(Pu0.4,Am0.6)O_{2-x}$ – MgO has been recommended. The specific characteristic of the composite fuels is that the individual component has to be viewed in its contribution to phase change processes. The matrix is the "continuous phase" and is a mechanically stabilizing structure whose disintegration point is a key safety criterion. Both the CERCER MgO and CERMET Mo based fuels have low disintegration points. Especially for MgO a fuel matrix destabilization has been identified around 1950 °C. In addition, these fuels present almost no Doppler effect and a low delayed neutron fraction [110].

5.5. Oxide fuels

In the 1960's oxide fuels became important because of their high tolerance to radiation. Mixed oxide (MOX) fuel was first used in a thermal reactor in early 1960, but did not come into commercial use until the 1980's mostly in pressurized water reactors (PWRs) in Europe. Oxide fuels present a high melting point and a good chemical stability. Experimental reactors like KNK-II [111], JOYO [25], BOR60 [112] or RAPSODIE [4] successfully employed mixed-oxide $(U,Pu)O_2$ fuels and led to prototype and commercial reactors based on oxide fuels. A large experience is available for these fuels providing a reliable background of knowledge of their behavior in normal and accidental conditions [94]. The most common mechanical form of oxide fuels is the standard pellet one. More exotic forms are investigated like the particle one. Both forms are treated in this section.

5.5.1. Pellet type fuels

5.5.1.1. Fabrication

As concerns MOX pellet fabrication, a large variety of fabrication processes is known worldwide. Only the French fabrication route will be detailed in this section.

MOX fabrication is usually performed by powder metallurgy techniques [25]. A description of the process is seen in Figure 5-1. At first plutonium and uranium oxides are mixed in the desired proportions through blending and milling steps. The homogeneous distribution of plutonium throughout the powder is crucial to avoid hot spots in the fuel during irradiation. The powder mix is finally pressed into a pellet and sintered at temperatures around 1600˚C. This step is required to densify the pellets up to the desired value – usually in the range of 85 to 95% TD [101]. The pellet is then grinded to achieve a uniform pellet size (dust is produced during this process). The pellet can be either full or annular (Figure 5-2).

UO_2 PuO_2 $(U, Pu)O_2$ scraps

DOSAGE

BLENDING-MILLING

Lubricant $\longrightarrow$ GRANULATION or FORCE SIEVING

PELLETIZING

SINTERING

INSPECTION
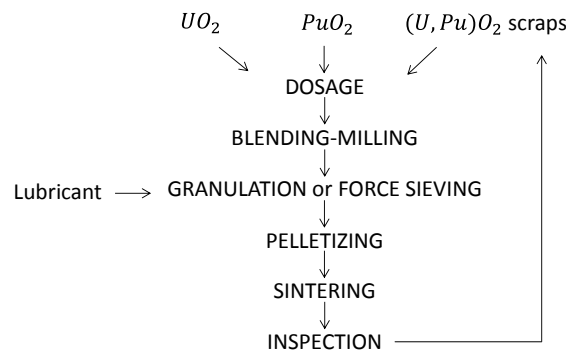
Figure 5-1. MOX pellet production scheme for FR fuel [101].
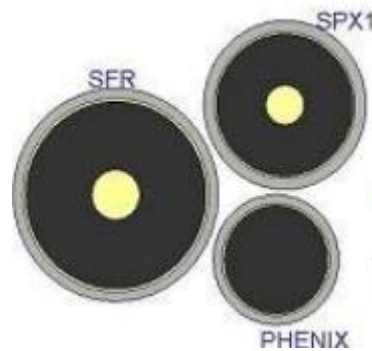
Figure 5-2. Pellet design [113] in PHENIX [4], SUPERPHENIX [4] and SFRV2B [42].

Once the pellets have been fabricated they are stacked into a cladding tube of fuel pins and He-bonded. The fuel pins are then assembled to a fuel assembly (Figure 5-3).
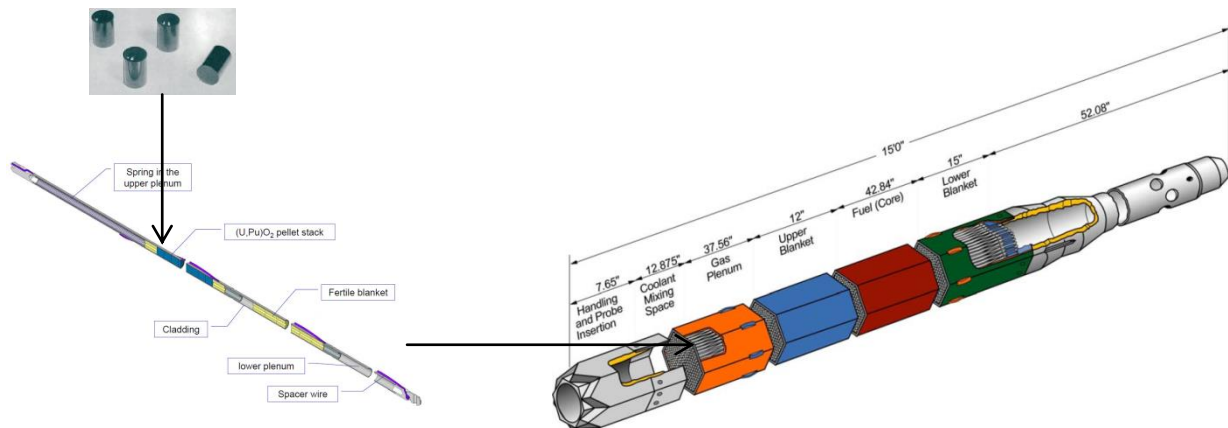
Figure 5-3. Pin and pin bundle assembly [114; 93; 115].

5.5.1.2. Standard pellet MOX fuel performance

Mixed oxide fuel is the most used fuel in fast reactors (FRs) in Europe and worldwide. This choice is based on the large experience obtained with light water reactor (LWR) fuels and the well-established fabrication and reprocessing processes. Even though the thermal conductivity of oxide fuel is poor

compared to carbide, metal or nitride fuel, its density of heavy atoms is quite low and it is incompatible with sodium, its advantages prevail. MOX fuel shows a high melting point, an excellent chemical stability, a good behavior under irradiation, a low swelling rate (0.6% per at% BU compared to 1.1-1.6% per at% BU in nitride fuels, [101]) and allows an aqueous reprocessing. The main properties of MOX pellet fuels at beginning of life (BOL) and under irradiation are discussed in this section.

Behavior at beginning of life

Heat transfer properties of the fuel are crucial to cope with safety requirements. Thermal conductivity is one of the most important fuel properties since it determines the heat transfer to the coolant and therefore the temperature in the nuclear fuel. It is a property rather difficult to determine from experiments as it depends on several other parameters like porosity, oxygen over metal ratio (O/M), burnup (BU), plutonium content etc. [94].

In practice, the thermal conductivity is deduced from thermal diffusivity measurements. The diffusivity value is multiplied by the material heat capacity and its density (Eq. 5-2).

$$k = a\rho C_p \qquad\qquad \textbf{5-2}$$

Where a is the thermal diffusivity in $m^2 \cdot s^{-1}$, ρ is the material density in $kg \cdot m^{-3}$ and C_p is the specific heat capacity in $J \cdot kg^{-1} \cdot K$

From a theoretical point of view, the thermal conductivity can be decomposed into 3 main contributions: the conductivity from phonons k_{ph}, from charge carriers k_{el} and from radiation k_r - Eq. 5-3. Up to 1800 K, conduction is mainly performed by phonons. At higher temperatures, the conduction through the kinetic energy of electrons and the one from radiation become more important.

$$k = k_{ph} + k_{el} + k_r \qquad\qquad \textbf{5-3}$$

Where:

- $k_{ph} = \dfrac{1}{A + BT}$, A corresponds to the scattering of phonons by imperfections and B to the scattering by phonon-phonon interactions. A is a function of burnup, plutonium content, oxygen over metal ratio. T is the temperature.

- $k_{el} = \dfrac{C}{T^2} exp(-\dfrac{W}{kT})$, where C is in $W \cdot m^{-1} \cdot K$

- k_r = D T^3, where D is in $W \cdot m^{-1} \cdot K^{-4}$

The thermal conductivity of oxide fuels is rather poor and in the range of 2-3 $W \cdot m^{-1} \cdot K^{-1}$ for an as fabricated 100% dense fuel. The temperatures in the fuel are hence relatively high and several thermally activated processes take place in the fuel.

The pellet macrostructure undergoes various changes during irradiation. Due to the radial temperature gradients inside the fuel, the pellet center tends to expand more than its outer periphery and internal stresses cause pellet cracks. Very soon after the reactor start-up the grains start to grow rapidly due to the high temperatures in the fuel and form the equi-axed grains. Close to the center of the pellet, where the temperature is the highest, the as-fabricated pores tend to collect and to migrate towards the center (up the temperature gradient) through vaporization/condensation processes where they form a central hole. They leave behind them very long grains called columnar grains, forming a very dense matrix. This occurs in the first hours of reactor operation [25]. The fuel material at the very edge of the pellet remains non-restructured (see Figure 5-4).

Closely linked to this restructuring process, a redistribution of constituents is systematically observed in the fuel. Indeed, through vapor transport i.e. through the vaporization/condensation process, and through thermal diffusion processes, plutonium and americium isotopes tend to migrate up the temperature gradients. Neptunium has appeared to be uniformly distributed throughout the fuel, but these conclusions are still very preliminary [94].
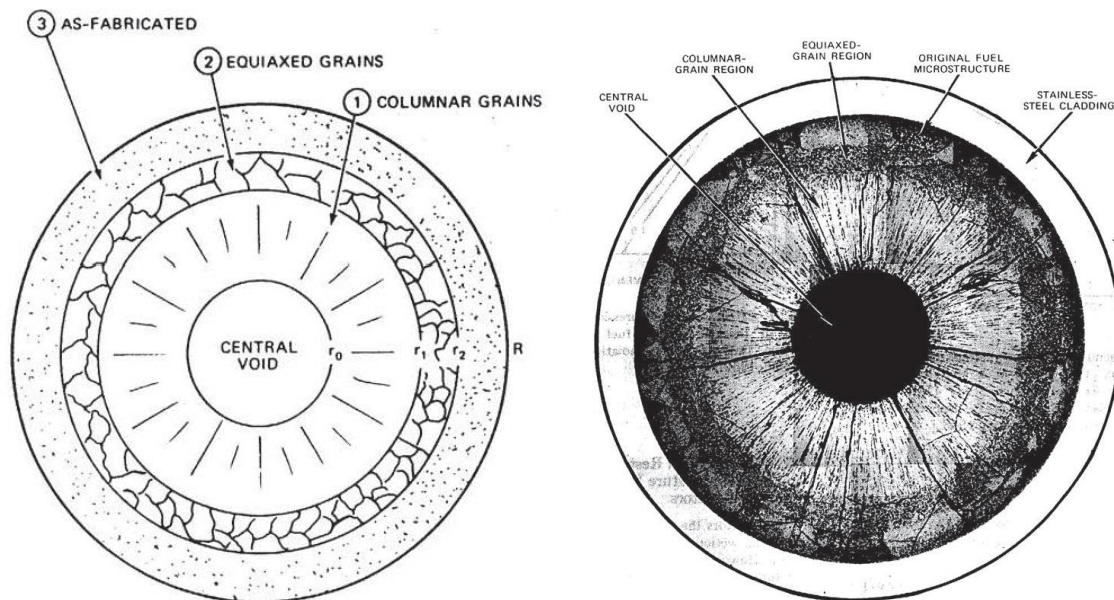
Figure 5-4. Schematics (left) and real (right) restructured FR MOX fuel with 2.7 at% BU [116].

In addition to restructuring, the gap between pellet and cladding tends to close due to fuel expansion, swelling and cracking. The axial temperature distribution in fast reactor pins leads the fuel macrostructure to vary along the axial axis. Most of these phenomena tend to decrease the centerline temperature of the fuel - Figure 5-5.
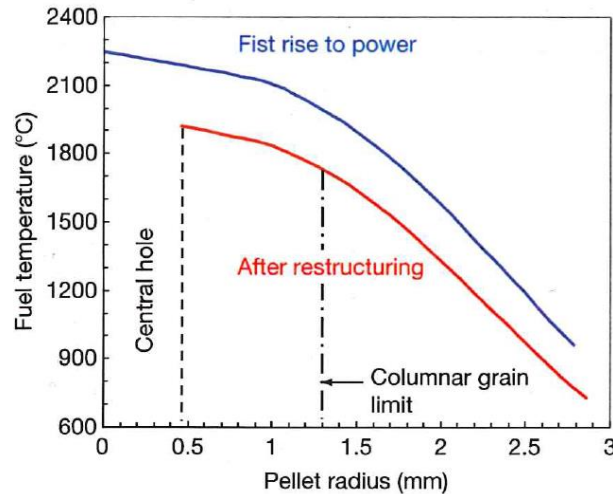
Figure 5-5. Radial temperature profile in a PHENIX oxide pellet [94].

Consequences of irradiation

During irradiation, fission gases are produced from fission or from the decay of fission products. The gas bubbles nucleate, grow, diffuse and eventually collect and condense at grain boundaries. They will then form "tunnels" and eventually be released by the fuel matrix. Tracks left by pore migration within the columnar grain zone as well as cracks caused by shutdown and restarting operation events allow the fission gases to be vented to the central void region and to eventually be collected in the fission gas plenum. Figure 5-6 depicts these details of the processes leading to fission gas release. The axial variation of fuel macrostructure leads to a different fission gas release at different axial heights.
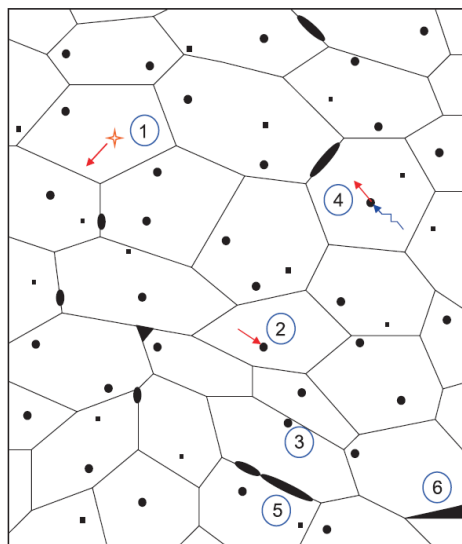
Figure 5-6. Schematics of steps leading to fission gas release [117]. 1) Fission products diffuse in the lattice and along grain boundaries 2) Capture of the fission gases in intragranular (within a grain) and intergranular (between grains) bubbles e.g. fabrication pores or newly formed bubbles 3) Bubbles migrate to grain boundaries 4) Re-solution of gas from the bubbles into the matrix, due to radiation 5) Coalescence of closed gas pores into pores along the grain boundaries 6) Release via open porosity tunnels formed by porosity aggregation [117].

A consequence of fission gas release is that they might accumulate at the fuel-cladding interface where they induce cladding oxidation. The main species responsible for corrosion are Cs, Te and I [94]. In addition to this fuel cladding chemical interaction (FCCI), fuel cladding mechanical interaction occurs as well (FCMI). FCMI results from two phenomena: a differential thermal expansion between fuel and cladding on one hand and fuel volume changes due to production and retention of fission products on the other hand [118]. Thanks to the low swelling rate of oxide fuels compared to carbide or nitride fuels, and to the high thermal and irradiation fuel creep rate, FCMI is of low importance in oxide pellet fuel. Nevertheless, the fuel burnup and the smear density have to be limited to avoid FCMI [94].

5.5.1.3. Recycling and high level waste management

Recycling of spent nuclear fuel (SNF) is performed in Europe essentially in France and the United Kingdom (UK) to chemically separate and recover fissionable plutonium from irradiated nuclear fuel in order to use it for the fabrication of fresh fuels.

After irradiation, the SNF is cooled down for some years before recycling. Even though several reprocessing techniques are known, focus is concentrated on the hydro-chemical PUREX process already used at an industrial level. Uranium, plutonium and waste – fission products (FPs) and MAs – are separated during this process. The process is divided into 4 steps: SNF dissolution, off-gas treatment, chemical separation and conversion of FPs and MAs waste into vitrified products. Schematics of the process can be seen in Figure 5-7.

At first, the fuel pins are cut into segments of some centimeters to ensure fuel dissolution. The slices fall into a basket containing hot nitric acid thus forming a nitrate solution of uranium, plutonium, minor actinides and fission products. Whereas elements as iodine, krypton or xenon volatilize during this dissolution step and are removed by the off-gas treatment, a percentage of more noble fission elements remain undissolved after this process. The cladding hulls are collected during this step. In the next step, separation of the different elements is obtained via solvent extraction, depending on affinities with the nitric acid and organic phases. Fission products and MAs are separated from uranium and plutonium. In a further step, uranium and plutonium are separated by adjusting the valence of plutonium to make it unextractable by the organic phase. The uranium is finally recovered. The separate solutions of uranium and plutonium are converted to solids through denitration in case of uranium and oxalate precipitation followed by calcination in case of plutonium. The waste solution is evaporated, calcinated and vitrified thanks to the addition of glass components [119; 120].
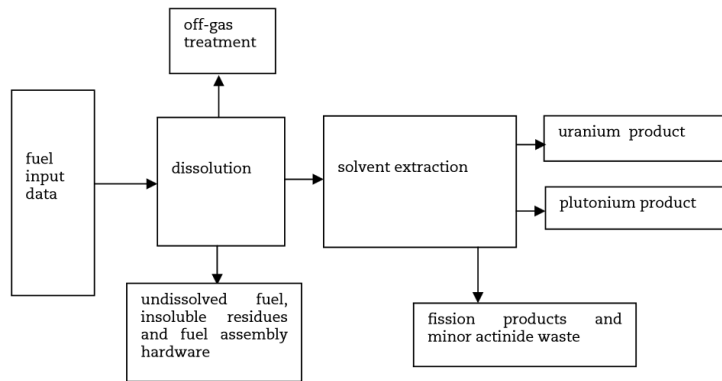
Figure 5-7. Flow sheet of the PUREX process (simplified) [120].

Instead of separating plutonium and uranium to form two distinct solids, the COEX process (CO-EXtraction process of Uranium and Plutonium) can be used as well. It has been developed by CEA France in order to co-extract simultaneously both components therefore increasing proliferation resistance [121].

When it comes to transmutation of MAs, the considered isotopes have to be recovered from the SNF. To that end, additional steps to the PUREX process are applied (these steps have been proven at a laboratory scale). First, the DIAMEX process (DIAMide EXtraction) separates actinides and lanthanides from non-lanthanide fission products and corrosion products. The SANEX (Selective ActiNide EXtraction) process finally separates actinides from lanthanides [122]. The recovered actinides are then used for fresh fuel fabrication. The overall flow sheet of the oxide fuel reprocessing is depicted in Figure 5-8. The current fabrication of oxide fuel pellets is based on a dry route and handling of powders. As the recycling step includes an aqueous route, it is of interest to develop wet fabrication routes as e.g. the sol-gel route which is detailed in a later section.
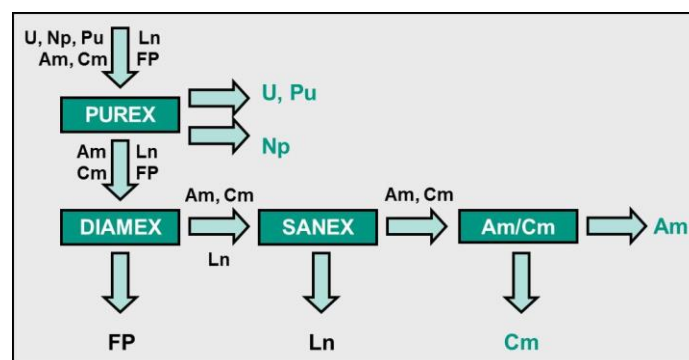
Figure 5-8. Flow sheet of oxide fuel full reprocessing [122; 120].

5.5.1.4. Conclusion on oxide pellet fuels

Oxide pellet fuels have been investigated since the 1960's. The oxide fuel and especially the MOX fuel present a large database provided by many irradiation experiments in both LWRs and FRs. Large experience for SFR fuels also exist in the transient and accidental domain of reactor operation.

Especially to mention are the TREAT [123] and FD experiments [124] in the US and the large French experimental program CABRI [125] which formed an unprecedented knowledge basis covering the whole range of phenomena up to fuel vaporization under severe accidental conditions. These experiments also lead to the development of today's sophisticated safety codes for pellet fuels (e.g. TRANSURANUS [126] or GERMINAL [127]). Referring to the above fore-mentioned problems of dissociation and FCI potentials (see nitride and carbide fuels) the oxide fuels show a remarkable stability (no separation of Pu from U under melting) and due to the low thermal conductivity the FCI potential is also low. In addition, oxide fuels are the most commonly used fuel type in industrial reactors. They are suitable for MA transmutation [95] but present nonetheless a concern ascribed to their production process (powder handling inclined to produce dust) and their tendency to swell under irradiation (mainly due to helium production from the decay of MAs). Other mechanical forms of oxide fuel are therefore envisaged as e.g. particle fuels. In the following section, focus lies on these specific fuel forms.

5.5.2. Sphere pac fuels

Particle fuel forms are of high interest for MA-bearing fuels. Several forms of particle fuels are known the major ones being the TRISO, vipac and sphere-pac fuels.

TRISO particles were primarily developed for the high temperature gas cooled reactors (HTGRs). These particles are composed of a fuel kernel of UO_2 or MOX, surrounded by several coating layers to make the particle gas-tight [128] (Figure 5-9). The reprocessing of this fuel, feasible though difficult, has been discarded for non-proliferation considerations and direct disposal is preferred nowadays [129].
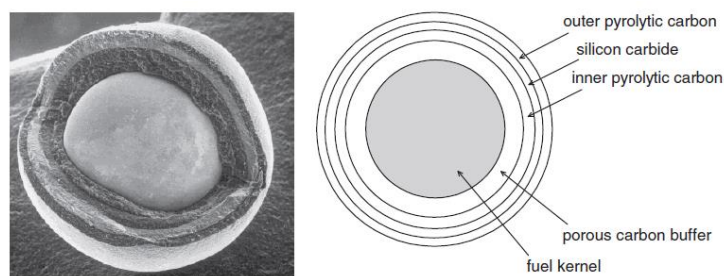
Figure 5-9. A TRISO coated particle [117].

Vipac fuels are randomly shaped particles poured into a cladding tube under vibration. Large experience was gained in Russia for this fuel [130]. Their simple handling is easily adaptable to remote handling of MA-bearing fuel [131].

Sphere-pac fuels are similar to vipac fuels. This time the particles are regularly shaped spheres poured into a cladding tube [131]. This concept is under investigation in the FP-7 PELGRIMM project [11] and is therefore detailed hereafter.

5.5.2.1. The sphere-pac concept: history, advantages, drawbacks

Sphere-pac fuels are investigated worldwide since the 1960's. The motivation lies in the development of an alternative production route to the standard pellet process. It is justified by the simplicity and cleanness (dust free process) of the fabrication process deriving from a wet reprocessing route and making it suitable to remote handling, a requisite due to the high radiation of the dissolved spent nuclear fuel [132]. Sphere-pac fuels are fabricated by sol-gel methods. This "wet" route limits the contamination risk of operators in case of an accident and facilities as it is a dustless process and milling and grinding steps required in the standard pellet fabrication are hence avoided. In addition, the sphere-pac fabrication process allows to control the particle size and no sieving is needed, the particles being directly separated. Furthermore, the spherical size of the particles reduces the friction resistance during the filling process. Moreover, these fuels are expected to present several advantages when it comes to the use of MAs in nuclear fuels. Since sphere-pac pins are composed of fuel microspheres of several particle size ranges poured into a cladding tube and surrounded by helium gas - Figure 5-10 - they are expected to behave well under irradiation. In fact, their specific macrostructure would provide enough space for fission gases and He released by MA decay to be accommodated and to relieve pressure on the cladding [133].

One major drawback of sphere-pac fuel stacks compared to pellets is their lower thermal conductivity at BOL, especially as "green fuel" (i.e. non-irradiated fuel). Indeed, due to the few and narrow contact points between the spheres, the heat transfer is reduced and leads to higher fuel temperatures. This drawback is compensated during the early lifetime of sphere-pac fuels as they rapidly restructure in the core - on a timescale of hours - due to the strong temperature gradients in the fuel. The thermal conductivity of sphere-pac fuels is therefore already enhanced during the start-up phase, due to sintering mechanisms as demonstrated, e.g., in the FUJI experiment [133].
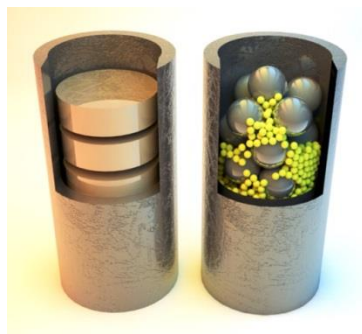
Figure 5-10. Pellet and sphere-pac fuel schematics [134].

5.5.2.2. Fabrication

As mentioned previously, the sphere-pac particles are produced by sol-gel methods. This process implies the gelation of droplets through hydrolysis resulting in a condensation and polymerization of the fissile material in gel spheres. These spheres are then converted into high density spheres via sintering.

One of the major advantages of using sol-gel methods is that they can be applied directly after the spent nuclear fuel recycling process step as they are fully aqueous methods. The distribution of fissile material is excellent, avoiding possible hotspots. In addition, the fabrication of sphere-pac fuel does not need any grinding or milling steps, considerably reducing the dust production and therefore preventing some possible contamination of operators and facilities. Reducing the number of steps for fuel fabrication makes the process cost-effective.

Nevertheless, this fabrication process includes the production of low level liquid waste streams if use of the internal gelation option (detailed later in this chapter) is made and induces additional reprocessing and storage steps [131].

Particle production

In case of a closed cycle option, the spent nuclear fuel is recycled and is therefore in an aqueous state, more specifically in form of a nitrate solution. The sphere-pac fabrication starts from this aqueous state. Even if the sol-gel process can be used for the standard pellet fuel, focus is put in this section to the application of the process to sphere-pac fabrication. Several methods for gelation are developed but only the three main ones are described hereafter: the internal gelation, the external gelation and the internal microwave gelation. For more details the reader is referred to [131].

The internal and external gelation processes are both based on an acidity shift driven precipitation of a metal nitrate solution by ammonia into ammonium metal hydroxide. For the internal gelation process this shift relies on a temperature driven decomposition of an ammonia precursor (added into the nitrate solution where it thermally decomposes to release ammonia internally within the droplet). The temperature shift is induced by a heat carrier (hot silicon oil or a microwave cavity). For the external gelation process only an external ammonium hydroxide solution in which the droplets (sol) fall is needed - Figure 5-11 [131]. No heat carrier is therefore needed.
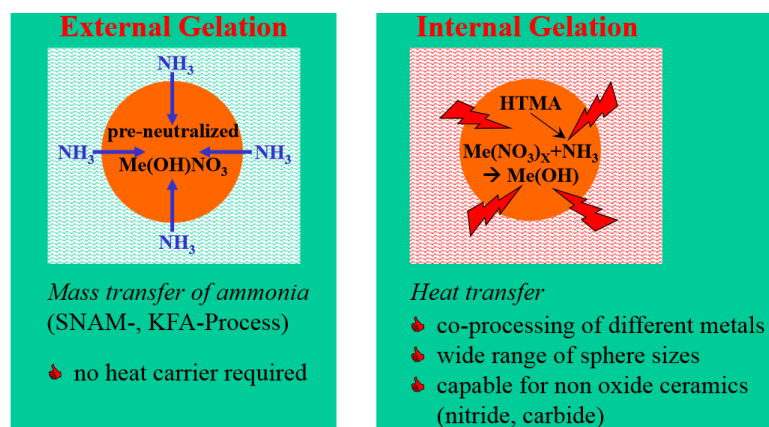
Figure 5-11. Internal and external gelation processes [131; 135]. SNAM (Societa Nazionale Metanodoti) and KFA (Kernforschungsanlage Jülich des Landes Nordrhein-Westfalen) processes have been developed in Italy and Germany, respectively.

The internal gelation process initially developed in the Netherlands allows the co-processing of various metals in a nitrate solution [131]. All chemical ingredients necessary to gelation are already in

the feed solution and temperature will drive the reaction. To start the gelation process, a nitrate solution of U, Pu and MA is needed. This solution is brought to a temperature close to 0 °C and mixed with gel agents as $CO(NH_2)_2$ urea and HMTA [136] (HexaMethyleneTetraAmine). The precipitation of the internal gelation is driven by formation of ammonia coming from the decomposition of HMTA, itself catalyzed by the acidity of the solution (coming from the adding of NO_3^-). The feed solution is then given to a drip unit which will produce particles of different sizes depending on the employed nozzle e.g. 6 droplets per second can be produced for the coarse fraction and up to 15000 droplets per second for the fine fraction. The coarse droplets fall into a silicon oil bath while the finer ones are carried via a jet of silicon oil to avoid aggregates. The silicon oil also serves as a heat carrier and its temperature determines the solidification of the droplets. In the next step, the solidified spheres are passed on a belt-filter where the silicon oil is removed with vacuum and the introduction of organic solvent. The spheres are then passed on a second belt where they undergo again cleaning under vacuum with a new solvent in order to remove the organic solvent. The rinsed spheres are then collected and washed with diluted ammonia to remove the residual reaction products and excess of nitrates [131]. Once the washing has been performed, the spheres are dried in hot air (at 150 °C [136]), calcinated (up to 500 ˚C [136]) and sintered to obtain spheres of high density. They are then poured into the cladding tube. The complete process can be seen in Figure 5-12.
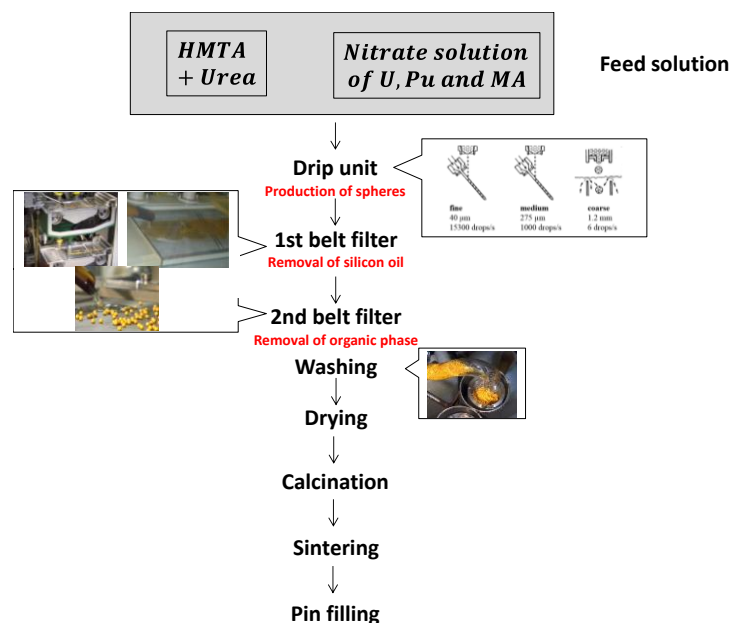
Figure 5-12. Internal gelation process [135].

The internal gelation process is an almost dust-free process. In addition few mechanical components are needed and the process has been proven to be reliable and reproducible [131]. The silicon oil is used as heating, droplet reception and transportation medium at the same time [108].

Nevertheless, this process involves some undeniable drawbacks. The employment of silicon oil and solvents for washing the spheres introduces additional recycling and disposal steps, and the liquid waste volume increases. Furthermore, the process would require a larger space than the standard pellet fabrication one and might increase the production costs if used at an industrial scale. In order to simplify the process, other heat sources than silicon oil are therefore considered. To that end, a technique based on microwave heating has been developed [132; 131].

As the internal gelation process is mainly driven by temperature and does not need any additional external chemical agent, the silicon oil can be replaced in its function of heat carrier by a microwave cavity - Figure 5-13. This is the so-called microwave technique [131]. After the drops are formed they freely fall into a microwave cavity where they will be heated up. The cavity operates in the X-band and is composed of a quartz tube to avoid contamination. The gel drops fall then into the ammonia wash column. Neither recycling of oil nor the two belt filters are then needed [132].
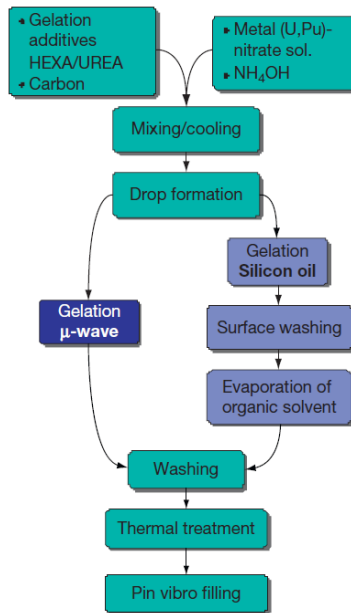
Figure 5-13. Internal gelation microwave process [131].

Alternatively to the internal gelation process, the external gelation process can be employed. This process was first developed in Italy and has been widely used for the production of TRISO particles [128]. To the contrary of the internal gelation process, the external gelation does not require the use of a heat carrier (no silicon oil is needed) [131]. This is attributed to the fact that the required acidity shift is induced by an external ammonium hydroxide solution.

The external gelation process is composed of a uranyl nitrate feed based solution, an organic polymer (Polyvinyl alcohol i.e. PVA) and a modifying agent (Tetrahydrofolic acid i.e. THFA).The feed solution is dispersed into droplets through a nozzle under vibration. The droplets fall through an ammonia gas layer inducing their surface to harden. During this fall, the particles get their final spherical shape. They are then collected in an ammonium hydroxide bath which will precipitate the uranyl nitrates into ammonium diuranate and induce the gelation process. The droplets are then aged to complete the reaction process, washed in two steps (first with water or diluted ammonium hydroxide to remove the excess of ammonium nitrate and then with isopropanol to dehydrate the gel particles), dried, calcinated at 400-600 ˚C in air, reduced and sintered. Schematics of the external gelation process can be seen in Figure 5-14 [135].

Since actinides are present in the feed solution, radiolysis can take place, therefore modifying the chemistry of the solution. In addition, the decay of e.g. Cm, if present, will heat up the solution, presenting an issue for the thermally driven gelation process. All these factors still have to be investigated.
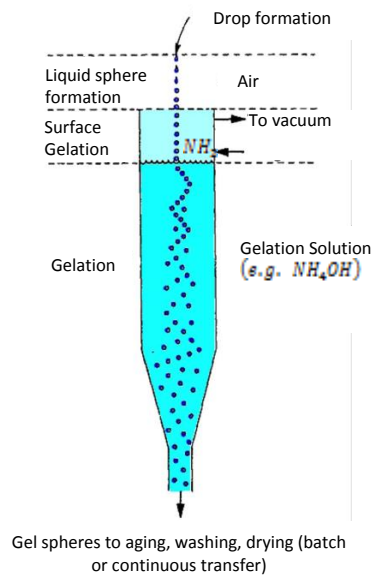
Figure 5-14. External gelation process [135].

Once the particles have been produced, they are filled into a cladding tube under vibration while using either a parallel or an infiltration filling technique.

Pin filling

The fuel pins can be produced either by parallel or by infiltration filling. Several size fractions are used to obtain the desired density. In practice two to three size fractions are used to fill the pins: a coarse one, a fine one and potentially an intermediate one. The size ratio between spheres of different diameters plays an important role in the achievable packing density - Figure 5-15 - and densities as high as 95% TD have been observed [137]. The original filling density has an important impact both on the fuel performance itself but also, if inserted in a reactor, on the basic reactor design and layout.
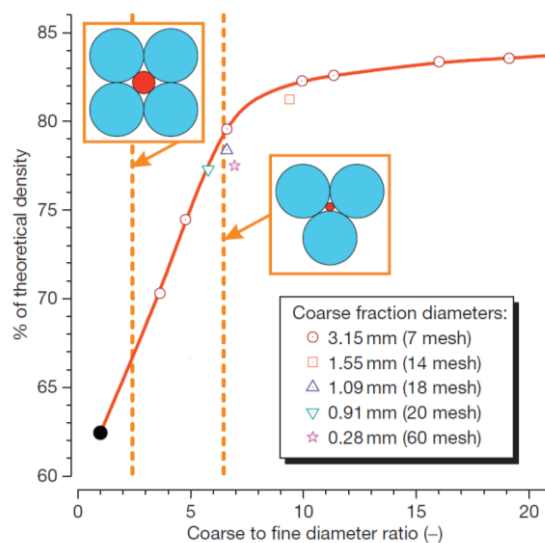
Figure 5-15. Impact of coarse to fine ratio for sphere-pac packing density [131].

With the parallel filling option, two sphere fractions (coarse and fine) are filled at the same time into the fuel pin. Vibration is employed during or after the filling process to avoid segregation. For this filling technique the ratio between coarse and fine sphere fractions can be lower than for the infiltration one (Figure 5-16 (a)) [131].

With the infiltration filling, the coarse fraction is filled first into the cladding tube. It is then fixed in order to keep the arrangement and the fine fraction is "infiltrated" through a sieve-like holder. The small spheres occupy the free space between the coarse spheres. Vibration is applied during the whole process in order to reach the highest possible packing density. This technique allows a very homogeneous distribution of spheres inside the cladding tube (Figure 5-16 (b)) [131].

(a)   (b)
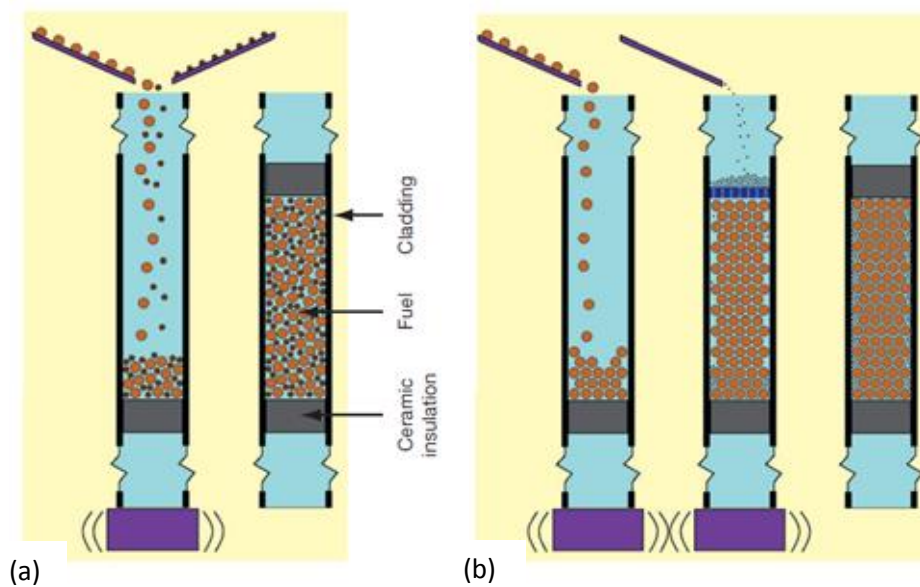
Figure 5-16. (a) Parallel filling (b) Infiltration filling [131].

Different filling techniques imply different behavior of fuels during irradiation (related e.g. to the different thermal conductivity). Nevertheless, the major difference to pellet fuel comes from the specific fuel form of sphere-pac fuel.

5.5.2.3. Physical properties and behavior under irradiation

Heat transfer properties

One of the major drawbacks of sphere-pac fuel stacks is their low thermal conductivity at BOL. Due to the macroscopic arrangement of spheres, the few and narrow contact points between them makes the heat transfer quite low if compared to the standard pellet fuel. This results in higher central temperatures than in pellet fuel and might cause an issue with regard to safety margins [131].

Due to the globally higher temperatures in sphere-pac than in pellet fuel (when operating at same linear power), a more extended restructuring process takes place at the beginning of irradiation in

the former one, largely impacting the thermal conductivity. Four zones can be distinguished when starting from the center and moving radially towards the cladding - Figure 5-17.

Zone II: Strongly sintered area
- Intermediate or final stage of sintering
- Original sphere structure not visible (similar to porous pellet)
- After 1 h temperatures typically >1400 ˚C (sphere diameter 70 μm and pressure 1bar)
- The zone proceeds toward the rim and lower temperatures with longer irradiation time, higher external load or smaller sphere size

Zone I: Center hole
- Emerges later in the life

Zone III: Transition zone
- Between fast and slow sintering areaing
- Moves outward and lower temperatures as irradiation proceeds
- On temperature scale, only 150-200 ˚C wide

Zone IV: Slow sintering
- Initial stage of sintering
- Original sphere structure visible
- Pores interconnected
- Temperature < 800 ˚C
- Irradiation creep dominates

Figure 5-17. Restructured sphere-pac fuel, schematics [138].

Pores in the central fuel zone, where the temperatures are the highest, are migrating towards the center and form a central hole. The temperatures are then the highest in the zone in the vicinity of the hole, leading to sintering. A dense matrix closely resembling the pellet structure forms. In fact, due to the softness of the fuel, the initial plastic deformation and thermal creep induce fast sintering.

A third zone can be distinguished by a higher porosity compared to the pellet-like structure but a sintered matrix is still present. It is a transition zone between the fast and slow sintering regions.

The fourth and last zone close to the cladding displays the initial macrostructure. In this zone the temperatures are much lower than in the center and no sintering occurs. The initial sphere structure remains with some necking between the spheres. This non restructured annulus provides two benefits: a lower stress on the cladding (as the spheres can move vertically) and a reduced fission product transport towards the cladding since the cracks in the pellet-like zone do not extend to the cladding (leading to a different distribution of gas in the pin) [118]. The macrostructural variation observed during the first hours of irradiation is shown in Figure 5-18.

Due to this restructuring process (however depending on the axial position of the considered fuel slice), the thermal conductivity is enhanced very quickly, especially in the first hours or few days.
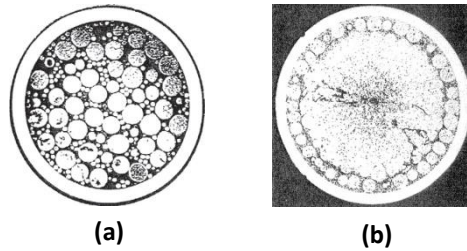
Figure 5-18. (a) Non irradiated sphere-pac pin (b) Irradiated sphere-pac pin [131].

In addition, caused by the higher temperatures and higher specific surfaces, more fission gases are released by the sphere-pac fuels than by the pellet fuels. Due to a reduced transport of FP towards the cladding, no FCCI has been observed.

Mechanical properties

As sphere-pac fuel is mechanically softer than the standard pellet fuel, the spheres deform and interstices between the spheres provide sufficient spaces to accommodate fuel swelling, thus relieving the mechanical constraint on the cladding [138].

5.5.2.4. Irradiation programs

Many irradiation programs were conducted worldwide for sphere-pac fuels in oxide or carbide form. In this section, attention will be devoted only to MOX oxide sphere-pac fuels irradiations.

The Oak Ridge National Laboratory (ORNL) in the US conducted an extensive irradiation program for sphere-pac fuels including thermal flux tests, transient tests and fast flux tests in the 1960's and 1970's. The aim of these experimental programs concerned the thermal performance of sphere-pac fuels, their restructuring process, the actinide and fission product redistribution, the FCMI and FCCI. The tests were performed in the Engineering Test Reactor (ETR) at Idaho [139], the EBR-II [29] and the TREAT [123] reactors. Comparison of sphere-pac and pellet fuels was performed in terms of e.g. fabrication and behavior under irradiation, giving insights into the specifics of sphere-pac fuels [140; 141].

Programs were conducted not only in the US but also in Italy, the Netherlands and Japan [131]. The most recent ones are the FUJI experiments (1996-2005) and the SPHERE irradiation (on-going) conducted in the frame of FAIRFUELS [142] and for which the post irradiation examinations (PIEs) are scheduled (2016-2017) in PELGRIMM [11].

In the FUJI experiment, jointly performed by PSI, JAEA (former JNC) and NRG, 4 tests were conducted for different periods of time. It addresses the question of fabrication of MOX fuel with high Pu content (20%) and its irradiation behavior during the start-up phase of the reactor. The tests aimed at comparing sphere-pac, vipac and pellet fuels [133]. The Initial Sintering Test (IST) simulates the behavior of sphere-pac fuel within the first 36 hours when the reactor goes from zero to full power. The Restructuring Test 1 (RT1) simulates fuel behavior from zero to full power within 36 hours of

operation followed by 48 hours at full power. The Restructuring Test 2 (RT2) resembles RT1 with a holding time of 96 hours at full power and the Power To Melt (PTM) follows RT1 and experiences later on a constant power increase until fuel melting is observed. In all tests, no rod failure was found, giving a promising basis for sphere-pac applications [133].

Moreover, the FP-7 European project PELGRIMM focuses on sphere-pac fuels as mentioned previously. Post-Irradiation Examinations of SPHERE irradiated pins within the European project FAIRFUELS should provide first results on the helium behavior in $(Am,U)O_2$ fuels and a comparison between sphere-packed and pelletized $(U,Pu,Am)O_2$ fuel performances. In addition, $(Am,U)O_2$ fuel qualification is performed in the MARINE fuel test (within PELGRIMM) in the High Flux Reactor [143] and the knowledge base of fuel fabrication processes of MA bearing fuels should be extended in order to limit secondary waste streams.

5.5.2.5. Conclusions on sphere-pac fuels

Sphere-pac fuels present a large advantage to pellet fuels if MAs are used. In fact, their fabrication process being based on an aqueous route reduces the dust production and therefore the risk of possible contamination of operators and facilities. In addition, their macrostructure enables to accommodate fission gases during irradiation, therefore reducing the FCCI and FCMI compared to pellet fuels. One major drawback of sphere-pac fuel is their low thermal conductivity at BOL. Quick restructuring nevertheless alleviates this issue and restricts its detrimental impact to the very first hours or days of irradiation.

5.6. Conclusions

The fuel types considered for GEN-IV reactors comprise a rather large variety: oxide, carbide, nitride, metallic and dispersion (CERCER and CERMET) fuels. All of them present advantages and drawbacks in the fabrication, irradiation or reprocessing steps. Their choice mainly depends on the reactor type and planned field of application. Special mechanical forms (e.g. particle fuels, vipac and sphere-pac fuels) are considered as well.

Currently the oxide fuels remain, in Europe, nevertheless the preferable choice as they benefit from a large fabrication, irradiation and reprocessing experience from commercial thermal reactors. Within the FP7-PELGRIMM project, two oxide fuel forms are considered for the transmutation of MAs: the standard pellet and the sphere-pac fuels. Fabrication processes and irradiation performance of these fuel types along with the available fundamental properties still have to be investigated in detail. Thus, within the project framework, capabilities of simulation codes for fuel behavior under irradiation should be extended, which is important for increasing the basic knowledge and providing confidence on transient and accidental behavior. Another target of PELGRIMM is the investigation of the possibility to insert $(U,Pu,Am)O_2$ sphere-pac fuel to a large sodium cooled fast reactor and perform a preliminary safety assessment. In this manner, information should also be obtained on necessary experimental information, including transient conditions and on needs for code development for transient and accidental conditions.

Results of this investigation are presented in chapter 8.

Chapter 6

A NEW METHODOLOGY FOR SIMULATING CORE EXPANSION EFFECTS IN SPATIAL KINETICS CODES

For recent fast reactor designs the probability of the occurrence of a severe accident is considered to be extremely low. Nevertheless as fast reactors loaded with mixed oxide (MOX) fuel are not in their most reactive configuration, Hypothetical Core Disruptive Accidents (HCDAs) due to recriticalities are investigated. In particular, the SIMMER-III and IV codes [73; 74] dedicated to severe accident analyses are under development and application. These codes are particularly tailored to mechanistically analyze accident sequences in already disrupted cores. Significant efforts are invested at KIT in improving the performance of the SIMMER codes for simulating the initiation phase of accidents. A special focus is on the impact of core thermal expansion phenomena on the reactivity. In fact, in the simulation of core disruptive accidents, the related reactivity effects might play an important role in particular in the early phase of the transient when the pin structure is still intact: the thermal expansion effect of fuel and/or structure e.g. mitigates the primary excursion in case of a loss of flow in a sodium cooled fast reactor [144].

In the present chapter options for the implementation of core thermal expansion feedbacks in SIMMER are described. First, fundamental quantities and equations as the time-dependent neutron transport equation used in reactor physics are introduced. This equation governs the variations in both amplitude and shape of the neutron flux in the reactor. Its numerical solution in the general case is only possible by numerical discretization and approximations. Different methods aiming at this purpose are thus detailed. The neutronics part of SIMMER uses a spatial kinetic neutron transport approach. Within this framework and the constraint of the Eulerian mesh of SIMMER, new methodologies for taking into account core thermal expansions are developed. The methodologies are based on the fact that density variations reflect dimensional variations and hence the original mesh can be used while taking into account dimensional variations. Applications of these methodologies to static and dynamic cases are presented and analyzed. As a result the technique can be used to compute the reactivity feedbacks induced by both uniform and non-uniform thermal expansions of the core.

6.1. Neutron transport theory

The neutron transport equation is used to determine the neutron distribution in a nuclear reactor. This general integro-differential equation is inherently complex and difficult to solve analytically except for very simplified cases. Discretization and approximations are thus needed to find a numerical solution. The approximation of using diffusion theory might often be sufficient for design purposes. However, due to the fairly complex geometrical arrangements usually encountered during HCDAs its application is not appropriate for analyzing such configurations.

6.1.1. Time-dependent neutron transport equation

In order to describe the evolution of the spatial distribution of the neutron population, the time-dependent neutron transport equation is usually analyzed. A neutron at a certain instant t is characterized by its position in space $\vec{r}$, its velocity v (or equivalently, its energy $E = \frac{1}{2} mv^2$ if relativistic effects are neglected, m being the neutron mass), and its direction represented by the unit vector $\vec{\Omega}$.

The neutron population is represented by a function $n(\vec{r}, E, \vec{\Omega}, t)$ so that $n(\vec{r}, E, \vec{\Omega}, t) \ d^3r \ dE \ d\vec{\Omega}$ represents the number of neutrons in the volume element $d\vec{r}$ around $\vec{r}$ in the range dE around E and in the solid element $d\vec{\Omega}$ around $\vec{\Omega}$ - Figure 6-1.
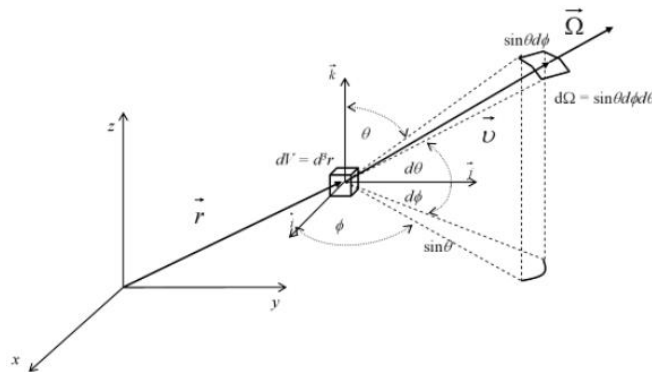
Figure 6-1. Spatial variables describing the neutron position at an instant t [145].

The variation of the neutron population results from an off-balance of production and losses of neutrons – Eq. 6-1.

$$\frac{\partial n}{\partial t}(\vec{r}, E, \vec{\Omega}, t) = \text{production - losses} \qquad \textbf{6-1}$$

The neutron flux is usually introduced and defined to be $\varphi(\vec{r}, E, \vec{\Omega}, t) = \text{v}(E)n(\vec{r}, E, \vec{\Omega}, t)$ where $\text{v}(E)$ is the neutron velocity. The neutron transport equation [146] - Eq. 6-2 - can then be derived as

$$\frac{1}{v(E)}\frac{\partial \varphi(\vec{r},E,\vec{\Omega},t)}{\partial t} = \underbrace{Q(\vec{r},E,\vec{\Omega},t) + S(\vec{r},E,\vec{\Omega},t)}_{\text{production}} - \underbrace{\left(\vec{\Omega}\cdot\vec{\nabla}\varphi(\vec{r},E,\vec{\Omega},t) + \Sigma_t(\vec{r},E,t)\varphi(\vec{r},E,\vec{\Omega},t)\right)}_{\text{losses}}$$ **6-2**

Where

- $\varphi(\vec{r},E,\vec{\Omega},t)$ is the neutron flux in the volume element d^3r around $\vec{r}$ in the energy range dE around E and in the solid element $d\vec{\Omega}$ around the angular direction $\vec{\Omega}$ at time t.

- $\dfrac{\partial \varphi(\vec{r},E,\vec{\Omega},t)}{\partial t}$ is the neutron flux variation.

- $\vec{\Omega}\cdot\vec{\nabla}\varphi(\vec{r},E,\vec{\Omega},t)$ represents the leakage term.

- $\Sigma_t(\vec{r},E,t)\varphi(\vec{r},E,\vec{\Omega},t)$ is the total interaction term (absorption + scattering).

- $Q(\vec{r},E,\vec{\Omega},t)$ is the neutron production term.

- $S(\vec{r},E,\vec{\Omega},t)$ represents a possible external neutron source.

The neutron production term $Q(\vec{r},E,\vec{\Omega},t)$ includes both scattering and fission terms, see Eq. 6-3. The scattering term is expressed via the scattering cross-section Σ_s and includes contributions from elastic scattering, inelastic scattering and (n,xn) reactions. Scattering is usually anisotropic in the laboratory system and Σ_s therefore depends on the scattering angle $\vec{\Omega}'$ of the incident neutron in addition to the incident neutron energy and space variable.

The fission term is expressed via the fission cross-section Σ_f. Each fission leads to the formation of lighter nuclei called fission products and the emission of $\nu(E)$ neutrons per fission in average emitted in a certain direction and with a certain energy.

It is assumed that the fission neutrons (both prompt and delayed ones) are emitted isotropically when produced by fission. Their energy distribution is often referred as fission spectrum and an example is given in Figure 6-2. The fission spectrum varies if prompt or delayed neutrons are considered.
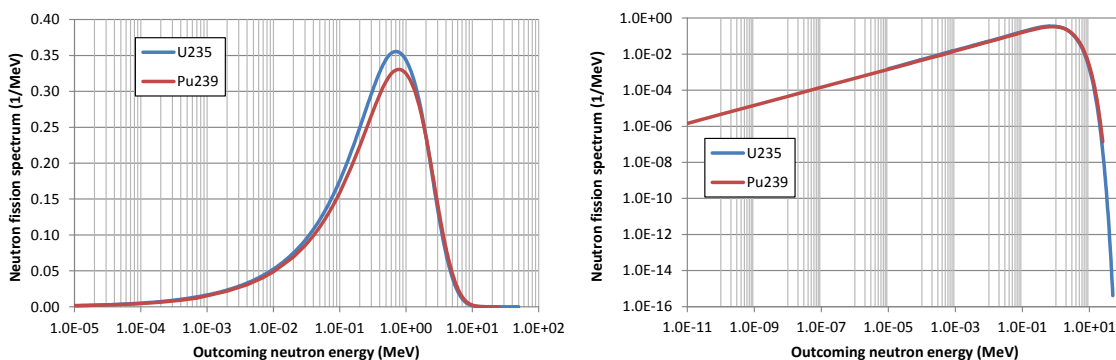
Figure 6-2. Prompt neutron fission spectra of ^{239}Pu and ^{235}U based on JEFF3.1 data (in lin-log and in log-log scale).

$$Q(\vec{r},E,\vec{\Omega},t) = \int_0^{+\infty} \oint_{4\pi} \Sigma_s(\vec{r},E' \to E, \vec{\Omega}' \to \vec{\Omega},t)\varphi(\vec{r},E',\vec{\Omega}',t)d\vec{\Omega}'dE'$$

Scattering term   **6-3**

$$+\frac{1}{4\pi}\left(\sum_{i=1}^{NF} \chi_i^p(E)\int_0^{+\infty} \nu_i^p \Sigma_{f,i}(\vec{r},E',t)\oint_{4\pi}\varphi(\vec{r},E',\vec{\Omega}',t)d\vec{\Omega}'dE' + \sum_{i=1}^{NF}\sum_{k=1}^{K}\chi_{k,i}^d(E)\lambda_k C_{k,i}(\vec{r},t) \right)$$

Fission term

In Eq. 6-3 the simplifying notation $\nu_i^p(E)\Sigma_{f,i}(\vec{r},E,t) = \nu_i^p \Sigma_{f,i}(\vec{r},E,t)$ has been introduced.

Eq. 6-3 can be rewritten as Eq. 6-5 by introducing the scalar flux (representing the number of neutrons per unit of area per unit of time) which is expressed as Eq. 6-4.

$$\phi(\vec{r},E,t) = \oint_{4\pi} \varphi(\vec{r},E,\vec{\Omega},t)d\vec{\Omega}$$

6-4

$$Q(\vec{r},E,\vec{\Omega},t) = \int_0^{+\infty} \oint_{4\pi} \Sigma_s(\vec{r},E' \to E, \vec{\Omega}' \to \vec{\Omega},t)\varphi(\vec{r},E',\vec{\Omega}',t)d\vec{\Omega}'dE'$$

6-5

$$+\frac{1}{4\pi}\left(\sum_{i=1}^{NF} \chi_i^p(E)\int_0^{+\infty} \nu_i^p \Sigma_{f,i}(\vec{r},E',t)\phi(\vec{r},E',t)dE' + \sum_{i=1}^{NF}\sum_{k=1}^{K}\chi_{k,i}^d(E)\lambda_k C_{k,i}(\vec{r},t) \right)$$

- $\Sigma_s(\vec{r},E' \to E, \vec{\Omega}' \to \vec{\Omega},t)$ represents the probability of an incident neutron of energy E' and direction $\vec{\Omega}'$ to scatter into the energy E and the direction $\vec{\Omega}$ within $(dE, d\vec{\Omega})$. By integration over all possible energies and angles, one obtains the total scattering contribution.
- NF is the number of fissile isotopes
- K is the number of delayed neutron families. Usually 6 or 8 families are considered. Sometimes instead of families the term groups is used; in this thesis families is preferred in order to avoid any confusion with energy groups.
- $\chi_i^p(E)$ is the prompt neutron spectrum of fission of the isotope i
- $\Sigma_{f,i}(\vec{r},E',t)\phi(\vec{r},E',t)$ is the fission rate of an isotope i for an incoming neutron of energy E'
- $\nu_i^p(E')$ is the number of prompt neutrons produced by the fission of an isotope i for an incoming neutron of energy E'
- $\chi_{k,i}^d(E)$ is the neutron spectrum for delayed neutrons emitted in the energy E (around dE) by the precursor family k due to the fission of isotope i.
- λ_k is the radioactive decay constant of the precursor family k, assumed to be independent of i.
- $C_{k,i}(\vec{r},t)$ is the precursor concentration of the precursor family k for a fission of isotope i

It can be mentioned that for steady state problems, the neutron spectrum for delayed and prompt neutrons are grouped into an effective neutron spectrum is considered (the same simplification is used for the number of neutrons ν).

It can be seen in Eq. 6-5 that the precursor concentration $C_{k,i}(\vec{r},t)$ is necessary to determine the solution of the transport equation. An additional equation to determine the precursor concentration and its evolution in time is hence necessary, as presented in the next section.

6.1.2. Time-dependent precursor concentrations

The precursor concentrations can be obtained by solving Eq. 6-6 for all isotopes and for all delayed neutron precursor families. Eq. 6-6 is obtained by considering that the delayed neutrons resulting from radioactive decay are emitted at the same location as the prompt ones resulting from fission i.e. at the spot of the fission event. This is a good approximation for a reactor using solid fuel but has to be modified e.g. for molten salt reactors due to fuel motion. Therefore, the precursor concentration only depends on the position and time variables.

$$\frac{\partial C_{k,i}(\vec{r},t)}{\partial t} = -\lambda_k C_{k,i}(\vec{r},t) + \beta_{k,i}(\vec{r},t)\int_0^{+\infty} v_i \Sigma_{f,i}(\vec{r},E,t)\phi(\vec{r},E,t)dE \qquad \text{6-6}$$

Where

- $-\lambda_k C_{k,i}(\vec{r},t)$ represents the disappearance of precursors due to radioactive decay

- $+\beta_{k,i}(\vec{r},t)\int_0^{+\infty} v_i \Sigma_{f,i}(\vec{r},E,t)\phi(\vec{r},E,t)dE$ represents the production of precursors due to the fission of isotope *i*.

- $\beta_{k,i}(\vec{r},t)$ represents the delayed neutron fraction of isotope *i*.

$$\beta_{k,i}(\vec{r},t) \overset{def}{=} \frac{\int_0^{+\infty} v_{k,i}^d(\vec{r},E)\Sigma_{f,i}(\vec{r},E,t)\phi(\vec{r},E,t)dE}{\int_0^{+\infty} v_i(\vec{r},E)\Sigma_{f,i}(\vec{r},E,t)\phi(\vec{r},E,t)dE}$$

- $v_{k,i}^d(E)$ is the average number of delayed neutrons emitted by the decay of an isotope *i* in the decay family *k* and $v_i(E)$ is the total number of neutrons emitted (both prompt and delayed) by isotope *i* in the energy range *dE* defined as

$$v_i(E) = v_i^p(E) + \sum_{k=1}^K v_{k,i}^d(E)$$

The delayed neutron fraction of ^{238}U for example is of 0.0158 while the one of ^{239}Pu is of 0.00215 [38] and indicates already that fast reactors with MOX fuel are more "nervous" than uranium fueled thermal reactors.

Indeed, the time between a fission event and the emission of a delayed neutron from a fission product goes from a fraction of seconds to a few tens of seconds. Delayed neutrons are essential for the control of the nuclear reactor as their existence increases the response time to a reactor

perturbation. This gives to the system and the operator some time to react to certain variations in reactivity and reactor power. A smaller amount of delayed neutrons leads to a shorter reaction time.

Eqs. 6-2 and 6-6 are coupled equations since the neutron precursor concentrations depend on the neutron flux which itself depends on the precursor concentration through the delayed neutron source term and both, the neutron flux and the precursor concentrations, are time-dependent quantities. Usually another formulation of the transport equation based on a unique average fissile isotope is chosen for convenience.

6.1.3. Average isotope equations

The previously described neutron transport equation and the precursor concentration equations have to be solved for all isotopes and all decay families. Therefore, for notation simplification, a unique averaged fissile isotope notation can be introduced to express these equations. Averaged prompt and delayed fission spectra as well as averaged delayed neutron fractions are hence defined – Eqs. 6-7, 6-8, 6-9.

$$
\beta_k(\vec{r},t) \overset{def}{=} \frac{\displaystyle\sum_{i=1}^{NF} \beta_{k,i}(\vec{r},t) \int_0^{+\infty} v_i \Sigma_{f,i}(\vec{r},E,t)\phi(\vec{r},E,t)dE}{\displaystyle\sum_{i=1}^{NF} \int_0^{+\infty} v_i \Sigma_{f,i}(\vec{r},E,t)\phi(\vec{r},E,t)dE}
\tag{6-7}
$$

$$
\chi^p(\vec{r},E,t) \overset{def}{=} \frac{\displaystyle\sum_{i=1}^{NF} \left[1-\sum_{k=1}^{K} \beta_{k,i}(\vec{r},t)\right] \chi_i^p(E) \int_0^{+\infty} v_i \Sigma_{f,i}(\vec{r},E',t)\phi(\vec{r},E',t)dE'}{\left[1-\displaystyle\sum_{k=1}^{K} \beta_k(\vec{r},t)\right] \displaystyle\sum_{i=1}^{NF} \int_0^{+\infty} v_i \Sigma_{f,i}(\vec{r},E',t)\phi(\vec{r},E',t)dE'}
\tag{6-8}
$$

$$
\chi_k^d(\vec{r},E,t) \overset{def}{=} \frac{\displaystyle\sum_{i=1}^{NF} \beta_{k,i}(\vec{r},t)\chi_{k,i}^d(E) \int_0^{+\infty} v_i \Sigma_{f,i}(\vec{r},E',t)\phi(\vec{r},E',t)dE'}{\beta_k(\vec{r},t)\displaystyle\sum_{i=1}^{NF} \int_0^{+\infty} v_i \Sigma_{f,i}(\vec{r},E',t)\phi(\vec{r},E',t)dE'}
\tag{6-9}
$$

The total fission production term is defined as Eq. 6-10.

$$
v\Sigma_f(\vec{r},E,t) = \sum_{i=1}^{NF} v_i \Sigma_{f,i}(\vec{r},E,t)
\tag{6-10}
$$

In addition to the average isotope notation, an operator notation is usually considered in order to further simplify the notation of the neutron transport equation, Eqs. 6-11 and 6-12 [147].

$$\frac{1}{v(E)}\frac{\partial \varphi}{\partial t} + \mathscr{H}\varphi = \mathscr{S}\varphi + \mathscr{F}_p\varphi + S_d + S \qquad \textbf{6-11}$$

$$\frac{\partial C_k}{\partial t} = -\lambda_k C_k + \beta_k \cdot \mathscr{F}\varphi \qquad \textbf{6-12}$$

Where

- $\mathscr{H}\varphi \stackrel{def}{=} \left[\vec{\Omega}\cdot\vec{\nabla} + \Sigma_t(\vec{r},E,t)\right]\varphi(\vec{r},E,\vec{\Omega},t)$ represents the neutron disappearance through leakage and interaction with the medium

- $\mathscr{S}\varphi \stackrel{def}{=} \int_0^{+\infty}\int_{4\pi}\Sigma_s(\vec{r},E'\to E,\vec{\Omega}'\to\vec{\Omega},t)\varphi(\vec{r},E',\vec{\Omega}',t)d\vec{\Omega}'dE'$ represents the neutrons appearing after a scattering collision

- $\mathscr{F}_p\varphi \stackrel{def}{=} \chi^p\int_0^{+\infty}\oint_{4\pi} v\Sigma_f(\vec{r},E',t)\varphi(\vec{r},E',\vec{\Omega},t)d\vec{\Omega}dE'$ represents the prompt fission term

  $= \chi^p\mathscr{F}\varphi$

- $\chi^p \stackrel{def}{=} \frac{1}{4\pi}\left[1 - \sum_{k=1}^K \beta_k(\vec{r},t)\right]\chi^p(\vec{r},E,t)$

- $\mathscr{F}_d\varphi \stackrel{def}{=} \frac{1}{4\pi}\sum_{k=1}^K \beta_k(\vec{r},t)\chi_k^d(\vec{r},E,t)\int_0^{+\infty}\oint_{4\pi} v\Sigma_f(\vec{r},E,t)\varphi(\vec{r},E,\vec{\Omega},t)d\vec{\Omega}dE$

  $\stackrel{def}{=} \sum_{k=1}^K \mathscr{F}_{d,k}\varphi$

- $\mathscr{F}\varphi = \int_0^{+\infty}\oint_{4\pi} v(\vec{r},E')\Sigma_f(\vec{r},E',t)\varphi(\vec{r},E',\vec{\Omega},t)d\vec{\Omega}dE' = \mathscr{F}_p\varphi + \mathscr{F}_d\varphi$

- $S_d(\vec{r},E,\vec{\Omega},t) \stackrel{def}{=} \frac{1}{4\pi}\sum_{k=1}^K \chi_k^d(\vec{r},E,t)\lambda_k C_{k,i}(\vec{r},t)$ is the delayed neutron source

- $S = S(\vec{r},E,\vec{\Omega},t)$

The set of equation 6-11 and 6-12 is a more compact way to write Eqs. 6-2 and 6-6.

6.1.4. Steady state transport equation

If the reactor is at steady state, the time-dependent terms in Eq. 6-11 and 6-12 vanish and Eq. 6-12 yields $\lambda_k C_k = \beta_k \cdot \mathscr{F}\varphi$ so that the transport and precursor equations are resumed by Eq. 6-13 and Eq. 6-14.

$$\mathcal{H}\,\varphi = \mathcal{S}\,\varphi + \mathcal{F}_p\varphi + \mathcal{F}_d\varphi + S \qquad \textbf{6-13}$$

$$C_k = \frac{\beta_k}{\lambda_k}\mathcal{F}\,\varphi \qquad \textbf{6-14}$$

If *S=0* and the reactor is at steady state and if in addition φ >0 then the reactor is called a critical reactor. This means that the number of neutrons produced is equal to the number of neutrons which are consumed. Eq. 6-13 then reduces to Eq. 6-15.

$$\mathcal{H}\,\varphi = \mathcal{S}\,\varphi + \mathcal{F}_p\varphi + \mathcal{F}_d\varphi \qquad \textbf{6-15}$$

Or

$$\left(\mathcal{H} - \mathcal{S} - \mathcal{F}\right)\varphi = 0 \qquad \textbf{6-16}$$

In reality or e.g. due to cross-section uncertainties or modeling approximations the reactor may slightly deviate from being critical, but it is still convenient to use a steady state equation. It has been proven that any reactor can be described with the "associated critical reactor" [146]. This means that by keeping the same geometry, the same materials etc. as in the off-critical reactor while modifying the fission term, one can solve the equation for a critical reactor to determine the flux representative for the off-critical reactor. Thus, the effective multiplication factor, k_{eff}, is introduced. The value of k_{eff} reflects the criticality situation of the reactor: if k_{eff} >1 the reactor is supercritical, if k_{eff}=1 the reactor is critical and if k_{eff}<1 the reactor is subcritical. Eq. 6-16 transforms into Eq. 6-17.

$$\left(\mathcal{H} - \mathcal{S} - \frac{\mathcal{F}}{k_{eff}}\right)\varphi = \left(\mathcal{H} - \mathcal{S} - \lambda\mathcal{F}\right)\varphi = 0 \qquad \textbf{6-17}$$

Eq. 6-17 is usually referred to the eigenvalue problem where $\lambda = \dfrac{1}{k_{eff}}$ is the eigenvalue and φ is the associated eigenfunction. If the number of neutrons per fission *v* of a reactor which is off-critical is divided by k_{eff}, the reactor becomes critical. Eq. 6-16 and Eq. 6-17 are homogeneous equations. Thus, the amplitude of φ is arbitrary. Usually this amplitude is normalized by considering the thermal power of the reactor.

When treating time-dependent problems, solving Eq. 6-17 provides an initial state and the time-dependent equations 6-11 and 6-12 are solved during the transient assuming that the reactor was initially in a steady-state condition.

6.2. Numerical solutions of the time-dependent neutron transport equation

Usually the neutron transport equation is solved numerically, except for very simple cases for which it might be solved analytically [148]. Each variable (angle, energy, space and time) has therefore to be discretized. Different methods can be considered for their discretization [149]. In SIMMER-III the

solution method is a finite difference scheme for space, a S_N method for angle, a multi-group method for energy and an improved quasistatic method for the time discretization. The different methodologies are described hereafter with special emphasis on the time discretization methods.

6.2.1. Angular and spatial discretization

Angular discretization

In SIMMER, the angular variable is discretized following a discrete ordinates method also called S_N method [150]. This method uses a set of discrete directions $\vec{\Omega}_n$ and associated weights w_n. The transport equation for these discrete angular domains can be written as Eq. 6-18:

$$\mathcal{H}\varphi_n = \mathcal{S}\varphi_n + \overline{\mathcal{F}_p\varphi_n} + \overline{\mathcal{F}_d\varphi_n} + S_n \qquad \textbf{6-18}$$

- $\mathcal{H}\varphi_n \overset{def}{=} \left[\overrightarrow{\Omega_n} \cdot \vec{\nabla} + \Sigma_t(r,E,t)\right]\varphi(\vec{r},E,\vec{\Omega}_n,t)$, $\mathcal{F}_p\varphi_n$ and $\mathcal{F}_d\varphi_n$ are similarly defined.

- $S_n = S(\vec{r},E,\vec{\Omega}_n,t)$

- $\mathcal{S}\varphi_n = \int_0^{+\infty} \oint_{4\pi} \Sigma_s(\vec{r},E' \to E,\vec{\Omega}' \to \vec{\Omega}_n,t)\varphi(\vec{r},E',\vec{\Omega}',t)d\vec{\Omega}'dE'$

In order to evaluate the integral over the angle a quadrature formula of the following type – Eq. 6-19 - is used to choose the N directions $\vec{\Omega}_n$ and the N weights w_n:

$$\int_{4\pi} f(\vec{\Omega})d\vec{\Omega} = \sum_{n=1}^{N} w_n f(\vec{\Omega}_n) \qquad \textbf{6-19}$$

The previously written Eq. 6-18 can then be written N times. A system of N equations, coupled by the sources, and to be solved for $\varphi_n = \varphi(\vec{r},E,\vec{\Omega}_n,t)$ is then obtained. A spatial discretization is then applied to these equations.

Spatial discretization

In SIMMER, the spatial variable is discretized through a finite difference method. This means that the spatial domain is divided into M intervals (axially and radially) and that the transport flux, solution of the transport equation, is found at the cell center. Boundary conditions are necessary [151].

6.2.2. Energy discretization

To further facilitate the solution of the transport equation a multi-group energy discretization is applied. The energy continuum of neutrons is divided into G groups, of width ΔEg. All neutrons of one group are assumed to be represented by the same energy i.e. to travel at the same velocity. The

representative quantities for each energy interval are obtained by integration over the energy interval - Eq. 6-20 to 6-22. Usually, at least for fast neutron systems, group 1 is attributed to neutrons with the highest energy.

$$\varphi_g(\vec{r},\vec{\Omega},t) = \int_{E_g}^{E_{g-1}} \varphi(\vec{r},E,\vec{\Omega},t)dE \qquad \textbf{6-20}$$

$$Q_g(\vec{r},\vec{\Omega},t) = \int_{E_g}^{E_{g-1}} Q(\vec{r},E,\vec{\Omega},t)dE \qquad \textbf{6-21}$$

$$S_g(\vec{r},\vec{\Omega},t) = \int_{E_g}^{E_{g-1}} S(\vec{r},E,\vec{\Omega},t)dE \qquad \textbf{6-22}$$

The cross-sections for a certain group are obtained by keeping the reaction rate constant and are determined as Eq. 6-23.

$$\Sigma_{i,g}(\vec{r},\vec{\Omega},t) = \frac{\int_{E_g}^{E_{g-1}} \Sigma_i(\vec{r},E,t)\varphi(\vec{r},E,\vec{\Omega},t)dE}{\varphi_g(\vec{r},\vec{\Omega},t)} \qquad \textbf{6-23}$$

where *i* stands for any interaction type. For the double differential scattering cross-section, Eq. 6-24 is applied.

$$\Sigma_{s,h\to g}(\vec{r},\vec{\Omega}'\to\vec{\Omega},t) = \frac{\int_{E_g}^{E_{g-1}} \int_{E_h}^{E_{h-1}'} \Sigma_s(\vec{r},E'\to E,\vec{\Omega}'\to\vec{\Omega},t)\varphi(\vec{r},E',\vec{\Omega}',t)dE'dE}{\varphi_h(\vec{r},\vec{\Omega}',t)} \qquad \textbf{6-24}$$

where h and g are the energy groups for incident and scattered neutrons, respectively.

The multi-group transport equation can then be written for each energy group g within [1, G] as Eq. 6-25.

$$\frac{1}{v_g}\frac{\partial\varphi_g(\vec{r},\vec{\Omega},t)}{\partial t} + \vec{\Omega}\cdot\vec{\nabla}\varphi_g(\vec{r},\vec{\Omega},t) + \Sigma_{t,g}(\vec{r},\vec{\Omega},t)\varphi_g(\vec{r},\vec{\Omega},t) = Q_g(\vec{r},\vec{\Omega},t) + S_g(\vec{r},\vec{\Omega},t) \qquad \textbf{6-25}$$

In practice, $\Sigma_{t,g}$ does not depend on angle and in Eq. 6-23 the scalar flux is used. In Eq. 6-25 the multi-group cross-sections are formally defined. However, as it can be seen from e.g. Eq. 6-23, for

determining energy averaged group constants one actually needs to already know the energy dependence of the neutron flux, i.e. the solution of the posed problem. Usually, the multi-group cross-sections are provided by a cross-section processing code for which the user has already determined the energy intervals and some suitably chosen problem-adapted weighting function [76].

A further simplification of the multi-group transport equation is the multi-group diffusion equation which involves the scalar flux. We will consider the case of time independent problems in the following. Going from the multi-group transport equation to its simplified diffusion form can be performed under certain approximations, the usual one being the decomposition of the group flux $\varphi_g(\vec{r},\vec{\Omega})$ into the group scalar flux $\phi_g(\vec{r})$ and the group current $J_g(\vec{r})$ considering that the source terms are isotropic in the laboratory system - Eq. 6-26 [152].

$$\varphi_g(\vec{r},\vec{\Omega}) \cong \phi_g(\vec{r}) + \overrightarrow{J_g}(\vec{r}) \cdot \vec{\Omega} \qquad \textbf{6-26}$$

It is as well considered that the current can be expressed following Fick's law for diffusion:

$$\overrightarrow{J_g}(\vec{r}) \cdot \vec{\Omega} = -D_g(\vec{r})\vec{\nabla}\phi_g(\vec{r}) \qquad \textbf{6-27}$$

Introducing Eq. 6-26 in Eq. 6-25 in its time independent form (i.e. $\dfrac{\partial \varphi_g(\vec{r},\vec{\Omega},t)}{\partial t} = 0$) yields Eq. 6-28 after rearrangement:

$$-\vec{\nabla} \cdot \left[D_g(\vec{r})\vec{\nabla}\phi_g(\vec{r}) \right] + \Sigma_{r,g}(\vec{r})\phi_g(\vec{r}) = Q_g(\vec{r}) + S_g(\vec{r}) \qquad \textbf{6-28}$$

Where
- $D_g(\vec{r})$ is the diffusion coefficient in energy group g and is given as

  $D_g(\vec{r}) = \dfrac{1}{3\Sigma_{tr,g}(\vec{r})}$ with $\Sigma_{tr,g}(\vec{r})$ the neutron transport cross-section in the energy group g.

  $\Sigma_{tr,g}(\vec{r}) = \Sigma_{t,g}(\vec{r}) - \bar{\mu}_g(\vec{r})\Sigma_{s,g}(\vec{r})$

  $\bar{\mu}_g(\vec{r})$ represents the mean cosine of the scattering angle in energy group g. If isotropic scattering is considered, $\bar{\mu}_g(\vec{r})$ equals 0 and the transport cross-section in group g equals the total cross-section in group g. Even if scattering is isotropic in the center of mass system, it is always anisotropic in the laboratory system. For heavy nuclei however, the mean cosine equals almost zero in the lower energy ranges.

  $\Sigma_{s,g}(\vec{r})$ is the scattering cross-section in energy group g.

- $\Sigma_{r,g}(\vec{r})$ is the removal cross-section in group g and is defined as $\Sigma_{r,g}(\vec{r}) = \Sigma_{t,g}(\vec{r}) - \Sigma_{s,g \to g}(\vec{r})$. $\Sigma_{s,g \to g}$ is often called "self-scatter cross-section" or "within group scattering cross-section".
- $Q_g(\vec{r})$ and $S_g(\vec{r})$ are the source terms in energy group g.

Similar to multi-dimensional multi-group neutron diffusion codes, discrete-ordinates multi-group neutron transport codes employ a two-level nested procedure to solve the neutron transport

equation. The two iteration levels are called outer and inner iterations. The outer iteration is used to determine the fission and upscattering source, while the inner one uses these sources to determine the angular and space dependent neutron flux within each energy group [76].

Accelerating the convergence of these iterations is necessary to reduce computational (CPU) time and for this purpose the diffusion synthetic acceleration (DSA) method is frequently employed (e.g. in DANTSYS [76] or PARTISN [153]). In this method a diffusion equation with adjusted space dependent coefficients is used. An alternative method applies so-called coarse mesh rebalancing.

Consider first the inner iteration number l for the equation of energy group g. The inner iteration equation is given as Eq. 6-29 where the fission and the scattering sources to the group have been combined with an external source into $QQ_g(\vec{r})$. For simplicity of presentation it is assumed here that $QQ_g(\vec{r})$ and scattering is isotropic. This term remains unchanged throughout the iteration in the energy group. In Eq. 6-29 $\varphi_g^{\,l}(\vec{r},\vec{\Omega})$ is the angular flux in iteration l and it is determined from the scalar flux at iteration $l-1$, $\phi_g^{\,l-1}$. $QQ_g(\vec{r})$ is computed using the fluxes from the preceding iterations.

$$\vec{\Omega}\cdot\vec{\nabla}\varphi_g^{\,l}(\vec{r},\vec{\Omega}) + \Sigma_{t,g}(\vec{r})\varphi_g^{\,l}(\vec{r},\vec{\Omega}) = QQ_g(\vec{r}) + \Sigma_{s,g\to g}(\vec{r})\phi_g^{\,l-1}(\vec{r})$$

6-29

To compute the scalar flux in iteration l, $\phi_g^{\,l}(\vec{r})$, needed for the next iteration $l+1$ on the angular flux a corrected diffusion equation is used which employs $\varphi_g^{\,l}$ [76]. Different schemes are possible [76] but their description is omitted here.

6.2.3. Time discretization

Usually, unless the reactor is at steady state, the analysis of the dynamic behavior of nuclear reactors needs the solution of the time-dependent neutron transport equation. The most straightforward solution scheme to treat the time-dependence is based on an implicit time discretization. This approach requires a high CPU time and, if transport theory is applied instead of diffusion theory, a fairly large storage capacity of computer memory for storing angular dependent neutron fluxes, even nowadays. Thus, this method is only used to check more complex or approximate methods. In the following, some alternative methods will be discussed, as to know the Improved Quasistatic Method (IQM), the adiabatic approach and the point kinetics approach. An overview of differences between these methods can be seen from Table 6-1.

Term	Methods			
	Direct	Improved quasistatic	Adiabatic	Point kinetics
$\dfrac{\partial \Psi}{\partial t}$	yes	yes	no	no
$\dfrac{1}{\text{v}} \cdot \dfrac{1}{\phi} \cdot \dfrac{d\phi}{dt}$	yes	yes	no	no
$S_d(\phi \Psi)$	yes	yes	no	no
Implicit coupling via feedback	yes	yes	yes	no
Decoupled shape distortion	yes	yes	yes	no
Initial shape	yes	yes	yes	yes

Table 6-1. Different time discretization schemes and their hypothesis [149].

Most of the methods in Table 6-1 are based on the perturbation theory. Hence, before going to the specificities of each individual method, an associated introduction to perturbation theory is presented here.

Perturbation theory (PT)

Strictly speaking, Eq. 6-17 should be solved for every change in the reactor state. Consider a reactor system near critical steady state conditions for which a calculation has already been performed. The system is fully described neutronically although in a somewhat approximate manner i.e. the flux is known, k_{eff} is known. Now let the system undergo a small change by e.g. a small variation in the material density or temperature distributions referred later as *perturbation.* The system will respond to this perturbation by a variation in the multiplication factor k_{eff}. It is not always necessary to solve again the neutron transport equation for this perturbed state to obtain a reasonably accurate response of the system if perturbation theory (PT) is used [149].

In the PT approach a weighting function is employed in order to better take into account "weights" of different neutrons in sustaining the reaction chain. In principle the weighting function is arbitrary but it is usually chosen to be the adjoint flux $\varphi^*(\vec{r}, E, \vec{\Omega})$ for improving the accuracy of perturbation calculations with approximate flux distributions[11] – details are provided in Appendix B. The static adjoint flux reflects the importance of a neutron to sustain the chain reaction including all subsequent neutron generations. For example, a neutron in the center position of the reactor has a high probability to cause a fission while a neutron placed at the surface of the reactor would have a high escape probability. Thus, the neutron placed in the center is more important to the chain reaction than the one placed at the periphery. Similarly, a neutron whose energy lies in the energy domain which has a higher reproduction factor is more important to the chain reaction than one in the resonance energy domain (where the capture probability may be extremely high) [146]. The mathematical definition of the adjoint flux is the solution of the adjoint equation of the flux (Eq. 6-30).

$$\left(\mathscr{H}^* - \mathscr{S}^* - \frac{\mathscr{F}^*}{k_{eff}^*} \right) \varphi^* = 0 \qquad \textbf{6-30}$$

---

[11] In this section perturbation theory is described for the continuous energy, angle and space domain.

In Eq. 6-31 the adjoint operators are introduced. An adjoint operator $\mathscr{H}^*$ of an operator $\mathscr{H}$ is defined by Eq. 6-31. This equation holds for all possible adjoint functions ψ and real functions φ of $\left(\vec{r}, E, \vec{\Omega}\right)$.

$$\left\langle \psi, \mathscr{H}\varphi \right\rangle = \left\langle \mathscr{H}^*\psi, \varphi \right\rangle = \left\langle \varphi, \mathscr{H}^*\psi \right\rangle \, {}^{12}$$

6-31

In Eq. 6-30, the fundamental eigenvalue in the adjoint flux equation is actually the same as in the direct flux equation in its analytical form (only approximate agreement in discretized form) i.e. $\lambda = \dfrac{1}{k_{eff}}$. The derivation is given in Appendix A.

Now that the adjoint flux has been defined, a brief overview of a PT approach is given in the following.

Consider an unperturbed state and a perturbed state, indexed 0 and 1 respectively. The two states are described by steady state equations Eq. 6-32 and 6-33, respectively.

$$\left(\mathscr{H}_0 - \mathscr{S}_0 - \frac{\mathscr{F}_0}{k_{eff,0}} \right)\varphi_0 = 0$$

6-32

$$\left(\mathscr{H}_1 - \mathscr{S}_1 - \frac{\mathscr{F}_1}{k_{eff,1}} \right)\varphi_1 = 0$$

6-33

By expressing the perturbed flux as a combination of the unperturbed flux and its first order variation i.e. $\varphi_1 = \varphi_0 + \Delta\varphi_0$ and by introducing this into Eq. 6-33 one obtains Eq. 6-34.

$$\left(\mathscr{H}_1 - \mathscr{S}_1 \right)_1 \varphi_0 = \frac{\mathscr{F}_1}{k_{eff,1}}\varphi_0 - \left(\mathscr{H}_1 - \mathscr{S}_1 - \frac{\mathscr{F}_1}{k_{eff,1}} \right)\Delta\varphi_0$$

6-34

A similar approach might be applied to the fission operator and the inverse of the multiplication constant – Eq. 6-35 and 6-36.

$$\Delta\mathscr{F} = \mathscr{F}_1 - \mathscr{F}_0$$

6-35

and

$$\Delta(\lambda) = \lambda_1 - \lambda_0 = \frac{1}{k_{eff,1}} - \frac{1}{k_{eff,0}} = \Delta\left(\frac{1}{k_{eff}}\right) = -\Delta(\rho)$$

6-36

---

[12] $\langle ... \rangle$ refers to an integration over the phase space domain.

In Eq. 6-36, ρ is the static reactivity which is defined as $\rho = 1 - \dfrac{1}{k_{eff}}$. The first term on the right hand side of Eq. 6-34 might be rewritten as Eq.6-37 if Eqs. 6-35 and 6-36 are applied.

$$\frac{\mathscr{F}_1}{k_{eff,1}} \varphi_0 = \frac{\mathscr{F}_0}{k_{eff,1}} \varphi_0 + \frac{\Delta \mathscr{F}}{k_{eff,0}} \varphi_0 + \Delta \left(\frac{1}{k_{eff}} \right) \Delta \mathscr{F} \varphi_0 \qquad \textbf{6-37}$$

Eq. 6-37 can be introduced into Eq. 6-34 and the resulting equation can be multiplied by the adjoint function for weighting prior to integration. The second order terms are dropped, Eq. 6-38 is obtained [149].

$$\left\langle \varphi_0^*, \left(\mathscr{H}_1 - \mathscr{S}_1 \right) \varphi_0 \right\rangle = \frac{1}{k_{eff,1}} \left\langle \varphi_0^*, \mathscr{F}_0 \varphi_0 \right\rangle + \frac{1}{k_{eff,0}} \left\langle \varphi_0^*, \Delta \mathscr{F} \varphi_0 \right\rangle - \left\langle \varphi_0^*, \left(\mathscr{H}_1 - \mathscr{S}_1 - \frac{\mathscr{F}_1}{k_{eff,1}} \right) \Delta \varphi_0 \right\rangle \qquad \textbf{6-38}$$

By subtracting the unperturbed equation Eq. 6-32, multiplied prior to integration by the adjoint function, to Eq. 6-38, Eq. 6-39 is obtained.

$$\left\langle \varphi_0^*, \left(\Delta \left(\mathscr{H} - \mathscr{S} \right) - \frac{1}{k_{eff,0}} \Delta \mathscr{F} \right) \varphi_0 \right\rangle = \Delta \left(\frac{1}{k_{eff}} \right) \left\langle \varphi_0^*, \mathscr{F}_0 \varphi_0 \right\rangle - \left\langle \varphi_0^*, \left(\left(\mathscr{H}_1 - \mathscr{S}_1 \right) - \frac{1}{k_{eff,1}} \mathscr{F}_1 \right) \Delta \varphi_0 \right\rangle \qquad \textbf{6-39}$$

The second term on the right hand side of Eq. 6-39 is then decomposed in its first and higher order contributions – Eq. 6-40.

$$\left\langle \varphi_0^*, \left(\left(\mathscr{H}_1 - \mathscr{S}_1 \right) - \frac{1}{k_{eff,1}} \mathscr{F}_1 \right) \Delta \varphi_0 \right\rangle = \left\langle \varphi_0^*, \left(\left(\mathscr{H}_0 - \mathscr{S}_0 \right) - \frac{1}{k_{eff,0}} \mathscr{F}_0 \right) \Delta \varphi_0 \right\rangle$$
$$+ \left\langle \varphi_0^*, \left(\Delta \left(\mathscr{H} - \mathscr{S} \right) - \frac{1}{k_{eff,0}} \Delta \mathscr{F}_0 - \mathscr{F}_0 \Delta \frac{1}{k_{eff}} \right) \Delta \varphi_0 \right\rangle \qquad \textbf{6-40}$$
$$+ \Delta \left(\frac{1}{k_{eff}} \right) \left\langle \varphi_0^*, \Delta \mathscr{F}_0 \Delta \varphi_0 \right\rangle$$

In first order perturbation theory (FOP) the higher order terms are neglected since the first order term is assumed to represent a small perturbation. Furthermore, the first order term i.e. the first term on the right hand side of Eq. 6-40 might be rewritten as Eq. 6-41 (due to Eq. 6-30).

$$\left\langle \varphi_0^*, \left(\left(\mathscr{H}_0 - \mathscr{S}_0 \right) - \frac{1}{k_{eff,0}} \mathscr{F}_0 \right) \Delta \varphi_0 \right\rangle = \left\langle \Delta \varphi_0, \left(\left(\mathscr{H}_0^* - \mathscr{S}_0^* \right) - \frac{1}{k_{eff,0}} \mathscr{F}_0^* \right) \varphi_0^* \right\rangle = 0 \qquad \textbf{6-41}$$

Therefore Eq. 6-39 results in Eq. 6-42.

$$\left\langle \varphi_0^{\ *}, \left(\Delta\left(\mathcal{H} - \mathcal{S}\right) - \frac{1}{k_{eff,0}} \Delta\mathcal{F} \right) \varphi_0 \right\rangle = \Delta\left(\frac{1}{k_{eff}}\right) \left\langle \varphi_0^{\ *}, \mathcal{F}_0\varphi_0 \right\rangle \qquad \text{6-42}$$

By noticing that $\Delta\left(\dfrac{1}{k_{eff}}\right) = -\Delta\rho$ one yields the FOP reactivity increment – Eq. 6-43.

$$\frac{\left\langle \varphi_0^{\ *}, \left(\dfrac{1}{k_{eff,0}} \Delta\mathcal{F} - \Delta\left(\mathcal{H} - \mathcal{S}\right) \right) \varphi_0 \right\rangle}{\left\langle \varphi_0^{\ *}, \mathcal{F}_0\varphi_0 \right\rangle} = \Delta\rho \qquad \text{6-43}$$

Any small reactivity variation induced by a perturbation of the reactor can thus be approximately calculated by applying Eq. 6-43 without needing to determine the perturbed flux. No additional solution of the transport equation is thus necessary which allows saving CPU time, in particular if the system undergoes several perturbations.

In order to improve the accuracy of the FOP results, exact PT is sometimes employed. In this method the perturbed flux, solution of the perturbed problem, needs to be known.

Eqs. 6-30 and 6-33 are multiplied by φ_1 and $\varphi_0^{\ *}$ respectively prior to integration.

$$\left\langle \varphi_1, \left(\mathcal{H}_0^* - \mathcal{S}_0^* - \frac{\mathcal{F}_0^*}{k_{eff,0}} \right) \varphi_0^{\ *} \right\rangle = 0 \qquad \text{6-44}$$

$$\left\langle \varphi_0^{\ *}, \left(\mathcal{H}_1 - \mathcal{S}_1 - \frac{\mathcal{F}_1}{k_{eff,1}} \right) \varphi_1 \right\rangle = 0 \qquad \text{6-45}$$

Revolving Eq. 6-44 results in Eq. 6-46.

$$\left\langle \varphi_0^{\ *}, \left(\mathcal{H}_0 - \mathcal{S}_0 - \frac{\mathcal{F}_0}{k_{eff,0}} \right) \varphi_1 \right\rangle = 0 \qquad \text{6-46}$$

Applying Eq. 6-35 to Eq. 6-46 one can rewrite Eq. 6-46 as Eq. 6-47.

$$\left\langle \varphi_0^{\ *}, \left(\mathcal{H}_0 - \mathcal{S}_0 + \frac{\mathcal{F}_1}{k_{eff,0}} - \frac{\Delta\mathcal{F}}{k_{eff,0}} \right) \varphi_1 \right\rangle = 0 \qquad \text{6-47}$$

Subtracting Eq. 6-47 and Eq. 6-45 results in Eq. 6-48.

$$\left\langle \varphi_0^*, \left(\Delta\mathcal{H} - \Delta\mathcal{S} - \frac{\Delta\mathcal{F}}{k_{eff,0}} - \mathcal{F}_1\left[\frac{1}{k_{eff,1}} - \frac{1}{k_{eff,0}} \right] \right) \varphi_1 \right\rangle = 0 \qquad \textbf{6-48}$$

Noticing that $\dfrac{1}{k_{eff,1}} - \dfrac{1}{k_{eff,0}} = -\Delta\rho$ and rewriting Eq. 6-48 gives Eq. 6-49.

$$-\Delta\rho = \frac{\left\langle \varphi_0^*, \left(\Delta\mathcal{H} - \Delta\mathcal{S} - \dfrac{\Delta\mathcal{F}}{k_{eff,0}} \right) \varphi_1 \right\rangle}{\left\langle \varphi_0^*, \mathcal{F}_1\varphi_1 \right\rangle} \qquad \textbf{6-49}$$

Eq. 6-49 gives the exact formula of the reactivity increment following a perturbation. Contrary to FOP, in Eq. 6-49 the perturbed flux should be considered.

The rest of this section deals with the time dependence treatment of the neutron transport equation. The direct method, the improved quasistatic method as well as the adiabatic and point kinetic methods, employed for its solution, are detailed. Note that other methods do exist but they are less relevant for the considered area of safety studies.

The direct method

The direct method [149] is based on a straightforward time discretization. Considering some discrete time points (t$_0$,….,t$_N$) and employing the implicit approach, the time derivatives can be written as Eq. 6-50 [149].

$$\frac{\partial X(t_n)}{\partial t} = \frac{X(t_n) - X(t_{n-1})}{\Delta t_n} \qquad \textbf{6-50}$$

where $\Delta t_n = t_n - t_{n-1}$

Solving the time-dependent multi-group equations with the direct method will admittedly yield the correct solution if the time steps Δt_n are sufficiently small. This requires, however, a cumbersome computational effort due to the large number of steps and other methods allowing longer time steps are thus preferred for transient analyses. The direct calculations usually serve as checks for these more complex methods.

The improved quasistatic method

As described previously the direct method requires a high CPU time and additional provisions are usually made to accelerate the treatment of the time dependence of the flux. Most of them rely on the fact that the spatial, angle and energy distribution of the flux – called flux shape – varies more slowly with time than its amplitude. The idea of the improved quasistatic approach hence lies in the factorization of the flux into two functions (separation ansatz): the amplitude function p(t) which

contains most of the time dependence and the shape function $\psi(\vec{r}, E, \vec{\Omega}, t)$ depending on space, energy, angle and to a lower extent on time Eq. 6-51 [149].

$$\varphi(\vec{r}, E, \vec{\Omega}, t) = p(t) \cdot \psi(\vec{r}, E, \vec{\Omega}, t) \tag{6-51}$$

The splitting of Eq. 6-51 is arbitrary since *p(t)* can be multiplied by a given factor and $\psi(\vec{r}, E, \vec{\Omega}, t)$ can be divided by the same factor. In order to make the splitting unique, the shape function is normalized. The normalization constant γ also called gamma constant is therefore imposed, that facilitates shape calculations as explained in the following.

$$\gamma = \left\langle \varphi_0^*, \frac{1}{v} \psi \right\rangle = \text{constant} \tag{6-52}$$

No approximation is made at this stage. Eq. 6-51 is put into Eq. 6-11 and Eq. 6-12. One then obtains Eqs. 6-53 and 6-54.

$$\frac{1}{v} \left(\frac{dp}{dt} \psi + p \frac{\partial \psi}{\partial t} \right) + p \mathcal{H} \psi = p \mathcal{S} \psi + p \chi^p \mathcal{F} \psi + S_d + S \tag{6-53}$$

$$\frac{\partial C_k}{\partial t} = -\lambda_k C_k + \beta_k p \mathcal{F} \psi \tag{6-54}$$

Eq. 6-53 and 6-54 are referred to the *shape equations* as they are used to calculate the flux shape and the corresponding precursor concentrations.

The next step is now to determine the amplitude function. For this purpose Eq. 6-53 is integrated over angle, space and energy. Prior to integration, Eq. 6-53 is multiplied by a weighting function usually chosen to be the static adjoint flux φ_0^*.

Application of the normalization constraint, Eq. 6-52, to the weighted Eq. 6-53 results in Eq. 6-55 due to the fact that $\dfrac{\partial \left\langle \varphi_0^*, \frac{1}{v} \psi \right\rangle}{\partial t} = 0$.

By taking the product of the precursor equation with the delayed neutron spectrum and the source-free adjoint flux, solution of a homogeneous problem, Eq. 6-56 is obtained. Eq. 6-55 and Eq. 6-56 are referred to the *amplitude equations or point kinetic equations*.

$$\frac{dp}{dt}(t) = \frac{\overline{\rho}(t) - \overline{\beta}(t)}{\overline{\Lambda}(t)} p(t) + \sum_k \lambda_k \overline{c_k}(t) + \frac{\overline{S}(t)}{\overline{\Lambda}(t)} \tag{6-55}$$

$$\frac{d\overline{c_k}}{dt}(t) = -\lambda_k \overline{c_k}(t) + \frac{\overline{\beta_k}(t)}{\overline{\overline{\Lambda}}(t)} p(t) \qquad \textbf{6-56}$$

The kinetic parameters appearing in Eq. 6-55 and 6-56 are defined as follows.

$$\overline{\rho}(t) = \frac{1}{\overline{\overline{\mathscr{F}}}}\left\langle \varphi_0^*, (\mathscr{F} - \mathscr{H} + \mathscr{S})\psi \right\rangle \qquad \textbf{6-57}$$

$$\overline{\Lambda}(t) = \frac{1}{\overline{\overline{\mathscr{F}}}}\left\langle \varphi_0^*, \frac{1}{v}\psi \right\rangle \qquad \textbf{6-58}$$

$$\overline{\beta_k}(t) = \frac{1}{\overline{\overline{\mathscr{F}}}}\left\langle \varphi_0^*, \mathscr{F}_{d,k}\psi \right\rangle \qquad \textbf{6-59}$$

$$\overline{\beta}(t) = \sum_k \overline{\beta_k}(t) \qquad \textbf{6-60}$$

Eq. 6-57 gives the definition of the reactivity in the improved quasistatic method. It is defined as a neutron balance per weighted neutron generation. Eq. 6-58 gives the neutron generation time and Eq. 6-60 gives the effective delayed neutron fraction i.e. the delayed neutron fraction is weighted by the adjoint function. This reflects the effectiveness of delayed neutrons with regard to fissions according to their energy and space distribution.

In addition, the following quantities are defined:

$$\overline{\overline{\mathscr{F}}}(t) = \left\langle \varphi_0^*, \mathscr{F}\psi \right\rangle \qquad \textbf{6-61}$$

$$\overline{S}(t) = \frac{1}{\overline{\overline{\mathscr{F}}}}\left\langle \varphi_0^*, S \right\rangle \qquad \textbf{6-62}$$

$$\overline{c_k}(t) = \frac{\left\langle \varphi_0^*, \dfrac{\chi_k^d(\vec{r},E,t)}{4\pi}C_k \right\rangle}{\left\langle \varphi_0^*, \dfrac{1}{v}\psi \right\rangle} \qquad \textbf{6-63}$$

The shape derivative $\dfrac{\partial\psi}{\partial t}$ in Eq. 6-53 might be replaced by a backward difference as shown in Eq. 6-64, similarly to the scheme explained for the direct method. The shape equation (Eq. 6.53) thus transforms into Eq. 6-65.

$$\frac{\partial\psi}{\partial t}(\vec{r},E,\vec{\Omega},t_n) = \frac{\psi(\vec{r},E,\vec{\Omega},t_n) - \psi(\vec{r},E,\vec{\Omega},t_{n-1})}{\Delta t_n} \qquad \textbf{6-64}$$

$$\left(\frac{1}{v}\frac{1}{p}\frac{dp}{dt} + \mathscr{H} + \frac{1}{v\Delta t_n}\right)\psi_n = \mathscr{S}\psi_n + \chi^p\mathscr{F}\psi_n + \frac{S_d}{p} + \frac{S}{p} + \frac{1}{v\Delta t_n}\psi_{n-1} \qquad \text{6-65}$$

Eq. 6-65 can be solved if the shape at the previous time step is considered as an external neutron source. In addition, it is seen from Eq. 6-65 that the amplitude function has to be known prior to solving the shape equation. The shape and amplitude equations hence form a set of non-linear equations: solving the shape equation requires knowledge of the amplitude which itself implicitly depends on the flux shape through the point kinetic parameters.

A first approximation has then to be introduced to solve this set of equations. Two different time levels are considered to solve the shape and amplitude equations. Taking advantage of the fact that usually the flux shape varies rather slowly with time, the shape equations are solved for a coarse time scale $[t^s_0, \dots t^s_n, t^s_{n-1} \dots t^s_N]$. The amplitude equations are solved for a much finer time scale $\{t^s_{n,i} = t_{n,i,0} \dots t_{n,i,j}, t_{n,i,j+1} \dots t_{n,i,J} = t^s_{n,i+1}\}$. It is important to mention that an improved quasistatic method solution is close to the "exact" one if all time steps are close to zero, similarly to the direct method. If the same shape steps are used for the IQM as for the times steps of the direct method the accuracy is usually higher.

From the point of view of the numerical solution it is worthwhile to mention that according to Eq. 6-64, an angular-dependent "source-term" appears on the right hand side of Eq. 6-65.

In addition to the IQM, several other methods have been developed [149]. In the subsequent sections the adiabatic method and the point kinetics method are detailed.

Adiabatic method

In the adiabatic method, the space-time factorization (Eq. 6-51) is employed but the shape function is recomputed during the transient for "coarse" time steps, solving an eigenvalue problem (Eq. 6-66).

$$\left(\frac{\mathscr{F}}{k_{eff}} - \mathscr{H} + \mathscr{S}\right)\psi = 0 \qquad \text{6-66}$$

The point kinetic parameters are computed in the same manner as in the IQM.

Point kinetic (PK) method

In the point kinetic (PK) method the flux shape is considered to remain unchanged during the whole transient i.e. is assumed to be equal to the initial flux shape.

As concerns the kinetic parameters, neutron generation time and delayed neutron fraction, they remain unchanged during the transient. The time dependence of the reactivity is usually treated with a so-called feedback model. For this purpose pre-computed reactivity coefficients are used to compute reactivity changes due to variations in temperatures or composition. The PK equations are written as Eq. 6-67 and 6-68.

$$\frac{dp}{dt}(t) = \frac{\overline{\rho(t)} - \overline{\beta_0}}{\overline{\Lambda_0}} p(t) + \sum_k \lambda_k \overline{c_k}(t) + \frac{\overline{S_0}}{\overline{\Lambda_0}}$$

6-67

$$\frac{d\overline{c_k}}{dt}(t) = -\lambda_k \overline{c_k}(t) + \frac{\overline{\beta_{k,0}}}{\overline{\Lambda_0}} p(t)$$

6-68

The PK method is usually quite accurate if no strong material relocation occurs. It is often employed in safety codes dedicated to initiation phase analyses like the SAS4A code [71]. Even though this method is quite approximate, it usually helps in providing trends in the accident evolution and facilitates the understanding of basic phenomena.

6.2.4. Conclusions

The neutron transport equation governing the neutron population variation in a nuclear reactor is highly complicated in the general case and usually requires approximations and numerical solutions. To that end, discretization of all variables i.e. space, angle, energy and time is performed. Several methods have been mentioned especially for treating the time dependence. The accuracy of the solution of the neutron transport equation depends on the applied numerical schemes.

6.3. Implementation of core thermal expansions in the SIMMER framework

As mentioned earlier, SIMMER uses an improved quasistatic scheme to discretize in time the neutron transport equation. SIMMER is a coupled fluid-dynamic neutronics code; the neutron flux depends on cross-sections themselves depending on material density and temperature distributions depending on the power distribution which is function of the neutron flux. Therefore neutronic and fluid-dynamic equations should be solved simultaneously. For that, approximations have to be used. The fluid-dynamic part of SIMMER depends on the flux amplitude, calculated with PK parameters. Periodical interruptions in the fluid-dynamic calculations are foreseen in order to perform calculations in the neutronic part. 3 time levels for discretization are therefore considered in the neutronic part, the smallest one being the amplitude time step where the amplitude equation is solved. The intermediate time step is the reactivity time step where the amplitude equation coupling terms (e.g. reactivity) are updated and the largest time step is the flux shape step where the flux shape equation is solved.

In Figure 6-3 the different neutronic time steps of SIMMER are depicted. The shape equation is solved over a macro time step i.e. $[t^s_0, \dots t^s_n, t^s_{n-1} \dots t^s_N]$. Within one macro time step, the PK parameters are calculated over reactivity time steps $\{t^s_{n-1} = t_{n-1, 0} \dots t_{n-1,i}, t_{n-1, i+1} \dots \dots t_{n-1, I} = t^s_n\} \in [t^s_{n-1}, t^s_n]$. Within one reactivity time step, the amplitude equations are solved over fine steps $\{t^s_{n,i} = t_{n,i,0} \dots t_{n,i,j}, t_{n,i,j+1} \dots \dots t_{n,i,J} = t^s_{n,i+1}\} \in [t^s_{n,i}, t^s_{n,i+1}]$. Within one amplitude step, several fluid-dynamic steps are performed.

Consider a macro time step [t^s_{n-1} , t^s_n]. To perform fluid-dynamic calculations, the fluid dynamic-part of SIMMER needs as input the power distribution and the power amplitude. The power shape distribution is kept constant during the fluid-dynamic steps as it depends on the flux shape, which is held constant over several fluid-dynamic steps. The power or the flux amplitude is parabolically extrapolated. At the end of a reactivity step, thanks to updated densities and temperatures coming from the fluid-dynamic calculation, the cross-sections are recalculated. The flux shape can then be linearly extrapolated based on the beginning and the end of shape step values i.e. values calculated at t^s_{n-1} and t^s_n respectively. Based on this updated flux shape, the PK parameters are recalculated. The specific power distribution (i.e. W/kg) is updated as well based on the extrapolated shape. The amplitude equation is then solved again based on the updated PK parameters. The amplitude is then calculated for the end of the reactivity step (prediction). An amplitude fit is then performed based on the current and the two previously calculated amplitudes. This function is then used for the next series of fluid dynamic steps. If the end of a reactivity step also happens to be the end of a shape step (or very close to it), the shape is not extrapolated based on new cross-sections but is calculated. The PK parameters are then calculated based on the new calculated flux shape and compared to the ones that were calculated based on the extrapolated flux shape. It is assumed that any discrepancy between the extrapolated and the calculated PK parameters is due to a linear accumulation of deviations during the shape step. The PK parameters are then corrected for each reactivity steps within the shape steps and the amplitude equations are solved again at each reactivity step. If the convergence criteria is fulfilled the algorithm goes to the next macro time step, otherwise all steps are repeated until full convergence is reached. The whole procedure is detailed in Figure 6-4.

It has to be mentioned that since the analyses become more and more refined and a three-dimensional representation of the reactor core enables realistic distribution of the materials constituting the core, including control rods, the development of the 3D version SIMMER-IV has been pushed. The parallelization of SIMMER-IV allows reactor simulations within available computational resources.
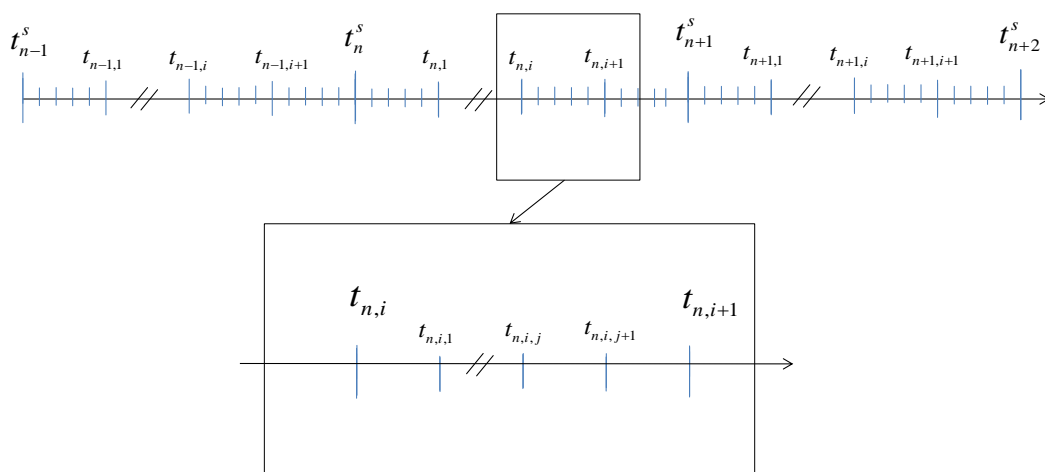
Figure 6-3. Neutronic time steps in SIMMER. Shape step: $\Delta t^s = t^s_{n+1} - t^s_n$. Reactivity step: $\Delta t^r = t_{n,i+1} - t_{n,i}$. Amplitude step: $\Delta t^a = t_{n,i,j+1} - t_{n,i,j}$.

At this point, it has to be mentioned that in SIMMER, the PT calculation is not performed for reactivity variations due to variation of cross-sections as it is usually performed in many other codes.

Instead of reactivity variations, the reactivity values are computed directly as a weighted neutron balance per neutron generation. Hence, it is defined as Eq. 6-69.

$$\overline{\rho}(t) = \frac{\left\langle \phi_0^*, \left(\frac{1}{k_{eff,0}} \tilde{\mathscr{F}} - \tilde{\mathscr{H}} + \tilde{\mathscr{S}} \right) \psi \right\rangle}{\left\langle \phi_0^*, \frac{1}{k_{eff,0}} \tilde{\mathscr{F}} \psi \right\rangle} \qquad \textbf{6-69}$$

In this equation, all operators denoted with a tilde are operators of the perturbed system, ψ is the unperturbed shape i.e. the shape at the beginning of a shape step. $k_{eff,0}$ and ϕ_0^* are the multiplication constant and the scalar adjoint flux at time zero, respectively.
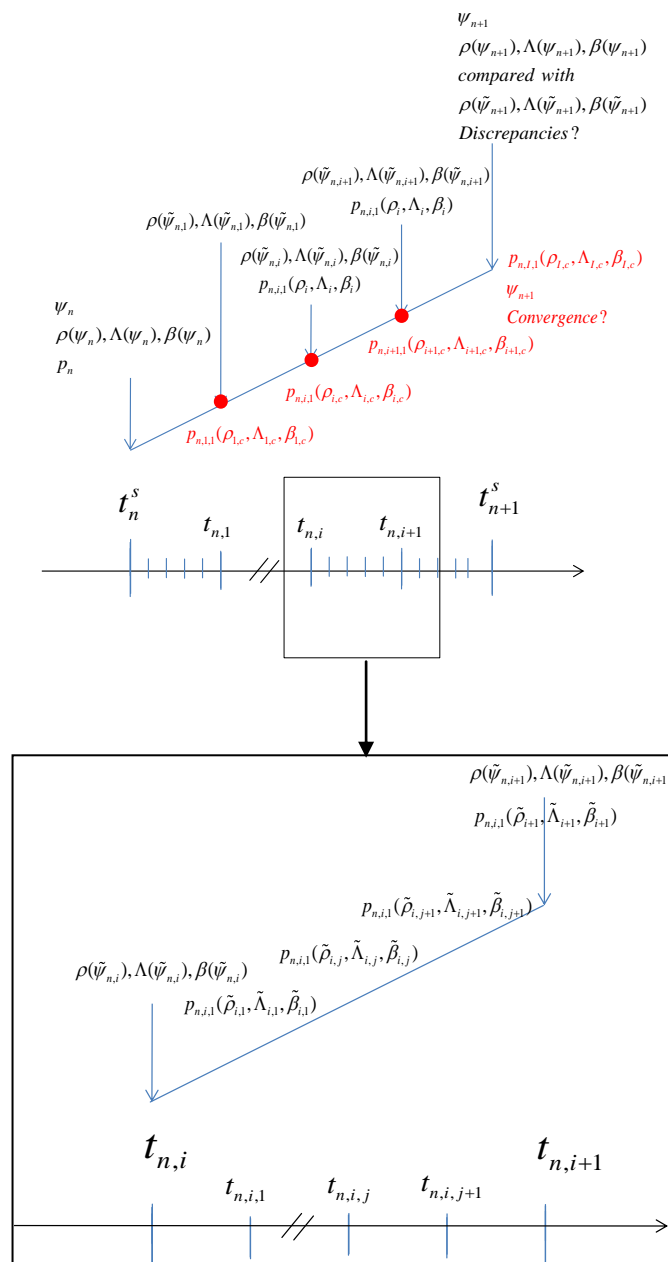
Figure 6-4. SIMMER neutronic scheme. Red values parameters are corrected ones. A tilde stands for extrapolation.

Within this framework, implementation of a core thermal expansion model is aimed at. As mentioned previously, the family of SIMMER codes was primarily developed to analyze later phases of a severe accident like the transition and expansion phases, therefore investigating the behavior of already disrupted cores [73]. The traditional route for calculating the evolution of a severe accident is usually a coupled SAS4A – SIMMER analysis: SAS4A is applied for modeling the initiation phase of the accident (the degradation of pins inside the can wall is simulated, usually, until the latter fails and radial motion of material is possible) and SIMMER is applied to later phases when also radial motion of melted materials occurs. Different models are used in SAS4A and in SIMMER. Indeed, in SAS4A, a channel-wise reactor model is used i.e. each SAS4A channel represents one or more sub-assemblies with either a single pin model or a multiple pin model and many individual channels without any mutual neutronic interaction are employed for a whole-core representation while SIMMER represents the whole core[13]. In addition SAS4A employs a neutron point kinetics model while SIMMER uses a spatial kinetics one. The axial flux and power shapes assumed in SAS4A will deviate in the general case from those determined in the SIMMER calculation after data transfer from SAS4A to SIMMER. Moreover, different approaches for describing material properties are used in SAS4A and SIMMER. Hence, certain approximations and adaptations may have to be applied with regard to the data transfer between the two codes [13]. As an alternative route, an extension of the application range of the SIMMER family codes to the initial phase of core disruptive accidents (CDAs) is therefore desirable and currently under implementation at KIT.

One of the most important feedbacks to take into account in the simulation of the initiation phase of a CDA is the core thermal expansion feedback. This feedback is of less or no importance in the later phases of the accident, when the core is partly or fully molten and important time scales are usually much shorter than the time scale of expansion feedbacks.

Safety codes for initiation phase analyses usually employ neutronic models based on the PK approximation detailed earlier. During the transient, the reactivity feedbacks for the full core or channel are evaluated by interpolating pre-computed reactivity coefficients for taking into account e.g. the Doppler effect or material density variations. These coefficients often remain the same during the whole transient. In the general case the axial and radial expansion coefficients are location dependent. The simplest approach applied in almost all codes for initiation phase simulations, except SAS4A, is to replace the location dependent coefficients by global ones for the axial and radial expansion. The SAS4A code employs an input file in which in particular, fuel reactivity profiles are provided. These profiles are reactivity worth values per kg for axial segments of SAS4A channels [154]. During transient simulations, the positions and dimensions of axial segments vary with time due to temperature variations and the related axial expansion reactivity feedbacks are computed on the basis of the fuel reactivity profiles.

Similar approaches can also be introduced into SIMMER. However, in view of the spatial kinetics approach used in SIMMER, more advanced models for taking into account expansion feedbacks can be considered and the approximation of using location-independent expansion coefficients may no longer be needed.

---

[13] Usually, a SAS4A channel is representative for several sub-assemblies. There exists a strategy for attributing members of a SAS4A channel to a particular ring of an RZ SIMMER-III model or to a particular sub-assembly of a SIMMER-IV 3D model. However, the attributing criteria are usually not unambiguous because various aspects have to be taken into account, among them fuel burnup and power-to-flow ratio.

SIMMER has already the capacity to take into account so-called external reactivity tables, which are provided by the user and contain time and reactivity values adjusting the reactivity in the subroutine used for reactivity calculations. These adjustment values are taken into account also in the spatial kinetics part i.e. during the shape calculation by normalization of the fission source term. Hence, one way to include the thermal expansion feedback could be to proceed along this line by extending the source code at places where the adjustment values are taken into account. However, this approach would make the adjustment algorithm less transparent for the code developer. Therefore, another option has been chosen namely to intervene at a lower level by modifying the cross-sections before they are used for reactivity and shape calculations, in particular by:

- modifying the neutron generation cross-section for taking "effectively" into account the thermal expansion effect while assuming that relative density variations for all materials (fuel, structure, coolant) are similar due to expansion
- modifying the coolant density and related coolant macroscopic cross-sections to compensate the assumption on similarity of relative density variations for the coolant and for other materials.

This approach is explained in detail later.

6.4. Core thermal expansion

6.4.1. Physics and modeling

Before addressing modeling details, an overview of the physics of the considered phenomena is proposed. During nominal and accidental conditions, the temperatures in the core will vary and induce variations in the core dimensions and material densities. This is referred to "thermal expansion".

This thermal expansion of the core may be subdivided into two components: the radial and the axial core thermal expansion[14].

In the following, "radial expansion" wording will be used also for compaction cases when at some radial locations the core diameter may decrease. Radial core expansion is caused primarily by the sub-assembly support diagrid which expands due to an increment of coolant inlet temperature. Additionally, the core constraint system present on top of some cores affects the core expansion as well since temperature variations at different canwall and other structure locations are influenced by the temperature of the coolant. The thermal expansion of these elements determines the sub-assembly grid pitch variation at different axial locations playing a crucial role on the reactivity state of the reactor. If the core structures (diagrid, constraint plate) heat up, the core undergoes an increase of its radius, the average fissile material density therefore decreases and leakage in the axial direction is enhanced. This leads to a negative reactivity feedback. Moreover, more sodium will flow into the core, leading to an additional negative or positive, depending on the fuel type and location, feedback as mentioned in Chapter 2. On the contrary, if the sub-assemblies come closer to each other, i.e. if the core is undergoing a compaction, the leakage is decreased and a positive reactivity increment will be observed. Examples of radial core expansion are given in Figure 6-5.

---

[14] It has to be mentioned that fuel bowing might occurs as well in a reactor, and is dependent on the core clamping system, as detailed in Chapter 2, section 2.4.2. It is however out of the scope of this thesis.
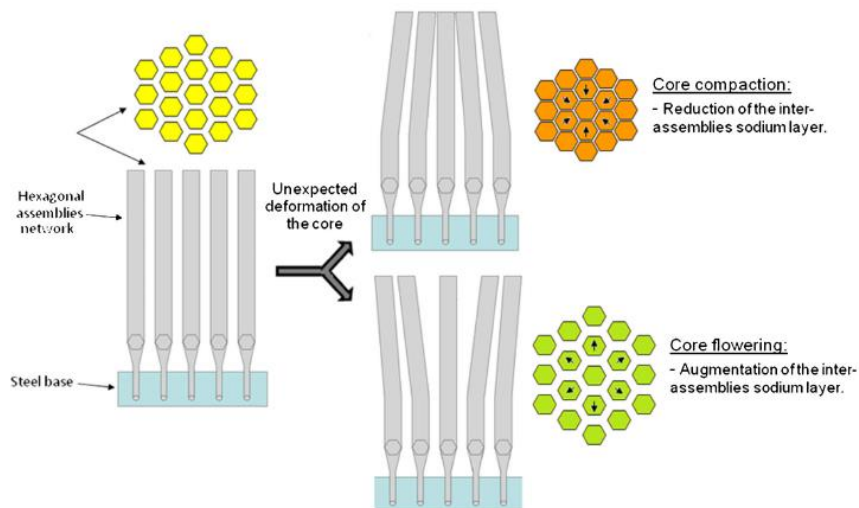
Figure 6-5. Radial core compaction or expansion [155].

In addition to the radial core expansion, axial expansion occurs as well in a reactor. Axial core expansion is related to the pellet-to-fuel gap state, itself depending on the fuel burnup (and on the influence of a possibly existing bonding material between the pellet and the inner clad wall). In a standard MOX pin there exists normally a small a gap between the fuel and the cladding at fabrication. Due to previously described phenomena – see Chapter 5 - the gap tends to close during irradiation. Depending on the gap state, the fuel can either freely expand in axial direction, or be restrained by the cladding due to friction forces, which slows down the expansion process.

Axial expansion increases the core height, therefore reducing the effective density of fissile core material. This leads to an increased leakage in radial direction, therefore introducing a negative reactivity feedback. In addition, more sodium will be present between the pins, thus introducing an additional feedback due to the neutron spectral variations and the leakage effects. The sign of this feedback will depend on the fuel type and the location of the expansion (core center or periphery).

The previously described phenomena are potentially of high importance under transient and accidental conditions as they might delay or hamper a possible power excursion or mitigate its consequences. For example, in the first seconds of an unprotected loss of flow (ULOF) the axial expansion is rather limited and is of the order of 4 mm in sodium cooled fast reactor cores using MOX fuels. During the fuel heat-up it may amount to a fuel height increase of e.g. 2-3 cm [94]. Small dimensional variations may lead to considerable reactivity variations and it becomes important to accurately model these effects.

Traditionally, to take into account core thermal expansions feedbacks the reactivity effect is calculated in most PK-based codes by employing a radial and axial expansion coefficients, applied to averaged variations in the core diameter and height. However, in order to simulate the expansion phenomena more accurately in order to take into account the previously described bowing phenomena (Chapter 2), non-uniform expansions (or to formulate it in another way region-wise expansions) may have to be considered. In this sense, the SIMMER codes can offer a more detailed expansion treatment compared to other codes, since they use a spatial kinetics scheme instead of a point kinetic one.

In SIMMER, dimensional variations in both directions and the related material density variations are computed by means of the linear expansion coefficient of either steel or fuel in the different mesh cells[15].

Radial core expansion

According to the previously described physical phenomena, two simplified expansion modes can be considered in SIMMER for the radial thermal expansion of the core: the cylindrical and the conic modes.

In case of the cylindrical mode, it is considered that only the diagrid at the core bottom drives the radial core expansion. The core parts above the diagrid follow the expansion of the diagrid - Figure 6-6. This means that the radial expansion of each cell of the diagrid is calculated based on its own temperature and the radial dimensions of all cells above the diagrid are set equal to the ones of the diagrid.

In case of the conic mode, both the diagrid at the bottom and the constraint plate at the top of the core are assumed to influence the radial core expansion. Both plates expand differently, reflecting the axial temperature distribution of the coolant. Radial mesh expansions are thus calculated for the cells of the core diagrid and of the constraint plate based on temperature. The cells in-between the two plates are assumed to experience variations of their radial dimension which can be obtained by linearly interpolating between the bottom (diagrid) and top (constraint plate) expansion - Figure 6-7. The cells above the constraint plate are assumed to have the same radial dimensions as the one of the constraint plate.

(a)   **(b)**
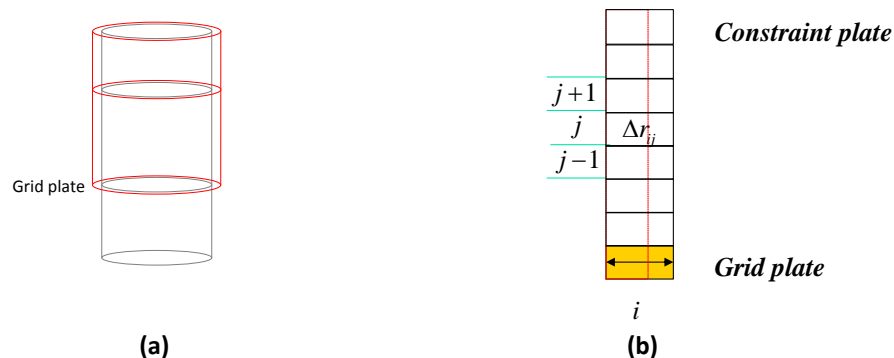
Figure 6-6. Cylindrical expansion mode: (a) whole core (b) one ring (orange = where expansion is calculated. Dotted line = original size).

---

[15] It has to be mentioned that in SIMMER no module is available for dealing with particular aspects of whole core structural mechanics.
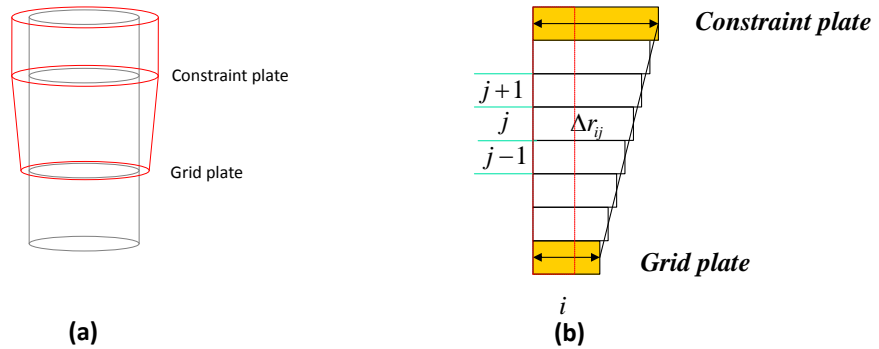
Figure 6-7. Conical expansion mode: (a)   whole core   (b) one ring (orange = where expansion is calculated, in-between: linear expansion. Dotted line = original size).

In both modes, the linear expansion coefficient of steel β_{steel} – Eq. 6-70 – is considered to calculate the new radial dimensions (denoted with index 1) of each cell of the diagrid and possibly of the constraint plate ($\Delta R_{1,i,j}$) depending on the chosen option (conic or cylindrical expansion) – Eq. 6-71.

$$\beta_{steel} = \beta_{s1} + \beta_{s2}(T - T_0) + \beta_{s3}(T - T_0)^2 \qquad \textbf{6-70}$$

where, T is the temperature of structure in the cell and T_0 a reference temperature (e.g. 20˚C).

$$\Delta R_{1,i,j} = \Delta R_{0,i,j} \cdot \eta \qquad \textbf{6-71}$$

where η obtained by integration is given by $\eta = 1 + \beta_{s1}\left(T - T_0\right) + \dfrac{1}{2}\beta_{s2}\left(T - T_0\right)^2 + \dfrac{1}{3}\beta_{s3}\left(T - T_0\right)^3$

and $\Delta R_{0,i,j}$ is the radial mesh size at the reference temperature T_0 and $\Delta R_{0,i,j} = R_{0,i+\frac{1}{2},j} - R_{0,i-\frac{1}{2},j}$ see Figure 6-8.
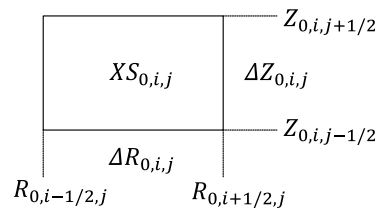
Figure 6-8. Description of an original cell at radial location i and axial location j. XS stands for cross-section.

Axial core expansion

To calculate the axial expansion of the core, the linear expansion coefficient of either fuel α_{fuel} or of cladding steel α_{steel} is considered, depending on the burnup state. In fact at low burnup, the traditional pellet-cladding gap present at fabrication and after initial loading in the reactor is still open and the considered coefficient for the pin axial expansion is the fuel one. At high burnup the gap is usually closed and the cladding coefficient is thus used for calculating the pin expansion. In reality however a stress/strain equation should be solved, but as a first approximation only the temperatures of either fuel or clad are considered to calculate the axial expansion – Eq. 6-72 or 6-73.

$$\alpha_{fuel} = \alpha_{f1} + \alpha_{f2}(T - T_0) + \alpha_{f3}(T - T_0)^2 \qquad \text{if the gap is open} \qquad \textbf{6-72}$$

$$\alpha_{steel} = \alpha_{s1} + \alpha_{s2}(T - T_0) + \alpha_{s3}(T - T_0)^2 \qquad \text{if the gap is closed} \qquad \textbf{6-73}$$

where T is the fuel bulk or the clad temperature, depending on the chosen option and T_0 a reference temperature.

Axial mesh sizes are calculated with Eq. 6-74.

$$\Delta Z_{1,i,j} = \Delta Z_{0,i,j} \cdot \delta \qquad \textbf{6-74}$$

With $\delta = 1 + \alpha_{f1}(T - T_0) + \dfrac{1}{2}\alpha_{f2}(T - T_0)^2 + \dfrac{1}{3}\alpha_{f3}(T - T_0)^3$ (open gap condition)

or $\delta = 1 + \alpha_{s1}(T - T_0) + \dfrac{1}{2}\alpha_{s2}(T - T_0)^2 + \dfrac{1}{3}\alpha_{s3}(T - T_0)^3$ (closed gap condition)

and where $\Delta Z_{0,i,j}$ is the axial mesh size at the reference temperature T_0, see Figure 6-8.

Material density variations due to expansion

Once the expanded radial and expanded axial dimensions are theoretically calculated in each cell, the material densities for this expanded geometry are computed - cf. Figure 6-9. For non-coolant components, material densities are obtained for the new dimensions by means of the mass conservation principle – Eq. 6-75. It has to be mentioned that in case of fuel driven expansion, also the cladding density is modified for simplification[16].

Because of the diagrid expansion, the sub-assemblies are pushed away from each other and more coolant is supposed to flow into the core. Thus, in first approximation, the coolant density is kept equal to the original one to reflect this mass increase – Eq. 6-76.

$$d_1 = d_0 \frac{\Delta Z_0 \cdot \pi (R^2_{0,i+\frac{1}{2},j} - R^2_{0,i-\frac{1}{2},j})}{\Delta Z_1 \cdot \pi (R^2_{1,i+\frac{1}{2},j} - R^2_{1,i-\frac{1}{2},j})} \qquad \text{for non-coolant materials} \qquad \textbf{6-75}$$

$$d_1 = d_0 \qquad \text{for coolant} \qquad \textbf{6-76}$$

---

[16] This can be easily justified when comparing the mass coefficient of reactivities for the main steel components (Cr, Fe, Ni) quoted in barns effective absorption cross-section normalized to the 3.65 barns for [239]Pu: -0.014, -0.013, -0.020 (barns) respectively [156].
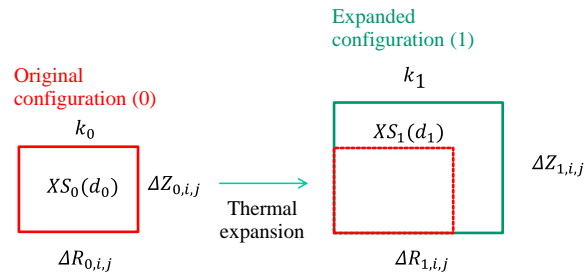
Figure 6-9. Schematics of the expansion of a cell. 0 stands for original, 1 for the expanded configuration. XS for cross-section.

By employing the FOP, reactivity effects induced by the thermal expansion of each cell can be treated independently i.e. they are summed up over the whole core. Consequently, one major assumption that has to be proven here is that the expansion effect is additive i.e. the superposition of mesh-wise contributions is valid. In addition, the expansion effect is assumed to be linear in the later described methodology and therefore both assumptions are verified hereafter.

6.4.2. Properties

At first the linearity and additivity of the expansion effect in case of uniform expansions in one dimension (i.e. the expansion is the same within one direction) is to be proven.

To prove linearity and additivity of the expansion effect in case of uniform expansions for sub-regions of the neutronic mesh, the European Reactor ANalysis Optimized calculation System ERANOS [157] is used and only direct calculations are performed. The reason for using ERANOS is that unlike SIMMER, for which tests of new calculation routes require code developments, the user determines the sequence of neutronics calculation steps in the ERANOS input. ERANOS has been developed over the past 20 years within the European Collaboration on Fast Reactors. It is a deterministic neutronics code system able to solve the Boltzmann transport equation and employs the S_N method. It allows performing reference and design calculations for fast reactors and provides the flux shape and amplitude (normalized e.g. to the thermal power), as well as the reactivity. In addition, ERANOS can perform perturbation or sensitivity calculations. The ERANOS code calculations are composed of two parts: the cell calculation and the core calculations. The cell calculations are performed with the European Cell COde (ECCO) [158], which provides cross-sections and matrices. Those are then used in the full core calculations.

For the following calculations a simplified CP-ESFR core model is set up as shown in Figure 6-10(a). The ESFR fissile core part has been kept while all other materials surrounding it have been replaced by sodium. The axial height of the fissile core (100 cm) has been subdivided into 5 layers of equal height, and symmetric to the core midplane as shown in Figure 6-10 (b). Several test cases have been analyzed to prove linearity and additivity of the expansion effect. They are listed in Table 6-2 (Case 2 will be treated separately later).
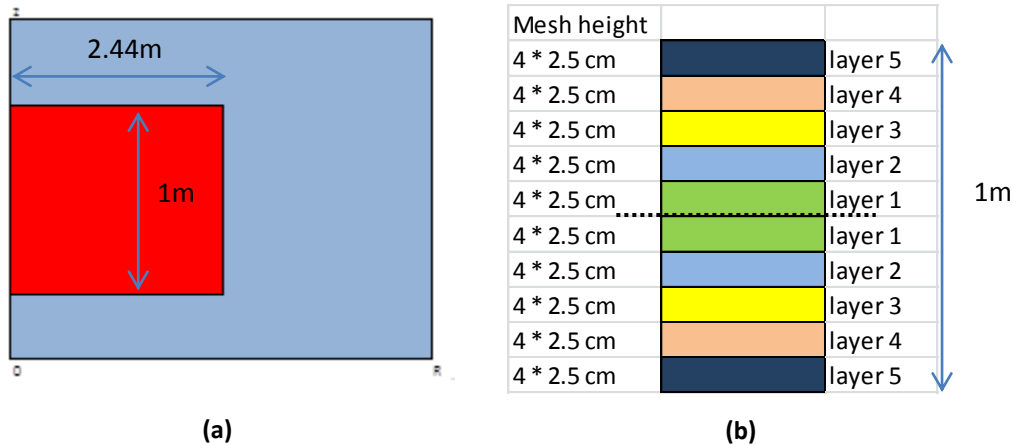
Figure 6-10. (a) Schematics of the simplified CP-ESFR model. Red: fissile core zone of the CP-ESFR core. Blue: liquid Sodium. (b) Axial layout of the fissile zone with symmetric layers.

Table 6-2. Considered test cases for proving the linearity and additivity of the expansion effect.

	Enrichment zones		Na treatment		Energy groups		Information
	1 Zone	2 Zones	Na mass conserved	Na density conserved	1 group	33 groups	
Case 1	X		X		X		Reference
Case 2	X			X	X		Effect of Na treatment if compared to reference
Case 3		X	X		X		Effect of enrichment zones if compared to reference
Case 4		X	X			X	Effect of energy groups if compared to case 3

The first case to be considered (Case 1) is the simplest one i.e. 1 enrichment zone, 1 energy group and sodium mass is conserved during expansion. To validate the linearity of the expansion effect, several expansion percentages (named x in the following) have been assumed. Heights and densities of the expanded layer are modified according to Eq. 6-77 and Eq. 6-78 respectively.

$$z^{layer}_{expanded\ by\ x} = z^{layer}_{original}.(1+x)$$ **6-77**

$$d^{M,layer}_{expanded\ by\ x} = \frac{d^{M,layer}_{original}}{(1+x)} \text{, M being fuel, steel, or sodium}$$ **6-78**

The central layer (layer 1, see Figure 6-10(b)) is expanded by 1%, 2% or 4%. A direct calculation is performed with the BISTRO solver [159] of ERANOS in each case with a precision on k_{eff} of 0.5 pcm.

Results are given in Table 6-3 and Figure 6-11. They show that the expansion effect is linear as could also be expected from literature [25].

Table 6-3. Values of the expansion effect of layer 1 for different axial expansion percentages, 1 enrichment zone, 1E group, sodium mass has been kept constant.

	k_{eff}	$\Delta k/k_1 k_2$ (pcm)
Reference	1.04278	
1% (layer 1)	1.04268	-9
2% (layer 1)	1.04258	-18
4% (layer 1)	1.04238	-37
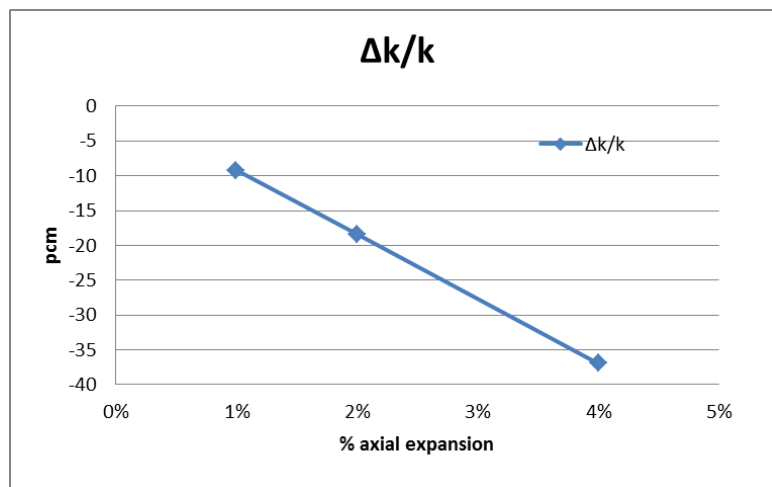
Figure 6-11. Linearity of the expansion effect of layer 1; 1 enrichment zone, 1 E group, sodium mass has been kept constant.

Successive layers have then been expanded by 1%: the 1st layer is expanded by 1%, then the 1st and 2nd layer, and so on. By subtraction, the contribution coming from each individual layer can be determined - Table 6-4.

Table 6-4. Calculated expansion effects of each layer for 1% axial expansion, 1 enrichment zone, 1E group, sodium mass has been kept constant.

	k_{eff}	$\Delta k/k_1 k_2$ (pcm)	Effect of layer n $(\Delta k/k_1 k_2)_{layer\ n} - (\Delta k/k_1 k_2)_{layer\ n-1}$
Reference	1.04278	/	/
1% (layer 1)	1.04268	-9	-9
1% (layer 1+2)	1.04259	-18	-8
1% (layer 1+2+3)	1.04251	-25	-7
1% (layer 1+2+3+4)	1.04246	-30	-5
1% (layer 1+2+3+4+5)	1.04242	-33	-3
Sum	/	/	-32

Of course the individual effect per layer decreases with increasing distance of the layer from the core midplane. Furthermore, one should have in mind that each k_{eff} value has an uncertainty of 0.5 pcm. An additional test has been performed, expanding only layer 2 (which is the one having the largest

effect after layer 1) in order to prove the independence of the expansion effect of the different layers. This yields the same effect as the one calculated in Table 6-4 (i.e. -8 pcm) and therefore, confirms the independence of the expansion effect of the different layers.

The effect of two distinct enrichment zones on the additivity and linearity properties of the expansion effect is also considered – Case 3. In this case, 1 energy group is considered and the sodium mass is conserved during expansion. The inner and the outer core enrichment of the CP-ESFR Working Horse (WH) core at beginning of life (BOL) have been considered for the calculations i.e. 14.05% and 16.35% respectively. Linearity is also proven in this case as shown in Table 6-5 and Figure 6-12. The same approach as in case 1 is also applied here and the effect of 1% expansion of each individual layer is thus calculated - Table 6-6.

Table 6-5. Values of the expansion effect of layer 1 for different axial expansion percentages, 2 enrichment zones, 1 E group, sodium mass has been kept constant.

	k_{eff}	$\Delta k/k_1 k_2$ (pcm)
Reference	1.07410	
1% (layer 1)	1.07395	-13
2% (layer 1)	1.07380	-27
4% (layer 1)	1.07349	-53

Table 6-6. Calculated expansion effects of each layer for 1% axial expansion, 2 enrichment zone, 1E group, sodium mass has been kept constant.

	k_{eff}	$\Delta k/k_1 k_2$ (pcm)	Effect of layer n $(\Delta k/k_1 k_2)_{layer\ n} - (\Delta k/k_1 k_2)_{layer\ n-1}$
Reference	1.07410	/	/
1% (layer 1)	1.07395	-15	-15
1% (layer 1+2)	1.07381	-29	-14
1% (layer 1+2+3)	1.07370	-40	-11
1% (layer 1+2+3+4)	1.07362	-49	-8
1% (layer 1+2+3+4+5)	1.07358	-55	-6
Sum	/	/	-54
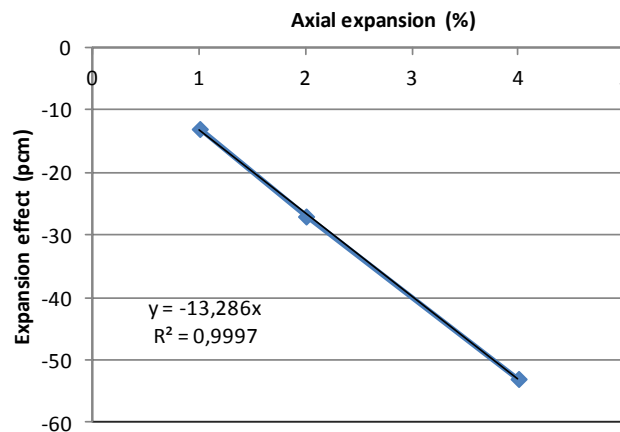
Figure 6-12. Linearity of the axial expansion effect of layer 1 for different axial expansion percentages, 2 enrichment zones, 1 E group, sodium mass has been kept constant.

The same test has been performed considering this time the inner core expansion only, the outer core expansion only or both expansions at the same time. Tests have been performed for 1% and 5% expansion. Additivity is shown in these cases - Table 6-7.

Table 6-7. Expansion effects of 1% or 5% axial expansion of all layers in the inner core only, the outer core only or both. 2 enrichment zones, 1 E group, sodium mass has been kept constant.

	1% axial expansion of all layers		5% axial expansion of all layers		
	k_{eff}	$\Delta k/k_{ref}k_2$ (pcm)	k_{eff}	$\Delta k/k_{ref}k_2$ (pcm)	Assessed (based on 1% axial expansion results)
Reference	1.07410	/	1.07410		
Inner Core	1.07396	-13	1.07334	-66	-65
Outer Core	1.07362	-42	1.07171	-208	-210
Inner and Outer Core	1.07348	-54	1.07100	-270	**-270**
Sum Inner + Outer Core	/	-55	/	-274	**-275**

Evaluation of the effect of energy groups on the expansion effect properties (linearity and additivity) is performed hereafter – Case 4. Results in Table 6-8 should be compared to Case 3 (Table 6-7).

Table 6-8. Expansion effects of 1% axial expansion of all layers in the inner core only, the outer core only or both, 2 enrichment zones, 33 E groups, sodium mass has been kept constant.

	1% axial expansion of all layers	
	k_{eff}	$\Delta k/k_{ref}k_2$ (pcm)
Reference	1.04322	/
Inner Core	1.04313	-8
Outer Core	1.04283	-36
Inner and Outer Core	1.04275	**-43**
Sum Inner + Outer Core	/	**-44**

Linearity and additivity are proven also for this case. Now that the linear and additive properties of the expansion effect have been demonstrated in uniform expansion cases, the same tests are repeated in case of non-uniform expansions (i.e. different expansions are possible within one direction).

Linearity and additivity of the expansion effect in case of non-uniform expansions

Only cases 1 and 3 in Table 6-2 are considered in this subsection. Based on values for 1% axial expansion of each layer - cf. Table 6-4 - an assessment can be performed to obtain values related to non-uniform axial expansion in the reference case (Case 1) as shown in Table 6-9. These values are then compared to the values obtained via direct calculation for the built up case - Table 6-10. Results have a very good agreement and additivity of the expansion effect is thus proven for the non-uniform axial expansion case within 6% relative discrepancy (representing 2 pcm difference at maximum having in mind the uncertainty of 0.5 pcm for each case).

Table 6-9. Assessed values based on 1% axial expansion values of each layer. 1 enrichment zone, 1E group, sodium mass has been kept constant.

	Assessment based on 1% values	
	$\Delta\rho$ (pcm)	
5% (layer 1)	5*(-9)	-45
4% (layer 2)	4*(-8)	-32
3% (layer 3)	3*(-7)	-21
2% (layer 4)	2*(-5)	-10
1% (layer 5)	1*(-3)	-3
Total		**-111**

Table 6-10. Values for a non-uniform axial expansion, 1 enrichment zone, 1E group, sodium mass has been kept constant. L stands for layer

	k_{eff}	$\Delta k/k_1 k_2$ (pcm)	Effect of layer n $(\Delta k/k_1 k_2)_{\text{layer n}}$ - $(\Delta k/k_1 k_2)_{\text{layer n-1}}$
Reference	1.04278	/	/
5% L1	1.04228	-46	-46
5% L1 + 4% L2	1.04191	-80	-34
5% L1 + 4% L2 + 3% L3	1.04168	-101	-21
5% L1 + 4% L2 + 3% L3 +2% L2	1.04157	-111	-10
5% L1 + 4% L2 + 3% L3 +2% L2 +1% L1	1.04154	-114	-3
Sum	/	/	**-114**

Besides, the effect of two distinct enrichment zones on the additivity and linearity properties of the expansion effect is considered in case of non-uniform expansions (Case 3). The inner and outer core enrichment of the CP-ESFR WH core at BOL is considered also in this case. Based on values for 1% axial expansion of each layer, values related to non-uniform axial expansions are assessed as shown in Table 6-11. These values are summed up and compared to direct calculation results of this expanded case listed in Table 6-12. Linearity and additivity of the expansion effect is proven for the non-uniform axial expansion case within 1% relative discrepancy (representing 1 pcm difference at maximum) – Figure 6-13.

Table 6-11. Assessed values based on 1% axial expansion values of each layer. 2 enrichment zones, 1E group, sodium mass has been kept constant.

	$\Delta\rho$ (pcm) assessment based on 1% values	
5% (layer 1)	5*(-13)	-65
4% (layer 2)	4*(-12)	-48
3% (layer 3)	3*(-10)	-30
2% (layer 4)	2*(-7)	-14
1% (layer 5)	1*(-3)	-3
Total		**-160**

Table 6-12. Values for a non-uniform axial expansion, 2 enrichment zones, 1E group, sodium mass has been kept constant. L stands for layer.

	k_{eff}	$\Delta k/k_1 k_2$ (pcm)
Reference	1.07410	/
5% L1 + 4% L2 + 3% L3 +2% L2 +1% L1	1.07227	**-159**
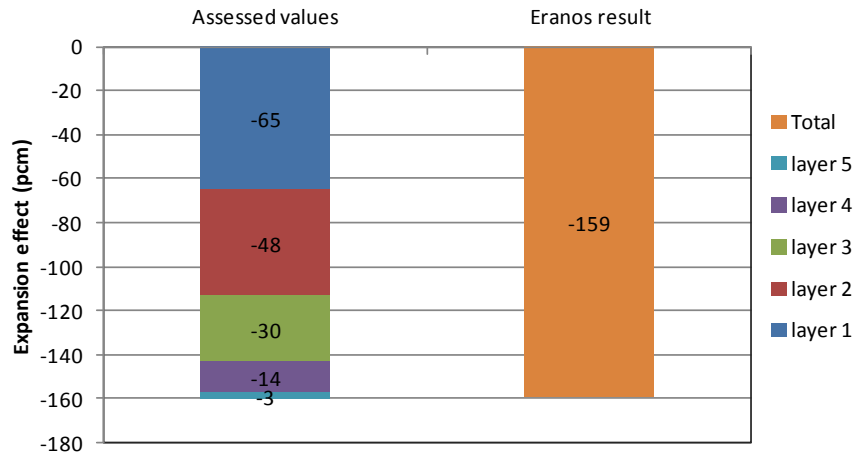
Figure 6-13. Additivity and linearity of the expansion effect: values for a non-uniform axial expansion, 2 enrichment zones, 1E group, sodium mass has been kept constant.

In all cases uniform and non-uniform expansions cause reactivity effects that show a linear and additive behavior. The assumption of summing up the expansion effect of each individual cell to obtain the overall reactivity effect can thus be safely accepted.

6.4.3. Particularity of the sodium treatment

This section explains why in Section 6.3, the expansion effects of a particular spatial sub-region subdivide into the effect of similar expansion of all materials for this sub-region and the effect of sodium density variations to compensate the assumption on similarity. The idea of the new methodology developed in SIMMER for taking into account the core thermal expansion feedbacks, similar for all materials, is to use density variations to reflect dimensional variations and hence be able to use the original mesh while taking into account dimensional variations.

We will now consider a perturbation of amount x in the densities. In the following equations, indices 1 and 0 refer to the perturbed and unperturbed case, respectively. All terms are adjoint-weighted reaction rates.

Consider the diffusion approximation. In this case, the leakage term is proportional to the diffusion coefficient which is itself proportional to the inverse of the transport cross-section (see previous section). The generation and absorption terms are proportional to the cross-sections. Hence, in case of a perturbation of x in the densities, the FOP reactivity is computed according to Eq. 6-80. When calculating the reactivity variation due to this perturbation, based on the original reactivity Eq. 6-79,

one obtains Eq. 6-81 if written in one group approximation (for the purpose of demonstration only) and assuming that no spectral or spatial flux shifts have to be taken into account [160].

$$\rho_0 = \frac{Leakage_0 + Absorption_0 + Generation_0}{Generation_0} \qquad \textbf{6-79}$$

With $Generation = \left\langle \phi_0^*, \chi \frac{\nu\Sigma_f}{k_{eff,0}} \psi \right\rangle$; $Absorption = \left\langle \phi_0^*, \Sigma_t \psi \right\rangle$; $Leakage = \left\langle \phi_0^*, \nabla \cdot D\vec{\nabla}\psi \right\rangle$ and

$\phi^*_0 = \phi^*(t=0)$

$$\rho_1 = \frac{Leakage_0(1+x) + Absorption_0 \dfrac{1}{(1+x)} + Generation_0 \dfrac{1}{(1+x)}}{Generation_0 \dfrac{1}{(1+x)}}$$

$$= \frac{Leakage_0(1+x)^2 + Absorption_0 + Generation_0}{Generation_0} \qquad \textbf{6-80}$$

$$\Delta\rho = \rho_1 - \rho_0 = Leakage_0\left[(1+x)^2 - 1\right] \qquad \textbf{6-81}$$

In SIMMER however, the (approximately) FOP reactivity in the perturbed case is defined as Eq. 6-82. When calculating the reactivity variation, one gets Eq. 6-83.

$$\rho_{1,simmer} = \frac{Leakage_0 + Absorption_0 \dfrac{1}{(1+x)} + Generation_0 \dfrac{1}{(1+x)}}{Generation_0 \dfrac{1}{(1+x)}}$$

$$= \frac{Leakage_0(1+x) + Absorption_0 + Generation_0}{Generation_0} \qquad \textbf{6-82}$$

$$\Delta\rho_{simmer} = \rho_{1,simmer} - \rho_0 = Leakage_0\left[(1+x) - 1\right] \qquad \textbf{6-83}$$

One may first notice that a reactivity variation due to density variation can be simulated under the previously mentioned assumption by a leakage variation only. In addition, one may see by comparing Eq. 6-81 and Eq. 6-83, that in SIMMER FOP calculations the variation of the leakage term is underestimated by a factor of $\dfrac{(1+x)^2 - 1}{(1+x) - 1} = 2 + x$ if the "diffusion" approach is reasonable.

Therefore the original SIMMER extrapolates the leakage between the shape steps instead of using first-order values.

When considering a density change, the leakage term cannot be easily modified in the existing SIMMER scheme since this would need a redetermination of the partial currents and thus practically a new calculation of the angular flux. Thus, in order to extend the code for taking into account core thermal expansion feedbacks, the leakage term in the new methodology is approximately recomputed (by introducing a factor 2, assuming that x is small).

This approach however cannot be applied when different materials undergo different expansions within one cell as is typically the case with sodium. Indeed, the sodium mass is, in general, not conserved during a core expansion since radial core expansion allows more sodium to flow into the core. A special treatment for sodium will hence be applied. The idea behind the treatment is to modify the original sodium densities in such a way that the distribution of sodium variation throughout the reactor is considered in the shape calculations. This approach is detailed in section 6.5.2.

To get an idea of the effect of sodium mass variation, the simplified core model described earlier is analyzed. Several expansion percentages are considered for layer 1 and results can be found in Table 6-13.

Table 6-13. Values of the expansion effect of layer 1 for different axial expansion percentages, 1 enrichment zone, 1 E group, sodium density has been kept constant.

	k_{eff}	$\Delta k/k_1 k_2$ (pcm)
Reference	1.04278	
1% (layer 1)	1.04259	-17
2% (layer 1)	1.04241	-34
4% (layer 1)	1.04204	-68

It can be noticed from Table 6-13 and Table 6-3 that a mass variation of 35 kg in total has an effect of 84% ($\frac{-68}{-37} = 1.84$) on the expansion effect value, indicating that this influence is not at all negligible.

In addition Table 6-13 confirms that the expansion effect remains linear. Additional tests have been performed for 33 energy groups - Table 6-14.

Table 6-14. Values of the expansion effect of layer 1 for different axial expansion percentages, 1 enrichment zone, 33 E group sodium density has been kept constant.

	k_{eff}	$\Delta k/k_1 k_2$ (pcm)
Reference	1.04322	
1% (layer 1)	1.04309	-12
2% (layer 1)	1.04296	-24
4% (layer 1)	1.04270	-48

Table 6-15. Values of the expansion effect for different layer expansions, 1 enrichment zone, 1 E group, sodium density has been kept constant or sodium mass has been kept. L stands for layer.

	k_{eff}	$\Delta k/k_1 k_2$ (pcm) Na mass conserved	$\Delta k/k_1 k_2$ (pcm) Na mass not conserved	Relative difference (%)
Reference	1.04278	/		
5% L1	1.04185	-85	-46	45.8
5% L1 + 4% L2	1.04118	-147	-80	45.7
5% L1 + 4% L2 + 3% L3	1.04077	-185	-101	45.4
5% L1 + 4% L2 + 3% L3 +2% L2	1.04059	-202	-111	45.1
5% L1 + 4% L2 + 3% L3 +2% L2 +1% L1	1.04053	-207	-114	44.8

The previous approach has been applied to the other layers, in case of 1 energy group calculations - Table 6-15. From Table 6-15 it can be seen that modeling the sodium in a correct way has a large impact on the expansion results. It is therefore crucial to accurately model the effect of the variation of the sodium mass within the core in the core expansion reactivity feedback.

6.5. A new methodology to take into account core expansion feedbacks in spatial kinetic codes

6.5.1. The equivalence principle

As previously described, SIMMER employs a spatial kinetic neutronic method and a Eulerian grid. Since the mesh is fixed, an alternative to changing the mesh has to be found and leads to the expansion models detailed hereafter [144]. The developed approaches rely on the fact that dimensional changes can be effectively simulated by cross-section variations for isotropic expansions by employing the so-called *equivalence principle*.

The equivalence principle was first published in 1959 [160] (according to the information available to the author) and attracted additional attention more recently [161]. It stipulates that if all dimensions of a given configuration 1 are multiplied by a certain factor α and all neutron cross-sections are multiplied by $\dfrac{1}{\alpha}$, the reactivity and other neutronic properties are the same in the new configuration 2 as in configuration 1. In other words, the equivalence is ensured as long as the products of cross-sections and dimensions are kept constant in each direction during the transformation – Eq. 6-84. Of course, masses are not conserved in this approach.

$$\begin{cases} R_1 \cdot \Sigma_1 = R_2 \cdot \Sigma_2 \\ Z_1 \cdot \Sigma_1 = Z_2 \cdot \Sigma_2 \\ \dfrac{R_2}{R_1} = \dfrac{Z_2}{Z_1} = \alpha \end{cases} \qquad \text{6-84}$$

To visualize this principle, an explanation based on [161] is given hereafter.

Consider a uniform isotropic core perturbation i.e. the perturbation is the same within one direction (uniform) and is applied to all directions (isotropic). For simplification, dimension and density related quantities in the reactor are submitted to the same perturbation.

The perturbation can for example be defined as a change in dimensions and densities.

The atomic density N is per definition proportional to the inverse of the core volume. A change in the atomic density induces a change in the macroscopic cross-sections defined as Eq. 6-85, where σ is the microscopic cross-section.

$$\Sigma = \sigma \cdot N \qquad \text{6-85}$$

A change in the macroscopic cross-sections induces a change in the neutron mean free path λ, defined as the average distance a neutron can travel before colliding with an atom and expressed as Eq. 6-86.

$$\lambda = \frac{1}{\Sigma}$$ **6-86**

Physically, a uniform isotropic perturbation as defined earlier causing the original volume V_1 to increase by a factor α^3 reaching a new volume V_2 (i.e. $V_2 = \alpha^3 V_1$) also increases the neutron mean free path by α^3. On the other hand, each individual dimension is increased by the factor α, which means that dimensions increase less than the neutron mean free path does. This causes the neutron leakage to globally increase and the reactivity to decrease.

If the aim is now to keep the original reactivity value in the perturbed configuration, the change in neutron mean free path has to be identical to the change in linear core dimensions. The neutron mean free path should thus be proportional to α. The macroscopic cross-section and therefore the densities should hence be proportional to $\frac{1}{\alpha}$. Therefore to keep the same reactivity state as in the original non perturbed configuration, densities and dimensions should vary by an inverse factor.

In conclusion, as long as the product of cross-sections and dimensions is kept constant between one configuration and its perturbed configuration, the reactivity and all other parameters are kept constant. An additional expansion of the equivalence principle is given in Appendix J.

An example of the application of the equivalence principle in uniform isotropic and anisotropic cases is detailed hereafter. For simplification, the perturbation is considered to be the same for all materials, including the coolant. In addition, we will consider that instead of modifying cross-sections one might modify densities instead[17]. In Figure 6-14 the original core with original radial dimension R_0, original axial dimension Z_0, original set of densities d_0 and therefore cross-sections Σ_0 and an original reactivity state k_0 is expanded isotropically by a factor α. The new dimensions and densities are expressed in Eq. 6-87.

$$\begin{cases} R_1 = R_0.\alpha \\ \\ Z_1 = Z_0.\alpha \\ \\ d_1 = d_0 \dfrac{V_0}{V_1} = d_0 \dfrac{1}{\alpha^3} \text{ (and therefore } \Sigma_1 = \Sigma_0 \cdot \dfrac{1}{\alpha^3} \text{)} \end{cases}$$ **6-87**

The core presents then a new reactivity state k_1. The equivalence principle is now applied to this expanded configuration and allows keeping the same reactivity state k_1 while using the configuration with original dimensions R_0 and Z_0 and modified densities d_2 (or cross-sections Σ_2) – Eq. 6-88.

---

[17] This is due to the fact that all number densities are changed by the same factor. Therefore, the so-called resonance self-shielding factors remain unchanged since they depend only on ratios of number densities.

$$\begin{cases} R_1.\Sigma_1 = R_0.\Sigma_2 \\ Z_1.\Sigma_1 = Z_0.\Sigma_2 \end{cases} \qquad \text{6-88}$$

$$\Rightarrow \qquad \Sigma_2 = \Sigma_1.\alpha$$

Figure 6-14. Uniform isotropic expansion. XS stands for cross-section.

The equivalence principle is now applied to an anisotropic expansion case. In Figure 6-15 the original core with original radial dimension R_0, original axial dimension Z_0, original set of densities d_0 and therefore Σ_0 and an original reactivity state k_0 is expanded anisotropically by a factor α in the radial direction and β in the axial direction. The new dimensions and densities are the ones in Eq. 6-89. If α=β, a uniform expansion is considered and the previously mentioned results are obtained.

$$\begin{cases} R_1 = R_0.\alpha \\[2mm] Z_1 = Z_0.\beta \\[2mm] d_1 = d_0 \dfrac{V_0}{V_1} = d_0 \dfrac{1}{\beta\alpha^2} \text{ (and therefore } \Sigma_1 = \Sigma_0 \cdot \dfrac{1}{\beta\alpha^2} \text{)} \end{cases} \qquad \text{6-89}$$

After expansion, the core presents another reactivity state k_1. The equivalence principle is applied to this expanded configuration to get the same reactivity state k_1 in the core with original radial dimensions R_0 and modified axial dimensions Z_2 and densities (or cross-sections) d_2 – Eq. 6-90. Note that the choice of having original radial dimensions instead of original axial dimensions is arbitrary (one could choose to have original axial dimensions instead of original radial ones and the following steps should then be adapted).

$$\begin{cases} R_1.\Sigma_1 = R_0.\Sigma_2 \\ Z_1.\Sigma_1 = Z_2.\Sigma_2 \end{cases} \qquad \text{6-90}$$

This yields, after calculation, a new set of cross-sections and axial dimensions – Eq. 6-91 - in general different from the original dimensions unless α=β.

$$\begin{cases} R_2 = R_0 \\[2mm] Z_2 = Z_1.\dfrac{1}{\alpha} \\[2mm] \Sigma_2 = \Sigma_1.\alpha \end{cases} \qquad \text{6-91}$$

$$k_0$$
$$\boxed{\begin{array}{c} d_0 \\ (XS_0) \end{array}}\ Z_0$$
$$R_0$$

Mass conservation for all materials

$$k_1$$
$$\boxed{\begin{array}{c} d_1 = d_0\ \dfrac{1}{\beta\alpha^2} \\ (XS_1) \end{array}}\ Z_1 = \beta Z_0$$
$$R_1 = \alpha R_0$$

Equivalence principle: Linear dimension*XS =constant

$$k_1$$
$$\boxed{\begin{array}{c} d_2 = d_1\alpha \\ (XS_2) \end{array}}\ Z_2 = \dfrac{1}{\alpha} Z_1 \neq Z_0$$
$$R_2 = R_0 = \dfrac{1}{\alpha} R_1$$
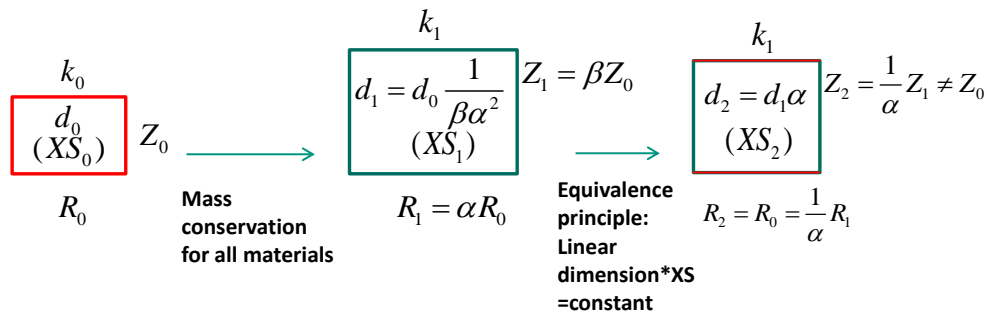
Figure 6-15. Uniform anisotropic expansion. XS stands for cross-section.

It might be worth mentioning that in case of an anisotropic expansion, it is not possible to obtain the same reactivity state k_1 with a core having both original radial __and__ axial dimensions. It is therefore necessary to consider 2 steps: the first one considering an isotropic uniform expansion and the second one considering a non-isotropic uniform expansion in order to reflect the considered expansion effect in a core with original axial and radial dimensions. The equivalence principal is not valid in the general case for non-isotropic, non-uniform expansions, but one would like to investigate whether an equivalence-based approach, sometimes also referred as equivalence principle in the following, would be a reasonably accurate approximation for relevant cases.

The equivalence principle has been checked for uniform expansions and the particular example of isotropic uniform expansions is shown in Figure 6-16. The tests are performed with SIMMER and the overall neutronic mesh is considered for the expansion. 1%, 2% and 5% isotropic expansions are considered in the CP-ESFR WH at BOL. Since the sodium relative density variation is treated separately, the sodium has been expanded as all other materials. Comparisons between a really expanded model and a model for which the input densities are modified accordingly to the equivalence principle are given in Figure 6-16. Results match within 5% relative error.
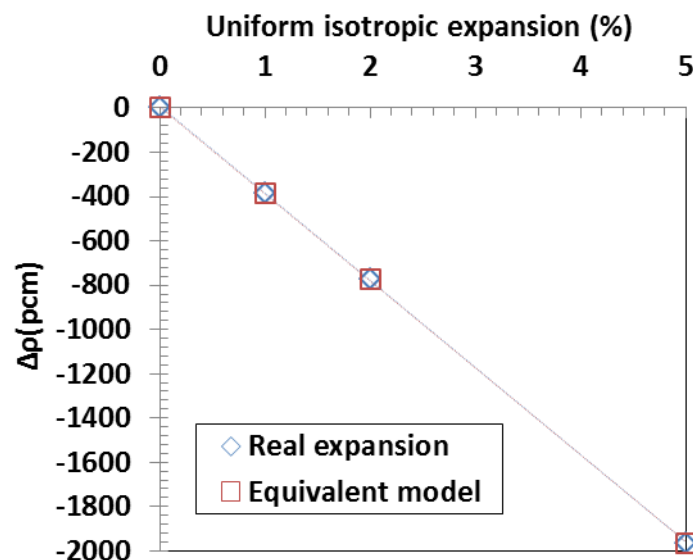
Figure 6-16. Comparison of the equivalence model and a real expansion for several isotropic expansion cases.

Additional calculations for non-isotropic expansions are performed with ERANOS due to the flexibility of this tool compared to SIMMER. Several cases are considered for a simple core based on the CP-

ESFR WH core. For these analyses however the average fuel mass in the outer core is half the one of the inner core, for convenience.

Only 3 cases are considered in this section. Case 1 consists in the expansion of the upper fissile core part (above midplane) by 10% radially and only 1 enrichment zone is considered. Case 2 is the same as Case 1 but this time 2 enrichment zones are considered (same as in the CP-ESFR WH at BOL). Case 3 is similar to case 2 but 1% radial expansion is considered instead of 10%. Direct calculations are performed, with 1 or 33 energy groups but only the results for 33 groups are discussed here. For each case, a calculation for a real expanded configuration as well as for the equivalent configuration (based on the equivalence principle) is considered. The sodium has been expanded as all other materials. Results are presented in Table 6-16, Table 6-17 and Table 6-18.

It can be noticed from Table 6-16 that in case the core has a homogeneous enrichment, the equivalence principle provides good results with a relative discrepancy of less than 2%. As soon as different enrichment zones are considered, the equivalence principle is less accurate due to the spectral and spatial flux shift that is not properly taken into account. This is especially seen when only the inner or only the outer core is expanded (27.7% and 18.3% relative discrepancy in absolute value, respectively). When both cores are expanded in the same way, the discrepancy between the results provided by the equivalence principle and the ones given by a real expansion reduces to 5.4% in absolute value (Table 6-17). This effect is even more reduced if only a small expansion percentage is considered (which is usually the case in the radial expansion of the core diagrid) as can be seen in Table 6-18. This means that as the expansions tend to be uniform within one direction, the equivalence principle based procedure becomes more accurate.

In other codes (e.g. CATHARE [162]) only one expansion coefficient is considered for the radial expansion thus assuming a homogeneous expansion in the diagrid. The developed method is therefore applicable within the same limits, and additionally recalculates the expansion at several time steps during the transient. For more complex cores, however, the equivalence procedure application for non-uniform expansions seems more difficult to prove.

Table 6-16. Comparison of direct and equivalent results for case 1.

	k-eff	Reactivity effect (pcm)
Unperturbed	1.01739	
Real expanded	1.00541	-1171
Equivalence principle	1.00559	-1154
Difference (pcm)		17
Relative discrepancy (%)		-1.51

Table 6-17. Comparison of direct and equivalent results for case 2

	Reactivity effect (pcm)	Difference to real expansion (%)
Real expanded (inner and outer core)	-1204	
Real expanded (inner core only)	-1040	
Real expanded (outer core only)	-193	
Equivalence principle (inner and outer core)	-1140	-5.4
Equivalence principle (inner core only)	-813	-21.7
Equivalence principle (outer core only)	-228	18.3

Table 6-18. Comparison of direct and equivalent results for case 3

	Reactivity effect (pcm)	Difference to real expansion (%)
Real expanded (inner and outer core)	-124	
Real expanded (inner core only)	-104	
Real expanded (outer core only)	-22	
Equivalence principle (inner and outer core)	-118	-4.7
Equivalence principle (inner core only)	-86	-17.2
Equivalence principle (outer core only)	-24	8.2

6.5.2. Uniform expansions in 1D: the Global DENSF Method

Based on the previously described equivalence principle, a first model has been developed and further improved to account for uniform core thermal expansions in SIMMER but having in mind that non-uniform expansions have to be treated: it is the so-called DENSF (density factor) method. It aims at evaluating core expansion feedbacks in an Eulerian mesh with the introduction, in addition to the equivalence model, of a globally calculated correction factor.

The expansion model procedure is a two-phased approach. At first, the DENSF value is computed at steady state (1st phase). Based on this factor, the transient calculation can be performed (2nd phase). The whole methodology is based on 4 steps which are indicated in Table 6-19. All steps are detailed in the following.

Table 6-19 – Overall methodology of the DENSF expansion model

Steps	Task	Methodology	Goal
Step 1 : Theoretical expansion of the cell	Calculate expanded axial dimensions	Based on: **Fuel temperature** if gap is open **Clad temperature** if gap is closed	Describe the expanded cell and the associated reactivity state
	Calculate expanded radial dimensions	Two modes can be considered: **Conic mode:** based on temperatures of diagrid and constraint plate **Cylindrical mode:** Based on temperatures of diagrid	
	Calculate related macroscopic densities	**Non-coolant materials:** Mass conservation **Coolant:** Density conservation	
Step 2 : Apply the equivalence model	Obtain original radial dimensions, modified axial dimensions, equivalent densities	X	Keep the reactivity state of the expanded cell while using original radial and modified axial dimensions
Step 3: Density correction factor	Obtain effect of axial dimensional change	Based on overall mesh variation	Account for the discrepancy between original axial dimensions and modified axial dimensions and determine effective densities.
Step 4: compute expansion effect	Use effective densities and original densities in original mesh	X	Obtain the expansion effect while using original mesh

At first, axial and radial core expansion factors are calculated mesh-wise meaning that expanded dimensions and related material densities are computed for each cell as has been explained in section 6.4.1 (Step 1 in Table 6-19). The core expansion is decomposed into a radial and an axial one as described earlier. The corresponding dimensional variations in both directions and the related material density variations are computed by means of the linear expansion coefficient of either steel or fuel for each fluid-dynamic cell in the neutronic mesh domain. Once the virtually expanded cell dimensions and related densities are known, the equivalence principle is applied to come back to a regular radial mesh.

If the relative dimension variations are the same in the radial and axial direction for this cell i.e. the expansion is isotropic, the equivalence principle simplifies the expansion treatment in SIMMER. In fact, instead of considering the effect of dimension variations experienced with thermal expansion one can consider the sole effect of cross-section variations. As previously demonstrated, in case of an isotropic expansion, the equivalent cell obtained through application of the equivalence principle has the original radial $\Delta R_2 = \Delta R_0$ and axial dimensions $\Delta Z_2 = \Delta Z_0$, but different macroscopic neutron cross-sections corresponding to a different material density.

However, the expansion is usually anisotropic i.e. the axial and radial expansion factors are different and the choice is made to treat an equivalent cell with original radial dimensions. The equivalent configuration is hence represented by a pseudo axial expansion i.e. a cell with original radial dimensions but with axial dimensions ΔZ_2 and cross-sections Σ_2 defined by Eq. 6-92 (where η is the radial expansion factor).

$$\left[\begin{array}{l} \Delta R_2 = \Delta R_1 . \dfrac{1}{\eta} \\[2em] \Delta Z_2 = \Delta Z_1 . \dfrac{1}{\eta} \\[2em] \Sigma_2 = \Sigma_1 . \eta \end{array} \right. \qquad \text{6-92}$$

This pseudo axially expanded cell is equivalent to the radially and axially expanded cell in terms of reactivity per definition of the equivalence principle. Nevertheless, this cell does not have the original axial dimension and a further step is necessary to be able to use the original SIMMER neutronic mesh to keep the reactivity effect of the expanded cell.

Assume first that all modifications in axial dimension for a particular radial mesh in the RZ model of SIMMER are similar (i.e. the initial ones are multiplied by the same factor leading to a uniform expansion in axial direction). This can be considered as a combination of two perturbations: uniform axial dimensional variation and density variation. The effect of uniform axial dimensional variation can be pre-computed for a given radial mesh for a particular case (e.g. variation by 1%) and used during the transient. The effect of density variations can be taken into account in SIMMER either "directly" or by employing a PT approach. This approach does not require any correction factor and is accurate since Doppler and void effects do not interfere with the expansion as demonstrated later on.

However, when non-uniformities are considered, a density factor has to be applied. We have seen that reactivity effects due to variations in dimensions and cross-sections are correlated. A simple

assumption would be that reactivity variations due to expansion can be computed by adding the missing effect due to the dimensional axial discrepancy to the effect obtained by employing the equivalent densities in the original mesh. To obtain this effect the DENSF factor is introduced.

In case of a uniform isotropic expansion, DENSF is equal to unity as explained earlier. In the general axial expansion case, the assumption is that reasonably accurate results could be obtained if DENSF is computed before the transient as the ratio of: (a) the reactivity effect due to an axial dimensional change of the whole neutronics domain of SIMMER by 1%, computed by direct calculation and (b) the reactivity effect due the same dimensional change but computed with SIMMER via FOP.

To obtain the DENSF correction factor, SIMMER performs two direct calculations. In the first one, the k_{eff} for a core with original mesh Z_0 and equivalent d_2 densities is calculated. For the second calculation the whole axial mesh is artificially increased by 1% (independently of temperature). The k_{eff} for a core with an axially expanded mesh Z' and the same equivalent densities d_2 is then calculated - Figure 6-17.
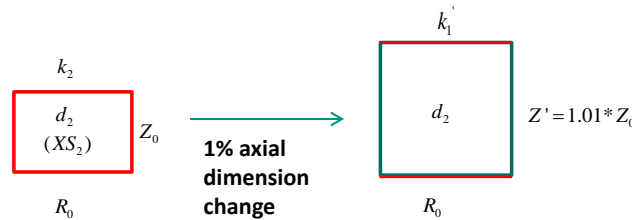
Figure 6-17. Axial dimensional increase of a cell. XS stands for cross-section.

The reactivity effect due to 1% axial dimensional increase obtained via the direct calculation is therefore known.

The previously calculated reactivity effect due to 1% axial dimensional increase obtained via the direct calculation effect is then compared to the one obtained with the FOP approach in SIMMER. This gives the DENSF factor – Eq. 6-93.

$$DENSF = \frac{\Delta\rho^{direct}_{1\% \, axial \; dimension \; variation}}{\Delta\rho^{FOP}_{1\% \, density \; variation}} \qquad \textbf{6-93}$$

An additional explanation of the DENSF factor is given in Apendix K. The omitted effect is then added through the densities to the effect given by using d_2 densities in the original configuration by applying Eq. 6-94.

$$d_3 = d_2 \cdot \frac{1}{1 + DENSF \cdot x} \qquad \textbf{6-94}$$

where x=$\dfrac{\Delta Z_{2,i,j} - \Delta Z_{0,i,j}}{\Delta Z_{0,i,j}}$ is the axial expansion percentage of the equivalent cell compared to the original one.

Equation 6-94 can be easily understood if one considers that the whole equivalent core has an expansion of x. The reactivity effect due to core thermal expansion effect is obtained by subtracting two reactivities: the reactivity obtained with d_3 densities in original mesh dimensions (i.e. configuration (3) in Figure 6-18, for the whole core) and the reactivity obtained with d_0 densities in original mesh (i.e. configuration (0) in Figure 6-18) as given in Eq. 6-95 (where all terms are adjoint weighted reaction rates). It has to be kept in mind that a reactivity variation due to density variation is reflected by a variation in the leakage term only (see section 6.4.3.).

$$
\begin{aligned}
\Delta\rho_{expansion} &= \frac{Leakage_0 + Absorption_3 + Generation_3}{Generation_3} - \frac{Leakage_0 + Absorption_0 + Generation_0}{Generation_0} \\[2em]
&= \frac{Leakage_0 + Absorption_2 \dfrac{1}{(1+DENSF \cdot x)} + Generation_2 \dfrac{1}{(1+DENSF \cdot x)}}{Generation_2 \dfrac{1}{(1+DENSF \cdot x)}} - \frac{Leakage_0 + Absorption_0 + Generation_0}{Generation_0} \\[2em]
&= \frac{Leakage_0 + Absorption_2 + Generation_2}{Generation_2} - \frac{Leakage_0 + Absorption_0 + Generation_0}{Generation_0} + \frac{Leakage_0(DENSF \cdot x)}{Generation_2} \\[1em]
&= \Delta\rho_{density\ variation\ of\ x} + \Delta\rho_{dimension\ variation\ of\ x}
\end{aligned}
$$

<div align="right">6-95</div>

The reactivity variation due to expansion is then multiplied by a factor 2 for each cell, the reason being previously explained. For SIMMER Eq. 6-94 becomes Eq. 6-96 since the reactivity component given by the DENSF part is already given by the direct calculation.

$$
d_3 = d_2 \cdot \frac{1}{1 + \dfrac{DENSF}{2} \cdot x}
$$

<div align="right">6-96</div>

In order to take into account the reactivity effect due to expansion in the spatial kinetics part of SIMMER, the effective fission source is modified by the ratio of reactivity variations.

Compared to the approach employed in simple point kinetics models which are based on using a global value of the expansion coefficient, this approach tries to take into account different expansion factors at different spatial locations. In addition, this FOP approach gives information on the actual contribution of a core expansion on the total reactivity since it can be explicitly calculated as a reactivity difference in the new SIMMER development.

Validation of the development

An important assumption that has been made through the use of the DENSF factor is that the expansion effect has no impact on void and Doppler Effect and vice versa. Indeed, the DENSF factor is calculated at the beginning of a simulation which means that one part of the reactivity effect due to expansion is computed at nominal conditions and used during the transient. It becomes therefore important to show that this approach is valid. This is proven in Table 6-20 for the CP-ESFR WH core in case of a cladding driven type expansion (additional tests have been performed for a simplified CP-ESFR model and led to similar conclusions which are omitted here). The calculation has been performed with the ERANOS tool. Core calculations are done with 33 energy groups by employing the BISTRO transport code [159].

Table 6-20. Independence of void, Doppler and expansion effect in a cladding driven type expansion in the CP-ESFR WH core.

	Original non-expanded configuration	Cladding driven expansion	Relative discrepancy (%)
Doppler Constant (pcm)	-1175	-1179	+0.3
Core Void (pcm)	+1351	+1347	-0.3

From Table 6-20 it can be seen that void and Doppler effects practically do not depend on the expansion effect. Therefore the hypothesis of computing DENSF at time zero and using it during the transient is confirmed.

To further validate the DENSF approach, 3 cases are investigated for the CP-ESFR WH core at BOL. The sodium mass is conserved during the first step in the expansion process in Table 6-19 since the distribution of sodium density variation due to expansion is put in the shape calculations. This means that all materials are subjected to the same expansion.

Case 1 consists in setting up the expanded configuration in input which means that increased dimensions and related densities are provided in the SIMMER input and a direct calculation is performed. Case 2 consists in modifying the original SIMMER input by modifying only the densities according to the DENSF method while keeping the original mesh dimensions and performing a direct calculation. Case 3 simply consists in running a SIMMER calculation with the expansion model and obtaining the FOP results.

The results for direct and FOP calculations match very well as is demonstrated in Table 6-21. The highest relative discrepancy is seen for the 1% axial expansion effect calculated with FOP (6 pcm difference corresponding to 11% relative discrepancy).

Table 6-21. Reactivity effects due to axial and/or radial core expansions in the CP-ESFR WH core at BOL – DENSF method.

Radial expansion\axial expansion	Δρ (pcm)			Relative discrepancy Case 1 to Case 2 (%)	Relative discrepancy Case 1 to Case 3 (%)
	Case 1 – direct calculation	Case 2 – direct calculation	Case 3 – FOP		
1.00\1.01	-65	-69	-72	**7.05**	**11.08**
1.00\1.02	-128	-135	-140	**4.99**	**8.90**
1.00\1.05	-315	-310	-322	**-1.60**	**2.07**
1.01\1.00	-321	-313	-325	**-2.36**	**1.28**
1.02\1.00	-645	-627	-650	**-2.80**	**0.85**
1.05\1.00	-1644	-1576	-1635	**-4.13**	**-0.55**
1.01\1.01	-385	-385	/	**-0.19**	**/**
1.02\1.02	-774	-774	/	**0.00**	**/**
1.05\1.05	-1965	-1965	/	**0.00**	**/**
1.01\1.02	-449	-454	-471	**1.03**	**4.80**
1.02\1.01	-710	-703	-729	**-1.05**	**2.64**

It can be noted as well from Table 6-21 that the expansion effect adheres to the linearity and additivity properties as already demonstrated in the simple core model in section 6.4.2.

The same tests are performed in case the sodium mass is not conserved which is usually the case during core thermal expansions as is mentioned in 6.4.1.

Since the coolant does not undergo the same expansion as the solid materials in the core, a new calculation is performed assuming, as a first approximation, a constant density of coolant instead of a constant mass. In fact, as already mentioned, a thermal expansion of core structures generally leads to more sodium flowing into the core (temperatures are kept). Results are depicted in the 2nd column of Table 6-22 and compared to the direct calculation ones. This large discrepancy can be explained by the fact that sodium behaves differently from the other materials (fuel, steel) in the cell. This leads to an uncertainty as concerns the reactivity contribution due to scattering in addition to the one due to leakage. The factor 2 previously added is hence not accurate anymore if the sodium is expanded in a different way as the other materials as was already indicated in section 6.4.1.

To overcome this issue, the differential expansion effect coming from sodium is put in the spatial kinetics part of SIMMER. This means that the distribution of sodium variation due to expansion is taken care of in the spatial kinetics instead of the "point kinetics" part of SIMMER. This idea is based on the fact that for expansions where all materials including sodium are subjected to the same expansion, the methodology provides good results.

The cross-sections of sodium in the original core are therefore modified in order to shift the spatial distribution of the sodium contribution to the expansion reactivity into the cross-section and shape calculation of SIMMER. Results for the new sodium treatment are shown in the 3rd column of Table 6-22. A significant improvement of the results is noted.

For a better understanding, the effect of expanding all materials by the same factor and the effect of the sodium distribution are both presented in Table 6-23. It can be seen that they add up to the total expansion effect where sodium is not subjected to the same expansion as the other materials.

It is hence concluded from Table 6-22 that the sodium has to undergo the previously described special treatment if FOP is used for thermal expansion feedback considerations in order to obtain similar results as in the direct calculations. The previously described verifications prove that the DENSF method provides accurate results in case of an overall and uniform expansion of the whole neutronic mesh.

To consider as well non-uniformities along one dimension in the core expansion, a regional approach is applied, based on the previously described model.

Table 6-22. Reactivity effects due to axial and/or radial core expansions in the CP-ESFR WH core at BOL if the sodium mass is increased – with and without special treatment for the sodium cross-section.

Radial expansion\axial expansion	Δρ direct (pcm)	Δρ FOP (pcm), original method	Δρ FOP (pcm)	Relative discrepancy Δρ FOP original method to Δρ direct (%)	Relative discrepancy Δρ FOP to Δρ direct (%)
1.00\1.00	/	/	/	/	/
1.00\1.01	-84	-124	-72	48	-14
1.00\1.02	-164	-245	-140	49	-15
1.00\1.05	-385	-586	-322	52	-16
1.01\1.00	-342	-429	-324	26	-5
1.02\1.00	-684	-860	-649	26	-5
1.05\1.00	-1712	-2164	-1623	26	-5
1.01\1.01	-429	-558	-399	30	-7
1.02\1.02	-861	-1123	-801	30	-7
1.05\1.05	-2180	-2861	-2020	31	-7
1.01\1.02	-513	-683	-470	33	-8
1.02\1.01	-774	-993	-726	28	-6

Table 6-23. Decomposition of the reactivity effects due to axial and/or radial core expansions in the CP-ESFR WH core at BOL into its uniform and non-uniform components.

Radial expansion\axial expansion	Δρ direct (pcm)		
	Effect due to the uniform expansion of all materials (pcm)	Effect due to the non-uniform sodium expansion (pcm)	Total (pcm)
1.00\1.00	/	/	/
1.00\1.01	-69	-14	-83
1.00\1.02	-135	-29	-164
1.00\1.05	-311	-72	-383
1.01\1.00	-313	-29	-342
1.02\1.00	-626	-59	-685
1.05\1.00	-1567	-148	-1715
1.01\1.01	-386	-43	-429
1.02\1.02	-772	-89	-861
1.05\1.05	-1952	-228	-2180
1.01\1.02	-454	-59	-513
1.02\1.01	-701	-74	-775
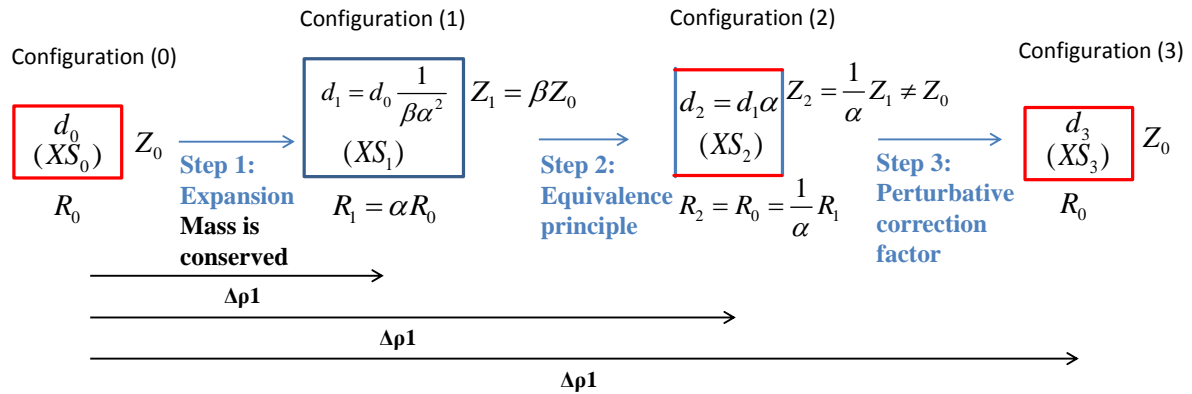
Figure 6-18 – Schematics of the DENSF method for expansion feedback considerations [144].

6.5.3. Non-Uniform expansions in 1D: the DENSFR Method

The previously described method serves as a basis for further improvements. Relying on the fact that cores present a radial power (and neutron importance) distribution and thus attribute a different weight to the expansion reactivity from each ring, the methodology described earlier was improved to consider radially dependent computed DENSF factors to take approximately into account the non-uniformity.

This treatment differs from the previous one due to the use of radially dependent (ringwise) DENSFR coefficients instead of a radially independent one (DENSF). The overview of the method called DENSFR method is given in Table 6-24 and the modified steps are highlighted in red.

Step 1 in Table 6-24 i.e. computing expanded dimensions and densities remains the same as in the previous method. The second step in Table 6-19 has been modified: instead of obtaining an equivalent system with original radial dimensions – as it is the case in the DENSF method – a system with original axial dimensions but transformed radial dimensions (usually smaller than the original ones) is sought for convenience due to SIMMER constraints. The third step in Table 6-19 is consequently modified and the contribution of each ring to the overall expansion reactivity is evaluated. For each ring, the reactivity effect due to the *radial* dimensional change of that ring is computed by direct calculation. This is performed by reducing all rings' radial size by 1% and by performing a direct calculation. This gives the effect of an overall reduction of the radial core mesh. A similar case is then considered: all rings but the first one are reduced in their radial size by 1%. Again a direct calculation is performed. The effect of the first ring can then be determined by comparing the two cases. The same approach is used to obtain the effect of the second ring. First all rings see their radial dimensions changed. Then the effect of radial dimensional decrease of all rings but the first two rings is calculated. The effect of the first ring is then subtracted. In the end, the effect of a radial dimensional reduction of any ring can be obtained for each ring by using Eq. 6-97, assuming as usual linearity and additivity.

$$\Delta \rho_n = \Delta \rho_{1...N} - \overline{\Delta \rho_{1...n}} - \sum_{i=1}^{n-1} \Delta \rho_i \qquad \text{6-97}$$

- $\Delta\rho_n$ is the reactivity effect of 1% radial dimensional decrease of ring n

- $\Delta\rho_{1...N}$ is the reactivity effect of 1% radial dimensional decrease of all rings, N being the total number of rings

- $\overline{\Delta\rho_n} = \Delta\rho_{1...N} - \Delta\rho_n$ is the reactivity effect of 1% radial dimensional decrease of all rings except ring n

- $\overline{\Delta\rho_{1...n}} = \overline{\Delta\rho_n} - \sum_{i=1}^{n-1}\Delta\rho_i$ is the reactivity effect of 1% radial dimensional decrease of all rings except rings 1 to n.

It has to be mentioned that $\Delta\rho_n$ does not represent the expansion effect of ring n solely but considers the influence of all other rings on ring n as well.

Once the effect of the individual dimensional change of each ring is known, the DENSF factor for each ring (called DENSFR) is calculated using Eq. 6-98.

$$DENSFR(n) = \frac{\Delta\rho^{direct}_{1\% \text{ radial dimension variation in ring n}}}{\Delta\rho^{FOP}_{1\% \text{ density variation in ring n}}} \qquad \textbf{6-98}$$

The final densities to be used in the original mesh – i.e. configuration (3) in Figure 6-18 are then obtained by Eq. 6-99.

$$d_3 = d_2 \cdot \frac{1}{1 - \frac{DENSFR(n)}{2} \cdot y} \qquad \textbf{6-99}$$

where $y = \frac{\Delta R_{2,i,j} - \Delta R_{0,i,j}}{\Delta R_{0,i,j}}$ represents the radial expansion percentage of the equivalent cell.

The calculation is then performed with the original meshing but with modified densities d_3 and the procedure continues as in case of the previous model. It is interesting to note that in case of a purely axial expansion, $d_2 = d_0$ and therefore the effect of expansion is exactly the effect of a dimensional change, calculated by the direct approach.

Table 6-24. Overall methodology of the DENSFR expansion model. Modified steps are highlighted in red.

Steps	Task	Methodology	Goal
Step 1 : Theoretical expansion of the cell	Calculate expanded axial dimensions	Based on: **Fuel temperature** if gap is open **Clad temperature** if gap is closed	Describe the expanded cell and the associated reactivity state
	Calculate expanded radial dimensions	Two modes can be considered: **Conic mode:** based on temperatures of diagrid and constraint plate **Cylindrical mode:** Based on temperatures of diagrid	
	Calculate related macroscopic densities	**Non-coolant materials:** Mass conservation **Coolant:** Density conservation	
Step 2 : Apply the equivalence model	Obtain original axial dimensions, modified radial dimensions, equivalent densities	X	Keep the reactivity state of the expanded cell while using original axial and modified radial dimensions
Step 3: Density correction factor	Obtain effect of radial dimensional changes	Based on each individual ring variation	Account for the discrepancy between original radial dimensions and modified radial dimensions and find effective densities.
Step 4: compute expansion effect	Use effective densities and original densities in original mesh	X	Obtain the expansion effect while using original mesh

Validation of the methodology

To validate the methodology, the simple core model detailed earlier has been considered for the tests. The sodium mass has been conserved during the expansion.

Several cases have been calculated with SIMMER and ERANOS for comparison. As the expansion effect is composed of a dimensional and a density effect, and, as the dimensional effect is computed through the direct calculation at the start of the calculation and is therefore assumed to be correct, the density effect (computed via FOP calculations) has been checked. Several configurations have been tested as can be seen in Table 6-25.

Table 6-25. Considered test cases for checking the density effect with direct and FOP methods.

	Density change				Zones for the density change	
	Central fuel ring	Outermost fuel ring	All fuel rings	Na around fissile core	Fissile core height	Whole neutronic mesh height
Case 1	X				X	
Case 1b	X					X
Case 2		X			X	
Case 2b		X				X
Case 3			X		X	
Case 3b			X			X
Case 4				X	/	/

In this section, only cases 3, 3b and 4 will be discussed. For more details on the other cases see Appendix C.

ERANOS calculations are performed with the BISTRO solver and integrals of angular fluxes are used for the PT based calculations. Both FOP and exact PT are used. A direct calculation is performed as well for reference. Cases with 1, 11 (to cross-check the SIMMER results) and 33 energy groups are used. The model is an RZ one. SIMMER calculations are performed with the standard 11 energy groups or with 1 energy group using the cross-section collapsing method developed at KIT [163]. Absolute values of BISTRO and SIMMER results are not directly comparable.

In all cases, the densities in the considered zones are modified by a factor $\frac{1}{1.01^2}$ to simulate a density variation obtained by a 1% radial expansion. At first, the fissile core zone densities are modified as shown in Figure 6-19 (a). Results are shown in Table 6-26.

Table 6-26. Density effect for a density variation in the fissile core zone of $\frac{1}{1.01^2}$. Comparison of SIMMER and ERANOS for direct and FOP calculations.

Energy groups	Tool	Calculation type	Reactivity effect (pcm)	Relative discrepancy to direct calculation (%)
1	BISTRO	FOP	-314	**-2**
		Exact PT	-321	**0**
		Direct	-321	/
	SIMMER	FOP	-241	**-31**
		Direct	-349	/
33	BISTRO	FOP	-296	**-2**
		Exact PT	-302	**0**
		Direct	-302	/
11	SIMMER	FOP	-209	**-29**
		Direct	-294	/
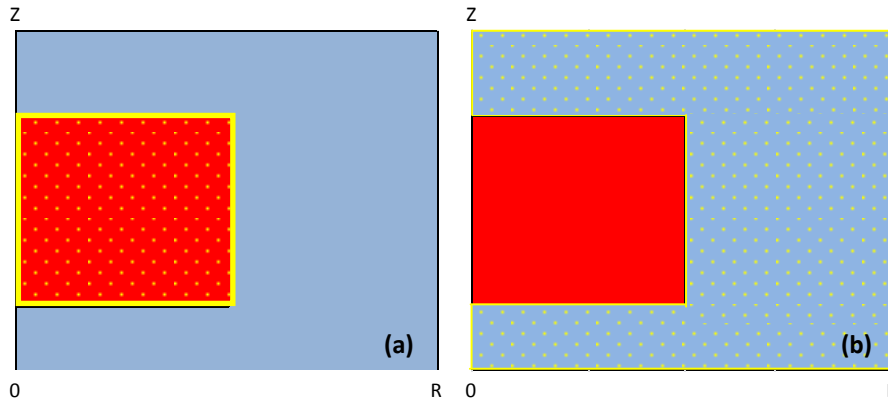
Figure 6-19. (a) Fissile zone considered for the expansion (b) Surrounding sodium is expanded.

If the BISTRO solver is used, results for direct, FOP and exact PT agree within 2% whether 1 energy group or 33 energy groups are considered. One can notice as well that SIMMER and BISTRO give similar results for the direct calculation. In case of SIMMER, even with the factor 2 already included, discrepancies as large as 31% can be observed between direct and FOP calculations, both if considering 1 or 11 energy groups. This can be ascribed to the way the FOP reactivities are computed in SIMMER. In fact, integrals of angular flux shapes and adjoint fluxes – i.e. scalar fluxes - are used for reactivity calculation [151]. To confirm this tendency, the same test has been performed for 1 energy group for the case of sodium surrounding the fissile core part as seen in Figure 6-19(b). Results of the calculation can be seen in Table 6-27.

Table 6-27. Density effect for a density variation in the sodium surrounding the fissile core zone of $\dfrac{1}{1.01^2}$. Comparison of SIMMER and ERANOS for direct and FOP calculations.

Energy groups	Tool	Calculation type	Reactivity effect (pcm)	Relative discrepancy to direct calculation (%)
1	BISTRO	FOP	-102	-1
		Exact PT	-103	0
		Direct	-103	/
	SIMMER	FOP	+26	-129
		Direct	-90	/

Also in this case BISTRO gives precise results both with FOP and exact PT when compared to direct calculations. This was expected as small perturbations are considered. SIMMER results show the same tendency as before, confirming that the way SIMMER performs FOP reactivity calculations leads to results which do not match the direct calculation even with the application of the factor 2. The reason for this discrepancy comes from the fact that the scalar adjoint flux and scalar direct flux for the unperturbed configuration are used to obtain the reactivity effect due to expansion.

Case 3b is then considered i.e. all the neutronic meshes see their density changed except the followers (Table 6-28).

Table 6-28. Density effect for a density variation in the overall neutronic mesh of $\dfrac{1}{1.01^2}$. Comparison of SIMMER and ERANOS for direct and FOP calculations.

Energy groups	Tool	Calculation type	Reactivity effect (pcm)	Relative discrepancy to direct calculation (%)
1	BISTRO	FOP	-416	-3
		Exact PT	-428	0
		Direct	-428	/
	SIMMER	FOP	-455	+3
		Direct	-442	/

It can be concluded that in this case, the factor 2 is sufficient to compensate the underestimation of FOP results compared to direct ones, showing only 3% relative discrepancy. This is due to the fact that the angular and spectral flux distribution shift occurs in the same way over the whole domain. If the sodium density in the followers is modified as well, the relative discrepancy reduces to 1.3% in case of SIMMER using 1 energy group for the calculation.

In conclusion, if the whole system is expanded in the same way, the factor 2 is applicable. In all other cases, because of the way SIMMER computes the reactivity component due to leakage the methodology seems to predict approximate results. The regional approach is a trial approach and possible uncertainties with this methodology have been described earlier. However, this methodology is of interest if one wants to exploit the full potential of SIMMER.

Another option, as mentioned earlier, is to consider the expansion effect in the spatial kinetics part instead of the point kinetic one – the treatment is then similar to the one already described for the sodium component. A new method is thus developed to take into account the reactivity effect due to expansion in the direct calculation instead of the FOP calculation. Nevertheless, this methodology does not allow the user to have knowledge of the value of reactivity due to expansion. Indeed, the effect is hidden in the overall reactivity variation (due to Doppler, sodium density variation, etc.). Recent improvements should allow to acquire knowledge of the value of the effect [164].

6.5.4. Further modeling development

The two previously developed methodologies provide accurate results in case of uniform expansions within one direction. However, when considering non-uniform expansions (even for only one direction), the accuracy and reliability of the methods becomes less satisfying. Hence the development of a third methodology has been started [165].

Once the configuration of a pseudo axial expansion is reached i.e. step 1 and step 2 in Table 6-19 are performed as in the DENSF method, the reactivity effect contributions for each ring due to its uniform axial expansion is computed on the basis of pre-computed values (for 1% axial expansion using the fact that the effect of an expansion has been proven to be linear). The effect of a uniform axial expansion of each radial mesh is then known.

To take into account the effect of non-uniform axial expansions inside one radial mesh a factor ε is applied. The way to calculate ε is the following: let δ be the axial expansion factor corresponding to the total increase of the neutronic domain height within one radial mesh and μ be the factor applied to the original densities to obtain the densities of the pseudo axially expanded cell configuration (i.e. configuration (2) in Figure 6-18).

The effect of a non-uniform axial expansion within one radial mesh is then taken into account by modifying the densities of the non-expanded configuration (configuration (0) in Figure 6-18) by the factor ε (Eq. 6-100), each axial zone having its own factor.

$$\varepsilon = \frac{1}{\delta} \cdot \frac{1}{\mu}$$

<div style="text-align: right">6-100</div>

Note that SIMMER conventionally re-computes material densities and thus cross-sections and reactivity (less frequently the neutron flux) during the transient. For the DENSF and DENSFR expansion treatment described earlier, the conventional procedure for re-computing the mentioned parameters has not been modified except for the coolant. The reactivity effect due to expansion is used for correcting the "conventional" SIMMER reactivity and for rescaling neutron generation cross-sections employed in neutron transport calculations. The value used for reactivity correction was printed and analyzed, which facilitated the development of the method. According to the new treatment, the difference in reactivity effects due to the non-uniform and corresponding uniform expansions is taken into account by modifying the densities used for conventional cross-section and reactivity calculations, while the reactivity effect due to the uniform expansion is used for the reactivity correction and cross-section rescaling. The value used for the reactivity correction no longer represents the "full" expansion effect. An effort should be devoted during post-processing to evaluate the full "non-uniform" effect, which is now assumed to be computed accurately. Results for proving this assumption are detailed in [165] and are recalled hereafter.

Preliminary checks of the improved methodology are performed with the CP-ESFR WH core. A 2D (RZ) model at BOL is considered. The effects are calculated while considering basically 2 radial zones i.e. the inner and the outer core and 4 axial zones for expansion (Figure 6-20). The followers are not expanded.
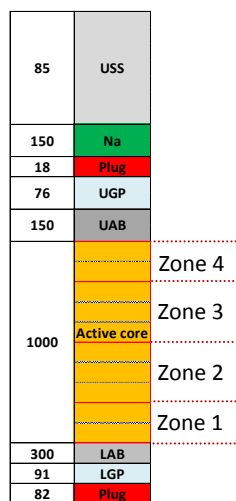
Figure 6-20. Schematics of the axial layout of the CP-ESFR WH core. Red frames represent the 4 axial zones considered for expansion. LAB = Lower Axial Blanket, UAB = Upper Axial Blanket, LGP = Lower Gas Plenum, UGP = Upper Gas Plenum, USS = Upper Steel Structure.

The ERANOS code is used to set up the model for checking the methodology and driving the development of SIMMER. Core calculations are performed for 33 energy groups by employing the BISTRO transport code. Effective neutron cross-sections are computed by the ECCO code [158], while employing the JEFF3.1 reference nuclear data library [166].

The methodology is applied after Step 1 and Step 2 in Table 6-19. First, reference cases are calculated (i.e. real expanded cases in input). Based on the temperature distribution given by SIMMER, the two earlier mentioned simplified expansion modes – clad driven and fuel driven expansion - are considered for the CP-ESFR WH core. The clad driven expansion has been stressed to ensure a large perturbation. The fuel driven expansion values have been used to simulate a small perturbation. All materials, coolant included, are expanded in the same way. The two considered core models are shown in Figure 6-21. The effect of these expansions, calculated by ERANOS is -292.6 pcm for the clad driven and -97.6 pcm for the fuel driven expansion.

(a)   (b)
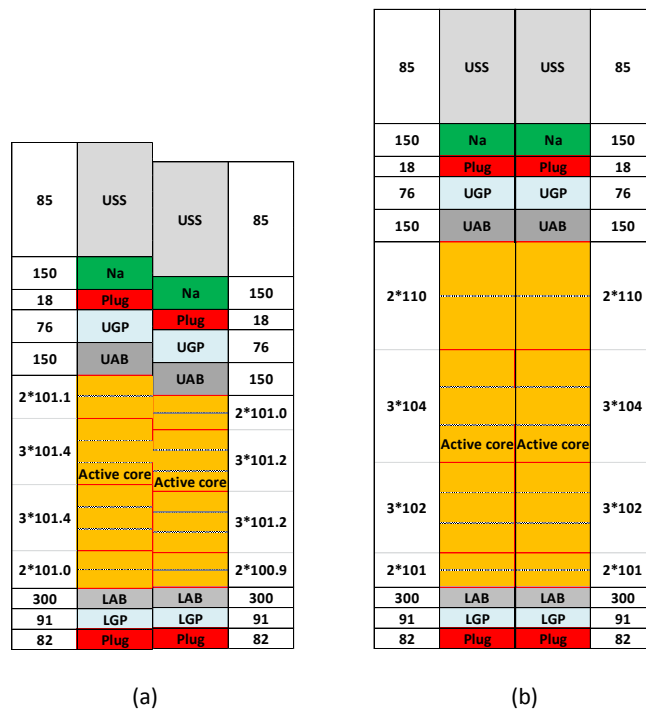
Figure 6-21. Axial layout of axially expanded configurations, dimensions are given in mm. (a) Fuel driven expansion, step core with 12.6 mm overall axial expansion for the inner core and 10.9 mm overall axial expansion for the outer core. (b) Clad driven expansion (large perturbation) 40 mm overall expansion for both inner and outer core [165].

The previously calculated values serve as a reference for comparison with the results obtained with the new technique. As mentioned earlier, the technique evaluates the expansion effect first by calculating the effect of a uniform axial expansion within one radial mesh and second by taking into account the effect of non-uniformity.

At first the uniform expansion effect is calculated. To that end, a layer of 1 cm (mesh) is added above all materials zones (fissile height, UAB, UGP etc.) to take into account a 1% axial expansion of the fissile height of the core. This means that the total height of fissile material is 1.01 m.

The calculations are performed for the expansion of the inner core only, the outer core only or both the inner and the outer core simultaneously (Table 6-29). It can be noticed that the expansion effects

of both cores are additive. As in SIMMER the overall neutronic mesh is fixed (Eulerian grid), some material is lost at the top zone (e.g. the upper core structure) when an expansion is performed by shifting the parts above the expanded zone. Nevertheless, the effect of losing this material from the neutronic mesh is negligible as seen in Table 6-29.

Table 6-29. Reactivity effects of 1% axial uniform expansion in the CP-ESFR WH core, BOL.

1% uniform axial expansion of the fissile height	Δρ (pcm)	
	Reduced upper steel structure	Additional node of void
Inner core expanded	-14.4	-14.4
Outer core expanded	-68.4	-68.4
Sum	-82.8	-82.8
Both inner and outer core expanded	-82.9	-82.9

In case of the fuel driven expansion, the inner core expands by 1.26 cm corresponding to a 1.26% uniform axial expansion and the outer one by 1.09 cm corresponding to a 1.09% uniform expansion. By applying the proven assumption that the effect is linear and additive, the effect of the inner core uniform expansion is then -18.1 pcm (i.e. -14.4 * 1.26) and the one of the outer core is -74.5 pcm (i.e. -68.4 * 1.09), the sum of both being -92.6 pcm.

In case of the clad driven expansion, both the inner and the outer core expand by 4%. The overall effect is then of -331.6 pcm (i.e. 4*-82.9). It is worth mentioning that the uniform expansion effect constitutes the main part of the expansion effect (comparison with reference values).

In order to take into account the non-uniform expansion along the Z axis of each radial zone a pseudo distribution of densities is calculated by applying factors determined with Eq. 6-85 and shown in Table 6-30.

Table 6-30. Coefficients to apply to original densities in the fissile zone to take into account non-uniform expansions, determined with Eq. 6-85.

	Factor to apply to original densities to put non-uniform expansion component into the densities		
	Small perturbation		Large perturbation
	inner core	outer core	inner and outer core
Zone 1	0.9973	0.9975	0.9712
Zone 2	1.0011	1.0007	0.9808
Zone 3	1.0017	1.0014	1.0000
Zone 4	0.9984	0.9991	1.0577

These coefficients are applied to the original densities and therefore for each mesh for cross-sections calculations in ERANOS.

In case of a small perturbation, one obtains an effect of +2.9 pcm due to the axial distribution of expansions. In case of a large perturbation one obtains -37.3 pcm.

By subtracting the non-uniform expansion values from the uniform expansion ones calculated earlier, one obtains values close to the real expanded ones with a discrepancy of less than 3% – a summary is given in Table 6-31.

This new treatment takes into account correctly non-uniform expansions, as checked with the ERANOS code. Preliminary results for the fissile core expansion showed good agreement with reference calculations (within 3% relative discrepancy). The same procedure is intended to be employed for other parts of the reactor (e.g. sodium plenum, axial fertile blanket) but additional analyses are necessary for these aspects in the future. The methodology should be implemented into SIMMER and validated for different reactor designs as e.g. the CONF2 core design or cores with an internal axial fertile blanket.

Table 6-31. Summary of reactivity effects of fuel driven (small perturbation) or clad driven (large perturbation) expansions

	$\Delta\rho$ (pcm)			
	Fuel driven expansion			Clad driven expansion
	inner core	outer core	Sum	inner and outer core
Uniform expansion (scaling)	-18.1	-74.5	-92.6	-331.4
Effect of axial distribution of expansion (direct calculation)	/	/	+2.9	-37.3
Total	/	/	**-95.5**	**-294.1**
Real expansion (direct calculation)	/	/	**-97.6**	**-292.6**

6.5.5. Application of the methodology to transient simulations

The expansion methods based on FOP (DENSF and DENSFR) have been tested in the SIMMER framework. While their application to a uniform and overall expansion of the neutronic mesh gives accurate results if compared to reference calculations, their application to non-uniform expansions of sub-domains of the neutronic mesh seems less accurate. Thus a new methodology avoiding the computation of expansion reactivities with FOP has been set up and preliminary tests have been performed with the ERANOS code. First results are considered to be reasonably accurate and an implementation of this method in SIMMER and further testing is planned in the near future but is out of the scope of this thesis.

The DENSF methodology has been applied to transient cases in addition to the static cases. The CP-ESFR WH core at equilibrium is loaded with pellet fuel and an axial expansion case is considered. An unprotected loss of flow with a flow halving time of 10 s is considered. Both the clad driven and the fuel driven axial expansion are considered. When applying the expansion model a delay in the power excursion can be observed – Figure 6-22. The largest delay is seen for the fuel-driven case as fuel temperatures are very high and the related expansion is thus increased compared to the cladding expansion; as expected. In addition, the expansion reactivity driven by the fuel expansion has been calculated to be -330 pcm which is in agreement with results provided by the SAS4A code in the CP-ESFR project [35].
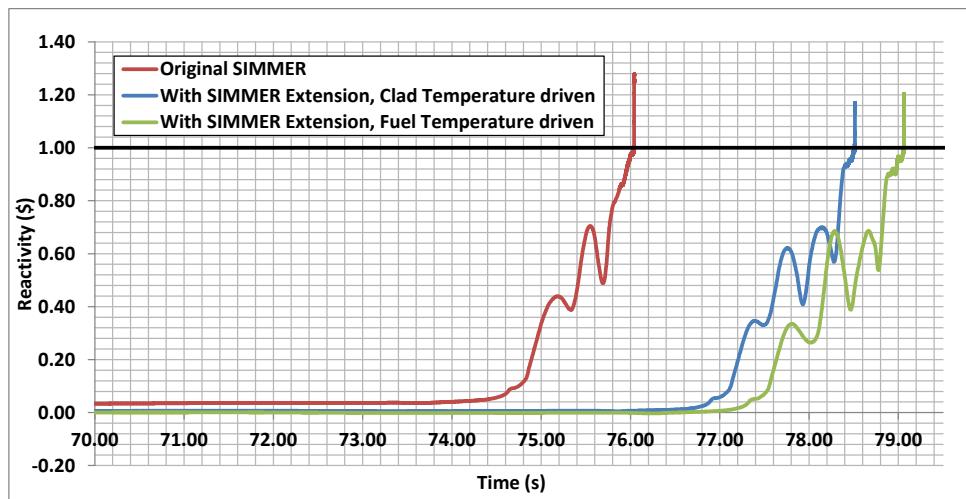
Figure 6-22. ULOF evolution in the CP-ESFR WH core at equilibrium, with and without expansion treatment.

An additional application of the method has been performed for the CONF2 core loaded with sphere-pac fuels and is detailed in Chapter 8. Recently, the methodology has been successfully applied to an ANL benchmark on EBR-II (details can be found in Appendix I).

6.6. Conclusions

Several innovative methodologies have been developed to take into account the core expansion reactivity effects in space-time kinetic codes like the SIMMER codes. The methodologies are all based on the equivalence principle and implementation of one or more density correction factors. Two out of the three methodologies are based on FOP. While the results in case of a uniform and overall mesh expansion agree well with the reference calculations, limitations of the FOP methodologies have been pointed out in case of non-uniform expansions of sub-domains of the neutronic mesh. This shortcoming has led to the development of a third method, avoiding the employment of FOP for expansion reactivity calculations. This last methodology shows promising results in the ERANOS framework and has still to be implemented in SIMMER. Preliminary results for the CP-ESFR WH core showed that the described methodologies based on the equivalence principle and FOP agree nevertheless well with other codes like the SAS4A code.

Chapter 7

A NEW FEATURE FOR SIMMER-III: CONSIDERATIONS FOR INNOVATIVE SPHERE-PAC FUELS

As mentioned in Chapter 1, an important aspect of the present PhD work is the adaptation of SIMMER to sphere-pac fuel specificities. The FP7-PELGRIMM project deals inter alia with the safety assessment of sphere-pac fuels loaded in SFRs. Calculations in the project are performed with several codes. Some pay mainly attention on the initiation phase of the accident, as e.g. SAS4A [71], BELLA [167] and the MAT5DYN code [168], others like the SIMMER-III code [73] could deal with the initiation phase but also deal with later accident phases and a potential whole core melting. All codes have to be adapted within their framework to the specificities of sphere-pac fuels. Important differences to the standard pellet fuel are e.g. the thermal conductivity, the fuel macrostructure i.e. the microspheres instead of pellets, the non-existence of an initial fuel-cladding gap and the fuel one column structure.

A first step toward the feasibility and safety performance assessment of sphere-pac fuels is to quantify the heat transfer in these pins. A key parameter here is the maximum achievable packing fraction of spheres and the related porosity as they finally define the fuel thermal conductivity. It was demonstrated in [137] that smear densities as high as 95% of the theoretical density (TD) could be obtained by packing spheres of different sizes. First, investigations have been started to assess the needed fuel density if one does not want to drastically change the CP-ESFR core design. With the high achievable packing density the fuel mass is kept equal using sphere-pac fuels instead of pellet fuels which is important for the core neutronics. Once this had been set, an adequate model for the thermal conductivity of sphere-pac fuels had to be incorporated. This chapter provides an overview of heat transfer models in SIMMER as well as of the existing correlations in literature for both pellet and sphere-pac fuels conductivity. Finally their adaptation and implementation into the SIMMER framework is described.

7.1. SIMMER-III structure model

In the SIMMER-III and SIMMER-IV severe accident codes two pin models - the simple SPIN and the more elaborate DPIN model - are available. As already mentioned previously, SIMMER-III was

primarily developed to evaluate the behavior of already disrupted reactor cores where most pins already failed. Therefore the simplified fuel-pin model (SPIN) was originally implemented [169].

The detailed pin model (DPIN) was added later to simulate more accurately the radial heat transfer in the fuel e.g. in a less degraded situation as well as potential molten cavity generation and within-pin fuel motion of still existing pin structures [73]. Both models are described in this section. These models have been validated to a certain extent on the basis of CABRI and SCARABEE-N experiments [78; 170] but are still of simple nature compared to fuel performance codes as GERMINAL [127]. As the SIMMER codes are transient codes, mostly covering the accident phases where the pins are already destroyed, the existing models are essentially sufficient. In addition, as the whole core is described in these transient codes and thousands of time-steps are calculated, the implemented fuel pin model must also be time efficient.

7.1.1. Simplified PIN model: SPIN

The SIMMER-III code can be run with the standard Simplified PIN model (SPIN). In this model, two nodes are used to calculate temperatures in the fuel. These nodes are defined as inner (bulk) and surface fuel zones and are calculated as in Figure 7-1 [169].

$$r_{pin} = r_{p6} = r_{pin}^i \cdot \sqrt{\frac{\alpha_{pin}}{\alpha_{pin}^i}} \qquad r_{p4} = r_{pin} \cdot \sqrt{\frac{\alpha_{int} + \alpha_{s1} + \alpha_{nf,pin} + \alpha_{s4}}{\alpha_{pin}}} \qquad r_{p3} = r_{pin} \cdot \sqrt{\frac{\alpha_{int} + \alpha_{s1}}{\alpha_{pin}}}$$

$$r_{p1} = r_{p3} - 2\delta_f \qquad r_{p5} = \sqrt{\frac{r_{p4}^2 + r_{p6}^2}{2}} \qquad r_{p2} = \sqrt{\frac{r_{p1}^2 + r_{p3}^2}{2}} \qquad r_{p0} = \frac{r_{p1}}{\sqrt{2}}$$
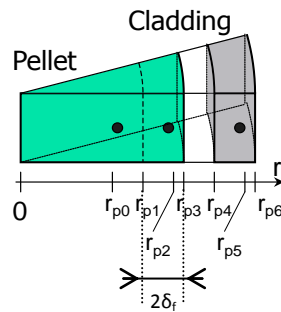
Figure 7-1. Radii calculation for the SIMMER-III pin modeling with SPIN [169].

In Figure 7-1 all variables with the index i are initial values, α_{int} and α_{s1} refer to volume fraction of fuel interior and fuel surface, respectively, α_{s4} is the cladding volume fraction, $\alpha_{nf,pin}$ is the non-flow volume fraction of the pin i.e. of the gap.

The thickness of the pin fuel surface node is defined with the thermal penetration length, considering the transient thermal response of the surface nodes. Therefore the boundary between inner and surface fuel zones (r_{p1}) depends on $2\delta_f$ – Figure 7-1. Once r_{p1} is known, it is used to define the

position of the fuel temperature nodes r_{p0} and r_{p2}. These radii are then used to calculate the heat transfer coefficients between the two fuel zones (Eq. 7-1) and from the surface fuel zone to the cladding – represented by one node (Eq. 7-2):

$$h_{\text{int},S1} = \frac{1}{r_{p1}} \left(\frac{1}{k_{\text{int}}} \ln\left(\frac{r_{p1}}{r_{p0}} \right) + \frac{1}{k_{S1}} \ln\left(\frac{r_{p2}}{r_{p1}} \right) \right)^{-1} \tag{7-1}$$

$$h_{S1,S4} = \left(\frac{r_{p3}}{k_{S1}} \ln\left(\frac{r_{p3}}{r_{p2}} \right) + \frac{1}{h_{gap}} + \frac{r_{p4}}{k_{S4}} \ln\left(\frac{r_{p5}}{r_{p4}} \right) \right)^{-1} \tag{7-2}$$

where the subscript S1 stands for the fuel surface, S4 for cladding, *int* for fuel interior, *k* for thermal conductivity and h_{gap} for the gap heat transfer coefficient.

These heat transfer coefficients are then used to calculate the fuel pin heat transfer. By adding the nuclear heat, average temperatures can be deduced through an implicit scheme by solving the energy conservation equation (Eq. 7-3):

$$\frac{\partial \overline{\rho_m e_m}}{\partial t} = h_{m,m-1} \cdot a_{m,m-1} \cdot (T_{m-1} - T_m) + h_{m+1,m} \cdot a_{m+1,m} \cdot (T_{m+1} - T_m) + Q_{Hm} + Q_{Nm} \tag{7-3}$$

where the subscript m denotes one of the three temperature nodes i.e. inner fuel, surface fuel or cladding temperature node. $\overline{\rho_m}$ and e_m are the macroscopic density and specific energy of fuel node m respectively, h stands for the heat transfer coefficient, a is an area per unit volume and Q_{Hm} and Q_{Nm} denote the energy transfer rates due to heat transfer from fluid and nuclear heating, respectively.

The energy conservation equations of gas in the gas plenum and of control material are solved through an explicit scheme due to the inertia of the heat response [169].

- **General aspects of the SPIN model**

The SPIN model does not allow simulating a detailed temperature profile. Thus, no maximum fuel temperature can be determined as observed at or close to the pin centerline. In addition, neither a cavity of molten material nor its motion inside the pin after failure can be modeled. Nonetheless the fuel pin failure is modeled based on a thermal criterion depending on melting fractions of fuel and cladding. A parametric model is available for simulating mechanical pin failure. Once the limit values of the melt fractions are exceeded, the molten part of the pellets is transferred into the liquid fuel field while the still solid fuel part is transferred into the chunks (representing large fuel pieces going up to pellet size) and particle field (molten fuel that has solidified again). The cladding can even fail earlier than the fuel in some cases. The region thus becomes available for material movement. Fission gas is released from liquid fuel instantaneously and from chunk fuel with a time-constant. Progressive release of gas from the fuel chunks can be simulated as well. Pin breakup modeling includes the downfall or collapse of unsupported pellets [169]. Both the SPIN model and the DPIN model allow the blow-down of fission gas from the gas plena after pin failure. This is an important

effect impacting the voiding of the core and the cooling of pins. In SPIN the inner node represents most of the fuel mass and describes the average fuel temperature. The fission gas pressure as well as the fuel ejection driving force are therefore underestimated.

SPIN provides correct information for core disruptive accident (CDA) sequences less sensitive to a precise fuel modeling as e.g. transients where clad melting occurs in advance of fuel melting. This is the case in the blockage accident and to a certain extent also in loss of flow accidents. It can be attributed to the thermal inertia of the pellet interior in a voided channel condition. TOP (transient over power) accident simulations, especially for mild overpower transients, need however a more refined description – the DPIN model. This model is detailed in section 7.1.2.

-   **Hole treatment with SPIN**

The SPIN model of SIMMER is incapable of explicitly simulating the central hole usually present in the new fast reactor (FR) pellet designs. A methodology was therefore developed for SIMMER, during the CP-ESFR project, to take implicitly into account the central hole for the heat transfer [35] and is detailed hereafter.

The methodology is based on adjusting the thermal conductivity coefficients to obtain correct fuel temperatures. At first a mass equivalence equation is written – Eq. 7-4 and 7-5.

$$m_{real}^{fuel} = m_{simmer}^{fuel} \qquad \text{7-4}$$

$$\left(1 - p_{real}\right)\left(R_f^2 - R_i^2\right)\pi = \left(1 - p_{sim}\right)R_f^2\pi, \qquad \text{7-5}$$

where R_f is the outer radius of fuel, R_i the inner radius of the fuel i.e. the radius of the hole, p_{real} the real fuel porosity and p_{sim} the modified porosity given to SIMMER as input and m is the mass. By applying this Eq. 7-5, an annular pellet can be treated as a full one by modification of the fuel porosity Eq. 7-6.

$$p_{sim} = p_{real} + \left(\frac{R_i}{R_f}\right)^2\left(1 - p_{real}\right) \qquad \text{7-6}$$

The fuel thermal conductivity dependence on porosity can be expressed either by the Maxwell-Eucken [171–173] or by the Harding et al. [174] correction – Eq. 7-7 and 7-8, respectively.

$$k_p = k_o \frac{1 - p_{real}}{1 + 2p_{real}} \qquad \text{7-7}$$

$$k_p = k_o\left(1 - p_{real}\right)^{2.5} \qquad \text{7-8}$$

Where k_o is the thermal conductivity of a fully dense fuel and k_p the one which takes into account the porosity of the material.

In SIMMER, according to the chosen option, porosity can be evaluated as Eq. 7-9.

$$k_{p\,sim} = k_{o\,sim} \left(1 - p_{sim}\right)^{2.5}.$$

7-9

In order to reflect the real thermal conductivity, k_p, the input value of fuel thermal conductivity for fully dense fuel has to be modified in order to take into account the modification associated to porosity – Eq. 7.10,

$$k_{o\,sim} = k_o \left(1 - p_{real}\right)^{2.5} \Big/ \left(1 - p_{sim}\right)^{2.5},$$

7-10

so that $k_{p\,sim} = k_p$.

In addition, the solution of the fuel thermal conduction equation is considered. The details are omitted here and the solution is given in Eq. 7-11:

$$4\pi \int_{T_s}^{T_i} k_p(T)dT = \chi \left(1 + 2\frac{R_i^2}{R_f^2 - R_i^2} \ln \frac{R_i}{R_f}\right)$$

7-11

where T_s and T_i are the fuel surface and center temperatures, $k_p(T)$ the fuel thermal conductivity that is a function of temperature and χ the linear power rating. If we define a variable K as in Eq. 7-12:

$$K(R_i, R_f) = \left(1 + 2\frac{R_i^2}{R_f^2 - R_i^2} \ln \frac{R_i}{R_f}\right)$$

7-12

To take into account the hole with the SPIN model, the original thermal conductivity has to be modified according to Eq. 7-13.

$$k_{sim} = \frac{k_p}{K(R_i, R_f)},$$

7-13

and

$$4\pi \int_{T_s}^{T_i} k_{sim}(T)dT = \chi,$$

7-14

where k_{sim} is the modified value of fuel thermal conductivity used in SIMMER.

7.1.2. Detailed PIN model: DPIN

The Detailed PIN model, DPIN, provides an alternative to the SPIN model and enables a more precise description of the temperature distribution in the fuel rod through an increased number of radial nodes (so that e.g. the fuel central temperature can be determined). It allows for example the modeling of the central hole and the application of various pin failure criteria (Figure 7-2).

The methodology is similar to the one used in SPIN: the energy conservation equation is used to evaluate energies and temperatures in the fuel and the cladding but this time they are evaluated at each radial node considering the heat flux between two adjacent cells and the nuclear heating.

The treatment of gas in the plenum and the control material has however not been changed as the explicit scheme provides accurate results. The pin breakup criteria as well as the transfer from the solid fuel field to particles and chunks or liquid fuel fields is kept equal to the procedure used in the SPIN model. Unlike the SPIN model, the local formation of molten fuel in the pin as well as the related gas transfer from dissolved to free gas can be simulated with DPIN. However, for heat transfer calculations the molten fuel cavity is not distinguished from the solid region. Cavity pressure, temperature and volume are calculated at each heat transfer time step. As the temperature gradients are very steep in oxide fuels due to the poor thermal conductivity, the cavity modeling is a significant improvement as fuel melting in the center of the pellet can thoroughly occur.

DPIN correctly evaluates the temperature profile in the fuel as well as the temperature of fission gases in the pin. The fission gases are at a high temperature in the center of the pin thus the fission gas pressure and the ejection pressure are influenced by this modeling [53].
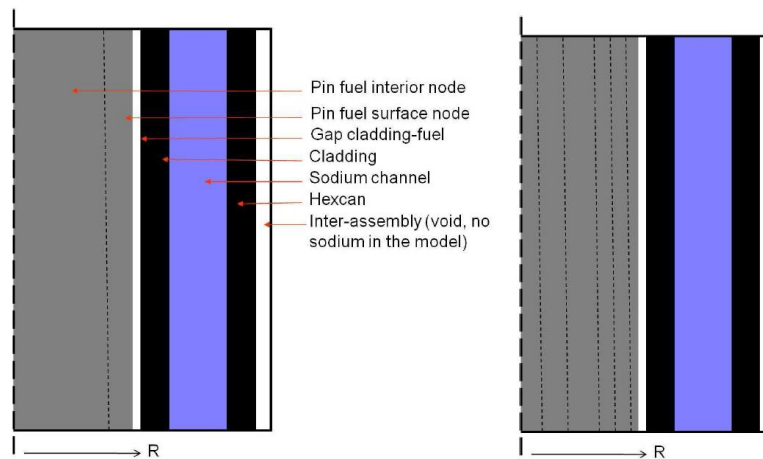
Figure 7-2. Pin modeling with SPIN (left) and DPIN (right) [53].

Being mainly interested in the ULOF (with clad failure preceding fuel failure) and given the lack of transient experiments with sphere-pac fuels, the SPIN model was assessed to be adequate as a first approach for the simulations of this type of fuel.

7.2. Literature overview of thermal conductivity models

Besides the well-known concept of pellet fuels sphere-pac fuels are investigated in the FP-7 PELGRIMM project. These fuels were already investigated in the 1970's and 1980's [140; 141; 118] and several heat transfer models were developed. As mentioned in Chapter 5, sphere-pac fuels have a low thermal conductivity especially at beginning of life where the fresh fuel is not yet restructured. Due to high fuel temperatures and thermal gradients at the beginning of irradiations in the reactor, the fuel restructures within some hours, thus enhancing the heat transfer. Therefore, thermal conductivity of sphere-pac fuels is a key parameter to be investigated if one wants to model properly the thermal performance of these fuels.

An overview of available models for sphere-pac fuel conductivity is presented in the following section. In section 7.3. their adjustment to the SIMMER framework is presented.

7.2.1. Philipponneau's equation of MOX fuels

An evident option for simulating sphere-pac fuels would be to use the thermal conductivity for MOX fuel with increased porosity. Philipponneau [173] and his team suggested a correlation for MOX fuels based on an extensive study of diffusivity measurements with varying parameters (burnup (BU), oxygen over metal ratio (O/M), Pu content). For their calculations, all available diffusivity measurement results in literature were multiplied by the same density and heat capacity values (according to Eq. 5-2 in chapter 5), providing consistent results for MOX thermal conductivity. In their derivation they considered the electronic and the radiation conductivity, both becoming important at high temperatures, as grouped in one single term $k_{HT} = CT^3$. Therefore the conductivity formula can be written theoretically as Eq. 7-15. :

$$k = \left(\frac{1}{A + B \cdot T} + C \cdot T^3 \right) \cdot \delta \qquad \textbf{7-15}$$

where δ is the porosity correction of Maxwell-Eucken $\delta = \dfrac{1-p}{1+2p}$, with p the porosity.

Again one can notice the decomposition in low and high temperature contributions: $k_{ph} = \dfrac{1}{A + BT}$

and $k_{HT} = CT^3$, respectively.

Based on diffusivity measurements, Philipponneau et al. deduced the following values for the parameters A, B, C and δ of Eq. 7-15.

$A = f(x, BU) = 1.528\sqrt{x + 0.00931} - 0.1055 + 0.44BU \ m \cdot W^{-1} \cdot K$ where x is the deviation from stoichiometry i.e. 2-O/M, BU is the fractional burnup and 0.44·BU gives the effect of solid fission products on conductivity.

$B = 2.885 \cdot 10^{-4} \ m \cdot W^{-1}$

$C = 76.38 \cdot 10^{-12} \ W \cdot m^{-1} \cdot K^{-4}$

$\delta = f(p) = \dfrac{1}{0.864} \dfrac{1-p}{1+2p}$

This correlation [173] is recommended in case of standard MOX pellet fuels. If one assumes the gas content in sphere-pac fuels to contribute to the δ term, this conductivity correlation might be one candidate for sphere-pac fuels.

7.2.2. Schulz's equation for porous media

In [175] B. Schulz analyses the reliability of general relationships for the thermal conductivity of two-phase materials. Materials with porosities as high as 96% are investigated. All equations are derived from the general equation for dispersion type structures. The case of "open porosity" is a particular case of dispersion type structure i.e. materials with porosities above 10% are considered. In this case [175] stipulates that the thermal conductivity relation is Eq. 7-16.

$$k(p) = k_0 \cdot \frac{4-9p}{10} + \sqrt{\left(\frac{4-9p}{10}\right)^2 + \frac{1-p}{5}}$$ **7-16**

Where k_0 is the thermal conductivity of the dense material, $k_0(p)$ is the thermal conductivity of the porous material and p is the porosity.

Nevertheless Eq. 7-16 seems to predict inaccurate results when considering fully dense materials since for zero porosity one does not obtain the thermal conductivity of a fully dense material.

7.2.3. Hall and Martin's equation for powder beds

Hall and Martin [176] investigated the thermal conductivity of powder beds, especially for UO_2 vibro-compacted spheres already in the early 1980's. They developed a model based on two simplified geometrical arrangements: a cubic packed sphere array and a square packed infinite cylinder array – Figure 7-3. The first one consists in an infinite layer of regularly piled up spheres parallel to the heat flow. The geometrically evaluated porosity of this arrangement is $(1-\pi/6) = 0.476$ – Eq. 7-17 and 7-19. The latter one consists of infinitely long cylindrical columns piling up parallel to the heat flow. In this case the porosity is $(1-\pi/4)=0.215$ (Eq. 7-18 and 7-20).

$$p_c = 1 - \frac{V_{spheres}}{V_{cell}}$$ **7-17**

$$p_{sq} = 1 - \frac{V_{cylinders}}{V_{cell}}$$ **7-18**

$$p_c = 1 - \frac{4 \cdot \frac{1}{4}\left(\frac{4}{3}\pi a^3\right)}{(2a)^3} = 1 - \frac{\pi}{6}$$ **7-19**

$$p_{sq} = 1 - \frac{4 \cdot \frac{1}{4}\left(\pi \cdot 2a \cdot a^2\right)}{(2a)^3} = 1 - \frac{\pi}{4}$$ **7-20**

- p_c is the geometrical porosity of the cubic packed array

- p_{sq} is the geometrical porosity of the square packed array

- V_{cell} is the volume of the elementary cell

- $V_{spheres}$ is the volume of the spheres in the elementary cell

- $V_{cylinders}$ is the volume of the cylinders in the elementary cell
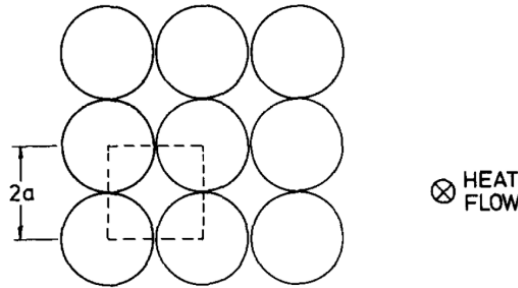
Figure 7-3. Heat flow in an elementary cell for the square packed or cubic packed array [176].

Hall and Martin [176] evaluate the thermal conductivity of packed granules as a combination of a cubic packed and a square packed array.

The thermal conductivity of the cubic packed array was found to be Eq. 7-21 while the one for the square packed array was found to be Eq. 7-22. Both equations do not take into account the influence of fuel radiation. They were nevertheless applied in UO$_2$ compacts with uranium particles [177].

$$k_c = k_g \left[\frac{\pi}{2(\delta-1)^2} \left\{ \delta - 1 - (1+m)\ln\frac{\delta+m}{1+m} \right\} + 1 - \frac{\pi}{4} \right] \qquad \text{7-21}$$

$$k_{sq} = k_g \left[\frac{1+m}{1-\delta} \frac{\pi - 2\sin^{-1}\sqrt{\dfrac{\delta+m}{2(1+m)}}}{\sqrt{(\delta+m)(2-\delta+m)}} - \frac{\pi}{2(1-\delta)} \right] \qquad \text{7-22}$$

- k_g is the thermal conductivity of the gaseous phase

- δ is the ratio $\dfrac{k_g}{k_s}$ where k_s is the thermal conductivity of the solid phase

- g is the temperature jump distance in meters evaluated with

$g = C_1 \dfrac{k_g T^{C_2}}{P_g}$. C_1 and C_2 being adjustable parameters and P_g (atm) and T (K) are the gas pressure and temperature, respectively.

- D is the average diameter of the granules (m) and is defined as $D = \dfrac{\sum_i w_i^{1/3}}{\sum_i \dfrac{w_i^{1/3}}{d_i}}$ with w_i and d_i being the mass fraction and diameter of the i-th size of the granule.

- m is the ratio $\dfrac{g}{D}$

The thermal conductivity k of any compact is then given by applying a Lagrangian interpolation method [177] (Eq. 7-23).

$$
\begin{aligned}
\ln(k) =& \frac{(p-p_c)(p-p_{sq})(p-p_g)}{(p_s-p_c)(p_s-p_{sq})(p_s-p_g)}\ln(k_s) \\
&+\frac{(p-p_s)(p-p_{sq})(p-p_g)}{(p_c-p_s)(p_c-p_{sq})(p_c-p_g)}\ln(k_c) \\
&+\frac{(p-p_s)(p-p_c)(p-p_g)}{(p_{sq}-p_s)(p_{sq}-p_c)(p_{sq}-p_g)}\ln(k_{sq}) \\
&+\frac{(p-p_s)(p-p_c)(p-p_{sq})}{(p_g-p_s)(p_g-p_c)(p_g-p_{sq})}\ln(k_g)
\end{aligned}
\tag{7-23}
$$

Where $p_c = 0.476$, $p_{sq} = 0.215$, $p_g = 1$ is the porosity of the gas phase, $p_s = 0$ is the porosity of the solid phase and p is the porosity of the powder bed. $C_1 = 6.888 \cdot 10^{-9}$ and $C_2 = 1.065$ were found in the numerical analysis of [177]. This correlation seems to provide accurate results for sphere-pac fuels [177].

7.2.4. Other models

Other models have been investigated in addition to the previous ones as to know: the model for composite fuels detailed in [178] and originally proposed by Maxwell and the model for powders proposed by Godbee [179].

- **Maxwell's equation for composite fuels**

Since sphere-pac fuels can be considered as composite fuel pellets in the sense that a dispersed phase i.e. the gas is present in a continuous phase namely the particles, another option could be to consider the conductivity of a composite medium. Therefore Maxwell's equation for composite fuels might be used (Eq. 7-24). This equation nevertheless is valid only for a "particle" concentration of the dispersed phase less than 10 to 15 % in volume, implicitly assuming no mutual influence of the particles on one another [180]. Therefore, for higher concentrations (up to 76%) Eq. 7-25 should be used instead.

$$
k_{eff,Maxwell} = \frac{k_M(2k_M + k_D - 2V_r(k_M - k_D))}{(2k_M + k_D - V_r(k_M - k_D))}
\tag{7-24}
$$

$$k_{eff} = k_D + (1 - V_r)(k_M - k_D)\left(\frac{k_{eff,Maxwell}}{k_M}\right)^{\frac{1}{3}} \qquad \textbf{7-25}$$

Where the index D stands for "Dispersed phase", M for "Matrix" i.e. continuous phase, k_D and k_M are the thermal conductivities of the dispersed phase and the continuous phase, respectively, and V_r is the volume fraction of the dispersed phase and can be defined as:

$$V_r = \frac{V_D}{V_D + V_M} \qquad \textbf{7-26}$$

Eq. 7. 25 could be applied in case of sphere-pac fuels if the dispersed phase is assumed to be the gas and the matrix is assumed to be the fuel.

- **Godbee's equation for powders**

Godbee and Ziegler [179] proposed a thermal conductivity model for powders in a semi-empirical manner.

They considered a well-mixed heterogeneous powder with isotherms as planes perpendicular to the x axis (Figure 7-4 (a)). This material is then sliced into thin layers parallel to the (x,y) plane. One slice has a depth such that the slice is full solid i.e. as in the case shown in Figure 7-4(c).
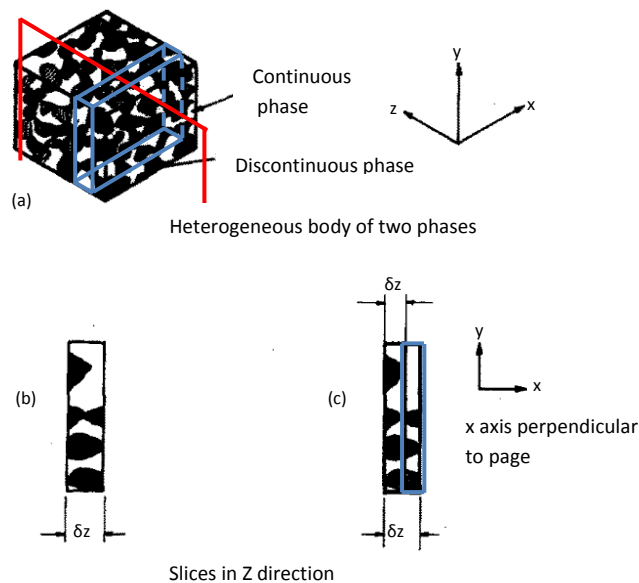
Figure 7-4. Sliced representation of the gas-powder system. [179]

The particles in each slice are then moved without rotation along the x axis. This does not change the conductivity of the medium as it is only a change in the resistances added in the series (the heat flow is perpendicular to the y-z plane i.e. parallel to the x axis). Once this has been performed, the system is sliced into thin layers parallel to the y-z plane, again considering only "full" slices in the x direction.

Again the particles in each slice are moved along the other axes. Therefore all particles are put together in one rectangle, forming a fully dense body. This body is shown in Figure 7-5.

(a) SIMPLIFIED HETEROGENEOUS BODY OF TWO PHASES

HEAT FLOW Q, PERPENDICULAR TO y-z PLANE

(b) PORTION OF SIMPLIFIED BODY BETWEEN x = O AND x = D$_s$

(c) PORTION OF SIMPLIFIED BODY BETWEEN x = D$_g$ AND x = X
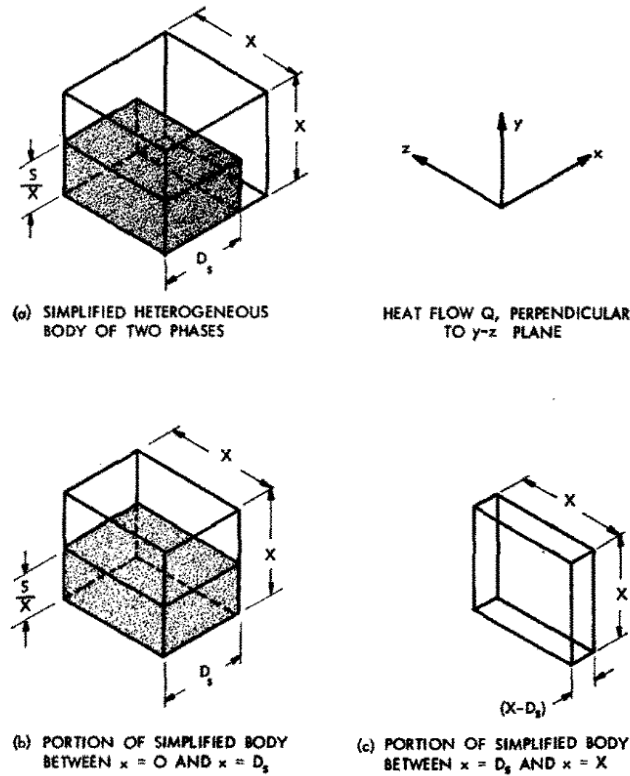
Figure 7-5. Representation of a simplified gas-powder system. [179]

The details are omitted here but can be found in [179]. The thermal conductivity of powders is expressed as in Eq. 7-27.

$$k = \cfrac{k_g^*}{\left\{ \left[\cfrac{\cfrac{Ds}{X}}{(1-\cfrac{S}{X^2})\cfrac{k_g}{k_g^*}+\cfrac{k_s}{k_g^*}\cfrac{S}{X^2}} \right] + \left[1-\cfrac{Ds}{X} \right] \right\}} + 4n_r^2 \sigma \varepsilon \left(\cfrac{1}{V_d}-1 \right) D_s T^3 \qquad \textbf{7-27}$$

With $k^* = k_g' \cfrac{S}{X^2} + k_g (1-\cfrac{S}{X^2})$ and

$$k_g' = \cfrac{k_g}{\left\{ 1+Z(\cfrac{2-a}{a})(\cfrac{\gamma}{1+\gamma})(\cfrac{T}{Pd\phi^2 N_{pr}}) \right\}}$$

- k_g is the thermal conductivity of the bulk gas

- k_s is the thermal conductivity of solid particles

- n_r is the refractive index of media between surfaces

- σ is the Stefan-Boltzmann constant

- ε is the emissivity of the system
- V_d is the volume of the dispersed phase
- a is the thermal accommodation coefficient for gas-solid surface (TAC)
- $\gamma = \dfrac{C_p^g}{C_v^g}$, C_p^g and C_v^g being the heat capacity of the gas at constant pressure and constant volume, respectively
- $d = X - D_s$ is the distance between adjacent parallel plates
- X and D_s are lengths, defined as in Figure 7-5.
- T and P are the absolute temperatures and pressures, respectively
- ϕ is the molecular diameter of the gas as determined from viscosity
- N_{pr} is the Prandtl number and is defined as $N_{pr} = \dfrac{\eta C_p^g}{k_g}$ with η the viscosity
- Z is a conversion factor and is equal to $1.26 \cdot 10^{-19}$.
- The ratio $\dfrac{D_s}{X}$ can be determined by

$$\frac{D_s}{X} = \sqrt[3]{\left(\frac{V_d}{\alpha}\right)} \text{ with } \alpha \text{ a shape factor}$$

Eq. 7-27 might be applied to sphere-pac fuels instead of powders.

7.2.5. Concrete applications

All previously developed models are based on macroscopic equations. In parallel to these models, several fuel codes devoted to the particular behavior of sphere-pac fuels were developed. In particular, two codes developed at the Paul Scherrer Institute in Switzerland (PSI) can be cited: SPACON [181] dedicated to the calculation of thermal conductivities for sphere-pac fuels - and SPHERE [182] - devoted to the irradiation behavior of sphere-pac fuels.

In reference [181] thermal conductivities covering a temperature range of about 400-1200 K for a two size fractions packed UO_2 sphere-pac fuel with a smear density of 82.37 % TD are presented for different necking ratios and pressures, Figure 7-6. The characteristics of the fuel and parameters used for the SPACON calculations in [181] can be found in Table 7-1. The binary fraction sphere-pac fuels at 1 bar and 0% necking (marked in red) is considered as the reference thermal conductivity to which the previously mentioned models will be compared (in order to identify the most suitable model for sphere-pac fuels). This fuel is in fact representative of the fuel state at start of a fast breeder reactor.

All previously described models are applied to this UO_2 sphere-pac particle case and compared to the data provided in [181] - Figure 7-7. In addition the conductivity for UO_2 with a porosity of 17.63% is plotted as well in Figure 7-7 based on the equation provided in Table 7-1.

Table 7-1. Characteristics and parameters used in the SPACON calculations of Figure 7-6. [181]

Packing Parameter		
Sphere size, μm	1200	35
Packing density, %	62.5	59.3
Density of spheres, %	98.56	98.65
Total smear density, %	61.6	58.5
Surface roughness distance, μm	0.1[a]	0.05[a]
Material Properties	(T is temperature in kelvin; p is pressure in bars)	
Thermal conductivity of UO_2 (Ref. 9), W/mK	$\lambda = 1/(0.035 + 0.000225 \cdot T) + 8.3 \times 10^{-11} \cdot (T)^3$	
Porosity correction[10] for thermal conductivity of UO_2	$\lambda_{cor} = \lambda \cdot (1 - \text{porosity})^{1.7}$	
Thermal conductivity of He (Ref. 11), W/mK	$\lambda = 2.639 \cdot 10^{-3} \cdot (T)^{0.7085}$	
Temperature jump distance at the gas/solid interface,[12] m	$j = 2 \cdot (2 - ac)/ac \cdot \kappa/(\kappa + 1) \cdot \Lambda_0/Pr \cdot T/273/p$	
Accommodation factor	$ac = 0.25$	
Isentropic exponent	$\kappa = 1.67$	
Mean free path, m	Λ_0 (at 1 bar, 0°C) $= 1.74 \times 10^{-7}$	
Prandtl number	$Pr = 0.667$	

[a]Negligible.
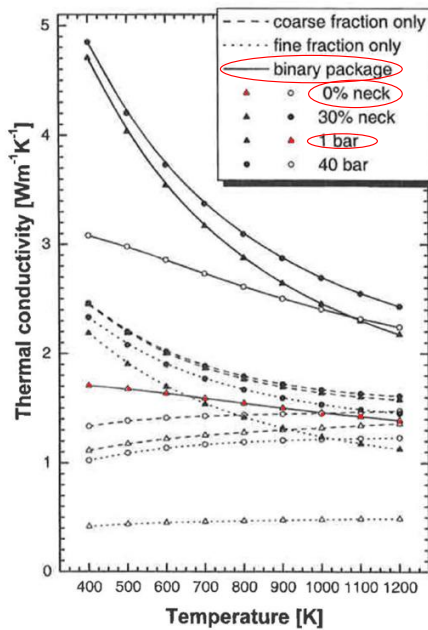
Figure 7-6. Thermal conductivities for two one-fraction packages of UO_2 spheres (1200 μm and 35 μm in diameter) and their binary package in the sintered and unsintered state, for different He pressures. [181]
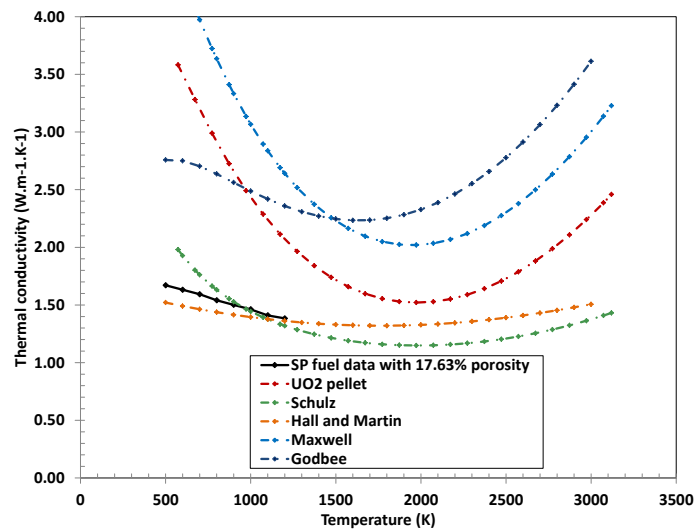
Figure 7-7. Thermal conductivity of UO_2 sphere-pac fuels of Figure 7-6 with various correlations. SP stands for sphere-pac.

According to Figure 7-7 the thermal conductivity correlations of Hall and Martin or of Schulz (adapted) reflect rather well the SP fuel data for UO_2 particles. Therefore those two correlations will be considered for adaptation of MOX SP fuels into SIMMER.

7.3. The SIMMER Framework

The previously mentioned models cannot be directly applied in SIMMER. Indeed, the thermal conductivity model implemented in SIMMER is based on a correlation constituted of 5 factors. In addition, in case a hole has to be taken into account for the fuel pellet design, the hole correction detailed in section 7.1.1. has to be applied since the SPIN model is used. In the following, the methodology applied for each fuel type – pellet and sphere-pac - and for different irradiation stages is detailed.

7.3.1. Beginning of life thermal conductivities

The thermal conductivities of pellet and sphere-pac fuels are very different at beginning of life (BOL). This is especially due to the specific macrostructure of sphere-pac fuels. Indeed, the few and narrow contact points between the spheres deteriorate the heat transfer properties of the fuel.

The reference BOL CP-ESFR core contains fresh pellet fuel with 5.00% porosity and a smear density of 88.8%TD or 83.41%TD – if smeared up to the fuel outer radius or the inner cladding radius, respectively. In case of sphere-pac fuels this implies that the microspheres' porosity and the helium surrounding them add up to a volume faction of 16.59% (no gap is present).

No data has been found in literature for sphere-pac pins with exactly 16.59% helium content. In [181] data for UO_2 sphere-pac pins with a helium content of 17.63% was provided. The assumption was therefore made that this small discrepancy in the helium content (16.59% vs. 17.63%) would not impact much the thermal conductivity and this data was used for BOL sphere-pac fuels.

Three cases are considered in the BOL CP-ESFR WH core for which one needs thermal conductivities. The different cases are depicted in Figure 7-8.

- The reference case consists in the CP-ESFR loaded with pins composed of annular pellet fuel presenting a gap (Figure 7-8(a)).
- The second case consists in loading the CP-ESFR with non-restructured sphere-pac fuel i.e. no necking of the spheres. For thermal conductivity calculations, 17.63% content of Helium was considered in the pin (because data was available only for this gas content), 1 bar of gas pressure. The fuel mass is kept as in the reference CP-ESFR pins (Figure 7-8 (b)).
- The third case consists in loading the CP-ESFR with full pellet fuel (no hole, no gap). For thermal conductivity calculations 17.63% of porosity is considered. The mass is kept as in the reference CP-ESFR (Figure 7-8 (c)).

(a)

Hole + gap
Fuel porosity 5%
Smear porosity 11.20%

(b)

No hole + no gap
Smear porosity 16.59%
Porosity for conductivity
calculation 17.63%

(c)

No hole + no gap
Smear porosity 16.59%
Porosity for conductivity
calculation 17.63%
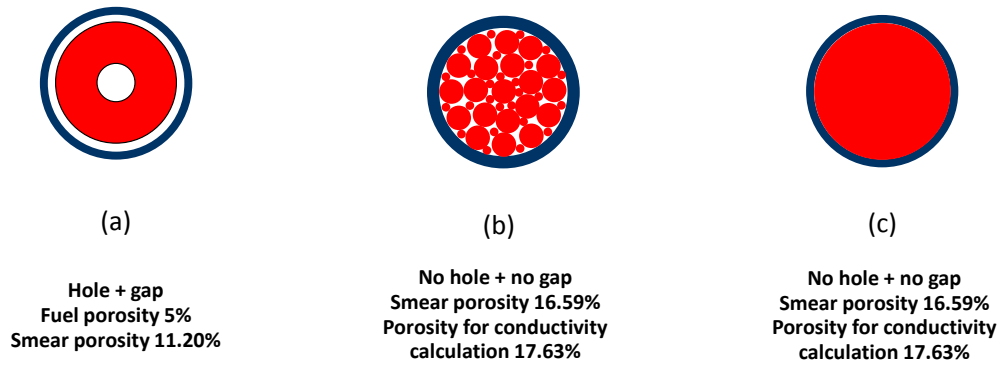
Figure 7-8. Cases considered for the CP-ESFR cores at BOL: (a) standard pin design (b) non-restructured sphere-pac pin (c) full pellet.

Analyzing case (a) and (b) provides information on the impact of the pin inner structure and fuel thermal conductivity on the pin behavior. Analyzing case (b) and (c) gives information on the impact of thermal conductivity solely on the pin behavior.

In order to perform calculations with these fuels, the first step is to obtain the conductivity correlation for both pellet and sphere-pac $U_{0.8}Pu_{0.2}O_2$ fuel.

- **Pellet fuel**

A 100% dense pellet (no porosity) composed of MOX fuel and no central hole is considered. To get the conductivity correlation to be used in SIMMER, the Philipponneau equation [173] (see section 7.2.1.) is applied – Eq. 7-28.

$$k_0 = \left(\frac{1}{A+B \cdot T} + C \cdot T^3 \right) \quad [\text{W} \cdot \text{m}^{-1} \cdot \text{K}^{-1}] \qquad \textbf{7-28}$$

Where

$A = f(x, BU) = 1.528\sqrt{x+0.00931} - 0.1055 + 0.44BU$ $\text{m} \cdot \text{W}^{-1} \cdot \text{K}$, x is the deviation from stoichiometry i.e. 2-O/M, BU is the fractional burnup in at%

$B = 2.885 \cdot 10^{-4} \, \text{m} \cdot \text{W}^{-1}$

$C = 76.38 \cdot 10^{-12} \, \text{W} \cdot \text{m}^{-1} \cdot \text{K}^{-4}$

T is the temperature in K, BU is the burnup in at%.

The data obtained by this formula is fitted and gives the following SIMMER correlation for <u>non-irradiated dense $U_{0.8}Pu_{0.2}O_2$ pellet fuel</u> – Eq. 7-29.

$$k_0^{MOX,pellet} = 4.8260 + 239.199\frac{1}{T} + 6.00062 \cdot 10^5 \frac{1}{T^2} - 2.90409 \cdot 10^{-3}T + 8.23153 \cdot 10^{-7}T^2 \qquad \textbf{7-29}$$

Based on the previously written correlation, the conductivity for case (a) and case (c) are determined.

Case (a)

Eq. 7-29 is modified using the hole correction treatment – section 7.1.1. - i.e. by applying Eq. 7-8 and Eq. 7-13 considering the BOL hole dimensions (i.e. 2.40904 mm in diameter) and the fuel initial porosity. The standard CP-ESFR pellet fuel therefore has the following thermal conductivity correlation – Eq. 7-30 - to be used in SIMMER together with the Harding correction (Eq. 7-8):

$$k_{CP-ESFR,ref}^{MOX,pellet} = 5.9452 - 162.134\frac{1}{T} + 1.93070 \cdot 10^5 \frac{1}{T^2} - 3.50597 \cdot 10^{-3}T + 1.06394 \cdot 10^{-6}T^2 \qquad \textbf{7-30}$$

Case (c)

Eq. 7-29 is used directly in the SIMMER input. The porosity correction is nevertheless modified in the SIMMER subroutines to take into account a porosity of 17.63% for conductivity calculations. This is accounted to the fact that the data for sphere-pac fuels [181] is given for 17.63% of Helium and the same porosity is hence applied to the pellet fuel.

The data available for sphere-pac fuels concerns UO_2 fuel [181]. It is assumed that the impact of additional plutonium in the uranium matrix on the conductivity of sphere-pac fuel is the same as the impact we get in pelletized fuel of the same density [183]. It is therefore possible to deduce from the sphere-pac UO_2 conductivity, the sphere-pac MOX conductivity by applying coefficients calculated on the basis of UO_2 and MOX pellet conductivity.

The <u>non-irradiated dense UO_2 pellet fuel </u>conductivity in SIMMER [184] is given in the following Eq. 7-31:

$$k_0^{UO_2,pellet} = 2.0207 + 4.68440 \cdot 10^3 \frac{1}{T} - 1.04430 \cdot 10^6 \frac{1}{T^2} - 2.60310 \cdot 10^{-3}T + 8.93780 \cdot 10^{-7}T^2 \qquad \textbf{7-31}$$

A plot of conductivities for $U_{0.8}Pu_{0.2}O_2$ and UO_2 pellet fuels with a density of 82.37%TD obtained from the previous correlations is given in Figure 7-9.
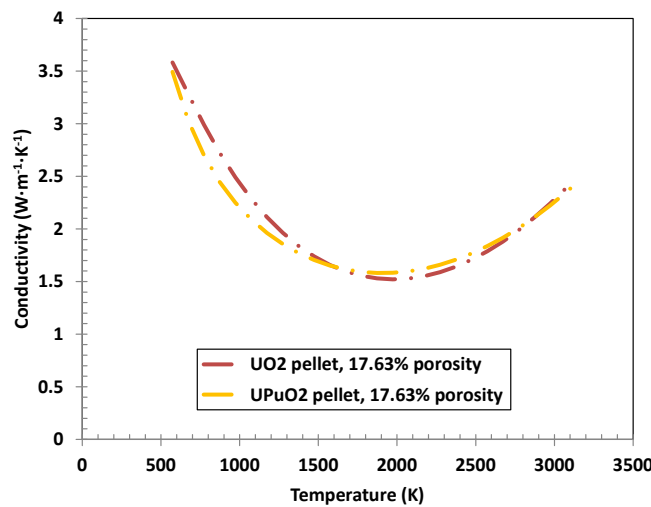
Figure 7-9. Conductivity for $U_{0.8}Pu_{0.2}O_2$ and UO_2 pellet fuels, density of 82.37%TD.

Based on Figure 7-9 the coefficients to apply to the pellet conductivity of UO$_2$ to obtain the one for MOX pellet are deduced. The same coefficients are then applied to sphere-pac fuels of the same density. The coefficients to be applied can be seen in Appendix D.

- **Sphere-pac fuels**

Conductivity data for UO$_2$ sphere-pac fuel with a smear density of 82.37%TD – i.e. sum of gas content and porosity of spheres - no necking and 1 bar of pressure is taken from [181]. The data covers the temperature range from 400 K to 1200 K and needs further extrapolation even though non-restructured sphere-pac fuels at temperatures as high as 3000 K will not exist in reality. An envelope case for BOL with completely non-restructured SP fuel is thus considered.

To extrapolate the data, sphere-pac fuels will be assumed to be close to a penetration type material i.e. a structure containing interconnected bodies of each phase: fuel and gas.

Eq. 7-16 [175] for penetration type materials with open porosity is then used to fit the sphere-pac data [181] with $p = 0.165$, $k_{fuel} = k_0 \cdot \left(1 - p_{spheres}\right)^{1.7}$ [181] and $p_{spheres} = 0.0144$ is the porosity of the spheres. This yields a smear porosity of 0.1763.

By using Eq. 7-16 and adapting it to the sphere-pac data [181], one obtains the following extrapolation for the conductivity of non-restructured UO$_2$ sphere-pac fuels with 82.37%TD, 1 bar of He – Eq. 7-32:

$$k_{p=0.1763}^{UO_2,sphere-pac} = 3.4148 - 926.694\frac{1}{T} + 2.11397 \cdot 10^5 \frac{1}{T^2} - 1.58093 \cdot 10^{-3}T + 3.41369 \cdot 10^{-7}T^2 \qquad \textbf{7-32}$$

Figure 7-10 gives an overview of the conductivity extrapolation for non-restructured sphere-pac fuels with 82.37%TD and 1 bar of He:
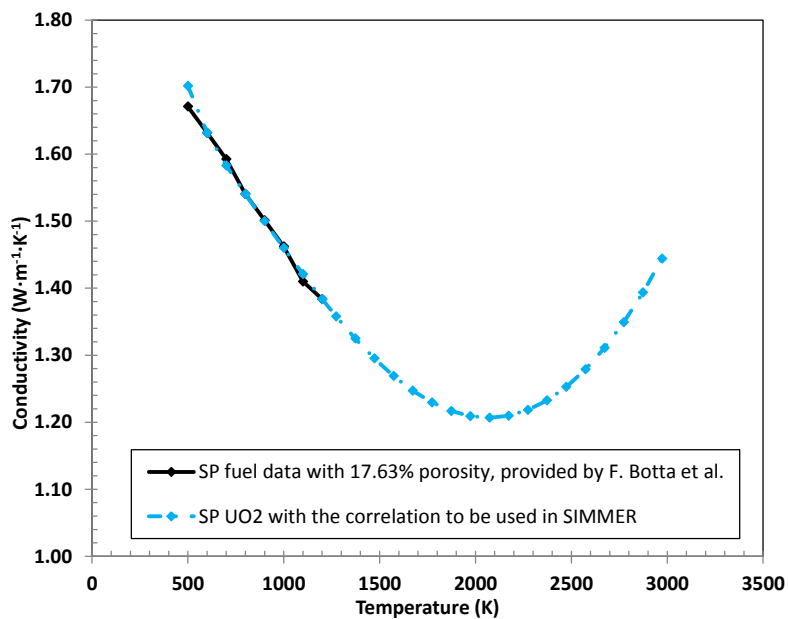
Figure 7-10. Thermal conductivity extrapolation for non-restructured UO$_2$ sphere-pac fuels based on data in [181].

By applying the coefficients of Appendix D to the conductivity of UO_2 sphere-pac fuel, one obtains Eq. 7-33 for the conductivity of $U_{0.8}Pu_{0.2}O_2$ sphere-pac fuel:

$$k_{p=0.1763}^{MOX,sphere-pac} = 1.6680 - 283.800\frac{1}{T} + 1.95890 \cdot 10^5 \frac{1}{T^2} - 3.6102 \cdot 10^{-4}T + 1.00260 \cdot 10^{-7}T^2 \qquad \textbf{7-33}$$

Eq. 7-33 already contains the porosity correction and the porosity correction in SIMMER is thus omitted.

It has to be mentioned that Eq. 7-16 from [175] does not yield accurate results in case of fully dense material. Nevertheless, comparing this equation with the one of Hall and Martin provides similar results in the considered temperature range for the considered material (within 5% relative discrepancy) – Figure 7-11.
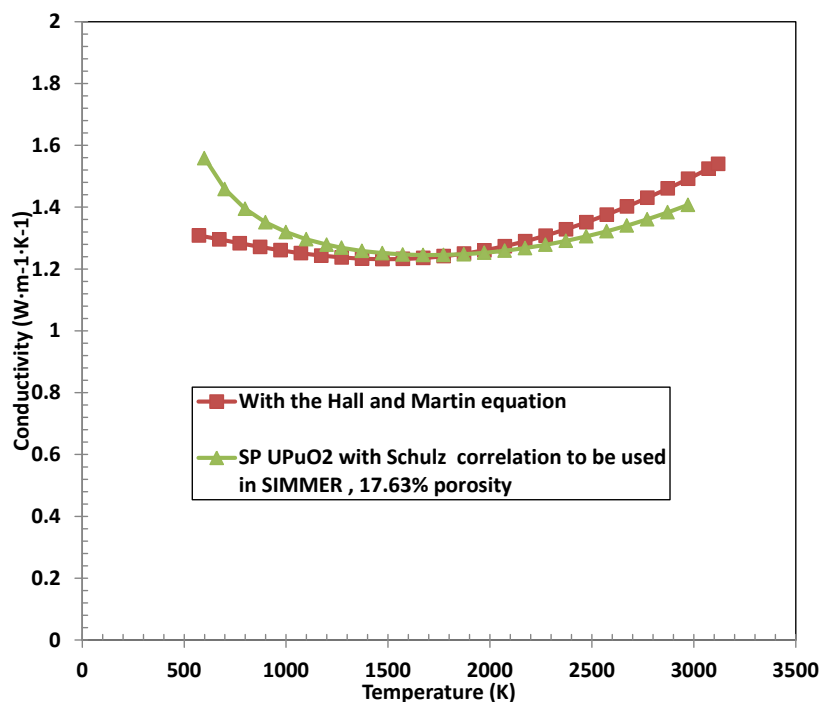
Figure 7-11. Comparison of the Ishii (Hall and Martin) and the Schulz equation for MOX sphere-pac (SP) fuels.

Once the BOL conductivities are known, the same procedure has to be applied to obtain end of cycle 3 (EOC3) conductivities.

7.3.2. End of cycle 3 conductivities

After 3 irradiation cycles, when the fuel represents the average fuel in the core at equilibrium, the WH pellet fuel is assumed to have a porosity of 7.50% and an oxygen over metal ratio of 2 [185]. At this stage of irradiation, a pin filled with sphere-pac fuel exhibits, in first approximation, two zones: one outer non-restructured zone displaying the BOL structure and another restructured zone with properties similar to a pellet fuel of the same density – Figure 7-12.

Characteristics of EOC3 fuels are listed in Table 7-2. Conductivities for both fuel types are determined in the following.
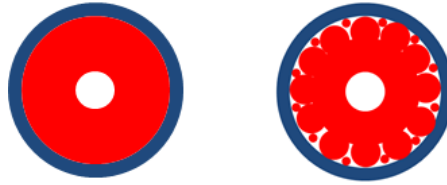
Figure 7-12. EOC3 pellet (left) and sphere-pac fuel (right).

Table 7-2. Characteristics of EOC3 fuel in the CP-ESFR core.

	Standard MOX pellet pin	Restructured MOX sphere-pac pin
Fuel smear porosity (*%*)	16.59	16.59
Fuel porosity and other characteristics	Fuel porosity 7.5%	2 fuel zones: restructured and non-restructured
		2 sphere diameters: 1200 μm and 35 μm
		Restructured zone porosity 7.5%
Central hole diameter (*mm*)	3.05	2.92 (30% of cladding inner diameter)
Burnup (*at%*)	6	6
Oxygen over metal ratio	2	2
Gap state	Closed gap	No gap

- **Pellet fuel**

The thermal conductivity of pellet fuel is obtained with Eq. 7-15 considering the characteristics listed in Table 7-2. Eq. 7-13 and Eq. 7-7 are then applied in order to compensate for the presence of the hole.

Eq. 7-34 is then used for conductivity in SIMMER with the Maxwell-Eucken porosity correction.

$$k_{p=0.1659}^{MOX,pellet,EOC3} = 8.5987 - 136.946\frac{1}{T} + 9.01439 \cdot 10^5 \frac{1}{T^2} - 0.005079T + 1.42400 \cdot 10^{-6}T^2 \quad \textbf{7-34}$$

- **Sphere-pac fuel**

To assess the thermal conductivity of the restructured sphere-pac fuel, conductivity correlations in each of the two zones are determined. In the non-restructured zone, Hall and Martin's approach is used while in the restructured zone Philipponneau's equation for MOX fuels is applied [173].Both conductivities are then combined into one single equation based on the linear power of each zone. This gives the effective fuel thermal conductivity Eq. 7-35 (same porosity in both regions for SIMMER)

$$k_{effective} = \ln\left(\frac{R_{fuel,\ outer}}{R_{Hole}}\right) \cdot \frac{1}{\dfrac{\ln\left(\dfrac{R_{Pellet-like\ structure}}{R_{Hole}}\right)}{k_{Pellet-like\ structure}} + \dfrac{\ln\left(\dfrac{R_{fuel,\ outer}}{R_{Pellet-like\ structure}}\right)}{k_{Sphere-pac\ fuel}}} \qquad \textbf{7-35}$$

with $R_{Pellet-like\ structure}$ the outer radius of the pellet-like structure, $R_{fuel,\ outer}$ the outer radius of the fuel, R_{hole} the inner radius of the pellet-like structure defined as:

$$R_{hole} = 30\%\,R_{fuel,\ outer}$$

$$R_{Pellet-like\ structure} = R_{hole}\sqrt{\frac{1 - p_{Pellet-like\ structure}}{p_{Non-restructured\ sphere-pac\ fuel} - p_{Pellet-like\ structure}}}$$

where p stands for porosity.

Applying Eq. 7-13 and Eq. 7-7 to Eq. 7-35 yields the conductivity correlation for sphere-pac fuels to be applied in SIMMER (Eq. 7-36) together with the Harding correction (Eq. 7-8).

$$k_{p=0.1659}^{MOX,sphere-pac,EOC3} = 7.01016 + 855.730\frac{1}{T} + 4.35492\cdot10^5\frac{1}{T^2} - 0.004203T + 1.23300\cdot10^{-6}T^2 \quad \textbf{7-36}$$

7.3.3. Summary concerning the determination of conductivities

A graphical summary of conductivities for both fuel types (sphere-pac and pellet) at BOL and EOC3 without any hole or porosity correction for SIMMER is shown in Figure 7-13. As can be seen from this figure, the conductivity of sphere-pac fuel at BOL is very low compared to the one of pellet fuel. However, after 3 cycles of irradiation, it recovers and is close to the pellet one (of same density), as expected.
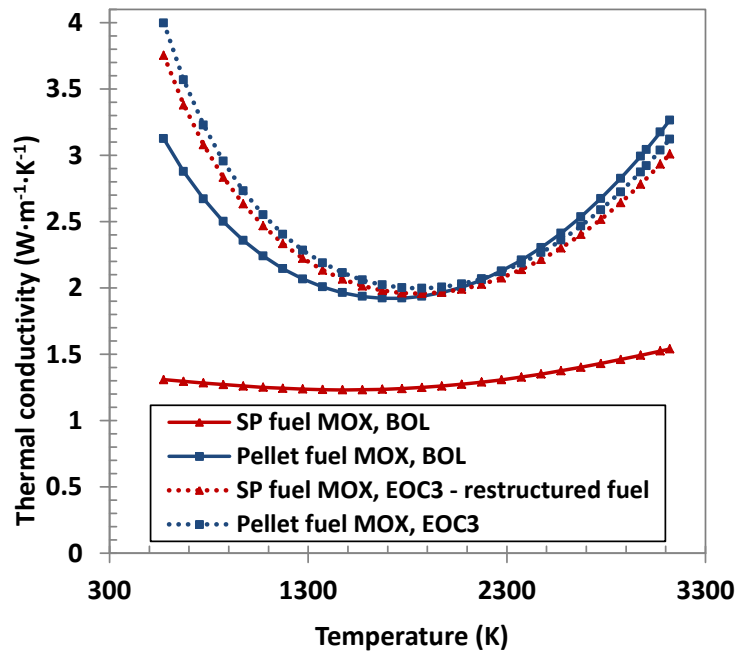
Figure 7-13. Summary of thermal conductivities for both pellet and sphere-pac fuel in the CP-ESFR at BOL and EOC3.

With the previously mentioned equation and options, several SIMMER runs were performed. Corresponding description and analysis will be presented in Chapter 8. One additional parameter to be investigated in case of sphere-pac fuels is the thermal penetration length of the fuel.

7.4. Studies on thermal penetration length

In a standard SIMMER-III calculation, no porosity is included in the calculation of $2\delta_f$. This parameter is determined by using material properties of dense fuel at solidus temperature. This reflects the case of a molten inner fuel zone touching the surface fuel zone, which is still in its solid state. The corresponding thermal penetration length would reflect the width (and therefore the delay time) of the heat transfer to the coolant.

Since the sphere-pac fuel used in the CP-ESFR WH core has a "porosity" of 16.59% – instead of 5% in case of standard pellet fuel - it has to be made sure that omitting the porosity in the thermal penetration length calculation has an acceptably small influence on the core behavior under transient conditions. For the intended investigation of a ULOF the SPIN model is sufficient and was therefore chosen [169]. The thermal penetration length $2\delta_f$ has an impact on the heat transfer calculation and hence on fuel temperatures as it determines the size of the surface node. It is evaluated as follows [169], assuming a parabolic temperature profile and a perfect contact between both zones Eq. 7-37:

$$2\delta_f = 2\sqrt{3}\sqrt{\frac{\tau_{str,f}k_f(T)}{\rho_f(T)c_f(T)}} = 2\sqrt{3}\sqrt{\tau_{str,f}a_f(T)} \qquad \textbf{7-37}$$

Where $\tau_{str,f}$ is called the structure time constant, k_f, ρ_f and c_f are the fuel thermal conductivity, density and heat capacity of the fuel, respectively, and a_f is the thermal diffusivity of fuel.

To determine the impact of porosity inclusion in $2\delta_f$ calculations on the core behavior under transient conditions, a fast unprotected transient over power (UTOP) has been chosen[18]. For a fast UTOP under reactor beginning of life (BOL) conditions, SPIN can be applied since the power increase leads to a melting of the complete pellet. In addition the fast UTOP has been chosen for minimizing computation time. A non-mechanistic arbitrary reactivity ramp rate of 50$/s is imposed to the CP-ESFR WH core [186] after it reaches its steady state. The following assumptions are made:

- calculations are performed at beginning of life
- for pellet fuel and sphere-pac fuel, in its non-restructured state
- for thermal penetration lengths calculated with fully dense properties – referred to as "reference PENTR" – and porous properties
- gagging scheme for CP-ESFR WH core at BOL with its reference fuel (pellet with hole).

---

[18] For these analyses, only the fuel has been replaced (pellet by sphere-pac) and the core design (and e.g. the power distribution or gagging scheme) has been kept; the aim being to determine if introducing sphere-pac fuel into a sodium cooled fast reactor is possible in principle.

Four cases are studied. For each fuel type, two sub-cases are considered – Table 7-3.

Table 7-3. Overview of the studied cases.

Cases	Sphere-pac fuel (16.59% porosity)	Pellet fuel (5% porosity)	Reference PENTR	PENTR with porosity
1a		x	x	
1b		x		x
2a	x		x	
2b	x			x

No expansion model is applied for reactivity feedback. Steady state is calculated for all 4 cases and the UTOP launched, once the steady state is reached. Geometric characteristics of pellet and sphere-pac fuels used for the calculations can be found in Chapter 4. The pin design in all four cases is the same as the CP-ESFR WH one. Only fuel porosity is adapted since sphere-pac fuel pins do not present a gap between fuel and cladding.

In all calculations, $\tau_{str,f}$ is set to the default value of 1 ms – the characteristic time scale of a power peak induced by a UTOP. The temperature is set to the solidus temperature of MOX fuel (3002 K [169]).

Porosity might be included in the calculation i.e. $k_f\left(p,T_{solidus}\right)$ and $\rho_f\left(p,T_{solidus}\right)$ are used. $c_{p,f}$ is assumed to be independent of porosity (see Appendix E).

Values of thermal penetration lengths for the four studied cases are listed in Table 7-4.

Table 7-4. Thermal penetration length values for the studied cases (1 stands for pellet fuel, 2 for sphere-pac fuel, a for the reference calculation, b for the calculation taking into account the porosity).

Cases	Hand calculation (µm)	Check with SIMMER-III (µm)
1a	89.43	89.43
1b	79.10	79.10
2a	89.43	89.43
2b	52.22	52.22

The studies are devoted first to the differences due to the porosity inclusion for the same fuel type which means first cases 1a and 1b are compared, followed by cases 2a and 2b. Only cases 2a and 2b dealing with sphere-pac fuels are presented in this section. Cases 1a and 1b can be found in Appendix F.

Sphere-pac fuels contain a higher gas amount, referred to as porosity, than standard pellet fuels. Therefore its effect on the thermal penetration length and core response to a transient is expected to be larger than for pellet fuels. There is no significant difference in the steady state of cases 2a and 2b.

A reactivity ramp of 50$/s is assumed for initiating the transient. The reactivity evolution due to this reactivity ramp is shown in Figure 7-14. With the fuel temperature raise, the Doppler effect brings the reactivity back to a lower value. This corresponds to the first reactivity peak. However, the fuel temperature raise is not yet sufficient to trigger core melting – Figure 7-16.

Since reactivity is continuously added by the external power ramp of 50$/s, a second reactivity and power peak is generated. This peak is sufficient to trigger the fuel melting at 26~27 ms after the accident starts. The fuel melting and dispersion leads the power to decrease again.

The calculations stop 29.3 ms and 37.8 ms after the accident initiation in case 2a and 2b respectively.

Even though both cases show almost the same core response to the imposed transient, very slight discrepancies can be identified (less than 0.2%).

After the first power peak, the fuel temperature in case 2a is lower than in case 2b. Therefore the temperature increase in case 2b is higher than in case 2a which leads to a larger Doppler feedback (cf. the steepness of the blue reactivity slope between 24.3 ms and 25.5 ms), Figure 7-15.
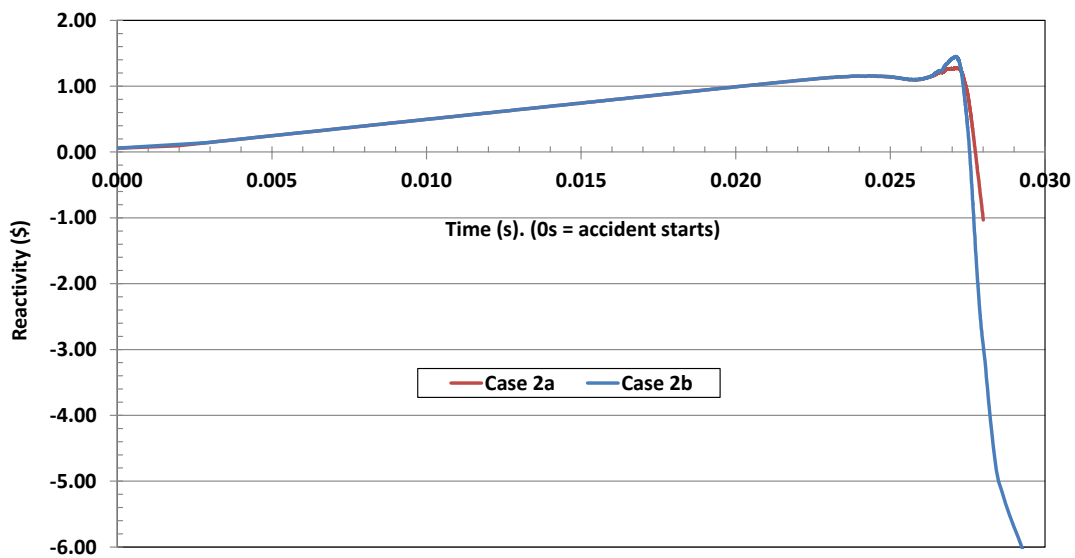
Figure 7-14. Reactivity evolution in case of sphere-pac fuel, during a UTOP of 50$/s.
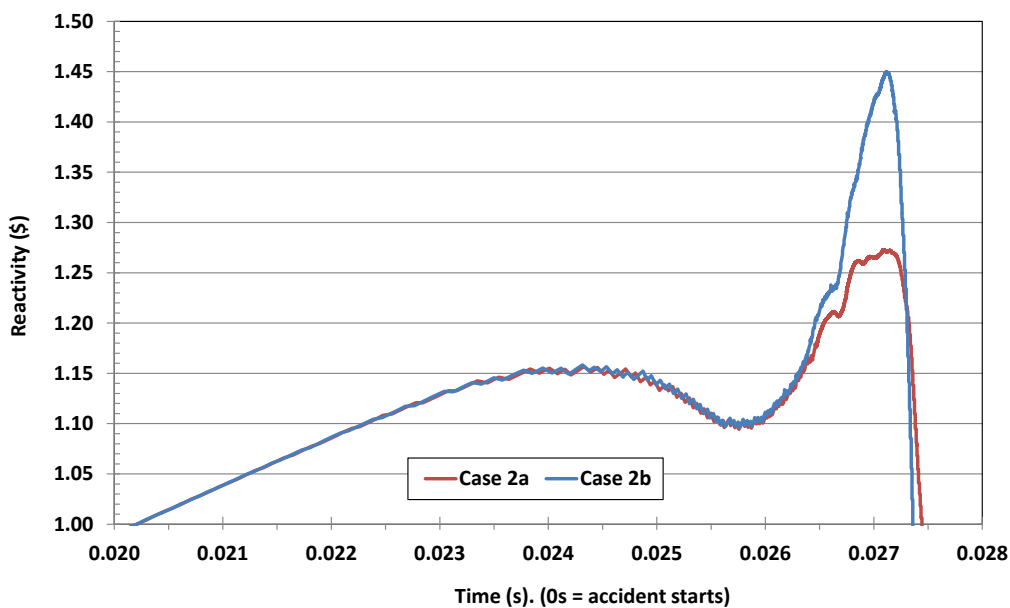
Figure 7-15. Zoom on reactivity peaks.

The front slope of the second reactivity peak is steeper in case 2b than in case 2a. The rapid fuel melting and higher molten fuel mass in case 2b - see zoom on the fissile core at 29 ms after the UTOP starts - Figure 7-17 - leads then the second power peak to be slightly higher in case 2b than in case 2a, Figure 7-16.
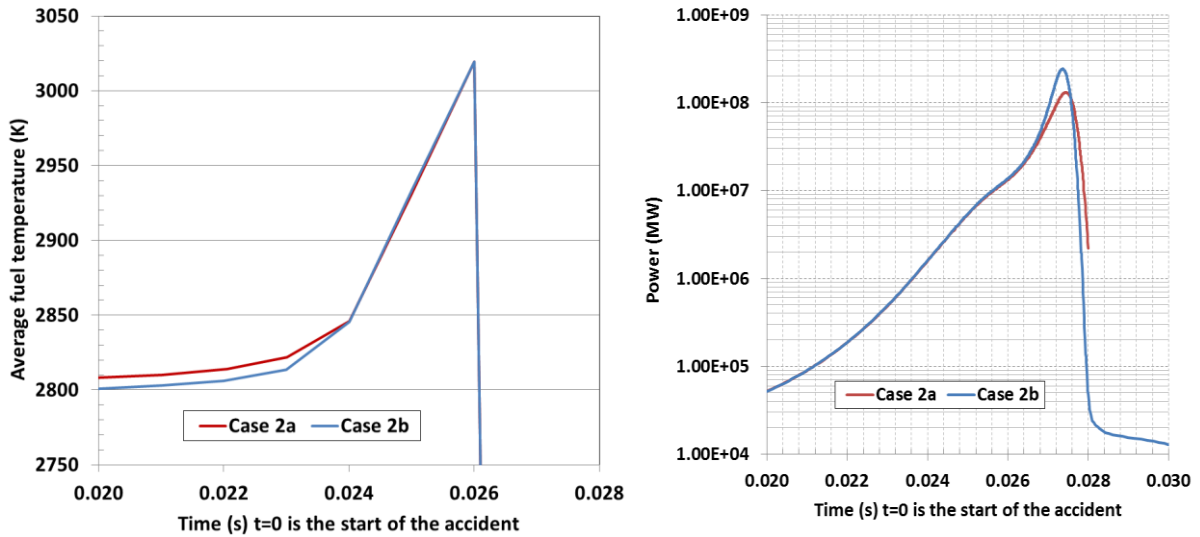
Figure 7-16. Average fuel temperature in the hottest cell, in case of sphere-pac fuels. Total power evolution in case of sphere-pac fuel, 50$/s UTOP starts at 0 s.
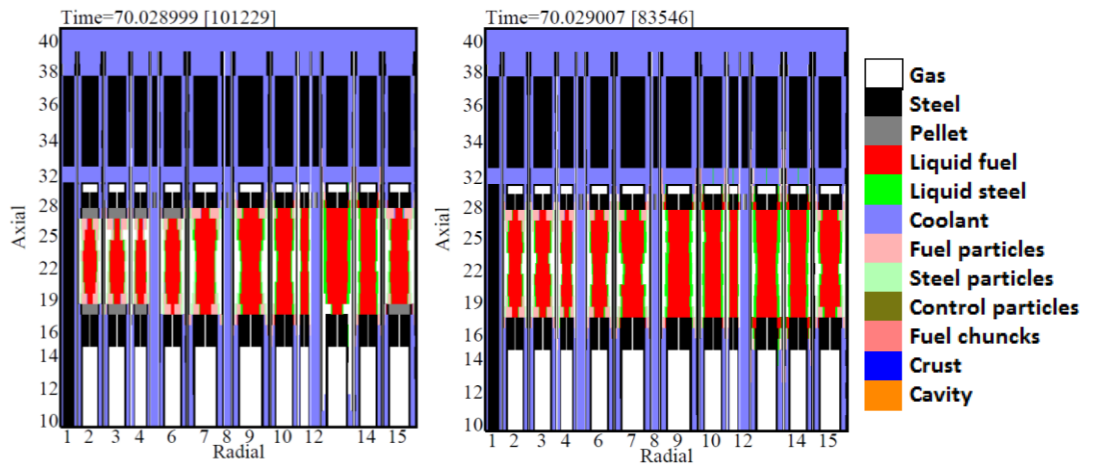
Figure 7-17. Snapshots 29 ms after the UTOP starts. Left: case 2a, right: case 2b.

The preceding discussion shows that the porosity inclusion in the thermal penetration length calculation has only a small impact on the core response to a reactivity transient since the transient evolution is almost the same in both cases. Therefore, the initial assumption of SIMMER-III to consider the properties of fully dense fuel for the thermal penetration length calculation is still a reasonably valid approximation and can be applied to sphere-pac fuels too.

7.5. Conclusions

As SIMMER has been mainly developed to describe already disrupted pin and core configurations, the SIMMER-III transient pin models are simpler than the ones found in advanced fuel performance codes. The models should describe the phenomenological range from steady state to pin break-up and failure and should not put an undue load on computing time. Two models can be applied i.e. the SPIN and DPIN models, both having their strengths and limitations. For the purposes targeted in the FP7-PELGRIMM project and due to the lack of experimental data for sphere-pac fuel behavior, the SPIN model was chosen for simulations. Using this model implies however some constraints like considering a special treatment for the central hole.

The conductivity of sphere-pac fuels is very different from the one of standard pellet fuels especially at BOL and needs special attention. A literature overview revealed that the Hall and Martin model for powder beds might be the most suitable candidate for modeling the thermal conductivity of these fuels. Equations adapted to the SIMMER framework have then been obtained for both pellet and sphere-pac fuel at BOL and EOC3 conditions. The low thermal conductivity of sphere-pac fuels at BOL raises some concerns related to the safety behavior of this fuel for the first hours of operation. Specific reactor start-up procedures are required to cope with this phase. Nevertheless the fairly quick fuel restructuring enhances the thermal conductivity rather soon, within a few hours or days after the start-up with fresh fuel. In the next chapter, these fuels, with their specific thermal conductivities, are analyzed both at steady and under transient conditions, when filled in the CP-ESFR cores

Chapter 8

SIMMER-III CODE SIMULATIONS

This chapter addresses the behavior of a core loaded with sphere-pac fuels. Comparison is made with the standard pellet case. The aim of the analyses is to investigate whether introducing sphere-pac fuels into a sodium cooled fast reactor (SFR) is possible in principle (i.e. no optimization is performed at this stage). As detailed in Chapter 4, the Working Horse (WH) and the CONF2 cores are under study: steady state conditions are analyzed based on which an unprotected loss of flow (ULOF) accident is considered.

The cores are assumed to be either in beginning of life (BOL) or in equilibrium conditions. For each case, the considered fuel state is considered i.e. either non-restructured or restructured in case of sphere-pac fuels and with or without gap closure in case of the pellet pins. To start the analysis, traditional MOX fuel is used. As sphere-pac fuels are assumed to present a better safety behavior when containing minor actinides (MAs) than pellet fuels, americium is additionally loaded into the cores in order to evaluate its impact on the core safety performances. Finally, the developed expansion model is applied to get an insight on its effect on the core behavior under transient conditions.

8.1. Modeling

The two core designs under study presented in detail in Chapter 4 have to be modeled with SIMMER-III. This section therefore recalls the main core and pin characteristics of each of the two cores and describes the performed modeling.

8.1.1. CP-ESFR WH

The CP-ESFR WH core is a 3600 MW$_{th}$ pool-type sodium cooled fast reactor core - Figure 8-1 (a). The Working Horse core consists of two core zones – an inner and an outer one – with different enrichments, specifically chosen to flatten the power profile at equilibrium. The inner core is composed of 225 sub-assemblies (SAs) with a plutonium enrichment of 14.43 at% at BOL while the outer core comprises 228 SAs enriched in plutonium with 16.78 at%. Each sub-assembly is a hexagonal wrapper tube of EM10 steel containing 271 pins in a triangular arrangement spaced by

helical wires. The original core uses pelletized fuels and has been fueled with sphere-pac pins later on for the purposes of this study. The average and maximum core burnups are of about 100 GWd/t_{HM} and 145 GWd/t_{HM} respectively, and the average power density is 206 W·cm^{-3} [187; 9]. The core is surrounded by altogether 3 rows of EM10 steel SAs, which serve as radial reflector – see Figure 8-1 (b).

(a)

(b)
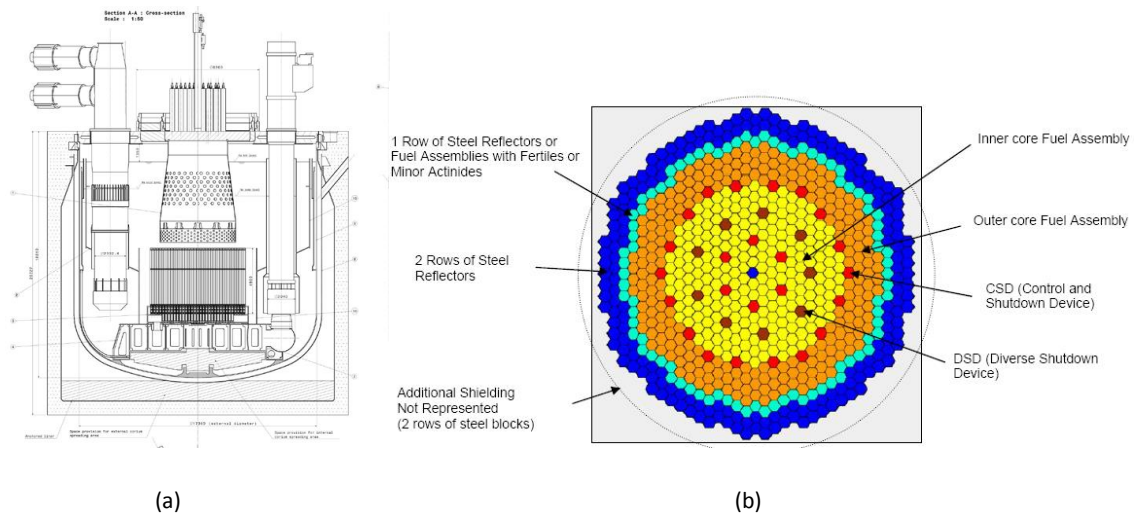
Figure 8-1. CP-ESFR Working Horse reactor vessel design (a) and core radial layout (b) [6; 14].

The core control is ensured by means of 24 control and shutdown devices (CSDs) and 9 diverse shutdown devices (DSDs). All safety rods are assumed to be withdrawn from the core.

Both steady state and transient analyses are performed for the CP-ESFR WH (steady state conditions are detailed in Table 8-1) with two different loading configurations: with the standard pellet-filled pins and with the sphere-pac pins. Core dimensions and main geometrical parameters are reported in Table 8-1 for both arrangements. It is considered that the core can be loaded with sphere-pac instead of pellet fuels assuming pins with a smear density as high as 83.41% can be fabricated based on [137]. However, if the required smear density cannot be reached, the fuel enrichment should be increased in order to compensate the mass discrepancy to reach criticality. As there is a strong correlation between the attainable sphere packing density and the thermal conductivity the core design will have to be changed.

Table 8-1 which summarizes the geometric characteristics of pellet and sphere-pac fuel pins also depicted in Figure 8-2, highlights the differences between the two configurations, which mainly reduces to a change in the fuel smear porosity, due to the absence of fuel-cladding gap in the sphere-pac configuration as well as the presence or absence of the 'central hole'. It has to be stressed that no design modification has been made when substituting the pellet fuel with sphere-pac fuel: expressed in other words, the pin design for sphere-pac fuel is exactly the same as the one defined for pellet fuel in the CP-ESFR WH [6].

Table 8-1. Main core parameters of the CP-ESFR Working Horse core [6; 187].

Parameter	Value
Reactor power (MWth)	3600
Core inlet temperature (˚C)	395
Core outlet temperature (˚C)	545
Average core structure temperature (˚C)	470
Average fuel temperature (˚C)	1227
Fuel assemblies pitch (mm)	210.8
Internal flat-to-flat distance of wrapper tube (mm)	197.3
External flat-to-flat distance of wrapper tube (mm)	206.3
Wrapper thickness (mm)	1.5
Fuel pins per sub-assembly (#)	271
CSD (#)	24
DSD (#)	9
Inner fuel sub-assembly (#)	225
Outer fuel sub-assembly (#)	228
Inner and Outer reflector (#)	84+186
Overall sub-assembly length (mm)	4739

Table 8-2. Basic fuel parameters for the sphere-pac and pellet pins in inner and outer core zones [6; 187].

Parameter	Value	
	Pellet	Sphere-pac
Overall pin length (mm)	2539	
Cladding outer diameter, cod (mm)	10.73	
Cladding thickness, thc (mm)	0.5	
Wire diameter (mm)	1.0	
Fuel outer diameter, fod (mm)	9.43	9.73
Central hole diameter (mm)	2.41	0.00
Fuel-clad radial gap (mm)	0.15	
Fuel porosity (%TD)	5.00	1.44
Smear porosity	11.20[19]	16.59[20]
Active height (mm)	1000	
Upper reflector height (mm)	150	
Lower reflector height (mm)	300	
Upper gas plenum height (mm)	76	
Lower gas plenum height (mm)	913	

---

[19] Smear porosity in case of pellet fuel, for SIMMER-III calculations, is given by the fuel porosity and the gas amount in the pellet inner hole. It is calculated as the void section normalized to the pellet outer section.
[20] Smear porosity in case of sphere-pac fuels is given by the porosity of the fuel microspheres and the pin gas content. It is calculated as the void section normalized to the inner clad section.

Figure 8-2. Layout of fuel SAs and fuel pins in case of sphere-pac (upper part) and pellet fuel (lower part) [6] (thw=wrapper thickness, xwin= Internal flat-to-flat distance of wrapper tube, xwout= external flat-to-flat distance of wrapper tube, wtptch= Fuel assemblies pitch, fid = fuel inner diameter).

The three-dimensional HEX-Z core has been modeled with SIMMER-III in a two-dimensional RZ geometry preserving the volumes – Figure 8-3. In particular, in the radial direction, this means that the core has been transformed into concentric rings, whose radii are defined such that the cross-sectional areas of the original layout are kept in the new one. During the CP-ESFR project [6; 187], the core has been modeled of 25 rings, as described in Table 8-3. The fuel sub-assemblies have been grouped into 12 fuel rings (8 in the inner core and 3 in the outer core). The inner fuel SAs are located at the radial mesh numbers 2, 3, 4, 6, 7, 9, 10 and 11 while the outer ones are found at ring numbers 13, 14 and 15. The first radial mesh is used to model the inner dummy SA composed of steel. CSDs are located at rings 5 and 12 while DSDs are in ring 8. The reflector is modeled by three rings located at the radial mesh number 16, 17 and 18.

Figure 8-3. SIMMER-III radial layout of the CP-ESFR Working Horse core [13].

Table 8-3. SIMMER-III radial modeling of the CP-ESFR Working Horse core [6].

Radial Ring	SAs/Ring	Radius (m)	ΔR (m)	Comments
1	1	0.11067792	0.11067792	Central Dummy
2	6	0.29282625	0.18214833	Inner Core
3	12	0.48243387	0.18960762	Inner Core
4	12	0.61622858	0.13379471	Inner Core
5	6	0.67322751	0.05699893	CSD
6	24	0.86442219	0.19119468	Inner Core
7	42	1.12325821	0.25883602	Inner Core
8	9	1.17130501	0.04804680	DSD
9	57	1.43881296	0.26750795	Inner Core
10	48	1.63038757	0.19157461	Inner Core
11	24	1.71818337	0.08779580	Inner Core
12	18	1.78119256	0.06300919	CSD
13	72	2.01360827	0.23241571	Outer Core
14	66	2.20524194	0.19163367	Outer Core
15	90	2.44244881	0.23720687	Outer Core
16	84	2.64471601	0.20226720	Radial Reflector
17	90	2.84552050	0.20080450	Radial Shield
18	96	3.04515168	0.19963117	Radial Shield
19	300	3.59830923	0.55315756	Bypass
20	468	4.32211095	0.72380172	Bypas+Barrel
21		5.14561095	0.8235	Hot/Cold Pool
22		5.96911095	0.8235	Hot/Cold Pool
23		6.40651095	0.4374	HX/Pump
24		6.84391095	0.4374	HX/Pump
25		8.50651095	1.6626	Cold Pool

Axially, as depicted in detail in Figure 8-4, the core includes: the sodium below the core; the assembly lower part; the lower gas plenum; the lower axial blanket made of steel, the fissile height; the upper gas plenum; the upper steel blanket, the assembly upper part; the sodium plenum; the steel reflector. The total axial height of the core is divided into 50 axial meshes. The whole core geometry and mesh distribution as modeled in SIMMER-III are displayed in Figure 8-4.
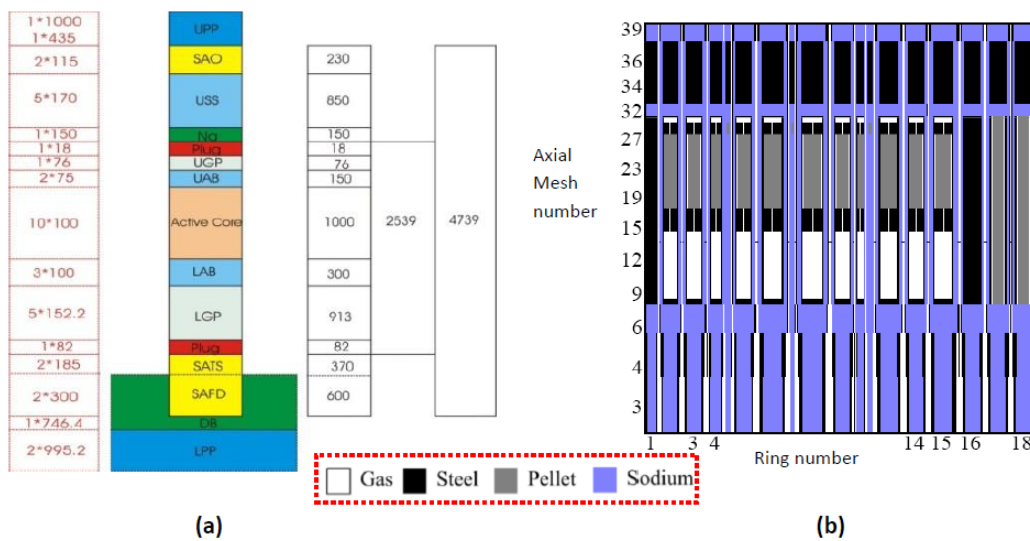
Figure 8-4. CP-ESFR WH core axial geometry and mesh distribution (a) and related SIMMER-III modeling (b) [13].

Figure 8-5 displays the CP-ESFR WH core enclosed in the vessel, as modeled with SIMMER-III. Additionally, heat exchangers and 3 pumps present in the CP-ESFR reactor have been modeled [13].
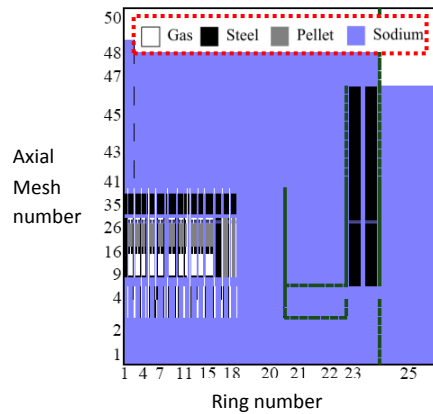
Figure 8-5. Overall SIMMER-III modeling of the CP-ESFR Working Horse core enclosed in the reactor vessel [13].

8.1.2. CONF2 Core

The CONF2 core is an optimized version of the CP-ESFR WH core aiming at decreasing the positive sodium void worth. The radial structure of the WH core is preserved, while the enrichment is slightly modified (14.67 at% and 17.07 at% in inner and outer core, respectively). The two cores differ mainly axially, as can be seen from Figure 8-6, with the replacement of the lower axial steel blanket with a fertile blanket (as already mentioned in Chapter 4), the suppression of the upper axial blanket and the enlargement of the sodium plenum (which has been put closer to the fissile part). The extensive changes to the upper part of the SAs also include the introduction of an absorber layer above the sodium plenum. Apart from axial material rearrangements, the pin design has been preserved and is equal to the WH core one. The SIMMER modeling has been accordingly modified [9].
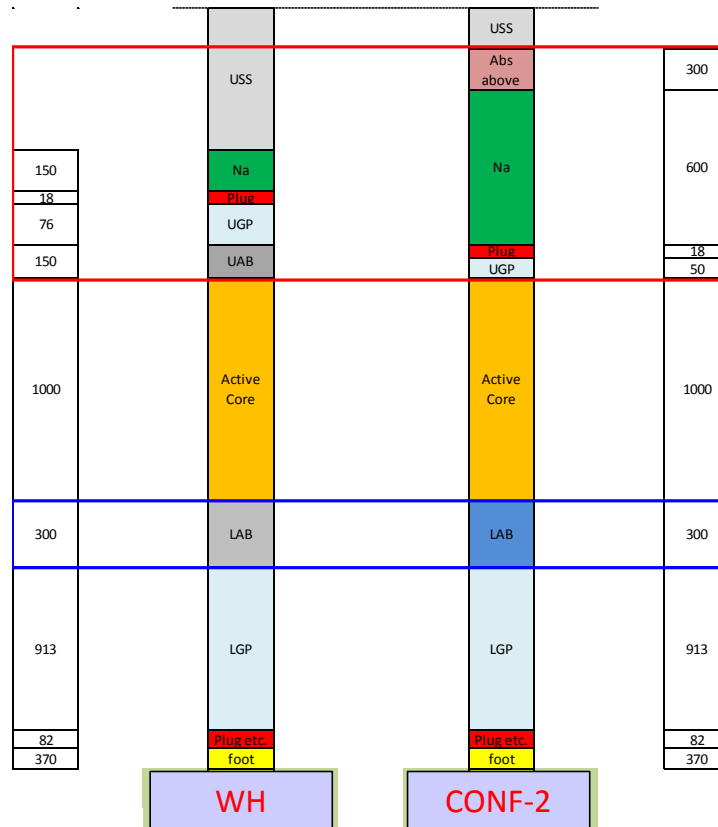
Figure 8-6. Axial layouts of the CP-ESFR Working Horse and CONF2 cores. Differences are highlighted in the red and blue boxes.

8.2. Steady state

Within the CP-ESFR project, the WH core has been extensively analyzed with pellet pins [9]. On the other hand no complete safety analyses have been performed for the CONF2 core within the CP-ESFR project. Hence in this thesis a first safety assessment has to be performed for the latter one loaded with pellet fuel as well as with sphere-pac fuel.

As already described in the previous section, one essential difference between pellet and sphere-pac pins used in the considered cores is that the pellets are annular whereas the non-restructured sphere-pac pins do not have a central hole, at least at BOL. In addition, the thermal conductivity of non-restructured sphere-pac fuels (i.e. at BOL) is very low compared to pellet fuels, as extensively expressed in Chapter 7. As a consequence, the central temperature of the sphere-pac pins at BOL is expected to be higher than the pellet one. This case is therefore the most conservative one. On the contrary, the heat transfer between the fuel surface and the cladding is enhanced in sphere-pac pins at BOL, due to the absence of the gap between the fuel and cladding tube, i.e. the gap is fully filled with particles. This advantage, however, vanishes when the gap in the standard pellet fueled pins closes.

These considerations are evident considering the cases described in Chapter 7 for BOL fuel, which are recalled hereafter for the sake of clarity – Figure 8-7.

(a) (b) (c)

Hole + gap
Fuel porosity 5%
Smear porosity 11.20%

No hole + no gap
Smear porosity 16.59%
Porosity for conductivity
calculation 17.63%

No hole + no gap
Smear porosity 16.59%
Porosity for conductivity
calculation 17.63%
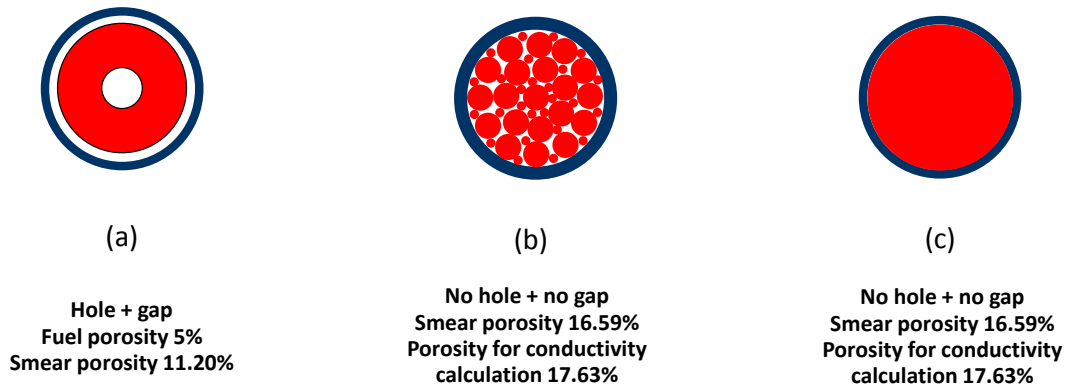
Figure 8-7. Cases considered for the CP-ESFR cores at BOL: (a) standard pin design (b) non-restructured sphere-pac pin (c) full pellet.

8.2.1. Working Horse Core

8.2.1.1. Beginning of life conditions

The radial coolant temperature profile at inlet and outlet in all three cases can be seen in Figure 8-8 while the radial profile of coolant mass flow per SA is provided in Figure 8-9. The radial coolant outlet temperature profile is rather flat in all three cases and the mass flow is appropriate to each SA power in order to meet the safety margins of 823 K on the clad. It has to be mentioned that the gagging scheme is optimized for the pellet loaded reference core and has been used for the sphere-pac fuel cases as well.
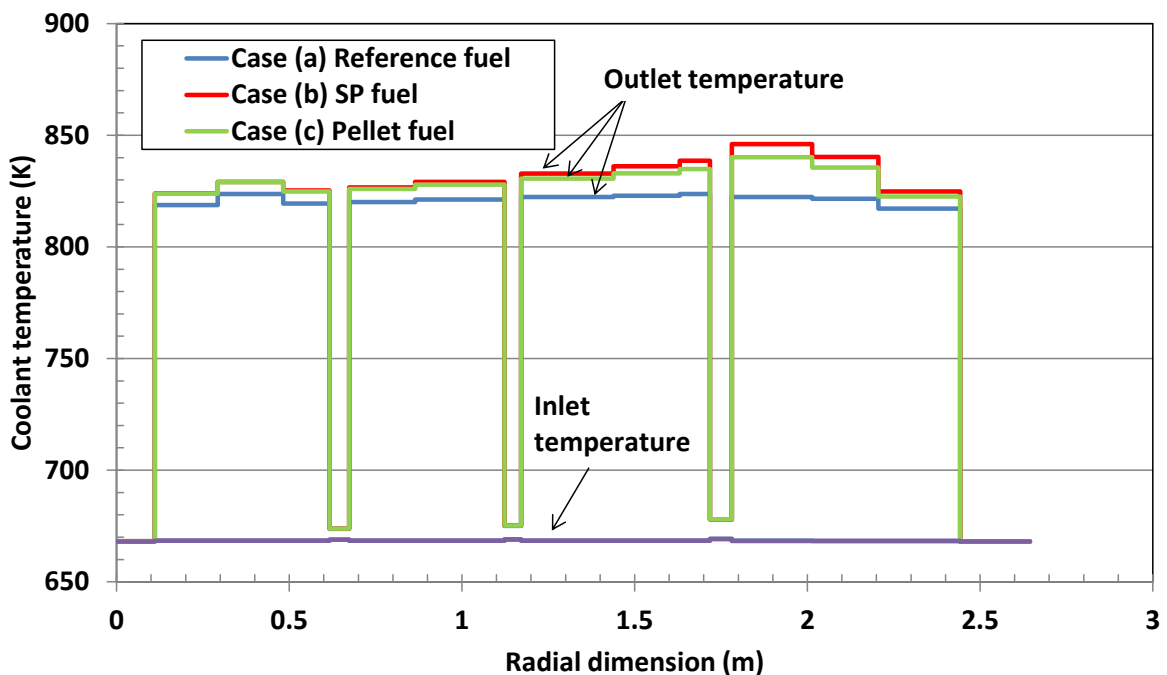
Figure 8-8. Outlet and inlet coolant temperature distribution in the BOL Working Horse core.
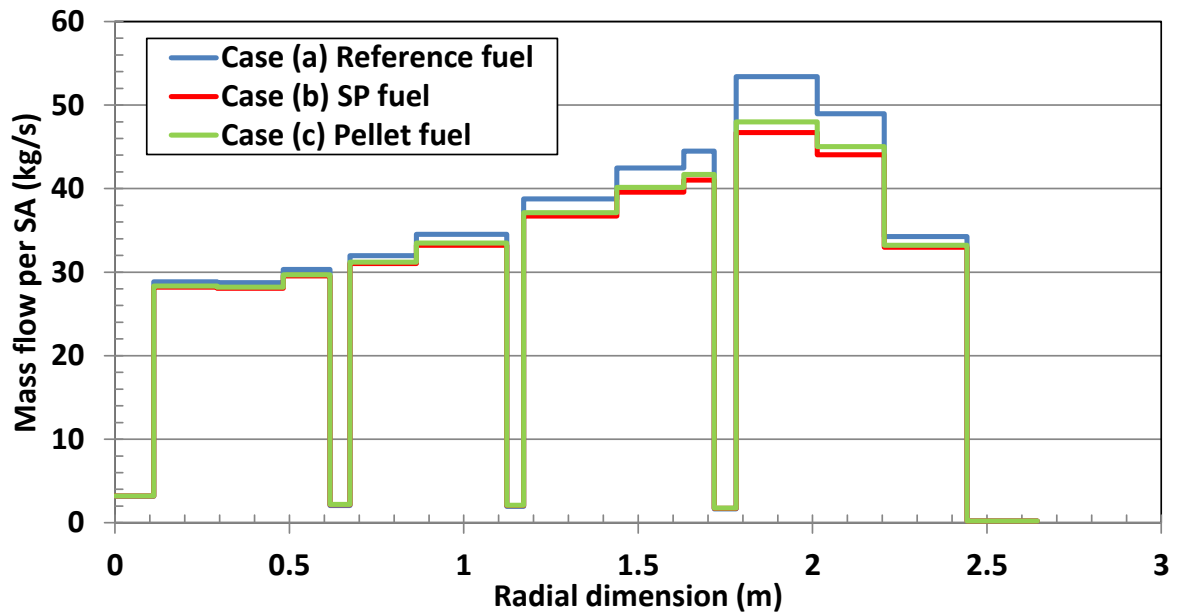
Figure 8-9. Mass flow per sub-assembly in the BOL Working Horse core for the three considered cases.

In all three cases the radial cladding temperature profile at core midplane is rather flat and stabilizes at about 775 K after 50 s of calculations, the maximum clad temperature limit being of 823 K. Therefore, the safety limits of the cladding are met.

As expected, the fuel surface temperature is globally higher by 45 K in the reference pellet (case (a)) than in the sphere-pac fuel case (case (b)). This trend is not followed in the hottest SIMMER ring, where a gap closure in the pellet fuel occurs due to its high power and hence reduces the fuel surface temperature. The fuel average temperature reaches a maximum difference of 831 K between sphere-pac and pellet fuel (case (b) and (a), respectively) in the hottest channel, leaving a lower margin to melting of 240 K in case of the sphere-pac pin than in case of the pellet pin, see Figure 8-10. One can notice from the comparison of case (b) and (c) that roughly half of the temperature difference is attributed to the thermal conductivity difference only.

Even though the fuel average temperature stays below its melting point of 3002 K, the center temperature of sphere-pac fuel pins – determined by using bulk and surface node temperatures – exceeds the melting point in at least 3 rings (SIMMER RZ modeling) and leads to fuel melting at steady state. This is also caused by the WH BOL power profile which is very peaked in the outer core part. Additionally, full nominal power has been assumed for BOL: decreasing this power is necessary to prevent pin failures.
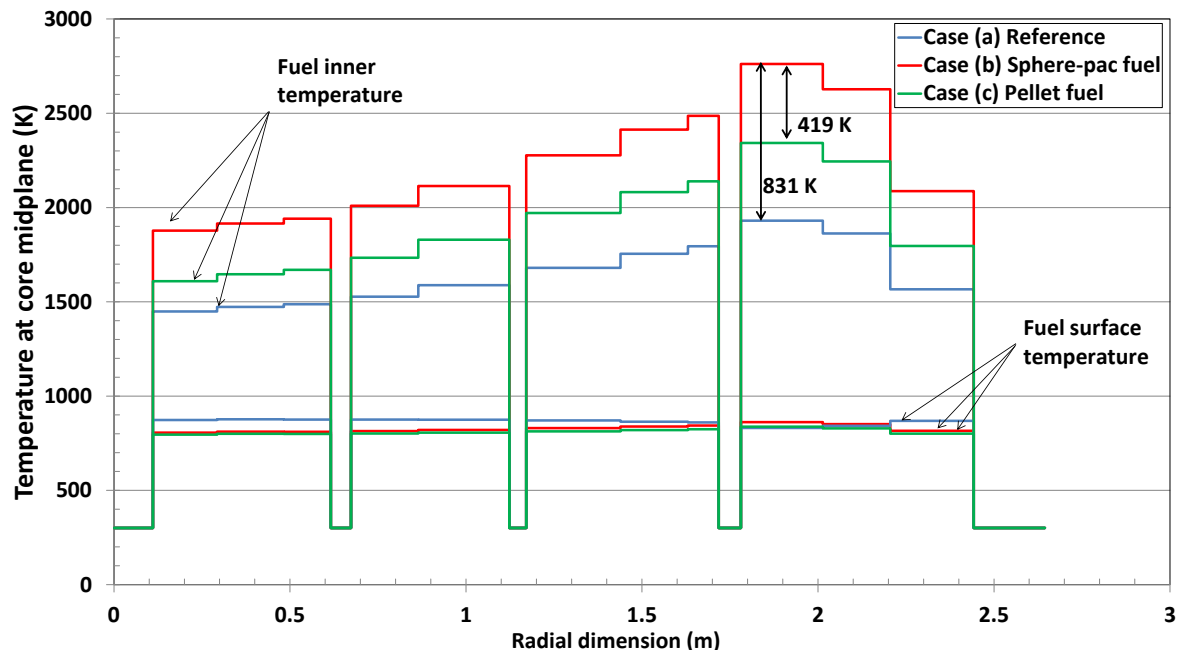
Figure 8-10. Bulk (called inner) and surface temperature distributions at core midplane in the CP-ESFR Working Horse core at BOL for different fuel loadings.

Attention is now devoted to the hottest ring (ring 13 see Figure **8-4**), for which axial temperature profiles are shown in Figure 8-11. There, the cladding temperature at steady state reaches 836 K in case of pellet and 856 K in case of sphere-pac pins, and the nominal conditions limit on cladding temperature, set at 823 K, is thus exceeded.

It has to be stressed, that the reference pellet fuel (case (a)) axial temperature distribution reflects the large thermal expansion of the pellet especially at core midplane. As the core is at nominal power, fuel-cladding contact is made over the central part of the pin, which experiences an enhanced gap conductance. As a consequence, while on the bottom and top of the fuel column, the fuel surface temperature of the sphere-pac pin is significantly lower than the one in the pellet pin, in the central part the tendency is reversed. Indeed, where both configurations present no gap, i.e. in the central region, the heat transfer is mainly governed by the thermal conductivity, which is higher for the pellet than for the sphere-pac pin. On the contrary, at the bottom and top of the column, the fuel temperature is not high enough to lead to a gap closure in the pellet pins (while it is still not-existing for the sphere-pac configuration), therefore hindering the heat exchange, which results to be enhanced for sphere-pac pins despite their lower thermal conductivity [188].

As concerns the fuel bulk temperature at nominal power at BOL, the sphere-pac pin presents considerably higher temperatures than the pellet pin, as expected from the large thermal conductivity difference (Figure 8-11(b)). Comparing case (b) and case (c) confirms that the fuel thermal conductivity mainly impacts the fuel bulk temperature, having only a very small effect on the fuel surface temperature, the main one being the gap condition (open or closed).
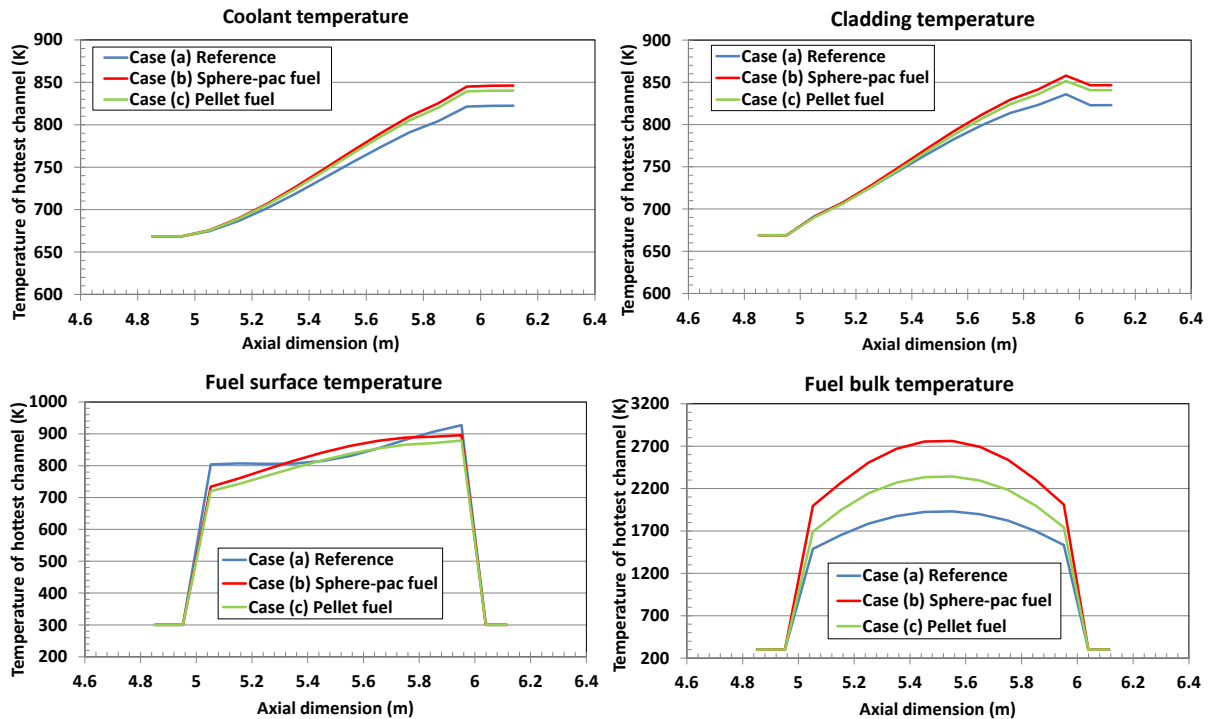
Figure 8-11. Axial temperature distributions of coolant, cladding, fuel in the hottest ring of the CP-ESFR Working Horse core at BOL.

8.2.1.2. End of cycle 3 conditions

In order to obtain information on a representative core, it is important to analyze the core at equilibrium, i.e. with EOC3 compositions. The two cases detailed in Chapter 7 are considered (Figure 8-12): a pellet fuel case, with closed gap and a sphere-pac fuel case, with no gap and restructured fuel as these configurations are representative for a fuel at this stage of irradiation.

(a)   (b)
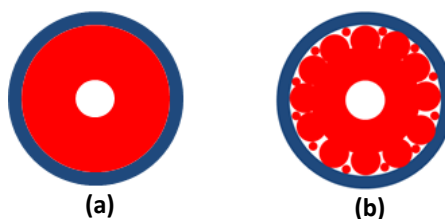
Figure 8-12. EOC3 pellet (a) and sphere-pac fuel (b).

Because of the similar thermal conductivities of the two fuels at this stage of irradiation (Figure 8-13) no significant difference is observed between the two configurations. The maximum fuel bulk temperature reaches 1620 K and remains appreciably below the melting temperature of 3002 K (Figure 8-14). Even if the hottest ring is now considered, no significant difference between sphere-pac and pellet fuel can be observed (Figure 8-15). In addition to the better fuel conductivity at this stage of irradiation, the Working Horse core radial power profile and related gagging scheme are

optimized to obtain a flat outlet coolant temperature distribution and stay below a clad temperature safety limit of 823 K.
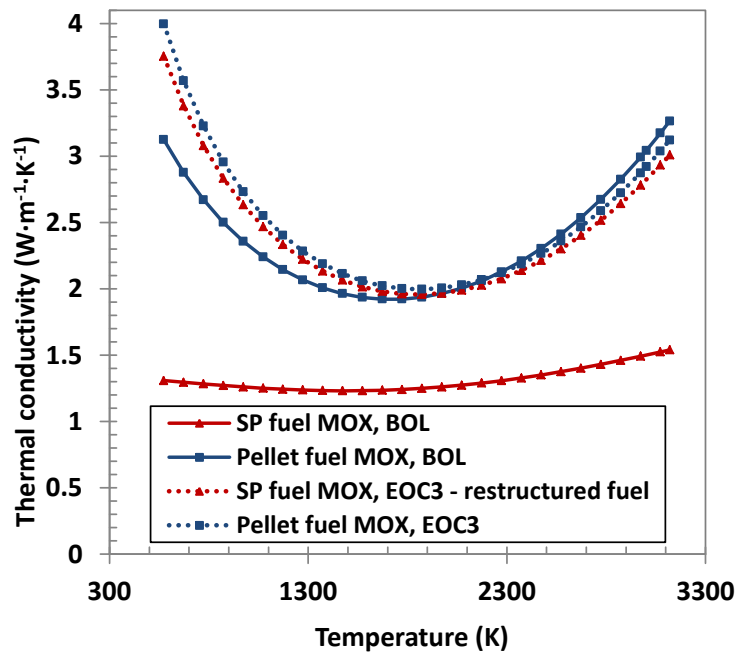
Figure 8-13. Thermal conductivities for sphere-pac and pellet fuels at BOL and EOC3 [188].
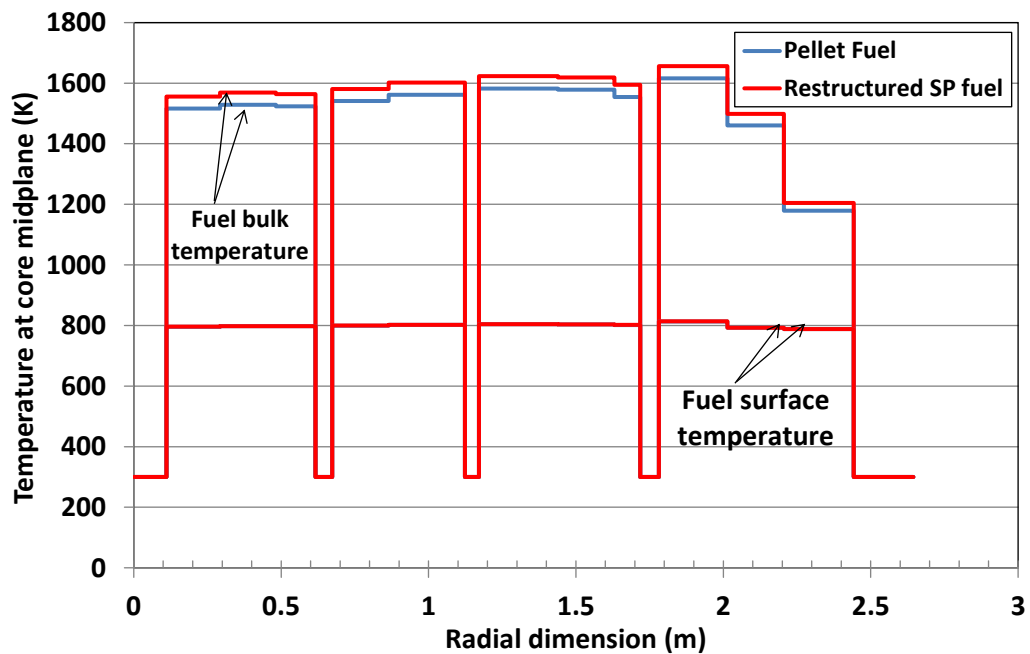
Figure 8-14. Bulk and surface temperature distributions at core midplane in the CP-ESFR Working Horse core at equilibrium with EOC3 compositions for different fuel loadings.
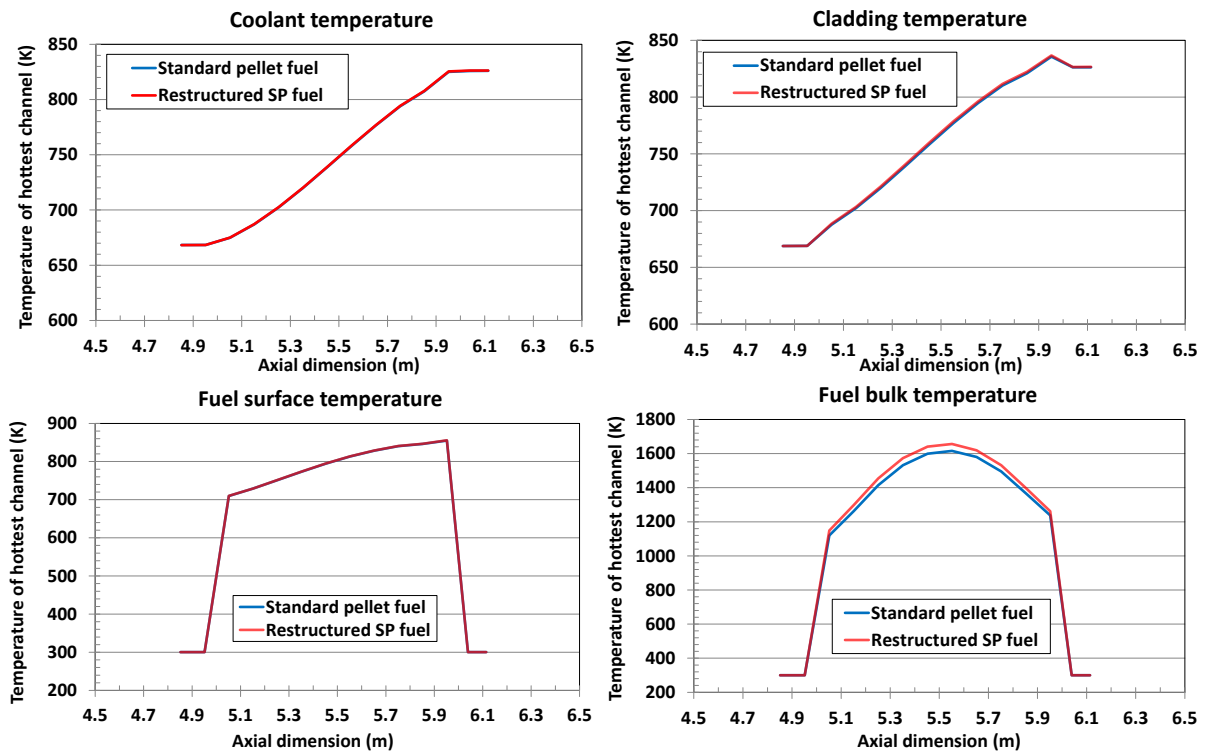
Figure 8-15. Axial temperature distributions of coolant, cladding, fuel in the hottest ring of the CP-ESFR Working Horse core at equilibrium.

8.2.2. CONF2 Core

8.2.2.1. Beginning of life conditions

The transition from the WH core to the CONF2 core is extremely efficient in the optimization of the sodium void worth, which changes, at BOL, from ~1400 pcm (see Chapter 4) to ~500 pcm (extended sodium void reactivity effect).

As already mentioned, no complete safety analysis of this core loaded with pellet fuel has been performed within the CP-ESFR project. Therefore, calculations for a pellet loaded CONF2 core are first performed to obtain a reference state.

Figure 8-16 depicts the radial temperature distribution of fuel at core midplane both in the WH and CONF2 cores loaded with either pellet or non-restructured sphere-pac fuels. The conclusions are the same as in case of the WH core: locally, in the outer high power core zone, centerline temperatures above the melting point are reached at steady state caused by the non-optimized CONF2 BOL power profile which is very peaked in the outer core part (as shown in Chapter 4). It confirms that a starting procedure of the reactor is necessary (i.e. a lower power is required) to achieve a restructured fuel condition, whose thermal properties are similar to those of the pellet fuel of same density.

It can be noticed from Figure 8-16 that the fuel average temperature reaches a maximum difference of 898 K between non-restructured sphere-pac and pellet fuel in the hottest channel, further reducing the margin to melt to 111 K in case of the sphere-pac pin.

In order to evaluate the benefit of such a starting procedure with respect to safety margins, an additional case with the thermal conductivity of the restructured EOC3 fuel is considered in the BOL core. Even though this is not the accurate formulation, it gives a hint on the benefits of reaching a restructured fuel state before reaching the full core power.

As expected, the restructured fuel in BOL core conditions significantly increases the margin to melt when considering the bulk fuel temperature (by about a factor 10 in comparison with the non-restructured sphere-pac case where it was of 111 K). Moreover, as already known from the similar radial temperature distribution in the CONF2 and in the WH core, the axial temperature distributions of fuel, cladding and coolant in the hottest ring are similar to the ones of the CP-ESFR WH core, and details are therefore omitted here but can be found in Appendix G.
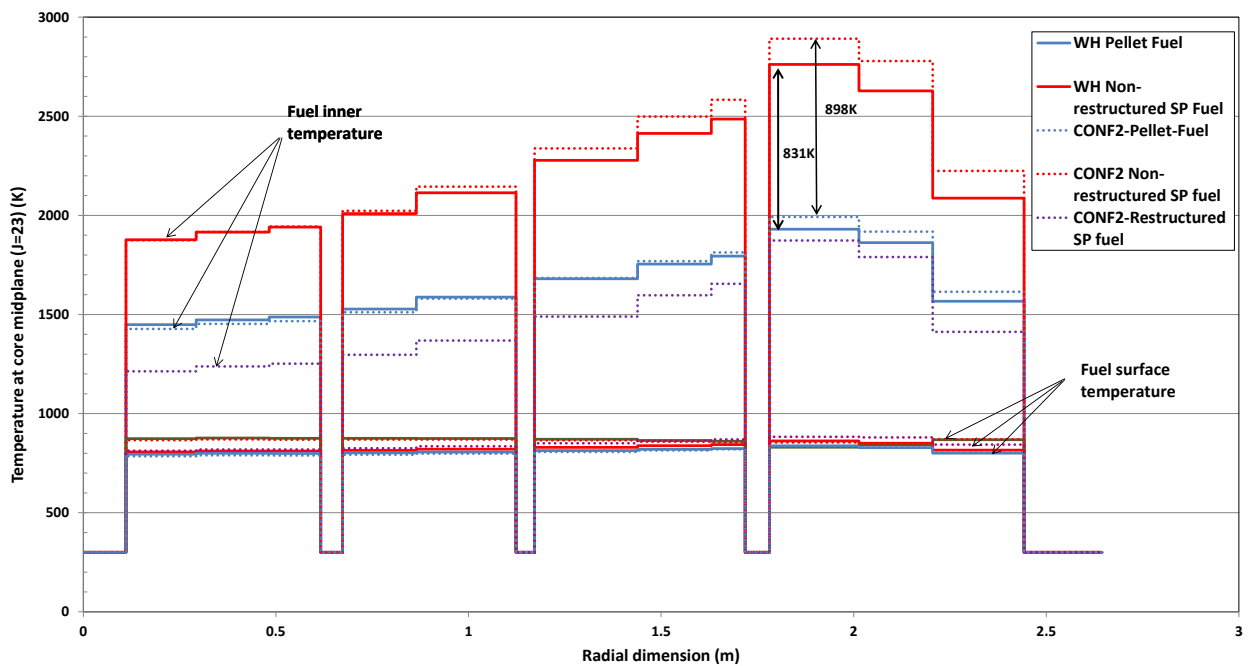
Figure 8-16. Bulk (called inner) and surface temperature distributions at core midplane in the CP-ESFR CONF2 core and the WH core at BOL for different fuel loadings.

8.2.2.2. End of cycle 3 conditions

In addition to the BOL core conditions, the equilibrium condition of the CONF2 core is analyzed. The radial temperature profile in the core for both fuel types is depicted in Figure 8-17 in addition to those of the WH core. No significant difference between the two cores can be noticed, as expected from the similar thermal conductivities of sphere-pac and pellet fuel at this stage of irradiation. The maximum fuel bulk temperature reaches 1656 K and remains appreciably below the melting temperature of 3002 K. The hottest ring shows the same tendency as in the WH case and similar conclusions can be drawn (details can be found in Appendix H).
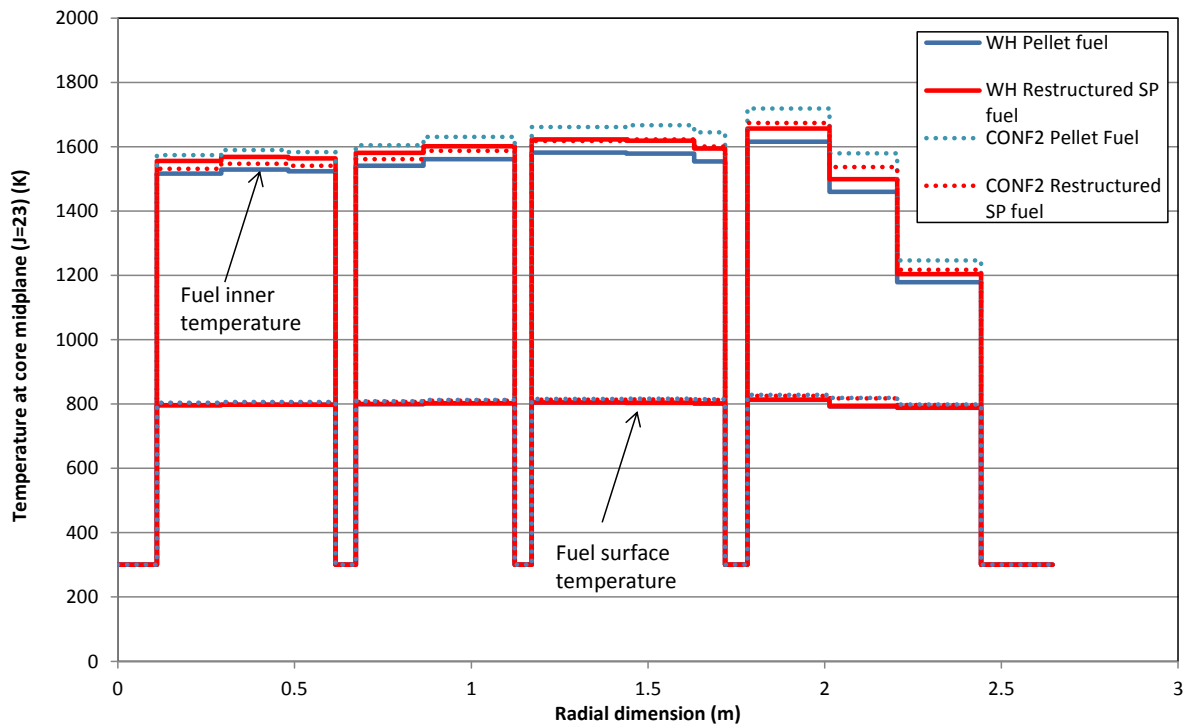
Figure 8-17. Bulk (called inner) and surface temperature distributions at core midplane in the CP-ESFR CONF2 core at equilibrium with EOC3 compositions for different fuel loadings.

8.3. Simulation of an unprotected loss of flow accident

Starting from the different steady states, an unprotected loss of flow (ULOF) simulation is performed with SIMMER to get a first insight into the accidental transient behavior of a sphere-pac fuel loaded core and to investigate model development needs for this innovative fuel. At first the WH core is analyzed [188], followed by the CONF2 core [189].

Since the ULOF simulation is started from steady state it requires the simulation of effects like axial fuel and clad expansion: the need for experimental support is evident. For a first calculation, the transient is simulated without any core expansion feedbacks, its main purpose being the identification of modeling needs. Starting from steady state, the loss of flow is modeled through a pump coast down with a flow halving time of 10 s, according to the following law (Figure 8-18):

$$\Delta p(t) = \Delta p_0 \frac{1}{\left(1 + \dfrac{t}{10}\right)}$$
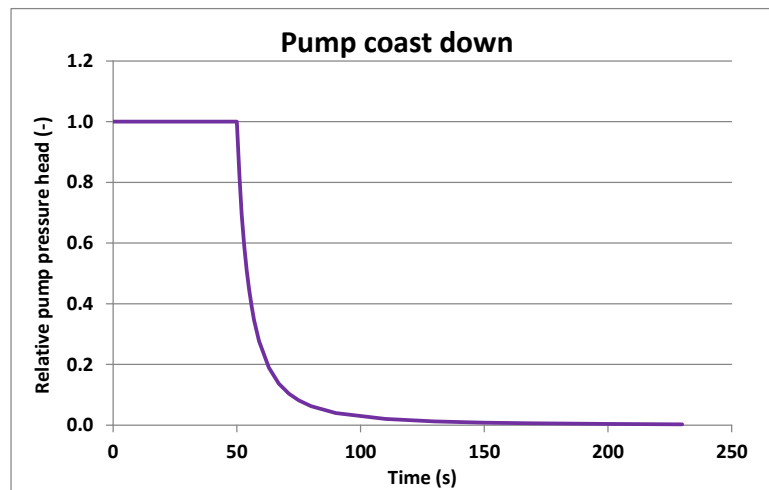
Figure 8-18. Assumed pump coast down for the unprotected loss of flow.

8.3.1. Working Horse Core

For the subsequent analyses the WH core at equilibrium is considered. Due to the lack of coolant circulation, heat is no more adequately removed from the fuel pins and the coolant temperature rises. The reactivity increases smoothly (Figure 8-19), as the rise in fuel temperature makes the Doppler effect counterbalance the sodium density effect. In case of the pellet fuel loaded core, sodium boiling starts at 21.5 s in the 13th channel, followed 2.8 s later by channels 9 and 10, and quickly after by channels 7, 11, 3 and 6 (Figure 8-20). During this voiding propagation, the reactivity is oscillating. 4.13 s after boiling onset all fuel channels, except the outermost one, experience voiding. At this time, reactivity reaches 1 $ in the calculation putting the reactor in a prompt supercritical state and triggering the first power peak. Simultaneously, fuel melting and pin disruption occurs in channel 13. Around 25.63 s, overall fuel melting has taken place. Due to fuel discharge out of the core region, the reactivity becomes negative and power rapidly decreases. It can be observed that under the previously described simulation conditions the accident evolution is similar for both fuel types (Figure 8-19 and Figure 8-21). Both first power peak values, and consequently both thermal energy releases, are close, leading to the conclusion that the accident behavior is independent of the fuel type in the current simulation (as already expected from the very similar thermal conductivities for both fuels at this stage of irradiation).
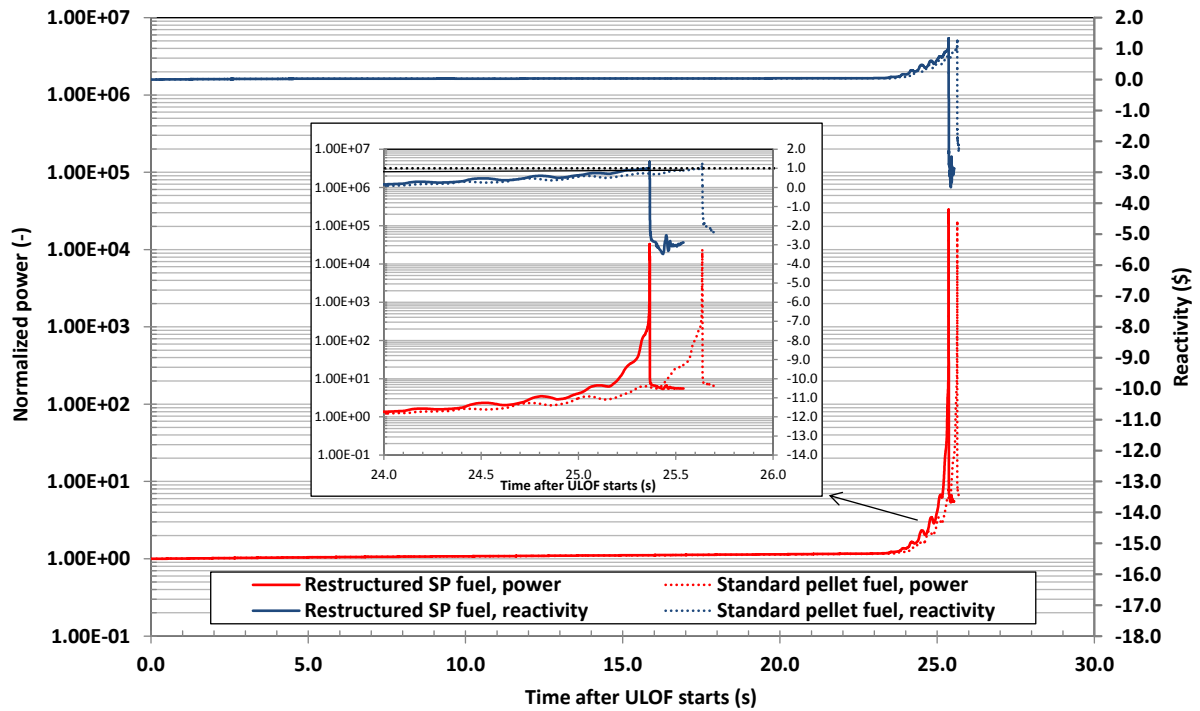
Figure 8-19. Normalized power and reactivity evolution during a ULOF in the CP-ESFR Working Horse at equilibrium with EOC3 conditions, either pellet or sphere-pac loaded [188]. 20 s here correspond to 70 s in Figure 8-20 and 8-21.
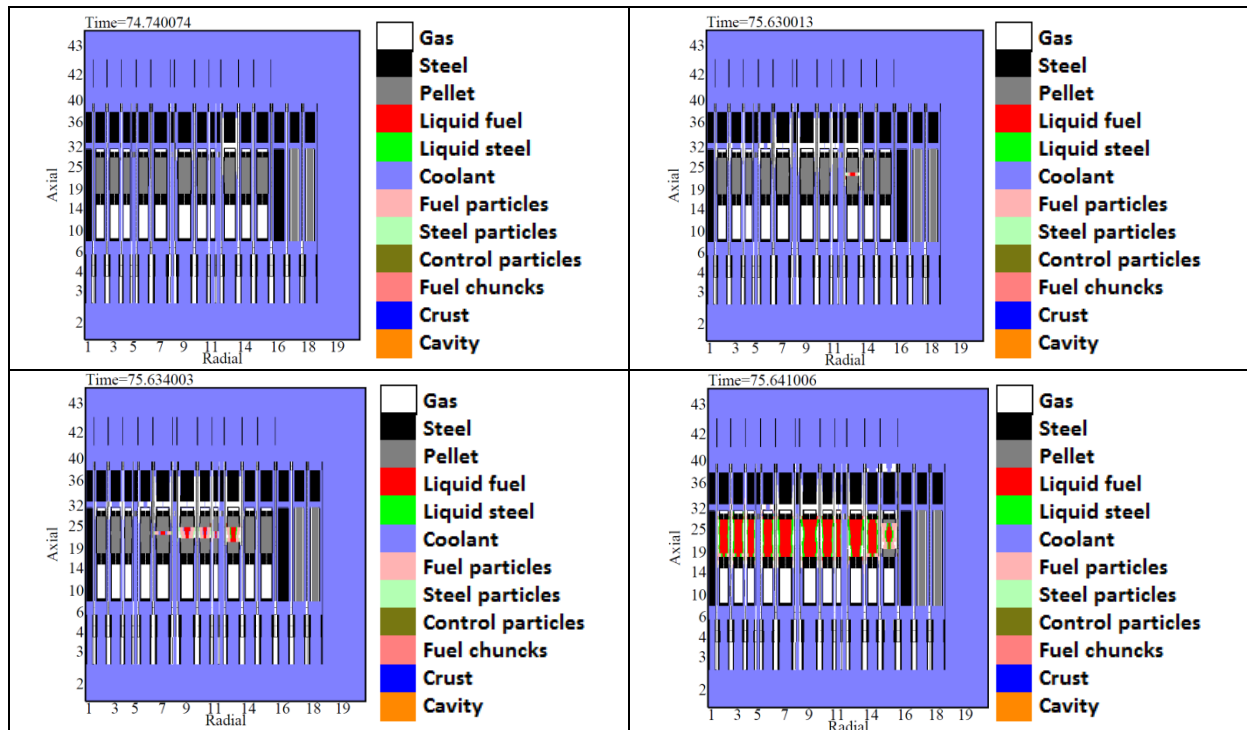
Figure 8-20. Material distributions during the ULOF of the WH pellet core at equilibrium.
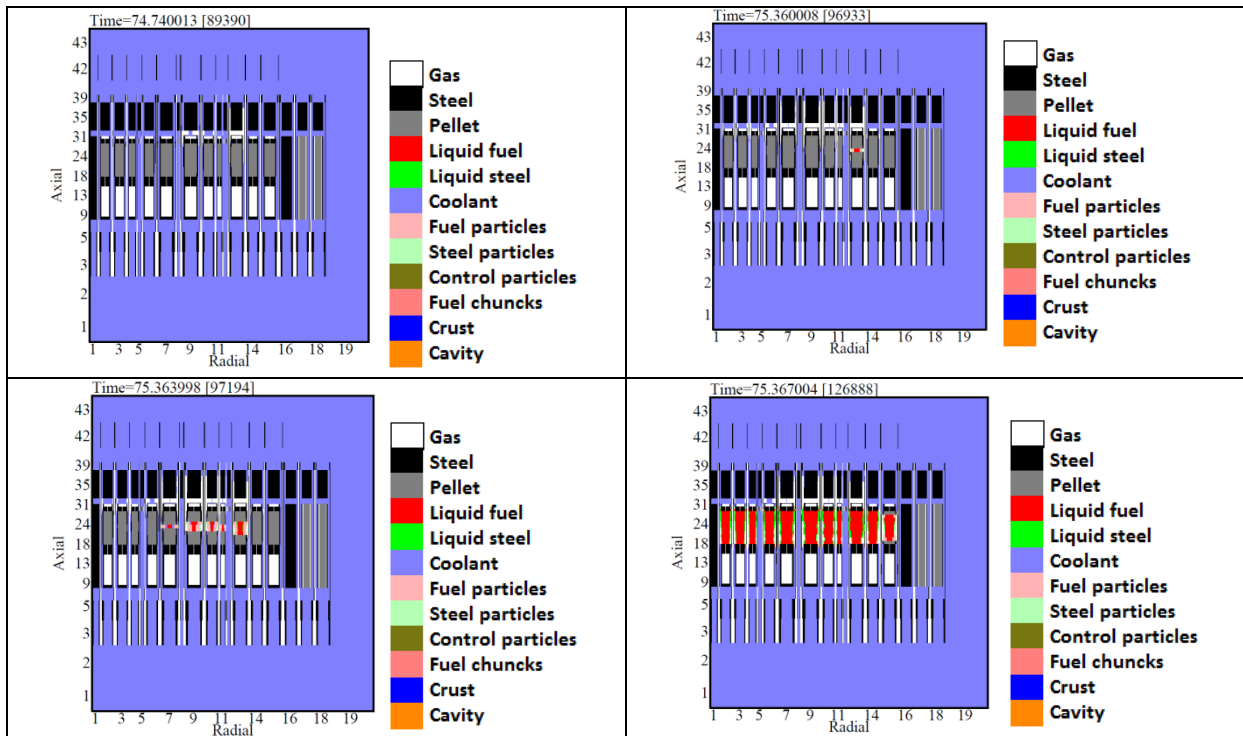
Figure 8-21. Material distributions during the ULOF of the WH sphere-pac loaded core

8.3.2. CONF2 Core

The WH core loaded with sphere-pac fuels has been analyzed at the beginning of the PELGRIMM project in order to obtain first information about the behavior of sphere-pac loaded cores. Once the analyses have been completed, focus turned on the CONF2 core, which is at present under study.

Starting from the different steady states, the same ULOF as in the WH core is run with SIMMER-III in the CONF2 core.

Beginning of life conditions

The transient behavior of the CONF2 core with pellet fuel under ULOF conditions can be observed in Figure 8-22, where both nuclear power (normalized to the nominal value) and reactivity, calculated by SIMMER spatial kinetics, are displayed. Prompt criticality, represented by the blue dotted line, is never reached and consequently no extreme power values are observed. Hence, the sodium plenum seems to effectively prevent positive reactivity surges caused by voiding and consequent power excursions. This is a large difference compared to the WH core [13].
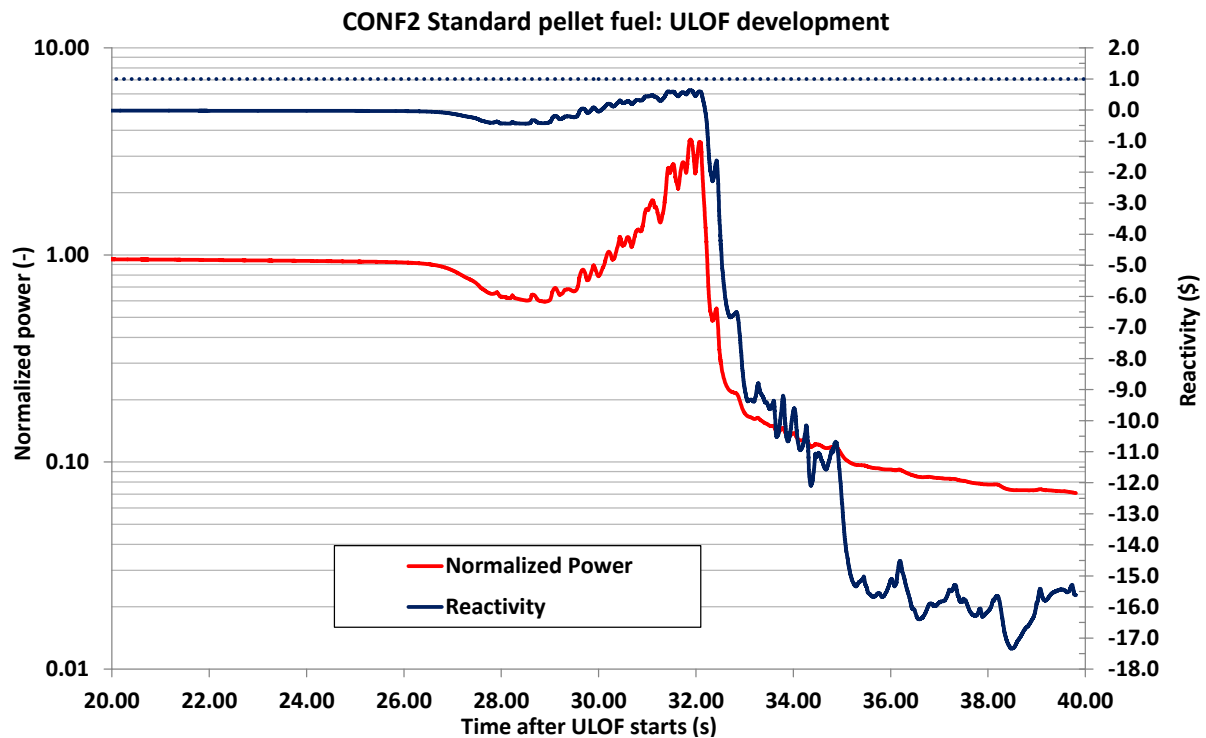
Figure 8-22. Normalized power and reactivity trace during the ULOF of the CP-ESFR CONF2 pellet core at BOL (time scale starts at the beginning of the ULOF transient which has been initiated after 50 s of steady state calculation, 20 s therefore correspond to 70 s in the time scale of Figure 8-23) [189].

It is also of interest to look for the material redistribution during the transient. The mitigating effect of the large upper plenum can clearly be identified in the performed simulations. Coolant boiling starts in the plenum of the outer core rings, mainly due to the BOL power profile, which is strongly peaked in these rings - Figure 8-23. The power shape is approximately the same as the one in the WH core, since the radial core design has not been changed from the WH to the CONF2 core. The progressive plenum voiding introduces first negative reactivity and balances positive reactivity effects such as the sodium voiding in the core region. The low power level reached during the ULOF transient allows a rewetting of the structures and the disruption process, after ejecting a limited amount of fuel from the core through entrainment by vapor and gas. The long-term development will be driven by decay heat. This late accident phase is currently not modelled.

During this long-term melt phase, recriticalities may occur, as most of the fuel inventory is still within the core region. Remelting processes are however slow and rapid fuel compactions with high reactivity ramp rates are not expected.
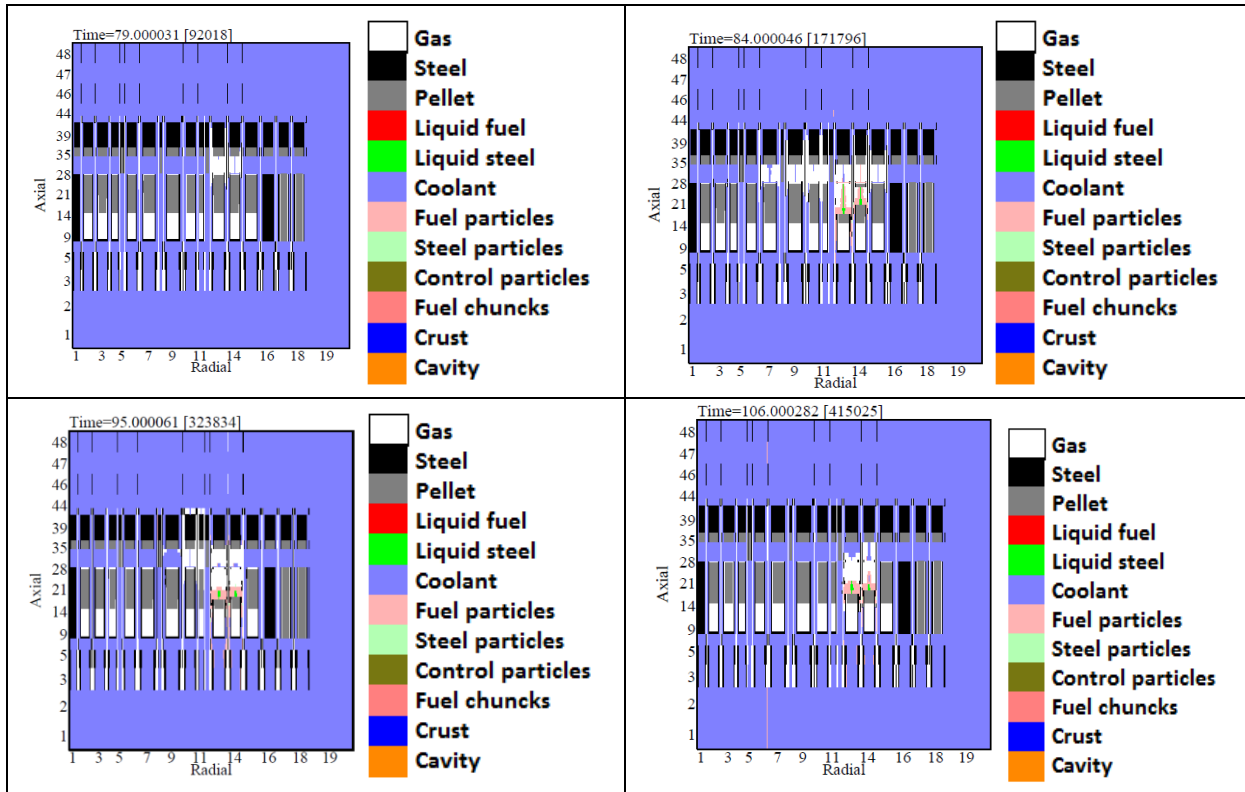
Figure 8-23. Material distributions during the ULOF of the CONF2 pellet core at BOL.

Now that the reference has been set, the case of the CONF2 loaded with non-restructured sphere-pac fuel is compared to the reference CONF2 loaded with pellet fuel. Figure 8-24 shows the power and reactivity evolution during the ULOF in the CONF2 core for both fuel types.
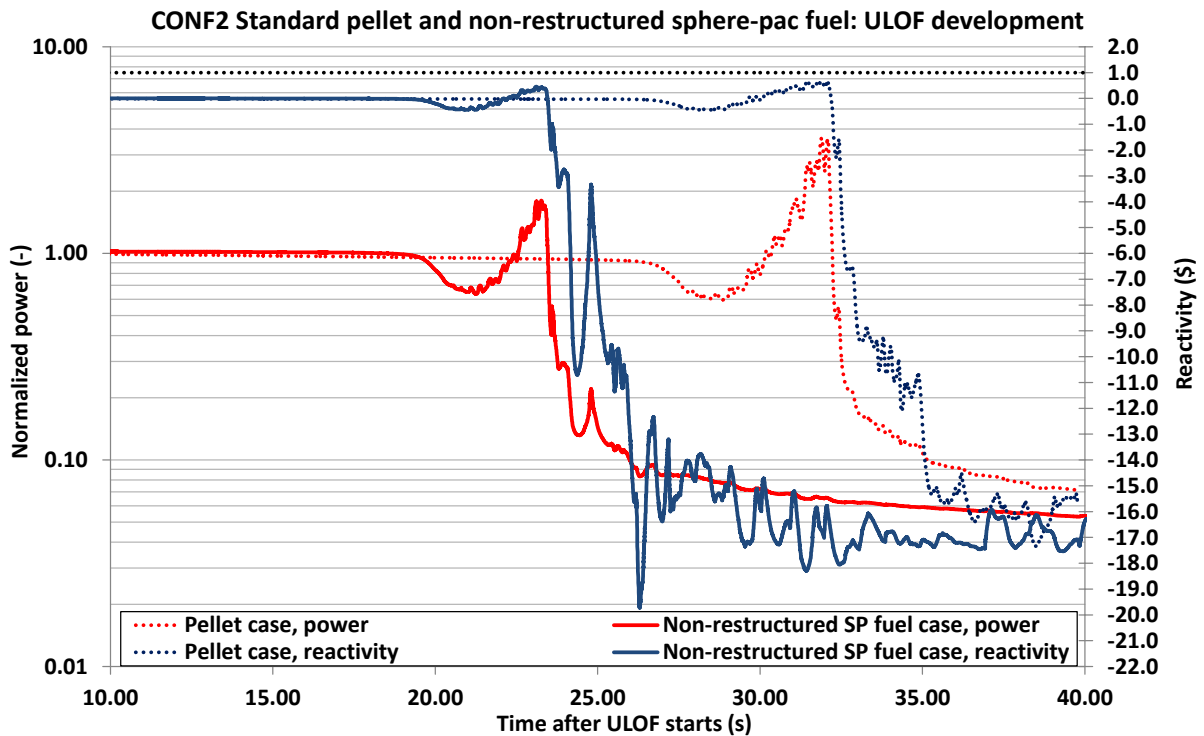
Figure 8-24. Reactivity and power evolution during in a ULOF in the CONF2 core at BOL loaded either with pellet or with non-restructured sphere-pac fuel.

In Figure 8-25 the material redistributions and the break-up of the pins in case of the non-restructured sphere-pac fueled core can be observed. Also in this case, the power transient is mild and shows a behavior similar to that of the pellet fuel. As locally "melt-conditions" in the pins have already been reached at steady state, the pins break-up 9 s earlier than for the pellet fuel. The power evolution reflects this situation as well (see Figure 8-24). The locally molten fuel is rapidly cooled and transferred into the particle field of SIMMER. Fuel dispersal is enhanced leading to early shutdown and limitation of further failure propagation. The mobilized particles are swept out of the core downward and a reactivity level of -18 $ is reached.
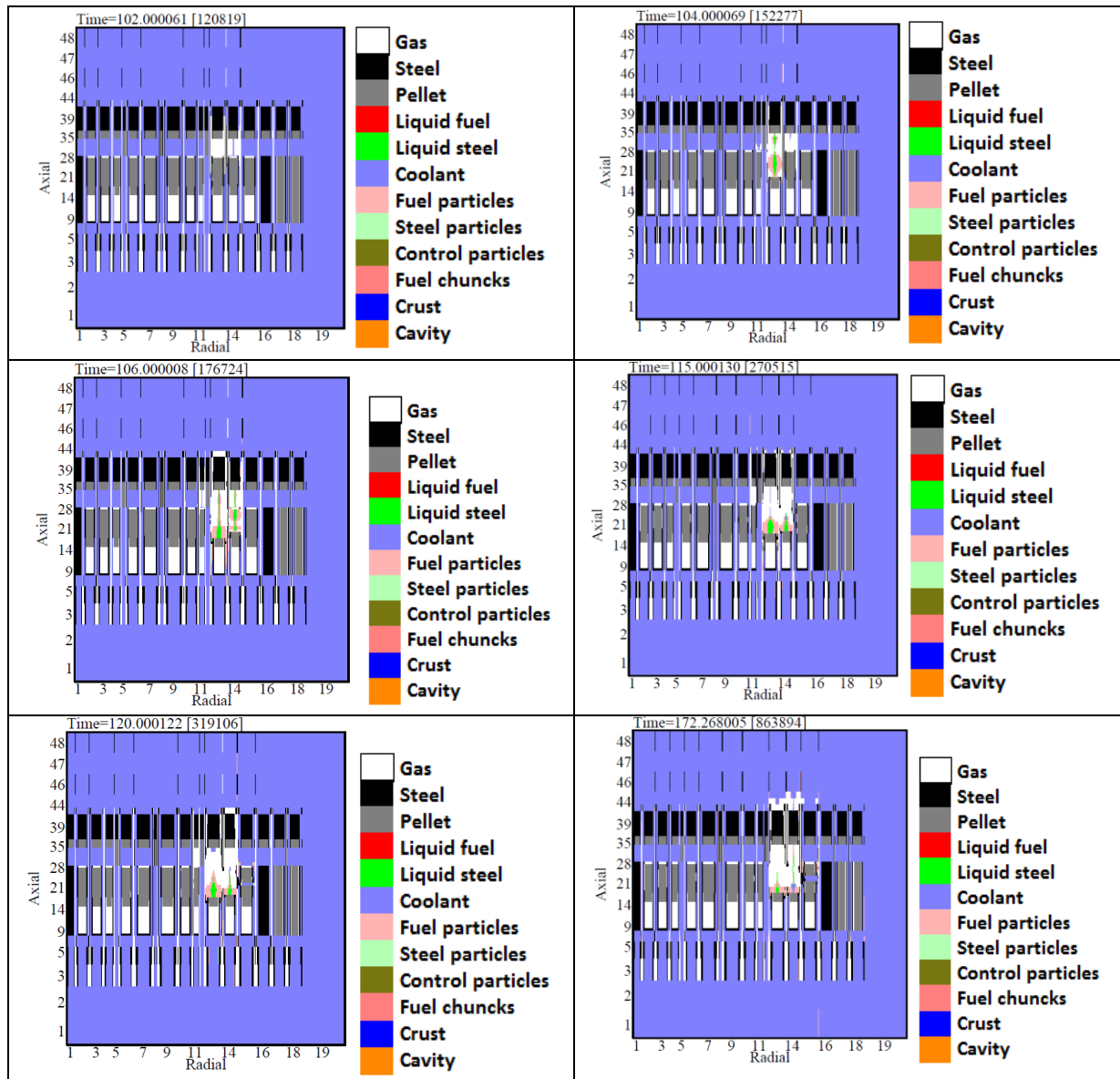
Figure 8-25. Material distributions during the ULOF of the CONF2 BOL core with non-restructured sphere-pac fuel. 90 s here correspond to 10 s in Figure 8-24.

After having assessed the effect of a non-restructured sphere-pac fuel on the core safety performance, the case of a restructured fuel after some hours of irradiation is analyzed.

In Figure 8-26 the normalized power and reactivity traces of the CONF2 BOL core with already restructured sphere-pac fuel is given and compared to the non-restructured sphere-pac fuel case.

The ULOF is started after 50 s achieving steady state. A very mild power transient with a power peak of roughly 1.3 times nominal (1.7 in case of non-restructured sphere-pac fuel) is shown in Figure 8-26 with reactivity levels staying way below prompt critical. A delay of 8 s in the power excursion can be noticed when the fuel is restructured.
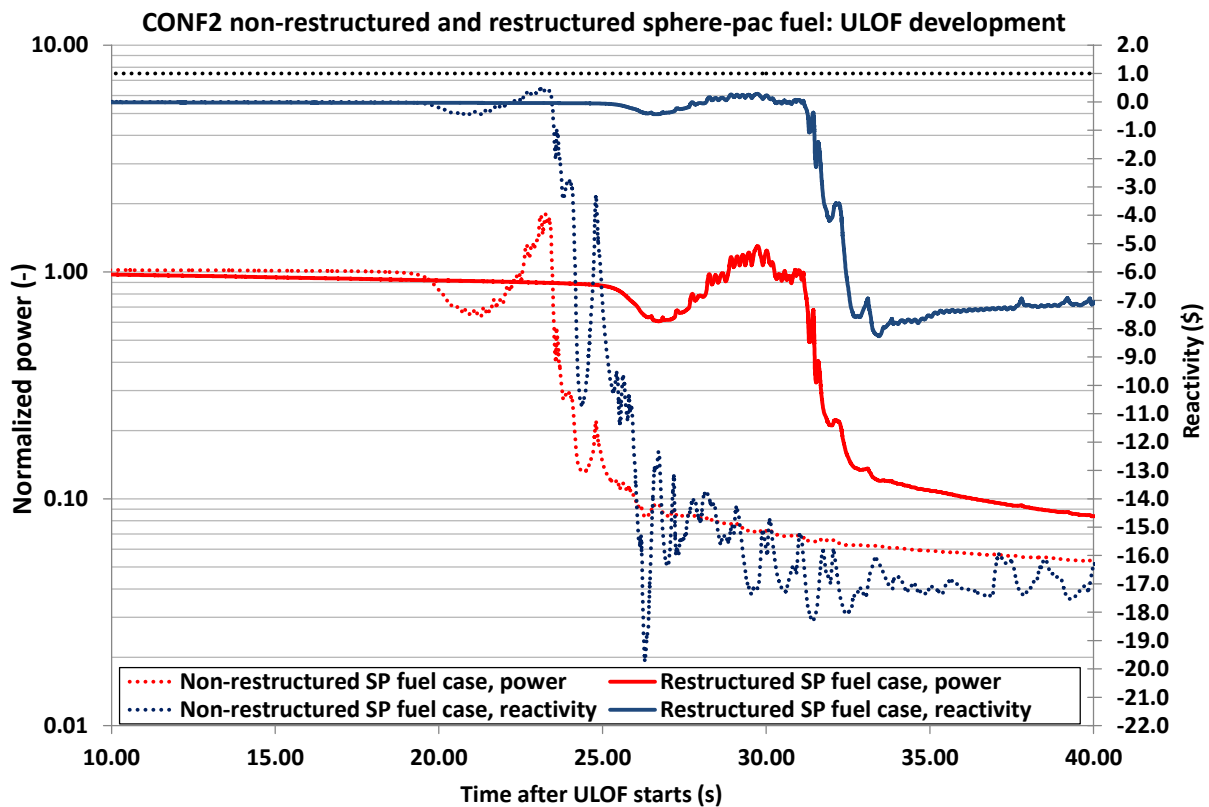
Figure 8-26. Power and reactivity trace during the ULOF of the CONF2 core with BOL restructured or non-restructured sphere-pac fuel [189].

In the CONF2 core with BOL restructured fuel (Figure 8-27) one experiences even a total re-wetting of the core in the last phase of the ULOF. Due to the initially restructured fuel conditions the ULOF leads to the smallest power peak as the temperatures at nominal conditions in this case are at lowest due to the higher thermal conductivity and the fuel's central hole at start of the simulation. Broken up fuel, mainly from the outer sphere rim is largely relocated downwards through the hexcan gap system and control rod guide tubes and lost from the core region. Compared to the "green fuel" less particles are swept out of the core causing a lower power reduction, as reflected by the reactivity level of -8 $. No fuel melting conditions are reached during the transient. This finally allows the achievement of a very mild transient letting the core in a subcritical state. The further accident evolution depends on the ability of cooling down the reactor i.e. of the capacity of sufficiently evacuating the residual heat.
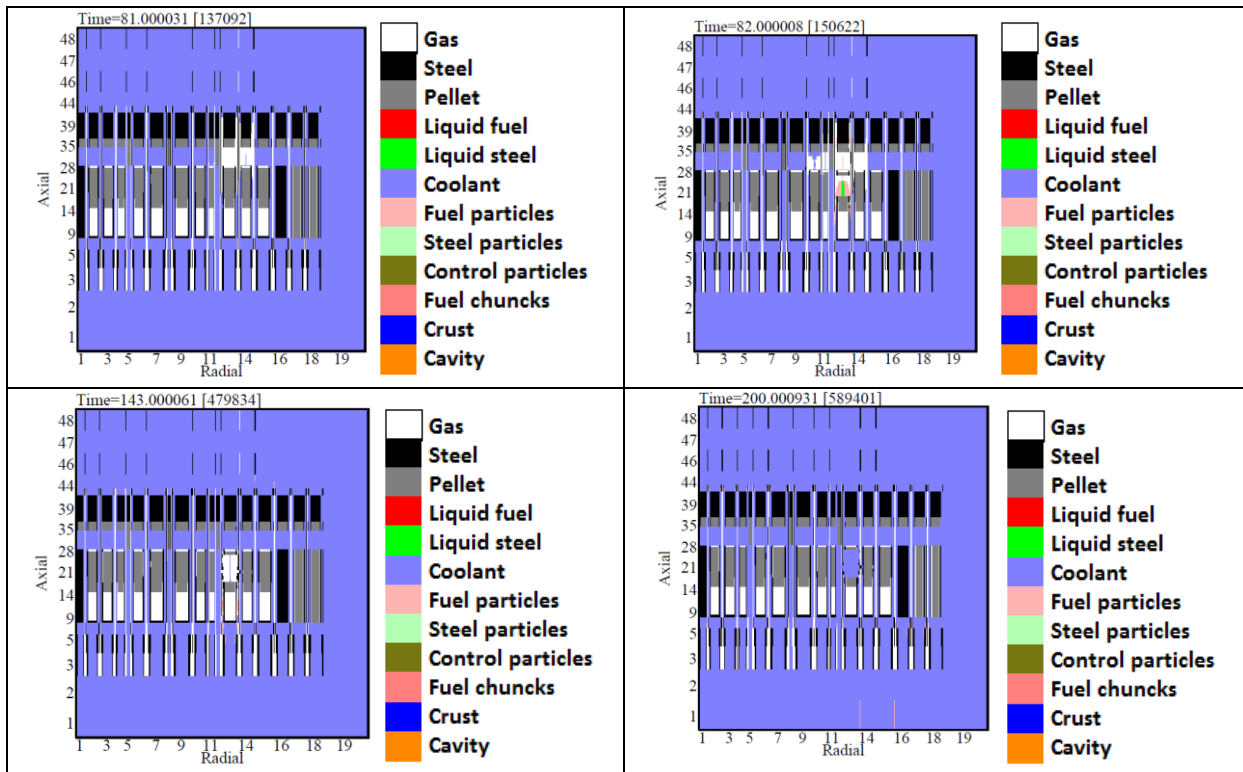
Figure 8-27. Material distributions during the ULOF of the CONF2 BOL core with restructured fuel. 60 s here correspond to 10 s in Figure 8-26.

All simulations in the BOL CONF2 core show very mild transients, mainly attributed to the action of the large upper plenum, which introduces upon its voiding sufficient negative reactivity to balance the positive voiding contributions within the core and reactivity additions from fuel compaction or steel loss. The first results clearly demonstrate that a core could be equipped with sphere-pac fuel without unduly compromising safety conditions.

Equilibrium core conditions

The same ULOF is then considered in the CP-ESFR CONF2 core in equilibrium conditions. As already seen in Chapter 4 the reduced void worth for the CONF2 core only holds for the BOL core without additional Am in the fuel; thus one expects a more energetic behavior of the core at this stage of irradiation (see Table 8-4). Therefore more severe transients than in the BOL core are expected, resembling the ones of the WH at equilibrium.

CONF-2, 0%Am, EOEC: ULOF development
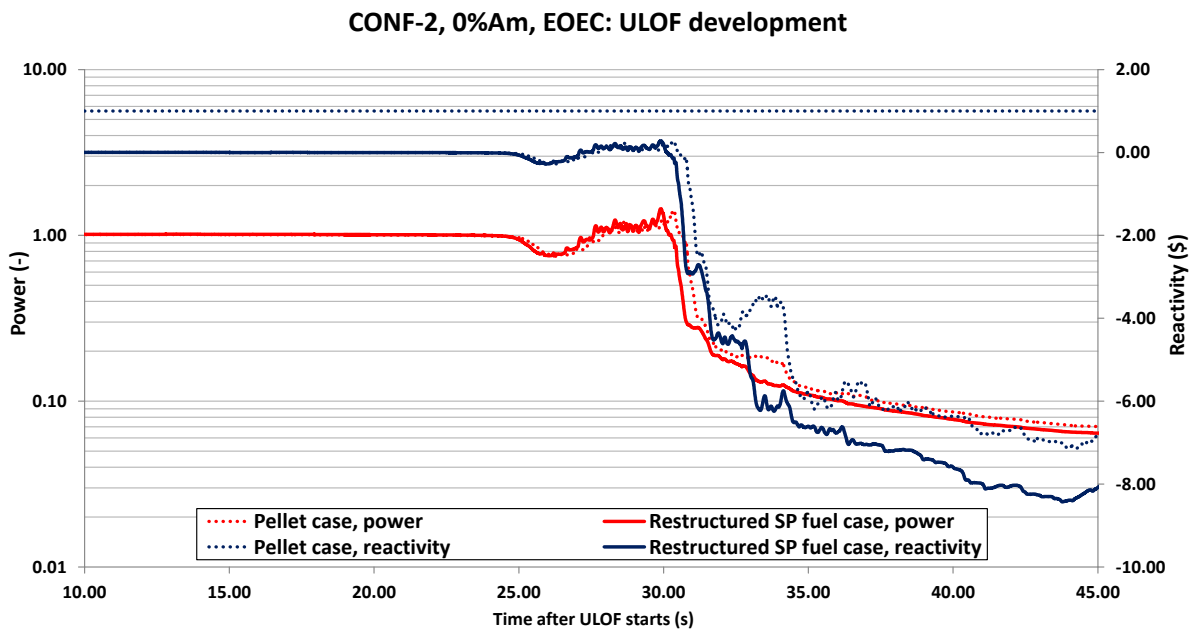
Figure 8-28. Reactivity and power evolution during in a ULOF in the CONF2 core at equilibrium loaded either with pellet or with restructured sphere-pac fuel.

In Figure 8-28 the nuclear power trace and reactivity development of the CONF2 core at equilibrium conditions is displayed both for pellet and sphere-pac fuel. Compared to the BOL case a slight increase of the nuclear power peak can be observed, but the negative reactivity effects can still balance the positive contributions from core voiding. As expected from the similar thermal conductivity and macrostructure of both fuel types at this stage of irradiation, the sphere-pac and pellet core show a very similar behavior under these accidental conditions. The unprotected transients end without any significant power excursion and gross core melting has to be prevented by a reactor scram to achieve permanent nuclear shut-down. The decay heat has to be evacuated to prevent further core degradation.

8.4. Impact of minor actinide introduction in the fuel

Sphere-pac fuels are primarily thought to be able to better handle minor actinide transmutation as they are expected to be less subjected to swelling than the standard pellet fuels due to their specific macrostructure. Hence, additional americium is introduced into the core (as well as in the lower axial blanket), leading to a further deterioration of the safety parameters (Table 8-1).

Table 8-4. Deterioration of the main safety parameters in the CONF2 core with burnup and additional minor actinide loading [9].

	CONF2		CONF2 with 2%Am		CONF2 with 4%Am	
	BOL	EOC3	BOL	EOC3	BOL	EOC3
Sodium void reactivity effect (pcm)	+1423	+1951	+1636	+2029	+1821	+2104
Extended Sodium void reactivity effect (pcm)	+496	+1170	+781	+1290	+1031	+1407
Doppler constant, K_D (pcm)	-1158	-843	-904	-785	−712	−600

The Doppler constant is decreasing (in absolute value) while the sodium void coefficient is increasing. Key void worth parameters are the core void and extended void (i.e. with both core and plenum region voided). The safety relevant ratio of void versus Doppler (in absolute values) at EOC3 conditions increases from 1.4 (0 wt% Am) to 1.6 (2 wt% Am) up to 2.3 (4 wt% Am) for the extended void worth and from 2.3 (0%Am) to 2.6 (2 wt% Am) up to 3.5 (4 wt% Am) for the core void [9]. This ratio gives an indication of the imbalance of augmenting versus mitigating reactivity effects. β_{eff} for BOL is 390 pcm, while for the burned-up core with an original 4 wt% Am load it is 352 pcm, meaning that from this point of view the values do not change significantly for the transient simulations shown later.

The core power distribution has been calculated by partners within the PELGRIMM project, at BOL a strong flux depression at the core centre is observed (see Chapter 4), with a power peaking toward core periphery. Maximum assembly power at BOL is about 11.3 MW while the minimum is 4.9 MW [189]. In Figure 8-29 the burnup behavior of the CONF2 core for different Am loadings in the core is displayed [189]. In the MA loaded cores the transmutation of Am to Pu leads to an increase of k_{eff}. The breeding of Pu in case of Am (~2 %) content leads to a rather constant k_{eff} curve.
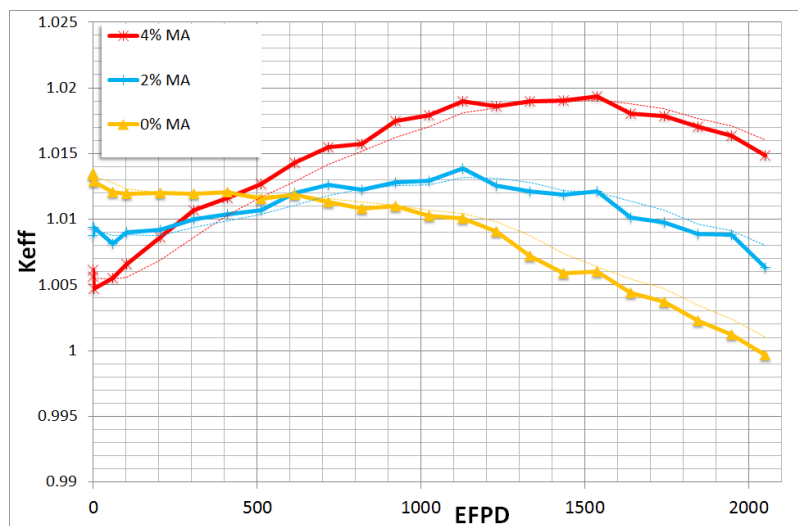
Figure 8-29. Results of burnup calculations for the CONF2 core with different Am content [189].
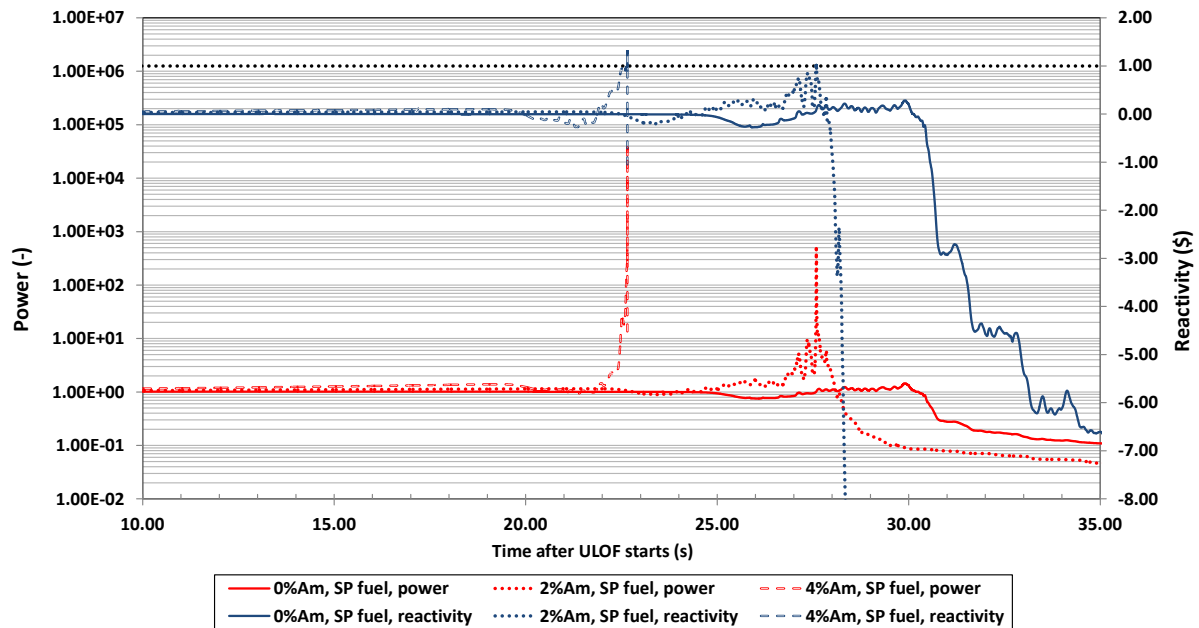
Figure 8-30. Normalized power and reactivity trace during the ULOF of the CONF2 core at equilibrium, with restructured sphere-pac fuel with 0 wt%, 2 wt% or 4 wt% additional Am loading in the lower axial blanket and the fissile zone.

Starting from the steady state conditions, an unprotected loss of flow accident with a flow halving time of 10 s is performed for the sphere-pac fuel loaded core in a restructured state. In Figure 8-30 the nuclear power trace and reactivity evolution in the equilibrium core with EOC3 compositions, initially loaded with 0 wt%, 2 wt% and 4 wt% Am both in the fissile core zone and lower axial blanket, can be observed.

From Figure 8-30 it can be seen that the higher the americium amount, the earlier the power excursion and the higher its extent, thus reflecting the impact of the deterioration of the safety parameters.

For the 4 wt% Am case one expects a release of both fission gases and He accumulated in the lower and upper fission gas plenum, whose pressure levels are assumed to be 60 bar in the calculation [80]. After clad failure both fission gas and He can escape through the cladding breach and can contribute to the voiding process in the core.

Analyzing the 2 wt% Am case, the transient starts after reaching the steady state after 60 s of calculations and presents a mild power increase. However, the positive reactivity contributions prevail and drive the core into a prompt critical excursion with a maximum value of 500 times nominal which can be explained by the larger positive void worth than in the CONF2 core without americium. In Figure 8-31 the core material redistribution is displayed. It is of interest to note that due to the limited fuel temperatures, the fuel breaks up into chunks and particles, without reaching the melting point. The solid disrupted fuel is then mixed into molten steel.

In comparison, the nuclear power trace and reactivity development of the equilibrium core with 4 wt% Am show a much sharper increase, due to the core void worth – Table 8-4 – which is of course larger than for the 2% Am case.

Also in this 4% Am case the ULOF is started after 60 s achieving steady state, but the core experiences a prompt critical power excursion leading to a core disruption. Due to the significant nuclear power increase, fuel melting is achieved, reaching a state of whole molten core pool – cf. Figure 8-32. The transient simulation stops due to a numerical problem, but the trend of the accident

evolution can be clearly identified: with the increased positive void worth and reduced Doppler values the beneficial impact of the upper plenum is reduced and the release of solid particles from the sphere-pac fuel is insufficient to stop the excursion.

The very promising safety behavior of the CONF2 core thus only holds for the BOL configuration with strong negative reactivity contributions. With increasing burnup and MAs addition into the core, the safety advantage of the upper plenum is insufficient and additional core design optimizations are necessary to reduce the void worth. A possible option might be to limit the addition of MAs to the blanket only.
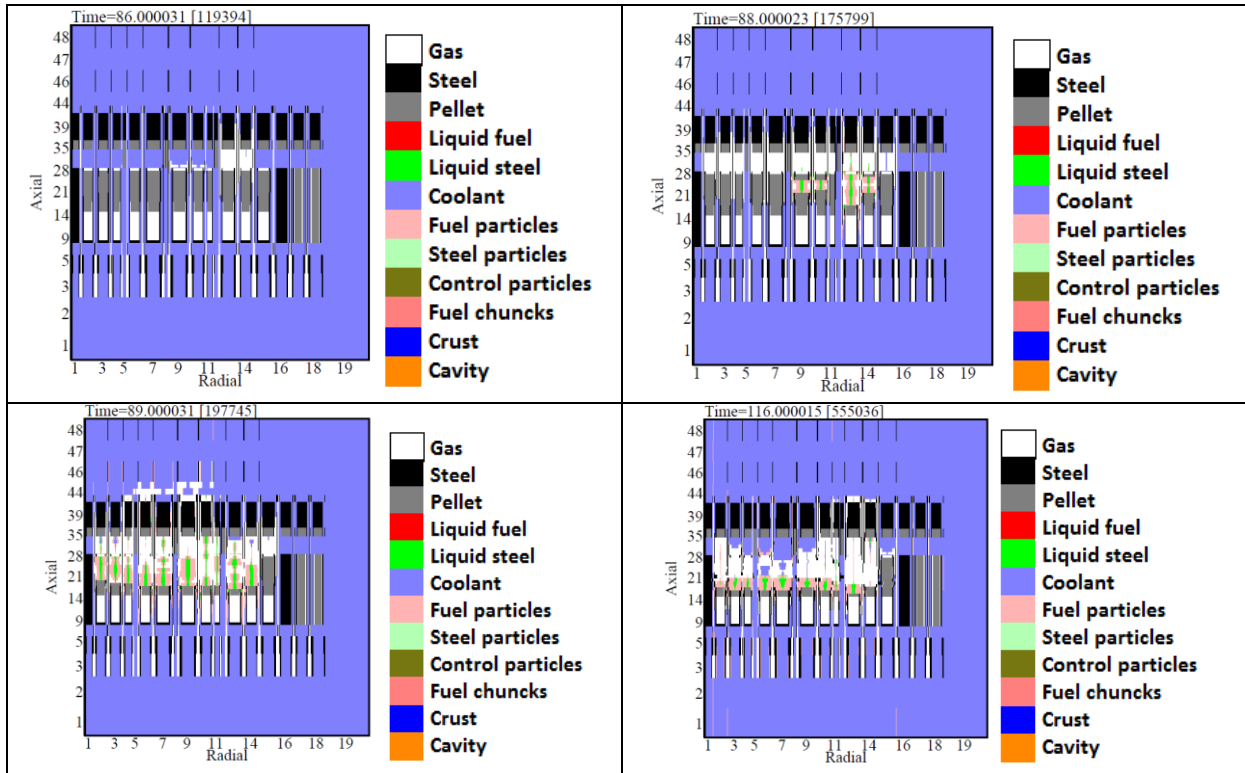
Figure 8-31. Material distributions during the ULOF of the CONF2 equilibrium core with restructured sphere-pac fuel and 2 wt% Am.
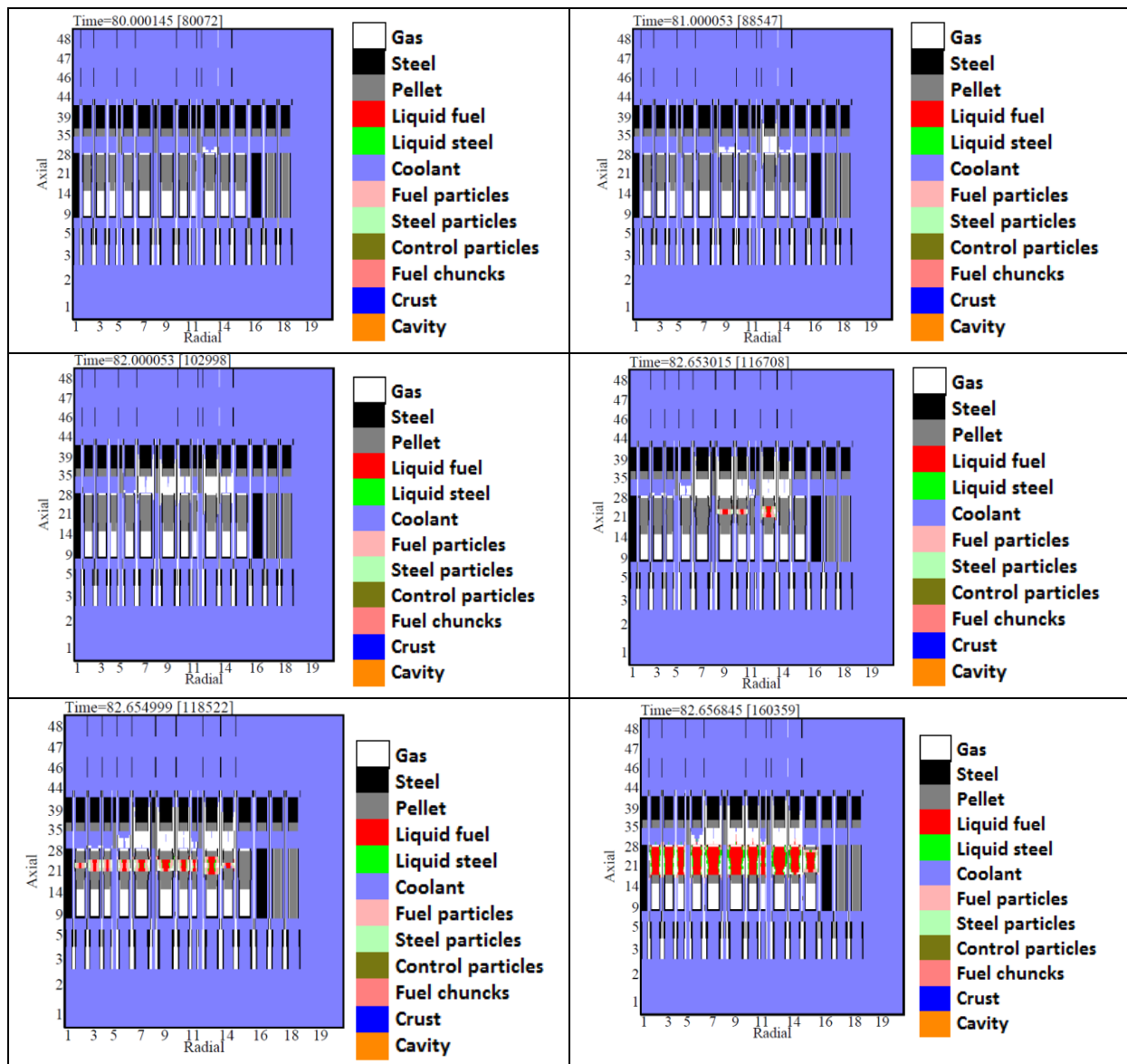
Figure 8-32. Material distributions during the ULOF of the CONF2 core at equilibrium with restructured sphere-pac fuel and 4 wt% Am.

8.5. Impact of the expansion model

To identify the impact of the expansion model developed during the PhD (and detailed in Chapter 6) on the safety calculations, the global density factor method (DENSF method) is applied to a sphere-pac fueled core. It is considered that the axial expansion is clad driven as no gap is present between the fuel and the cladding tube. For the radial expansion the cylindrical expansion is chosen i.e. the diagrid drives the radial core expansion.

The BOL CONF2 core with restructured sphere-pac fuel is analyzed. The power and reactivity trace during the ULOF accident is given in Figure 8-33. When the core expansion feedbacks are taken into account, delays on the onset of sodium boing by 1 s, on the fuel melting by 2 s, and on the initial power peak of 2.6 s are observed. In addition the power peak is reduced by 15%. It has to be

mentioned that in case of a fuel driven expansion, the effect would be much more pronounced. Indeed, the significantly higher fuel temperatures (compared to the cladding ones) lead to a larger thermal expansion even if the expansion coefficient of the fuel is lower than that of the cladding.

CONF2 BOL restructured sphere-pac fuel: ULOF development
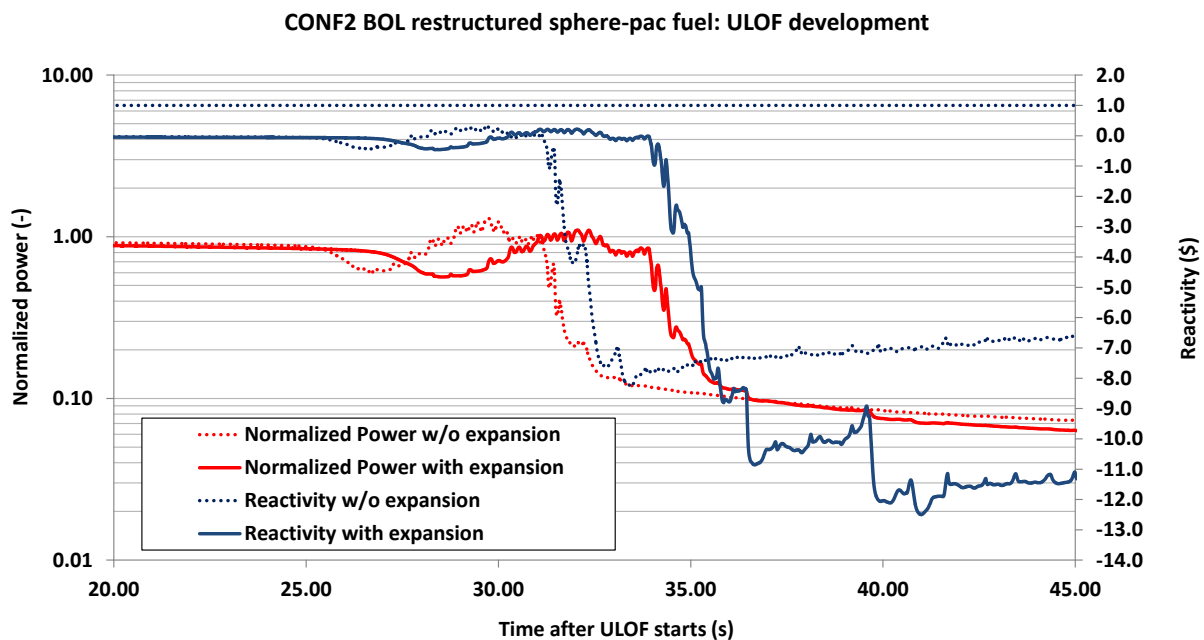
Figure 8-33. Normalized power and reactivity evolution during a ULOF in the CP-ESFR CONF2 core at BOL with restructured sphere-pac fuel with and without taking into account the core thermal expansion feedbacks.

8.6. Conclusions

The previous safety analyses have demonstrated that no specific safety issue is raised when inserting sphere-pac fuels in a sodium cooled fast reactor as the Working Horse or CONF2 core. However, a specific starting procedure would have to be defined for sphere-pac fuels in order to give the fuel enough time to restructure before reaching the nominal power conditions.

In addition it has been demonstrated that the claimed safety improvement of the CONF2 core with regard to safety in comparison with the Working Horse core actually is verified. The BOL CONF2 core indeed does not reach a whole core melt situation when subjected to a ULOF and the accident undergoes a very mild transient, leaving the core in a subcritical state. The further accident evolution then strongly depends on the ability of cooling down the reactor i.e. removing decay heat. The unprotected transients end without any significant power excursion and gross core melting. The decay heat has to be evacuated to prevent further core disruption. In case of restructured sphere-pac fuels the core even experiences a total rewetting of the assemblies. However, the very promising safety behavior of the CONF2 core only holds for the BOL MOX configuration with strong negative reactivity contributions. With burnup and addition of MAs into the core and lower axial blanket, the safety advantage of the upper plenum is decreased. Additional measures on core design basis level are necessary to achieve a low void worth both for equilibrium conditions and the possible homogeneous loading of MAs into the core.

Chapter 9

CONCLUSION AND OUTLOOK

Nuclear energy demonstrates all prerequisites to play an important role in the world energy and, in particular, electricity supply for the next decades, under the conditions that a sustainable use of this energy source is made and long-lived radioactive waste is managed. Fast reactor concepts, especially the sodium cooled ones, are considered to be among the most promising options viable to meet these requirements. Fast reactors, when loaded with minor actinides, do however show a deterioration of their safety feedbacks and therefore require a detailed analysis of their safety behavior under normal and accidental conditions.

Embedded in this topic, the present PhD work aims at investigating the impact of innovative sphere-pac fuels for minor actinide transmutation on the safety performances of sodium cooled fast reactors, both in nominal and accidental conditions. The study, which followed the accident evolution from its very beginning, has been performed with the SIMMER-III code for two low-void sodium cooled fast reactor designs developed in the framework of the CP-ESFR project: the working horse (WH) core and the optimized CONF2 core, equipped either with the traditional pellet or with the special sphere-packed fuel form. The safety analyses for the WH core revealed that the sodium reactivity worth was still too high and in case of an unprotected Loss of Flow (ULOF) accident a large scale core disruption could not be prevented. Therefore, within the CP-ESFR project the CONF2 core was developed with a further decreased void worth due to a large upper sodium plenum. For the CONF2 core no deep safety analyses had been performed within the CP-ESFR project.

Traditionally, only the later phases of an accident transient are studied when using the SIMMER codes, specifically developed for core disruptive accidents, while for the initial phase a point kinetics code (e.g. SAS4A) is employed. The tendency in recent years is however to perform the overall accident sequence simulation with the SIMMER-III code, extending its field of application to the initiation phase of the accident. When simulating this phase, additional phenomena have to be simulated. In this framework, the PhD work also targeted the development of a model to take into account the core thermal expansion feedbacks since they impact the accident evolution.

Usually the reactivity feedback of axial and radial expansion of reactor components i.e. fuel and structural materials is taken into account via point kinetics reactivity models with specifically chosen parameters. The reactivity worth of the materials is pre-calculated by static neutronics codes and is fed into the safety codes and processed there. In addition, most safety codes use a so-called channel approach, where one representative pin for a couple of sub-assemblies is expanded in a Lagrangian manner. The safety analyses for the CP-ESFR revealed that point kinetics was not sufficient to describe correctly the initiation phase neutronic effects. The delicate balances of reactivity for low void cores require more advanced methods than point kinetics.

In the current work the development related to the thermal expansion feedbacks is put into a more general framework, taking into account the needs of spatial kinetics codes in an Eulerian fluid-dynamics context with fixed neutronic mesh. Though developed within SIMMER, the model is a general one and can be easily exported to other space-time kinetics codes. A first model was functional and has been further improved. The present PhD work has resulted in an improved methodology which has the potential to take into account core thermal expansion feedbacks in a spatial kinetics framework with Eulerian mesh. An important point is the time-efficiency of the method, which does not require a significant increase in additional shape function recalculations.

In the developed methodology, neutronic effects of core expansions both in radial and axial dimensions are modeled via equivalent density changes, which allows keeping fixed the Eulerian fluid-dynamics mesh. Two models have been established based on a first order perturbation theory (FOP) approach to cope with the SIMMER framework. The first model is based on a global density factor whose aim is to accurately predict uniform core expansion effects and serves as a basis for the second model. This second model takes full advantage of the SIMMER-III spatial kinetics capabilities as it is based in RZ-geometry on a ring-wise density factor in order to model accurately non-uniform expansions within the core.

Both models give satisfying results in case of uniform expansions, both isotropic or anisotropic, if applied to the whole neutronic mesh using FOP and comparing the outcome with direct calculations (within 11% relative discrepancy). A special treatment for sodium has been developed: the fairly important effect of sodium distribution in case of core expansion is put in the direct calculation instead of the FOP. Results between FOP and direct calculations are in good agreement. The validation phase of these models has however highlighted some limitations related to density variation calculations in individual sub-domains of the neutronic mesh.

A third innovative method relying on the fact that the contribution of non-uniform expansions is taken into account in the direct calculations has hence been developed. The tests performed with the ERANOS code, chosen instead of SIMMER for its flexibility, clearly show that this new solution scheme is able to take correctly into account non-uniform expansions. Preliminary results for the fissile core expansion show an agreement within 3% discrepancy with reference calculations when applying the method to traditional core designs, such as the Working Worse core design. The same procedure is expected to be suitable for other parts of the reactor e.g. sodium plenum, axial fertile blanket but further analyses are essential. This methodology will be fully implemented in SIMMER and new validation studies have to prove its efficiency for advanced non-conventional reactor designs as cores with a variable core height and an internal axial fertile blanket.

The second part of the work has consisted in the model development for sphere-pac fuel pins with the focus on the thermal conductivity of sphere-pac fuel under beginning of life and irradiation conditions. Indeed, the conductivity of sphere-pac fuels is very different from the one of standard pellet fuels especially at beginning of life due to the fuel specific macrostructure and needs special attention. A literature review has revealed that the Hall and Martin model for powder beds is the most suitable candidate for modeling the thermal conductivity of these fuels. Formulas have been adapted to the SIMMER framework for both pellet and sphere-pac fuel (further developed or newly implemented) at beginning of life and end of cycle 3 conditions and casted into the specifics of the SIMMER framework so that the models can describe all phenomena in the range from steady state to pin break-up and failure, without putting an undue load on computational time.

For the subsequent simulations, the CP-ESFR Working Horse pellet fuel has then been substituted with sphere-pac fuel. The basic structure of the core has been kept since, according to literature, sphere-pac fuel with an optimal theoretical density can be inserted in a standard core without significant changes. A first preliminary safety assessment has been performed for non-restructured fuel conditions at core beginning of life. The interest in investigating this "green fuel" case is because of its low thermal conductivity and consequently possible high fuel centerline temperatures, which raises some concerns related to the safety behavior of this fuel in the first hours of operation. Analysis show that indeed specific reactor start-up procedures are required to cope with thisrather short phase, giving the fuel time to restructure, hence enhancing its thermal conductivity.

A ULOF accident has been chosen as a representative transient since the impact of the void reactivity reduction for the CONF2 core could be investigated. The ULOF covers most of the important phenomena in a core melt accident, especially the behavior of the fuel pins, and revealed for the CP-ESFR to be the most severe accident.

The ULOF simulations for the equilibrium cycle conditions in the Working Horse core show a very similar behavior of the core whether fueled with standard pellet fuel or with sphere-pac fuel. For this core the ULOF transient leads to core melting and core disruption conditions.

The safety behavior of the optimized CONF2 core has then been studied because no extended safety analyses for that core had been performed in the past. First, the analyses for the CONF2 core loaded with pellet fuel had to be carried out. As within the CP-ESFR project only the safety behavior of the Working Horse core had been analyzed, this work was additionally necessary to implement a basis for comparison. The CONF2 core has as a main feature a large upper sodium plenum for void reduction and is hence expected to have increased safety features. The beginning of life core with MOX fuel has been selected to start the analyses especially for assessing the claimed improvement by introducing this large upper sodium plenum. Indeed under these conditions the positive extended void (including the upper plenum) is reduced by a factor of 2.4 compared to the working horse core. Results confirm that the sodium plenum seems to effectively prevent positive reactivity surges by voiding and subsequent power excursions: the plenum voiding introduces enough negative reactivity to counterbalance positive reactivity effects. The low transient power allows the rewetting of structures and the disruption process remains limited. Indeed after a first mild power excursion no recriticality appears and the possible outcome would be a slow melting under decay heat conditions.

In the second step, analyses have been performed for the CONF2 core equipped with sphere-pac fuel. The analyses start with the beginning of life core and investigate the conditions of both a green fuel with pure sphere-filling (representing the situation before any restructuring) and a restructured fuel after some hours in the operating reactor. SIMMER analyses confirm that under these non-restructured conditions the centerline temperatures locally exceed the melting point in the high power core zone at steady state. Therefore, also for the CONF2 core a starting procedure of the reactor is required to allow the fuel achieving a restructured state, which is closer to the pellet fuel from the thermal point of view. For both fuel conditions the plenum effect prevents a scenario with multiple recriticalities, even leading to a total rewetting of the structures in the last phase of the ULOF in case of the CONF2 core with beginning of life restructured fuel.

The equilibrium core with already irradiated fuel, especially when initially loaded with additional americium for transmutation purposes, shows a significant deterioration in its safety behavior due to

the worsening of void values and of the other safety parameters (e.g. Doppler). Additional voiding effects caused by the fission gas and helium blow-out of the pins after their failure might further complicate and possibly deteriorate the accident situation. Consequently the safety advantages observed in the beginning of life core vanish and one experiences severe transients with total core disruption and melting.

The developed thermal expansion model based on the global density factor has been applied later on for improving the safety analysis and results confirm an improvement in the accident timing and a lowering of its energetic potential.

The key findings of the safety assessment of the CONF2 core loaded with sphere-pac fuel can be summarized as follows:

- ❖ Sphere-pac fuel can be inserted in a sodium cooled fast reactor core without significantly changing the design and having a major impact on the core behavior or safety coefficients.
- ❖ The start-up of a sphere-pac fueled core with "green fuel" requires a special start-up procedure to avoid fuel melting. In practice the start-up should be performed at lower power until restructuring has been achieved.
- ❖ The transient ULOF analyses with SIMMER do not show a significant change in the accident scenario when using sphere-pac fuel compared to the behavior with conventional pellet fuel. The possibility of spalling of the sphere-pac particles and their release in the core might generally lead to an even milder accident behavior and achievement of lower reactivity levels.
- ❖ For beginning of life conditions and in a core without additional americium the introduction of the large sodium plenum gives a strong safety advantage as no fuel melting conditions are reached during the transient. This advantage decreases or even vanishes both with increasing burnup and Am insertion for transmutation.

Within the PELGRIMM project, experiments have been initiated to provide information on sphere-pac fuel behavior under irradiation. For transient conditions the currently existing experimental data base is even scarcer.

The preliminary safety analyses also served the purpose to identify open issues which need better modeling and experimental information. Further investigations should e.g. take into account the detailed kinetic behavior of fission gas and of He release during operation as well as the gas release during accident situations. Experimental data or expert-agreed evaluations of data would also be needed for the behavior of sphere-pac fuel under high thermal loads and transient conditions. An additional issue is to model in more detail the rim behavior of the restructured fuel in case of clad breaching and melting.

Bibliography

[1]   OECD IEA*, World Energy Outlook 2014,* France : Organization for Economic, 2014, 726 p.

[2]   OECD NEA*, Uranium 2014: Resources, Production and Demand (The Red Book).* NEA No. 7209, OECD, 2014, 504 p.

[3]   Generation IV International Forum*, Technology Roadmap Update for Generation IV Nuclear Energy Systems,* 2014.

[4]   COCHRAN T. B., FEIVESON H.A., PATTERSON W., et al*., Fast Breeder Reactor Programs: History and Status,* IPFM Research Report #8, USA, 2010.

[5]   MARTH W*., The Story of the European Fast Reactor Cooperation.* KfK5255, Karlsruhe, Germany, 1993.

[6]   FIORINI G.L. et al*., The Collaborative Project on European Sodium Fast Reactor (CP-ESFR)*. In *FISA2009,* Prague, Czech Republic, June 22 – 24, 2009.

[7]   VASILE A., WAHIDE C., LATGE CH. et al*., The European Project ESNII Plus*. In *ICAPP'15,* Nice, France, May 3-6, 2015.

[8]   LE COZ P., SAUVAGE J.F., SERPANTIE J.P. et al*., Sodium-Cooled Fast Reactors: the ASTRID Plant Project*. In *ICAPP'11,* Nice, France, May 2-6, 2011.

[9]   VEZZONI B., GABRIELLI F., RINEISKI A. et al*., Safety-Related Optimization and Analyses of an Innovative Fast Reactor Concept.* Sustainability, 4(12), p. 1274–1291.

[10]   OECD NEA*, Homogeneous versus Heterogeneous Recycling of Transuranics in Fast Nuclear Reactors.* NEA No. 7077, OECD, 2012, 91 p.

[11]   *http://www.pelgrimm.eu/wp-content/uploads/2014/07/delage-full.pdf,* last accessed on 30.11.2015.

[12]   BUIRON L., VASILE A., SUNDERLAND R. et al*., CP ESFR: Collaborative Project for a European Sodium Fast Reactor*. In *International Conference on Fast Reactors and Related Fuel Cycles: Safe Technologies and Sustainable Scenarios (FR13),* Paris, France, March 4-7, 2013.

[13]   FLAD M., ZHANG D., MATZERATH BOCCACCINI C. et al*., ESFR Severe Accident Anlayses with SIMMER-III*. In *International Conference on Fast Reactors and Related Fuel Cycles: Safe Technologies and Sustainable Scenarios (FR13),* Paris, France, March 4-7, 2013.

[14]   RINEISKI A., VEZZONI B., ZHANG D. et al*., ESFR core optimization and uncertainty studies*. In *IAEA FR13,* Paris, France, March 4-7, 2013.

[15]   International Energy Agency (IEA)*, World Energy Outlook 2014 Factsheet,* Paris, France, 2014.

[16]   *http://www.iea.org/,* last accessed on 30.11.2015.

[17]   *https://www.gen-4.org/gif/jcms/c_9260/public,* last accessed on 30.11.2015.

[18]   OECD NEA*, Physics and Safety of Transmutation Systems.* NEA No. 6090, OECD, 2006, 120 p.

[19]   IAEA*, Estimation of Global Inventories of Radioactive Waste and Other Radioactive Materials.* IAEA-Tecdoc-1591, IAEA, 2008.

[20]   IAEA*, Classification of Radioactive Waste.* IAEA Safety Standards serie No. GSG-1, IAEA, 2009.

[21]   REUSS P*., Neutron Physics,* France : EDP Sciences, 2008, 669 p.

[22]   OECD NEA*, Nuclear Fuel Cycle Transition Scenario Studies.* NEA No. 6194, OECD, 2009, 121 p.

[23]   SALVATORES M., SLESSAREV I., TCHISTIAKOV A., 1996*, Analysis of Nuclear Power Transmutation Potential at Equilibrium.* Nuclear Science and Engineering, 124, p. 280–290. [Corrigendum. Nuclear Science and Engineering 125: March 1997, following table of contents].

[24] IAEA*, International Atomic Energy Agency Bulletin,* 1980, 22(Number 2), p. 11–22.

[25] WALTAR A. E., REYNOLDS A. B.*, Fast Breeder Reactors,* USA : Pergamon Press, 1981, 853 p.

[26] TAIWO T. A., HILL R. N.*, Summary of Generation-IV Transmutation Impacts.* Argonne National Laboratory, ANL-AFCI-150, 2005.

[27] NEWTON T.D., SMITH P.J.*, A Moderated Target Sub-Assembly Design for Minor Actinide Transmutation*. In *GLOBAL2003,* New Orleans, LA, USA, November 16-20, 2003.

[28] SUDREAU F., BONNEROT J. M., BRUNON E. et al.*, Oxide fuels and targets for transmutation*. In *OECD/NEA Proceeding 9th International Exchange Meeting on Partitioning and Transmutation,* Nîmes, France, September 25-29, 2006.

[29] KOCH L. J.*, Experimental Breeder Reactor-II (EBR-II),* USA : American Nuclear Society, 2008, 288 p.

[30] KUMMERER K.*, Selection of Liquid Metals in Reactor Technology.* Atomkernenergie (ATKE), 1964, 9, p. 159–165.

[31] KUMMERER K.*, Selection of Liquid Metals in Reactor Technology.* KFK 239, KfK, Karlsruhe, Germany, 1964.

[32] OECD NEA*, Table of simple integral neutron cross section data from JEF-2.2, ENDF/B-VI, JENDL-3.2, BROND-2 and CENDL-2.* JEF Report 14, France, 1994, 236 p.

[33] ROCHMAN D., KONING A.J., DA CRUZ D.F. ET al.*, On the evaluation of 23Na neutron-induced reactions and validations.* Nuclear Instruments and Methods in Physics Research Section A: Accelerators, Spectrometers, Detectors and Associated Equipment, 612(2), p. 374–387.

[34] KESSLER G.*, Sustainable and Safe Nuclear Fission Energy :* Springer, 2012, 466 p.

[35] *http://www.cp-esfr.eu/,* last accessed on 30.11.2015.

[36] IAEA*, Liquid Metal Coolants for Fast Reactors Cooled By Sodium, Lead, and Lead-Bismuth Eutectic.* No. NP-T-1.6, 2012.

[37] MIKAMI H., SHONO A., HIROI H.*, Sodium Leak at Monju (I) – Cause and Consequences*. In *Tech. Committee Meeting on Evaluation of Radioactive Materials Release and Sodium Fires in Fast Reactors,* O -arai, Ibaraki, Japan, November 11-14, 1996.

[38] WALTAR A. E., TODD D. R., TSVETKOV P. V.*, Fast Spectrum Reactors,* USA : Springer, 2012, 720 p.

[39] KEEPIN G. R.*, Physics of nuclear kinetics :* Addison-Wesley Pub. Co, 1965, 435 p. (Addison-Wesley series in nuclear science and engineering).

[40] HUMMEL H. H., OKRENT D.*, Reactivity Coefficients in Large Fast Power Reactors :* American Nuclear Society, 1970, 386 p. (Monograph series on nuclear science and technology).

[41] BOGENSBERGER H. G., CALDAROLA L., MITZEL F. et al.*, Analysis of SEFOR Experiments.* KFK 2095, EUR 5200e, KfK, Karlsruhe, Germany, 1975.

[42] BUIRON L., FONTAINE B., ANDRIOLO L.*, Transmutation abilities of the SFR low void effect core concept "CFV" 3600 MWth*. In *ICAPP '12,* Chicago, IL, USA, June 24-28, 2012.

[43] THOMPSON T. J., BECKERLEY J. G.*, The Technology of Nuclear Reactor Safety - Vol. 1: Reactor Physics and Control,* Cambridge, Massachusetts, USA : The MIT Press, 1964, 755 p.

[44] BOPP A.*, The Calculation of Fuel Bowing Reactivity Cofficients in a Subcritical Advanced Burner Reactor.* Master Thesis, Georgia Institute of Technology, 2013.

[45] MORAN T. J.*, Core restraint contributions to radial expansion reactivity.* Joint ASME/ANS Nuclear Power Conference, Philadeplphia, Pennsylvania, USA, 1986.

[46] PILARSKI S.*, Étude du potentiel de concepts innovants de réacteurs à neutrons rapides (RNR) vis-à-vis des exigences du développement durable.* PhD Thesis, 2008.

[47] VASILE A.*, SFR CORE DESIGN PERFORMANCE AND SAFETY*. In *IAEA Workshop on Nuclear Power Technology Development,* 2012.

[48] PALMIOTTI G., SALVATORES M., ASSAWAROONGRUENGCHOT M.*, Innovative Fast Reactors: Impact of Fuel Composition on Reactivity Coefficients*. In *FR09,* Kyoto, Japan, December 7-11, 2009.

[49] BUIRON L., VARAINE F., VERRIER D. et al.*, Heterogeneous Minor Actinide Transmutation on a UO_2 blanket and on $(U,Pu)O_2$ fuel in a Sodium-cooled Fast Reactor - Assessment of core performances*. In *GLOBAL2009,* Paris, France, September 6-11, 2009.

[50] MASCHEK W., STRUWE D.*, Accident analyses and passive measures reducing the consequences of a core melt in CAPRA/CADRA reactor.* Nuclear Engineering and Design, 2000, 202(2-3), p. 311–324.

[51] EHSTER S.*, Safety objectives and design principles.* Deliverable SP3.1. D1, European Sodium Fast Reactor Reactor Consortium, 2009.

[52] BECKJORD M.A., CUNNINGHAM M. A., MURPHY J. A.*, Probabilistic safety assessment development in the United States 1972-1990.* Reliability Engineering & System Safety, 1993, 39, p. 159–170.

[53] POUMEROULY S.*, Neutronics aspects associated to the prevention and mitigation of severe accidents in sodium cooled reactors cores :* PhD thesis, Institut Polytechnique de Grenoble, 2010, 306 p.

[54] IAEA*, Basic Safety Principles for Nuclear Power plants, 75-INSAG-3 Rev. 1.* INSAG-12, 1999.

[55] AREVA-NP. UK-EPR*, Fundamental Safety Overview.* Technical report, 2008.

[56] SAMOUR G.*, The EPR of Flamanville.* Technical report, Nuclear Physic Institute of ASCR, 2009.

[57] IAEA*, Assessment of Defence in Depth for Nuclear Power Plants.* IAEA Safety Reports Series No.46, 2005.

[58] WENRA RHWG*, Report Safety of new NPP designs,* 2013, 52 p.

[59] IAEA*, Safety of Nuclear Power Plants: Design.* No SSR-2/1, 2012.

[60] IAEA*, Severe Accident Management Programmes for Nuclear Power Plants.* IAEA Safety Standards series No. NS-G-2.15, Vienna, Austria, 2009.

[61] CARLUEC B., GIRAUD B.*, The European Project PDS-XADS "preliminary Design Studies of an Experimental Accelerator-Driven System".* Utilisation and Reliability of High Power Proton Accelerators Workshop Proceedings, Daejeon, Republic of Korea, May 2004.

[62] DELANEY M. J., APOSTOLAKIS G. E., DRISCOLL M. J.*, Risk-informed design guidance for future reactor systems.* Nuclear Engineering and Design, 2005, 235(14).

[63] IAEA*, Guidance for the Application of an Assessment Methodology for Innovative Nuclear Energy Systems INPRO Manual - Overview of the Methodology.* IAEA-TECDOC-1575 Rev. 1, 2008, 128 p.

[64] RSWG*, An Integrated Safety Assessment Methodology (ISAM) for GENERATION IV Nuclear Systems.* GIF/RSWG/2010/002/Rev 1, 2011.

[65] IAEA*, INES The International Nuclear and Radiological Event Scale, User's Manual 2008 Edition,* 2013.

[66] IAEA*, INES The International Nuclear and Radiological Event Scale.* Information Series / Division of Public Information, 08-26941 / E, 2013.

[67] European Technical Safety Organisations Network (ETSON)*, Technical Safety Assessment Guide - Deterministic Severe Accidents Analysis.* ETSON/2013-003, 2013.

[68] MASCHEK W.*, Transition phase analysis for hypothetical loss of flow accidents*. In *Ispra Courses on Nuclear Engineering and Technology, Multiphase processes in LMFBR Safety Analyses,* 1982.

[69]   SATO I., TOBITA Y., KONISHI K. et al*., Safety Strategy of JSFR Eliminating Severe Recriticality Events and Establishing In-Vessel Retention in the Core Disruptive Accident.* Journal of Nuclear Science and Technology, 2011, 48, 4, p. 556–566.

[70]   BETHE H. A., TAIT J. H*., An Estimate of the Order of Magnitude of Vigorous Interaction Expected Should the Core of a Fast Reactor Collapse.* RHM (56)/113, Harwell, 1956.

[71]   *http://www.ne.anl.gov/codes/sas4a/,* last accessed on 30.11.2015.

[72]   ROYL P., PFRANG W., STRUWE D*., Reactivity feedback evaluation of material relocations in the Cabri-1 experiments with fuel worth distributions from SNR-300.* Nuclear Engineering and Design, 1994, 147, 1, p. 85–91.

[73]   KONDO Sa., YAMANO H., SUZUKI T. et al*., SIMMER-III: A Computer Program for LMFR Core Disruptive Accident Analysis.* JNC TN9400 2001-002, 2000.

[74]   YAMANO H., FUJITA S., TOBITA Y. et al*., SIMMER-IV: A Three-Dimensional Computer Program for LMFR Core Disruptive Accident Analysis.* JNC TN9400 2003-070, 2003.

[75]   MASCHEK W., RINEISKI A., SUZUKI T. et al*., SIMMER-III and SIMMER-IV Safety Code Development for Reactors with Transmutation Capability*. In *Mathematics and Computation, Supercomputing, Reactor Physics and Biological Applications,* Avignon, France, September 12-15, 2005.

[76]   ALCOUFFE R. E., BAKER R. S., BRINKLEY F. W. et al*., DANTSYS: a diffusion accelerated neutral particle transport code system.* LA-12969- M, LANL, 1995.

[77]   SORAN P. D*., Neutronics rebalance algorithms for SIMMER.* LA-6152-MS, 1975.

[78]   TOBITA Y., KONDO S., YAMANO H. et al*., The Development of SIMMER-III, An Advanced Computer Program for LMFR Safety Analysis*. In *Proc. IAEA/NEA Technical Meeting on Use of Computational Fluid Dynamics (CFD) Codes for Safety Analysis Reactors Systems Including Containment,* Pisa, Italy, November, 2002.

[79]   SRINIVASAN G., SURESH KUMAR K.V. , RAJENDRAN B. et al*., The Fast Breeder Test Reactor—Design and operating experiences.* Nuclear Engineering and Design, 236(7-8), p. 796–811.

[80]   IAEA*, Fast Reactor Database 2006 Update.* IAEA-TECDOC-1531, 2006.

[81]   SAUVAGE J. F*., Phénix - 30 years of history: the heart of a reactor :* Ellipse Documentation, 2004, 230 p.

[82]   BABELOT J. F., FIORINI G. L., ABRAM T. et al*., Sodium cooled Fast Reactor (SFR)*. In *FISA2006, Proceedings of the Int. Conf. on Euratom Research and Training in Reactor Systems,* Luxembourg, March 13-16, 2006.

[83]   SCIORA P., BUIRON L., RIMPAULT G. et al*., A break even oxide fuel core for an innovative French Sodium cooled fast reactor: neutronic studies result*. In *GLOBAL2009,* Paris, France, September 6-11, 2009.

[84]   KLUEH R. L., SHINGLEDECKER J. P. , SWINDEMAN R. W. et al*., Oxide dispersion-strengthened steels: A comparison of some commercial and experimental alloys.* Journal of Nuclear Materials, 341(2-3), p. 103–114.

[85]   SAGARADZE V. V., SHALAEV V. I., ARBUZOV V. L. et al*., Radiation resistance and thermal creep of ODS ferritic steels.* Journal of Nuclear Materials, 295(2-3), p. 265–272.

[86]   TOBITA Y., YAMANO H., SATO I*., Analytical study on elimination of severe recriticalities in large scale LMFBRS with enhancement of fuel discharge.* Nuclear Engineering and Design, 2008, 238, p. 57–65.

[87]   BARTHOLD W. P., BEITEL J. C., LAM P. S. K. et al*., Low Sodium Void Cores*. In *Proceedings of the Int. Conf. ENS/ANS Topical Meeting on Nuclear Power Reactor Safety,* Brussels, Belgium, October 16–19, 1978.

[88] HILL R. N., KHALIL H.*, An Evaluation of LMR Design Options for reduction of Sodium Void Worth*. In *Int. Conf. on the Physics of reactors: Operation, Design & Computation,* Marseille, France, April 23-26, 1990.

[89] IAEA*, Evaluation of Benchmark Calculations on a Fast Power Reactor Core.* Final Report of an International Benchmark Program, IAEA-TECDOC-731, 1994.

[90] HONG S. G., KIM Y., VENNERI F.*, Characterization of a sodium-cooled fast reactor in an MHR–SFR synergy for TRU transmutation.* Annals of Nuclear Energy, 2008, 35, p. 1461–1470.

[91] KESSLER G.*, Proliferation-Proof Uranium/Plutonium Fuel Cycles,* KIT Scientific Publishing, 2011, 408 p.

[92] HILL R. N., KHALIL H.*, Overview of Global Nuclear Energy Partnership and advanced burner reactor*. In *233rd American Chemical Society Meeting,* Chicago, IL, USA, March 25-29, 2007.

[93] Commissariat à l'énergie atomique*, Nuclear fuels,* Paris : Le Moniteur, 2009, 147 p.

[94] KONINGS R. J. M., Ed., Material properties/oxide fuels for light water reactors and fast neutron reactors, Spain : Elsevier, 2012, p. 547-578(Comprehensive nuclear materials, 2).

[95] DELAGE F., CARMACK J., LEE C. B. et al.*, Status of advanced fuel candidates for Sodium Fast Reactor within the Generation IV International Forum.* Journal of Nuclear Materials, 2013, 441(1-3), p. 515–519.

[96] IAEA*, Status and trends of nuclear fuels technology for sodium cooled fast reactors.* IAEA Nuclear Energy series No. NF-T-4.1, Vienna, 2011.

[97] KONINGS R. J. M.*, Advanced fuel cycles for accelerator driven systems: fuel fabrication and reprocessing.* EUR 19928 EN, 2001.

[98] CHANG Y. I.*, The Integral Fast Reactor.* CONF-8810155--28, USA, 1988.

[99] CHANG Y. I.*, Technical rationale for metal fuel in fast reactors.* Nuclear Engineering and Technology, 2007, 39, 3, p. 161–170.

[100] SUMNER T.*, Effects of fuel type on the safety characteristics of a sodium cooled fast reactor.* PhD Thesis, Georgia Institute of Technology, 2010.

[101] BAILLY H., PRUNIER C., MENESSIER D.*, The nuclear fuel of pressurized water reactors and fast reactors design and behaviour,* France : TEC & DOC, 1999, 642 p.

[102] LANHAM W. B., RUNION T. C.*, PUREX Process for Plutonium and Uranium Recovery.* USAEC, ORNL-479, USA, 1949.

[103] WALLENIUS J., PILLON S.*, N-15 Requirement for 2nd stratum ADS nitride fuels*. In *Proceedings of the AccApp/ADTTA 2001 Meeting,* Reno, USA, November 11-15, 2001.

[104] MASCHEK W.*, Core Disruptive Accident Analyses for Advanced CAPRA Cores*. In *ICONE-4,* New Orleans, LA, March 10-14, 1996.

[105] BURKES D. E., FIELDING R. S., PORTER D. L. et al.*, A US perspective on fast reactor fuel fabrication technology and experience. Part II: Ceramic fuels.* Journal of Nuclear Materials, 2009, 393(1), p. 1–11.

[106] VARAINE F., RIMPAULT G., MIGNOT G. et al.*, Comparative review on different fuels for GEN IV Sodium Fast Reactors: merits and drawbacks*. In *FR09,* Kyoto, Japan, December 7-11, 2009.

[107] YOUNG M. F., MURATA K. K., HITCHCOCK J. T. et al.*, The FCI potential of oxide and carbide fuels.* SAND-79-0752C, Bournemouth, UK, 1979.

[108] OECD NEA*, State-of-the-art Report on Innovative Fuels for Advanced Nuclear Systems.* NEA No. 6895, OECD, 2014, 195 p.

[109] MASCHEK W.*, Safety and Design Concepts of the 400 MWth-Class EFIT AcceleratorDriven Transmuter and Considerations for Further Developments.* Energy conversion and management, 2010, 51, p. 1764–1773.

[110] CHEN X. N., RINEISKI A., MASCHEK W. et al., 2011*, Comparative studies of CERCER and CERMET fuels for EFIT from the viewpoint of core performance and safety.* Progress in Nuclear Energy, 53(7), p. 855–861.

[111] KATHOL W*., KNK II - an experimental power station equipped with a fast core.* Nuclear Engineering International, 1979, 24, p. 41–44.

[112] GADZHIEV G. I. et al., Review of experimental works in the BOR-60 reactor, 1999.

[113] PILLON S*., Les combustibles de la Génération IV : combustible RCG & combustible SFR*. In *Atelier GEDEPEON,* 2010.

[114] CHAUVIN N*., Ceramic fuels for MA homogeneous and heterogeneous recycling in sodium fast reactors*. In *The 2013 Frédéric Joliot & Otto Hahn Summer School,* Karlsruhe, Germany, August 2013.

[115] FAZIO C*., Front-end of the nuclear fuel cycle*. In *ITU Training Course: Introduction to the front-end of the nuclear fuel cycle,* Karlsruhe, Germany, 2014.

[116] OLANDER D., Fundamental aspects of nuclear reactors, USA : Us Dept. of Energy, 1976, p. 113-144.

[117] MORSS L. R., EDELSTEIN N. M., FUGER J. et al., The Chemistry of the Actinide and Transactinide Elements, 2011, p. 3665-3811(The Chemistry of the Actinide and Transactinide Elements, 6).

[118] PETERSON S*., Assessment of Gel-Sphere-Pac Fuel for Fast Breeder Reactors.* ORNL- 5468, Oak Ridge, USA, 1978.

[119] CEA*, Les énergies bas carbone.* CLEFS CEA - N° 61, Printemps 2013.

[120] OECD NEA*, Spent nuclear fuel reprocessing flowsheet.* NEA/NSC/WPFC/DOC(2012)15, OECD, 2012, 120 p.

[121] KONINGS R. J. M., Ed., Material performance and corrosion/waste materials, Spain : Elsevier, 2012, p. 343-366(Comprehensive nuclear materials, 5).

[122] MALMBECK R*., Back-end of the nuclear fuel cycle*. In *Training Course: Introduction to the back-end of the nuclear fuel cycle,* Karlsruhe, Germany, 2014.

[123] DEITRICH L. W., DICKERMAN C. E., KLICKMAN A. E. et al*., A review of experiments and results from the transient reactor test (TREAT) facility.* ANL/RE/CP-96982, Oak Ridge, USA, 1998.

[124] WRIGHT S. A., WORLEDGE D. H., CANO G. L. et al*., Fuel-Disruption Experiments Under High-Ramp-Rate Heating Conditions.* NUREG/CR-3662, SAND81-0413, R7, 1983.

[125] SATO I., LEMOINE F., STRUWE D*., Transient fuel behavior and failure condition in the CABRI-2 experiments.* Nuclear technology, 2004, 145(1), p. 115–137.

[126] LASSMANN K*., TRANSURANUS: a fuel rod analysis code ready for use.* Journal of Nuclear Materials, 188, p. 295–302.

[127] MELIS J. C., ROCHE L., PIRON J.P. et al*., GERMINAL-A computer code for predicting fuel pin behavior.* Journal of Nuclear Materials, 1992, 188, p. 303–307.

[128] KONINGS R. J. M., Ed., Advanced fuels/fuel cladding/nuclear fuel performance modeling and simulation, Spain : Elsevier, 2012, p. 143-150(Comprehensive nuclear materials, 3).

[129] ABDELOUAS A., NOIRAULT S., GRAMBOW B., 2006*, Immobilization of inert TRISO-coated fuel in glass for geological disposal.* Journal of Nuclear Materials, 358(1), p. 1–9.

[130] HERBIG R., RUDOLPH K., LINDAU B. et al*., Vibrocompacted fuel for the liquid metal reactor BOR-60.* Journal of Nuclear Materials, 1993, 204, p. 93–101.

[131] KONINGS R. J. M., Ed., Advanced fuels/fuel cladding/nuclear fuel performance modeling and simulation, Spain : Elsevier, 2012, p. 275-312(Comprehensive nuclear materials, 3).

[132] COZZO C., CABANES-SEMPERE M., POUCHON M. A.*, Methods of advanced waste conditioning by microwave internal gelation: Set-up development and modelling.* In *IEMPT-12,* Prague, September 24-27, 2012.

[133] MORIHIRA M., NAKAMURA M., OZAWA T. et al.*, Final Report of the FUJI Project concerning the Research and Development of Advanced Sphere-pac Fuel among JNC, PSI and NRG.* JNC TY8400 2005-006, 2005.

[134] D'AGATA E., HANIA P. R., McGINLEY J. et al.*, SPHERE: Irradiation of sphere-pac fuel of UPuO$_{2-x}$ containing 3% Americium.* Nuclear Engineering and Design, 2014, 275, p. 300–311.

[135] POUCHON M.*, Gas-cooled Reactors for Power Production, Heat Generation, and High-temperature applications.* In *The 2012 Frédéric Joliot & Otto Hahn Summer School,* Cadarache, France, August 2012.

[136] VAIDYA V. N.*, Status of sol–gel process for nuclear fuels.* Journal of Sol-Gel Science and Technology, 2008, 46, p. 369–381.

[137] McGEARY R.K.*, Mechanical packing of spherical particles.* Journal of The American Ceramic Society, 1961, 10, p. 513–522.

[138] KONINGS R. J. M., Ed., Advanced fuels/fuel cladding/nuclear fuel performance modeling and simulation, Spain : Elsevier, 2012, p. 789-817(Comprehensive nuclear materials, 3).

[139] KAISER L. L., ROLFE R. L., SNEED B. J. et al.*, Characterization of the Engineering Test Reactor Facility.* No. EGG-PR-5784, Idaho National Engineering Lab, Idaho Falls, USA, 1982.

[140] BEATTY L., NORMAN R. E., NOTZ K. J. et al.*, Gel sphere-pac fuel for thermal reactors - Assessment of fabrication technology and irradiation performance.* ORNL-5469, Oak Ridge National Laboratory, Oak Ridge, Tenn., USA, 1979, 183 p.

[141] LOTTS A. L., Ed.*, Fast breeder reactor oxide fuel development - Final report.* ORNL-4901, Oak Ridge National Laboratory, Oak Ridge, Tenn., USA, 1973.

[142] *http://www.fp7-fairfuels.eu/,* last accessed on 30.11.2015.

[143] *https://ec.europa.eu/jrc/sites/default/files/hfr_mini_blue_book.pdf,* last accessed on 30.11.2015.

[144] ANDRIOLO L., RINEISKI A., CHEN X-N. et al.*, Extension of the SIMMER code for the assessment of core thermal expansion feedbacks for transient analysis.* In *International Youth Nuclear Congress,* Burgos, Spain, July 6-12, 2014.

[145] JEVREMOVIC T.*, Nuclear Principles in Engineering :* Springer, 2008, 546 p.

[146] BUSSAC J., REUSS P.*, Traité de neutronique: physique et calcul des réacteurs nucléaires avec application aux réacteurs à eau pressurisée et aux réacteurs à neutrons rapides :* Hermann, 1978, 662 p. (Collection Enseignement des sciences).

[147] GUYOT M.*, NEUTRONICS AND THERMAL-HYDRAULICS COUPLING: SOME CONTRIBUTIONS TOWARD AN IMPROVED METHODOLOGY TO SIMULATE THE INITIATING PHASE OF A SEVERE ACCIDENT ON SODIUM FAST REACTORS :* PhD Thesis, Université d'Aix-Marseille, 2014, 252 p.

[148] SANCHEZ R., McCORMICK N. J.*, A Review of Neutron Transport Approximations.* Nuclear Science and Engineering, 1982, 80, p. 481–535.

[149] OTT K. O., NEUHOLD R. J.*, Introductory nuclear reactor dynamics :* American Nuclear Society, 1985, 362 p.

[150] LATHROP K. D.*, The early days of the SN method.* Trans. Am. Nucl. Soc., 1992, 66, p. 241–242.

[151] BOHL W. R., LUCK L. B.*, SIMMER-II: A Computer Program for LMFBR Disrupted Core Analysis.* LA-11415-MS, Los Alamos National Laboratory, New Mexico, USA, 1990.

[152] ALCOUFFE R. E.*, Diffusion Synthetic Acceleration Methods for the Diamond-Differenced Discrete-Ordinates Equations.* Nuclear Science and Engineering, 1977, 64, p. 344–355.

[153] ALCOUFFE R. E., BAKER R. S., DAHL J. A. et al.*, PARTISN: A Time -Dependent, Parallel Neutral Particle Transport Code System.* Los Alamos National Laboratory, LA - UR -08 -07258, November 2008.

[154] CAHALAN J. E., DUNN F. E., HERZOG J. P. et al.*, The SAS4A/SASSYS--1 Safety Analysis Code System; Chapter 4 Reactor Point Kinetics, Decay Heat, and Reactivity Feedback.* ANL/NE--12/4, Argonne National Laboratory, IL, USA, 2012.

[155] ZYLBERSZTEJN F., TRAN H. N., PAZSIT I. et al.*, Calculation of the Neutron Noise Induced By Periodic Deformations of A Large Sodium-Cooled Fast Reactor Core.* Nuclear Science and Engineering, 2014, 177(2), p. 203–218.

[156] DIETRICH J.R.*, The Physics of Advanced Reactors.* Br. J. Appl. Phys, 1956, Supplement No. 5, p. 9-23.

[157] RIMPAULT G., PLISSON D., TOMMASI J. et al.*, The ERANOS Code and Data System for Fast Reactor Neutronic Analyses*. In *PHYSOR02,* Seoul, Korea, October 7-10, 2002.

[158] RIMPAULT G.*, Algorithmic features of the ECCO cell code for treating heterogeneous fast reactor assemblies*. In *International Topical Meeting on Reactor Physics and Computation,* Portland, Oregon, May 1-5, 1995.

[159] PALMIOTTI G., RIEUNIER J. M., GHO C. et al.*, Optimized Two-Dimensional Sn Transport Code (BISTRO).* Nuclear Science and Engineering, 1990, 104, p. 26–33.

[160] SHIKHOV S. B.*, Perturbation theory formulas for the effect of the dimensions on the critical mass in a fast reactor.* The Soviet Journal of Atomic Energy, 1959, 6(2), p. 90–94.

[161] REED M., SMITH K., FORGET B.*, The "Virtual Density" Principle of Neutronics and Its Application to Geometric Perturbation Theory.* Trans. Am. Nucl. Soc., 2012, 107.

[162] *http://www-cathare.cea.fr/,* last accessed on 30.11.2015.

[163] MASSONE M., GABRIELLI F., RINEISKI A.*, SIMMER extension for cross-section collapsing introduction*. In *International Youth Nuclear Congress,* Burgos, Spain, July 6-12, 2014.

[164] MARCHETTI M.*, Personal communication,* Karlsruhe.

[165] ANDRIOLO L., RINEISKI A., VEZZONI B. et al.*, An Innovative Methodology for Evaluating Core Thermal Expansion Feedbacks in Transient Analyses*. In *ICAPP'15,* Nice, France, May 3-6, 2015.

[166] OECD NEA*, The JEFF-3.1 Nuclear Data Library.* JEFF Report 21, NEA No. 6190, 2006.

[167] BORTOT S. et al.*, The BELLA code for point dynamic simulations of transients*. In *ESNII+ Workshop On Safety,* Stockholm, Sweden, May, 2014.

[168] DARMET G., MASSARA S.*, Dynamical Analysis of Innovative Core Designs Facing Unprotected Transients with the MAT5DYN Code*. In *ICAPP'12,* Chicago, IL, USA, June 24-28, 2012.

[169] KAMIYAMA K., KONDO S.*, SIMMER-III Structure Model – Model and Method Description.* JNC TN9400 2004-043, O-arai Engineering Center, Japan Nuclear Cycle Development Institute, 2004.

[170] YAMANO H., TOBITA Y.*, Experimental Analyses by SIMMER-III on Fuel-Pin Disruption and Low-Energy Disrupted Core Motion.* Journal of Power and Energy Systems, 2010, 4(1), p. 164–179.

[171] CARBAJO J. J., YODER G. L., POPOV S. G. et al.*, A review of the thermophysical properties of MOX and UO_2 fuels.* Journal of Nuclear Materials, 2001, 299(3), p. 181–198.

[172] LUCUTA P.G., MATZKE HJ., HASTINGS I. J.*, A pragmatic approach to modelling thermal conductivity of irradiated UO_2 fuel: review and recommendations.* Journal of Nuclear Materials, 1996, 232(2-3), p. 166–180.

[173] PHILIPPONNEAU Y.*, Thermal conductivity of (U, Pu)O_{2-x} mixed oxide fuel.* Journal of Nuclear Materials, 188, p. 194–197.

[174] HARDING J. H., MARTIN D. G., POTTER P. E.*, Thermophysical and thermodynamic properties of fast reactor materials.* Commission of the European Communities, EUR 12402 EN, 1989.

[175] SCHULZ B.*, Thermal conductivity of porous and highly porous materials.* High Temperatures - High Pressures, 1981, 13, p. 649–660.

[176] HALL R. O. A., MARTIN D. G.*, The thermal conductivity of powder beds. a model, some measurements on UO$_2$ vibro-compacted microspheres, and their correlation.* Journal of Nuclear Materials, 1981, 101(1-2), p. 172–183.

[177] ISHII T., YUDA R., HIRAI M. et al.*, Thermal conductivities of granular UO$_2$ compacts with/without uranium particles.* Journal of Nuclear Science and Technology, 2004, 41, 12, p. 1204–1210.

[178] POWERS A. E.*, Conductivity in aggregates.* Knolls Atomic Power Laboratory, General Electric Co., KAPL-2145, 1961.

[179] GODBEE H. W., ZIEGLER W. T.*, Thermal Conductivities of MgO, Al2O3, and ZrO2 Powders to 850°C. II. Theoretical.* Journal of Applied Physics, 1966, 37(1), p. 56.

[180] MILLER J. V. et al.*, Estimating thermal conductivity of cermet fuel materials for nuclear reactor application.* National aeronautics and space administration, Cleveland, Ohio, USA, 1967, 31 p.

[181] BOTTA F., HELLWIG C.*, SPACON - A theoretical Model for Calculating the Heat Transport Properties in Sphere-pac Fuel Pins.* Nuclear Science and Engineering, 2000, 135, p. 165–176.

[182] WALLIN H., NORDSTROEM L. A., HELLWIG C.*, The sphere-pac fuel code "SPHERE-3".* In *IAEA-TECDOC-1233, Proceedings of a Technical Committee meeting, Nuclear fuel behaviour modelling at high burnup and its experimental support,* Windermere, UK, June 19-23, 2000, p. 323-338.

[183] KRISHNAN R. V., NAGARAJAN K., CLEMENT RAVICHANDAR S. et al.*, Sol–gel development activities at IGCAR.* Journal of Sol-Gel Science and Technology, 2011, 59, p. 394-403.

[184] MORITA K., TOBITA Y., KONDO Sa. et al.*, SIMMER-III Analytic Thermophysical Property Model.* JNC TN9400 2000-004, O-arai Engineering Center, Japan Nuclear Cycle Development Institute, 1999.

[185] MASCHEK W., FLAD M., MATZERATH BOCCACCINI C. et al.*, Prevention and Mitigation of Severe Accident Developments and Recriticalities in Advanced Fast Reactor Systems.* Progress in Nuclear Energy, 2011, 53, p. 835–841.

[186] ZHANG D., CHEN X.-N.*, CP-ESFR Modeling and its steady state results -- Update for overall configuration.* KIT, IKET-TRANS, Internal report, Karlsruhe.

[187] VASILE A., FIORINI G. L., DUFOUR Ph. et al.*, The Collaborative Project for a European Sodium Fast Reactor CP-ESFR.* In *ICAPP'11,* Nice, France, May 2-6, 2011.

[188] ANDRIOLO L., CHEN X-N., MATZERATH BOCCACCINI C. et al.*, Preliminary safety analysis of mixed oxide sphere-pac driver fuels in the CP-ESFR WH core.* Energy Procedia, 2015, 71, p. 149–158.

[189] MASCHEK W., ANDRIOLO L., MATZERATH BOCCACCINI C. et al.*, Safety Analyses for Sodium-Cooled Fast Reactors with Pelletized and Sphere-pac Oxide Fuels within the FP-7 European Project PELGRIMM.* In *ICAPP'15,* Nice, France, May 3-6, 2015.

[190] CORAPCIOGLU M. Y., Ed.*, Advances in Porous Media,* (3) 1996, 454 p.

[191] MORITA K., FISCHER E. A , THURNAY K.*, Thermodynamic properties and equations of state for fast reactor safety analysis, Part II: properties of fast reactor materials.* Nuclear Engineering and Design, 1998, 183, p. 193–211.

[192] MORITA K., FISCHER E. A*., Thermodynamic properties and equations of state for fast reactor safety analysis, Part I: analytic equation-of-state model.* Nuclear Engineering and Design, 1998, 183, p. 177–191.

[193] BRIGGS L., MONTI S., HU W. et al*., EBR-II passive safety demonstration tests benchmark analyses; Phase 2*. In *NURETH-16,* Chicago, USA, August 30 - September 4, 2015.

[194] BRIGGS L., SUMNER T., FEI T. et al*., EBR-II Passive Safety Demonstration Tests Benchmark Analyses – Phase 1.* Trans. Am. Nucl. Soc., 2014, 111, p. 1263–1266.

[195] SOFU T., BRIGGS L. L*., Benchmark Specifications for EBR-II Shutdown Heat Removal Tests*. In *ICAPP'12,* Chicago, IL, USA, June 24-28, 2012.

[196] VEZZONI B*., Personal communication*.

[197] GABRIELLI F*., Personal communication*.

[198] PALMIOTTI G., CAHALAN J., PFEIFFER P. et al*., Requirements for Advanced Simulation of Nuclear Reactor and Chemical Separation Plants.* ANL-AFCI-168, May 2005.

[199] PALMIOTTI G., SALVATORES M., ALIBERTI G*., Validation of Simulation Codes for Future Systems: Motivations, Approach, and the Role of Nuclear Data.* INL/CON-07-13351, October 2007.

[200] VEZZONI B., MARCHETTI M., ANDRIOLO L. et al*., SIMMER/PARTISN analyses of EBR-II shutdown heat removal tests*. In *PHYSOR 2016 (in press),* Sun Valley, Idaho, USA, May 1-5, 2016.

Chapter 10

APPENDICES

APPENDICES

In a steady state reactor without external neutron source, the neutron balance equation is given as Eq. A-1.

$$\mathscr{M}\,\varphi = \lambda \mathscr{F}\,\varphi \qquad \text{A-1}$$

where $\mathscr{M} = \mathscr{F} - \mathscr{H} + \mathscr{S}$

The adjoint problem of Eq. A-1 is written as Eq. A-2

$$\mathscr{M}^{*}\varphi^{*} = \lambda^{*}\mathscr{F}^{*}\varphi^{*} \qquad \text{A-2}$$

Multiplying Eq. A-1 by φ' and Eq. A-2 by φ and integrating over space, angle and energy yields Eq. A-3 and Eq. A-4 respectively.

$$\left\langle \varphi^{*}, \mathscr{M}\,\varphi \right\rangle = \lambda \left\langle \varphi^{*}, \mathscr{F}\,\varphi \right\rangle \qquad \text{A-3}$$

$$\left\langle \varphi, \mathscr{M}^{*}\varphi^{*} \right\rangle = \lambda^{*} \left\langle \varphi, \mathscr{F}^{*}\varphi^{*} \right\rangle \qquad \text{A-4}$$

Revolving Eq. A-4 yields Eq. A-5

$$\left\langle \varphi^{*}, \mathscr{M}\,\varphi \right\rangle = \lambda^{*} \left\langle \varphi^{*}, \mathscr{F}\,\varphi \right\rangle \qquad \text{A-5}$$

Substracting Eq. A-3 and Eq. A-5 results in Eq. A-6

$$\left\langle \varphi^{*}, \mathscr{M}\,\varphi \right\rangle - \left\langle \varphi^{*}, \mathscr{M}\,\varphi \right\rangle = 0 = \left(\lambda - \lambda^{*}\right)\left\langle \varphi^{*}, \mathscr{F}\,\varphi \right\rangle \qquad \text{A-6}$$

Since $\left\langle \varphi^{*}, \mathscr{F}\,\varphi \right\rangle$ only equals zero if φ respectively φ^{*} equals zero, if follows that $\lambda = \lambda^{*}$

APPENDIX A

Appendix B:
Selection of the weighting function [149]

Consider a simple eigenvalue problem containing a single operator $\mathscr{F}$. Eq. B-1 describes the unperturbed and Eq. B-2 the perturbed problem. φ and φ_0 represent functions of the phase space and energy domain, λ and λ_0 are numbers.

$$\mathscr{F}_0 \varphi_0 = \lambda_0 \varphi_0$$

<div align="right">B-1</div>

$$\mathscr{F} \varphi = \lambda \varphi$$

<div align="right">B-2</div>

Introducing that $\varphi = \varphi_0 + \Delta\varphi$ in Eq. B-2 yields Eq. B-3

$$\mathscr{F}\varphi_0 = \lambda\varphi_0 - (\mathscr{F}\Delta\varphi - \lambda\Delta\varphi)$$

<div align="right">B-3</div>

Eq. B-1 and Eq. B-3 are then multiplied by an arbitrary weighting function w of the phase space and energy domain and integrated over this domain. This results in Eq. B-4 and Eq. B-5, respectively

$$\langle w, \mathscr{F}_0\varphi_0 \rangle = \lambda_0 \langle w, \varphi_0 \rangle$$

<div align="right">B-4</div>

$$\langle w, \mathscr{F}\varphi_0 \rangle = \lambda \langle w, \varphi_0 \rangle - (\langle w, \mathscr{F}\Delta\varphi \rangle - \lambda \langle w, \Delta\varphi \rangle)$$

<div align="right">B-5</div>

By subtracting Eq. B-4 to Eq. B-5 one obtains Eq. B-6 where $\Delta\mathscr{F} = \mathscr{F} - \mathscr{F}_0$ and $\Delta\lambda = \lambda - \lambda_0$

$$\langle w, \Delta\mathscr{F}\varphi_0 \rangle = \Delta\lambda \langle w, \varphi_0 \rangle - \langle w, \{\mathscr{F} - \lambda\}\Delta\varphi \rangle$$

<div align="right">B-6</div>

The right hand side term of Eq. B-6 can now be rewritten as Eq. B-7

$$\langle w, \{\mathscr{F} - \lambda\}\Delta\varphi \rangle = \langle w, \{\mathscr{F}_0 - \lambda_0\}\Delta\varphi \rangle + \langle w, \{\Delta\mathscr{F} - \Delta\lambda\}\Delta\varphi \rangle$$

<div align="right">B-7</div>

The second term on the right hand side of Eq. B-7 is composed of a product of two differenced quantities, this second order term is hence small compared to the first order term if the perturbation is small. Hence this term can be neglected.

The first term on the right hand side of Eq. B-7 can be rewritten as Eq. B-8

$$\left\langle w, \left\{ \mathscr{R}_0 - \lambda_0 \right\} \Delta\varphi \right\rangle = \left\langle \Delta\varphi, \left\{ \mathscr{R}_0^* - \lambda_0 \right\} w \right\rangle$$

<div align="right">B -8</div>

Where $\mathscr{R}_0^*$ is the adjoint operator of $\mathscr{R}_0$. If the weighting function w is chosen to be φ_0^*, the right hand side of Eq. B-8 becomes zero as φ_0^* is the eigenfunction of the adjoint eigenvalue problem Eq. B-9

$$\mathscr{R}_0^* \varphi_0^* = \lambda_0 \varphi_0^*$$

<div align="right">B -9</div>

Eq. B-6 hence reduces to Eq. B-10

$$\left\langle \varphi_0^*, \Delta\mathscr{P}\varphi_0 \right\rangle = \Delta\lambda \left\langle \varphi_0^*, \varphi_0 \right\rangle$$

<div align="right">B -10</div>

The first order perturbation formulation for this eigenvalue perturbation is hence given by Eq. B-11

$$\Delta\lambda = \frac{\left\langle \varphi_0^*, \Delta\mathscr{P}\varphi_0 \right\rangle}{\left\langle \varphi_0^*, \varphi_0 \right\rangle}$$

<div align="right">B -11</div>

From Eq. B-11 is follows that only the known parameters φ_0^*, φ_0 and $\Delta\mathscr{P}$ are required to calculate the eigenvalue perturbation. To obtain this result, the introduction of the adjoint function φ_0^* has been necessary to eliminate the dependence on the flux perturbation.

The previously described approach is also applied to reactor eigenvalue value problems, though it involves additional terms due to additional operators.

<div style="text-align:center">

<u>Appendix C:</u>

Comparison of FOP, exact PT and direct calculations with SIMMER and ECCO/ERANOS (BISTRO)

</div>

Several cases for a density change of $\dfrac{1}{1.01^2}$ have been considered and partly detailed in chapter 6. This appendix aims at giving additional information on cases 1, 1b, 2 and 2b – see Table C-1.

Table C-1. Considered test cases for checking the density effect with direct, FOP and exact PT calculations.

	Density changes				Density changes (axial height)	
	Inner fuel ring	Outer fuel ring	All fuel rings	Na around fissile core	Fissile height	Whole neutronic mesh height
CASE 1	x				x	
CASE 1b	x					x
CASE 2		x			x	
CASE 2b		x				x
CASE 3			x		x	
CASE 3b			x			x
CASE 4				x	/	/

In the different cases, masses of fuel and steel are always kept constant. Sodium mass depends on the considered case. The calculations presented hereafter are performed considering a simplified core with a single enrichment zone. Calculations have been run assuming 1 energy group. In a later section results for a 2 enrichment zones core and Na treated differently are presented as well.

Case 1 and case 1b: Density modification in the innermost fuel ring.

The density has been reduced in the innermost fuel ring by a factor $d_{\text{expanded}} = \dfrac{d_{\text{not expanded}}}{1.01^2}$ either in the fissile part only (Case 1) or in the whole ring, including the sodium above and below the fissile core (Case 1b).

ERANOS calculations [157] have been performed with the BISTRO solver [159] (RZ geometry). In the perturbation calculations scalar fluxes i.e. integrals of angular fluxes are used (recommended option). Nevertheless, integral of scalar fluxes were used as well and results for both options are presented hereafter.

Case 1 a

The density is changed in the first fuel ring, in the fissile part only as can be seen in Figure C-1.
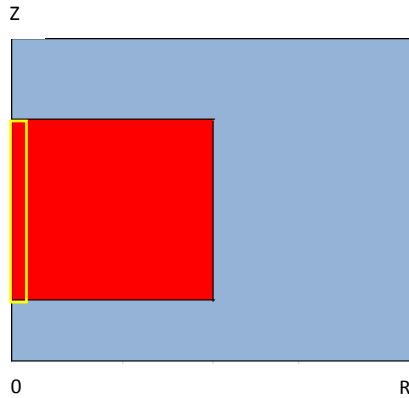
Figure C-1. Zone considered for the density change

The reactivity effect due to density change in the first ring calculated by means of FOP, exact PT and direct calculations is shown in Table C-2.

Table C-2. Density effect for a density variation of $\frac{1}{1.01^2}$ in the fuel zone of the innermost fuel ring. Comparison of ERANOS (BISTRO) results for direct, FOP and exact PT calculations.

	Calculation type	Reactivity effect (pcm)	Difference (pcm)	Direct/PT
BISTRO (angular fluxes)	FOP	-2.0	0.0	1.0
	Exact	-2.0	0.0	1.0
	Direct	-2.0		

The results for direct method and exact PT agree very well. Similarly, the FOP agrees well with the direct method and the exact PT results, confirming that the perturbation is small enough to consider the use of FOP valid.

The same case is now calculated with SIMMER-III and with BISTRO (assuming the integral of scalar fluxes instead of the recommended integral of angular fluxes). The results are shown in Table C-3. In all the SIMMER calculations here reported the factor 2 (introduced in the methodology, see Chapter 6) has not been applied.

Table C-3. Density effect for a density variation of $\frac{1}{1.01^2}$ in the fuel zone of the innermost fuel ring. Comparison of SIMMER and ERANOS for direct and FOP calculations.

	Calculation type	Reactivity effect (pcm)	Difference (pcm)	Direct/PT
BISTRO (scalar fluxes)	FOP	-1.6	0.4	1.27
	Exact	-1.6	0.4	1.28
	Direct	-2.0		
SIMMER	FOP	-1.7	0.6	1.37
	Direct	-2.3		

From Table C-3 it can be seen that both in case of BISTRO and of SIMMER, the direct and the FOP results differ by roughly 30%. BISTRO (integral scalar fluxes) and SIMMER results agree quite well. It therefore appears that using scalar fluxes instead of angular ones does not allow accurately reflect the effect of a density modification calculated by the direct scheme. However, for this specific case the perturbation is very small and the direct calculation may not be so accurate. The other cases have been considered as extra tests.

Case 1b

The density is changed in the first fuel ring but this time the change is made on the whole axial height as can be seen in Figure C-2.
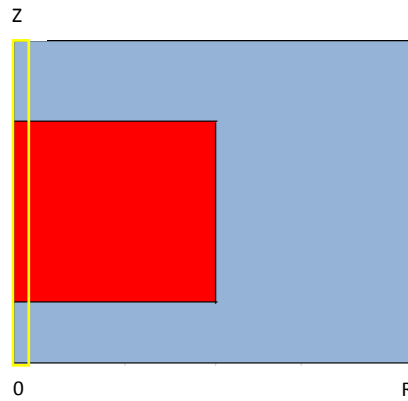
Figure C-2. Zone considered for the density change (in yellow).

An ERANOS calculation with the BISTRO solver using angular fluxes is performed. Direct, exact and FOP results agree very well as shown in Table C-4.

Table C-4. Density effect for a density variation of $\dfrac{1}{1.01^2}$ in the innermost fuel ring. Comparison of ERANOS (BISTRO) results for direct, FOP and exact PT calculations.

	Calculation type	Reactivity effect (pcm)	Difference (pcm)	Direct/PT
BISTRO (angular fluxes)	FOP	-2.4	0.0	1.0
	Exact	-2.4	0.0	1.0
	Direct	-2.4		

The same case is then calculated with SIMMER-III and with BISTRO (scalar fluxes are used instead of angular ones). The results can be seen in Table C-5.

Table C-5. Density effect for a density variation of $\dfrac{1}{1.01^2}$ **in the innermost fuel ring. Comparison of SIMMER and ERANOS for direct and FOP calculations.**

	Calculation type	Reactivity effect (pcm)	Difference (pcm)	Direct/PT
BISTRO (angular fluxes)	FOP	-1.5	0.9	1.6
	Exact	-1.5	0.9	1.6
	Direct	-2.4		
SIMMER	FOP	-1.6	1.1	1.7
	Direct	-2.7		

From Table C-5 it can be seen that in case of BISTRO and of SIMMER, the direct and the FOP still differ, confirming the tendency observed in case 1. The factor between direct and FOP results has even increased compared to case 1. BISTRO and SIMMER results agree quite well.

Since the effect of a density change in ring 1 is rather small (only one SA is present in this ring) the same approach is considered for the outermost fuel ring containing several SAs. The results are shown in the following section. However, also for this specific case the perturbation is very small and the direct calculation may not be so accurate.

Case 2 and case 2b: Density modification in the outermost fuel ring.

The density has been reduced in the outermost fuel ring by a factor $d_{\text{expanded}} = \dfrac{d_{\text{not expanded}}}{1.01^2}$ either in the fissile part only (Case 2) or in the whole axial height of the outermost ring, including the sodium above and below the fissile core (Case 2b).

Calculations have been performed with SIMMER, ERANOS-BISTRO and ERANOS-BISTRO modified (scalar fluxes integral). The calculations are performed with 1 and 11 energy groups in case of SIMMER and 1, 11 and 33 energy groups in case of ERANOS in order to analyze the impact of the energy structure.

Case 2 a

As mentioned previously, in Case2, the density is changed in the outermost fuel ring, in the fissile part only as can be seen in Figure C-3.

Figure C-3. Zone considered for the density change (yellow)
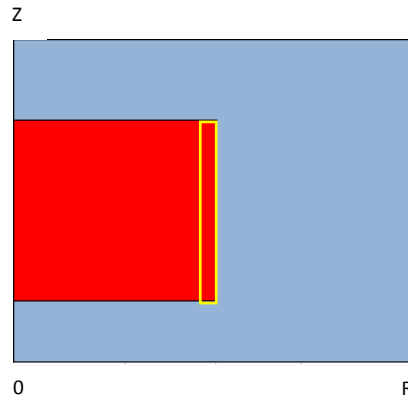
The reactivity effect due to a density change in the fissile part of the outermost ring can be seen in Table C-6, where a comparison between direct, exact and first order PT calculations is presented.

Table C-6. Density effect for a density variation of $\dfrac{1}{1.01^2}$ in the fissile zone of the outermost fuel ring. Comparison of ERANOS (BISTRO) results for direct, FOP and exact calculations for different energy groups using angular fluxes.

	Calculation type	Reactivity effect (pcm)	Difference (pcm)	Direct/PT
BISTRO 1 E group (angular fluxes)	FOP	-16.6	-0.0	1.0
	Exact	-16.6	-0.0	1.0
	Direct	-16.6		
BISTRO 11 E groups (angular fluxes)	FOP	-14.0	-0.0	1.0
	Exact	-14.0	0.0	1.0
	Direct	-14.0		
BISTRO 33 E groups (angular fluxes)	FOP	-13.7	0.2	1.0
	Exact	-13.6	0.2	1.0
	Direct	-13.9		

From Table C-6 it can be concluded that the calculation with 11 or 33 energy groups does not significantly impact the results. Therefore, the standard 33 groups ERANOS calculation might be used as a reference for comparison with the standard 11 E groups calculation of SIMMER. Moreover the results for direct and exact PT agree very well in all cases (within 2%, the discrepancy increasing with number of energy groups). Similarly, the FOP agrees well with the direct and the exact PT, confirming that the use of FOP is valid.

The same cases are now calculated with SIMMER-III and with BISTRO (scalar fluxes are used instead of angular ones). The results can be seen in Table C-7.

Table C-7. Density effect for a density variation of $\dfrac{1}{1.01^2}$ in the fissile zone of the outermost fuel ring. Comparison of ERANOS (BISTRO) results for direct, FOP and exact calculations for different energy groups, using scalar fluxes.

		Calculation type	Reactivity effect (pcm)	Difference (pcm)	Direct/PT
1E group	**BISTRO (scalar fluxes)**	FOP	-7.3	9.3	2.27
		Exact	-7.2	9.4	2.29
		Direct	-16.6		
	SIMMER	FOP	-6.3	10.0	2.60
		Direct	-16.3		
11E groups	**BISTRO (scalar fluxes)**	FOP	-5.9	8.0	2.36
		Exact	-5.9	8.0	2.38
		Direct	-13.9		
	SIMMER	FOP	-5.5	8.1	2.45
		Direct	-13.6		
33E groups	**BISTRO (scalar fluxes)**	FOP	-5.8	8.1	2.39
		Exact	-5.8	8.1	2.41
		Direct	-13.9		

From Table C-7 it can be seen that the results for direct and the FOP do not agree anymore (they differ roughly by a factor 2.3 to 2.6 in all cases). Nevertheless, if one compares BISTRO and SIMMER results– both in case of FOP or direct calculations – they agree quite well.

To confirm the previously mentioned conclusions, the density modification is now extended to the complete outermost fuel ring, including therefore the sodium above and below the fissile zone.

Case 2b

In case 2b, the density is changed in the overall height of the outermost fuel ring, as can be seen in Figure C-4
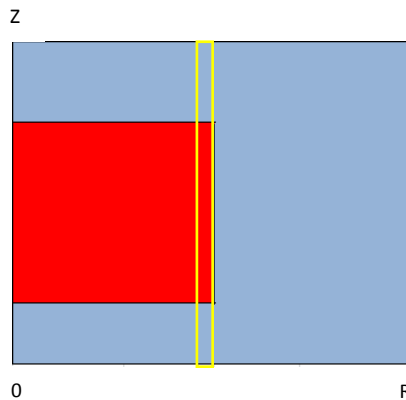

Figure C-4. Zone considered for the density change (in yellow).

Again, an ERANOS calculation with the BISTRO solver using angular fluxes is performed. Direct, exact and FOP results agree very well (within 2%) as shown in Table C-8. The good agreement is confirmed for different energy group structures. The 11 energy groups applied are consistent with the 11 energy groups of SIMMER.

Table C-8. Density effect for a density variation of $\dfrac{1}{1.01^2}$ in the outermost fuel ring. Comparison of ERANOS (BISTRO) results for direct, FOP and exact calculations for different energy groups using angular fluxes.

	Calculation type	Reactivity effect (pcm)	Difference (pcm)	Direct/PT
BISTRO 1 E group (angular fluxes)	FOP	-22.2	-0.0	1.0
	Exact	-22.2	-0.0	1.0
	Direct	-22.2		
BISTRO 11 E groups (angular fluxes)	FOP	-17.8	-0.0	1.0
	Exact	-17.8	0.0	1.0
	Direct	-17.8		
BISTRO 33 E groups (angular fluxes)	FOP	-16.1	0.2	1.0
	Exact	-16.1	0.2	1.0
	Direct	-16.3		

The same cases are then calculated with SIMMER-III and with BISTRO, using scalar fluxes instead of angular ones. The results can be seen in Table C-9.

Table C-9. Density effect for a density variation of $\dfrac{1}{1.01^2}$ in the outermost fuel ring. Comparison of ERANOS (BISTRO) results for direct, FOP and exact calculations for different energy groups using scalar fluxes.

		Calculation type	Reactivity effect (pcm)	Difference (pcm)	Direct/PT
1E group	**BISTRO (scalar fluxes)**	FOP	-6.9	15.3	3.22
		Exact	-6.8	15.4	3.25
		Direct	-22.2		
	SIMMER	FOP	-5.8	14.9	
		Direct	-20.7		
11E groups	**BISTRO (scalar fluxes)**	FOP	-6.0	11.8	2.99
		Exact	-5.9	11.9	3.02
		Direct	-17.8		
	SIMMER	FOP	-5.0	11.6	3.31
		Direct	-16.6		
33E groups	**BISTRO (scalar fluxes)**	FOP	-4.9	11.5	3.35
		Exact	-4.8	11.6	3.39
		Direct	-16.4		

From Table C-9 it can be seen that in case of BISTRO and of SIMMER, the direct and the FOP results still do not agree and the factor between direct and FOP results has even increased compared to case 2. BISTRO and SIMMER results agree quite well also for this case.

The results confirm the conclusions drawn in Chapter 6, section 6.5.3.

Appendix D:

Coefficients to apply to UO₂ pellet conductivity to obtain the U$_{0.8}$Pu$_{0.2}$O$_2$ pellet conductivity

The following coefficients have been determined and have to be applied to the UO$_2$ pellet conductivity to obtain the one for U$_{0.8}$Pu$_{0.2}$O$_2$ pellet fuel:

T (K)	Factor k(UPuO$_2$)/k(UO$_2$)
573	0.975030909
673	0.923204371
773	0.902446085
873	0.898085888
973	0.903224863
1073	0.914158159
1173	0.928648995
1273	0.945180122
1373	0.962600077
1473	0.979953000
1573	0.996405698
1673	1.011231342
1773	1.023825695
1873	1.033737257
1973	1.040695204
2073	1.044622548
2173	1.045627769
2273	1.043975201
2373	1.040040454
2473	1.034260196
2573	1.027085329
2673	1.018943767
2773	1.010215509
2873	1.001219585
2973	0.992210622
3073	0.983382074
3120	0.979336441

Impact of porosity on heat capacity

From [190; 190] it is known that the heat capacity in porous media is written as Eq. E-1.

$$\left(\rho c\right)_{e} = \Phi \rho_{f} c_{f} + \left(1 - \Phi\right) \rho_{s} c_{s}$$ E-1

Where f stands for fluid i.e. helium in our case, s stands for solid, ρ and c are the density and heat capacity respectively, Φ stands for the porosity.

In a fast reactor, e.g. CP-ESFR, at BOL and at nominal conditions, the fuel temperature is assumed to be about 1500 K, and the pin pressure is at around 1 bar. He and MOX inside the fuel pin are considered to be in thermal equilibrium, therefore $T_{He} = T_{MOX}$.

Let's consider the case of sphere-pac fuels with 16.59% Helium content at 1 bar of pressure (therefore Φ is 0.1659). If the system is considered to be at MOX melting temperature, the corresponding pin pressure is of about 2 bars if no additional gas release is considered. Therefore:

$\rho_{He}\left(T = 3002 \ K, P = 2 \ bar\right)$ = 0.032053 kg/m3

$c_{He} = \dfrac{5}{2} \dfrac{1000}{A_{He}} R$ = 5192.875 J/(kg · K)

Concerning MOX properties at 3002 K, data from [191; 192] is used:

$\rho_{MOX}\left(T = 3002 \ K\right)$ = 9977.053 kg/m3

c_{MOX} = 594.6 J/(kg · K)

By applying Eq. E-1, one obtains that $\left(\rho c\right)_{sphere-pac}$ is equal to 4948205 J/(m^3 · K).

Considering Eq. E-2, one obtains $c_{sphere-pac}$ = 594.6 J/(kg · K) = c_{MOX}

$$\rho_{tot} = \Phi \rho_{f} + \left(1 - \Phi\right) \rho_{s}$$ E-2

It can be concluded that porosity has no impact on the fuel heat capacity. It has to be noted that the influence of the remperature distribution within the pin is not taken into account here since the average temperature is used as fuel temperature.

APPENDIX E

Appendix F:
Impact of porosity in the thermal penetration length calculations for the CP-ESFR WH core loaded with pellet fuel.

The entire appendix F is devoted to steady state and UTOP analyses for cases 1a and 1b of chapter 7. The thermal penetration lengths with and without porosity consideration are recalled in Table F-1.

Table F-1. Considered pellet cases. Case 1a: thermal penetration length calculated without porosity consideration. Case 1b: thermal penetration length calculated with porosity consideration.

Cases	By hand calculation (µm)	Check with SIMMER-III (µm)
1a	89.43	89.43
1b	79.10	79.10

Steady state analyses

Steady state analyses with SIMMER-III showed no difference between case 1a and 1b in terms of core wide power distribution, mass flow distribution, inlet and outlet coolant temperatures, as well as in the temperature distributions at core mid-plane and in the hottest channel see Figure F-1 through Figure F-5.
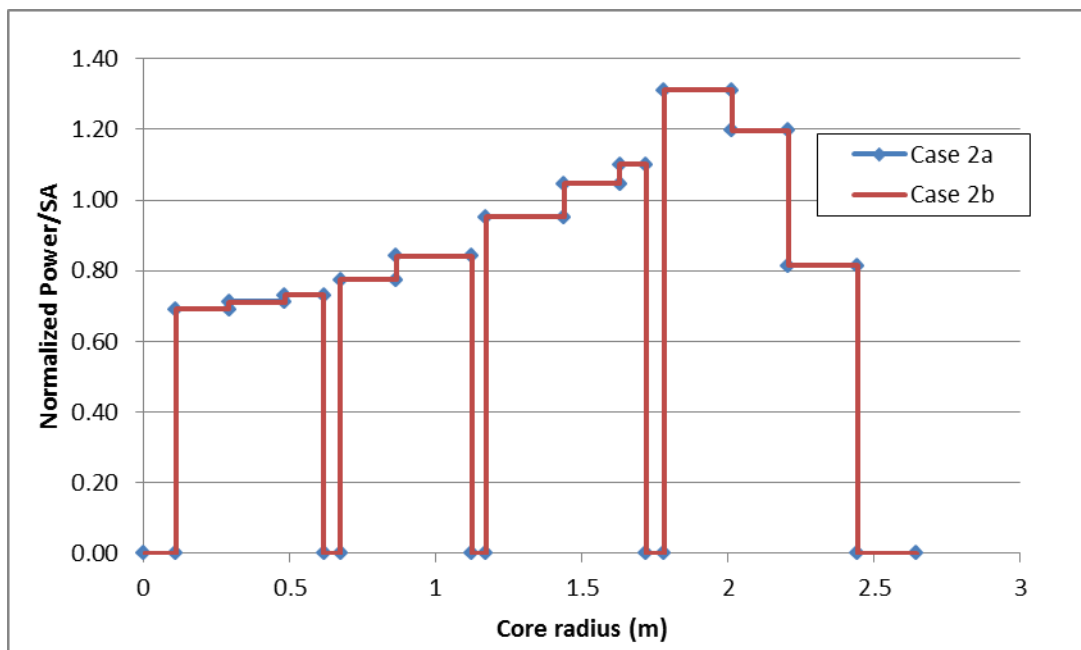

Figure F-1. Normalized fission power per SA radial distribution, pellet type fuel.
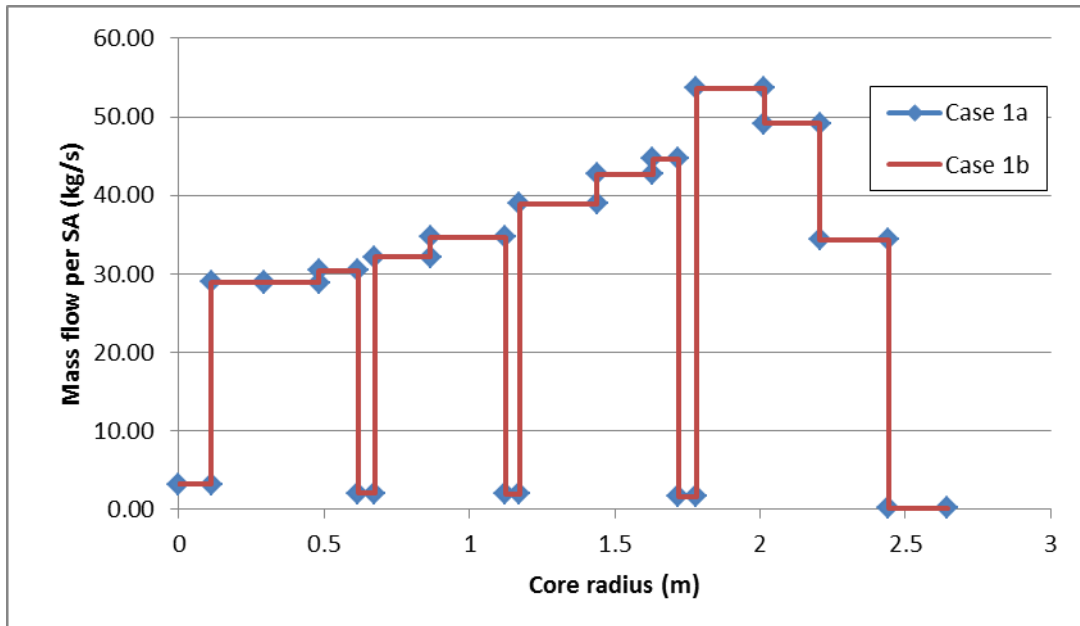
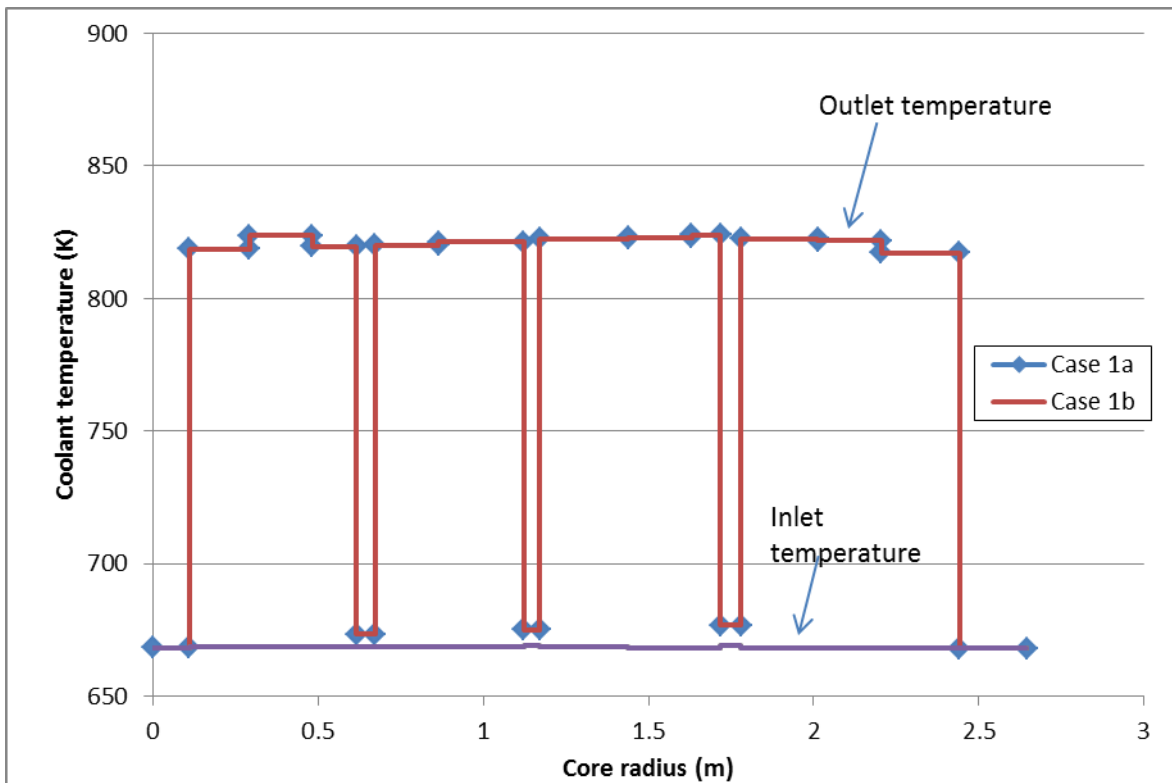**Figure F-2. Mass flow per SA radial distribution, pellet type fuel.**

Figure F-3. Outlet and inlet coolant temperature distribution, pellet type fuel.
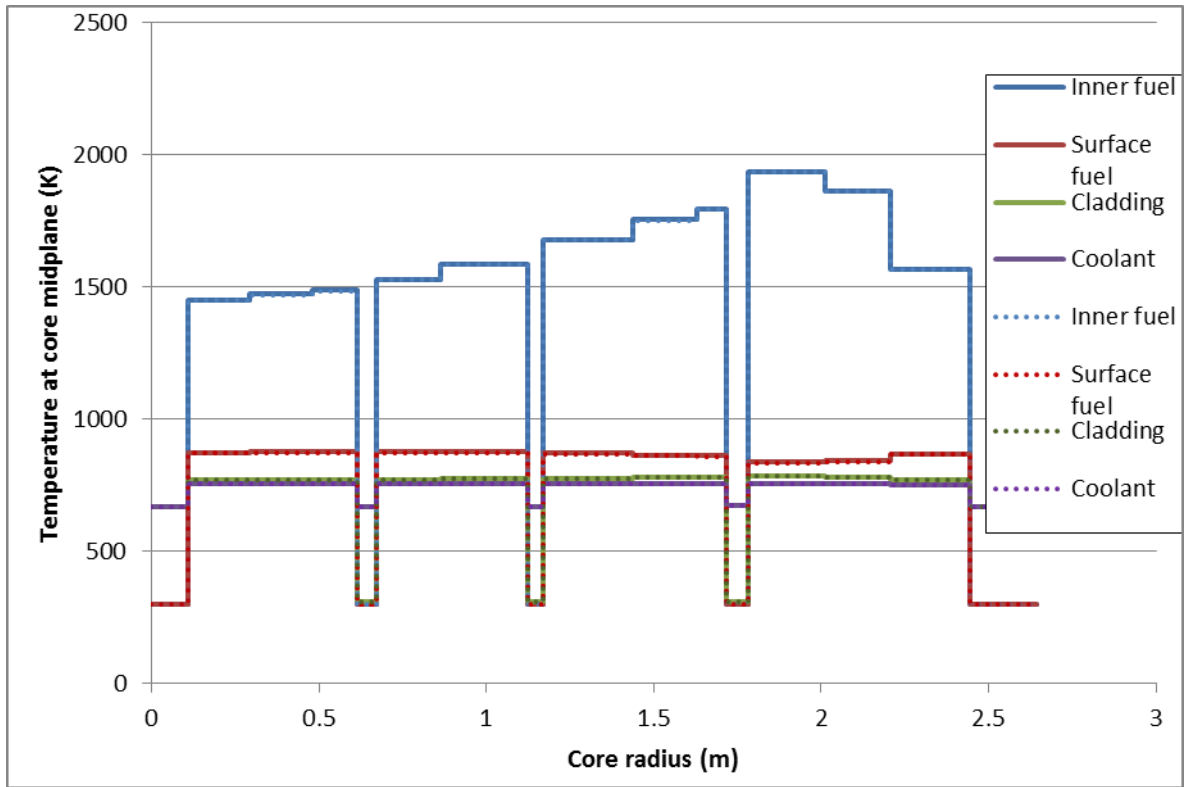
Figure F-4. Radial temperature distribution at core midplane, pellet type fuel. Dotted lines: Case 1b, full lines: Case 1a.
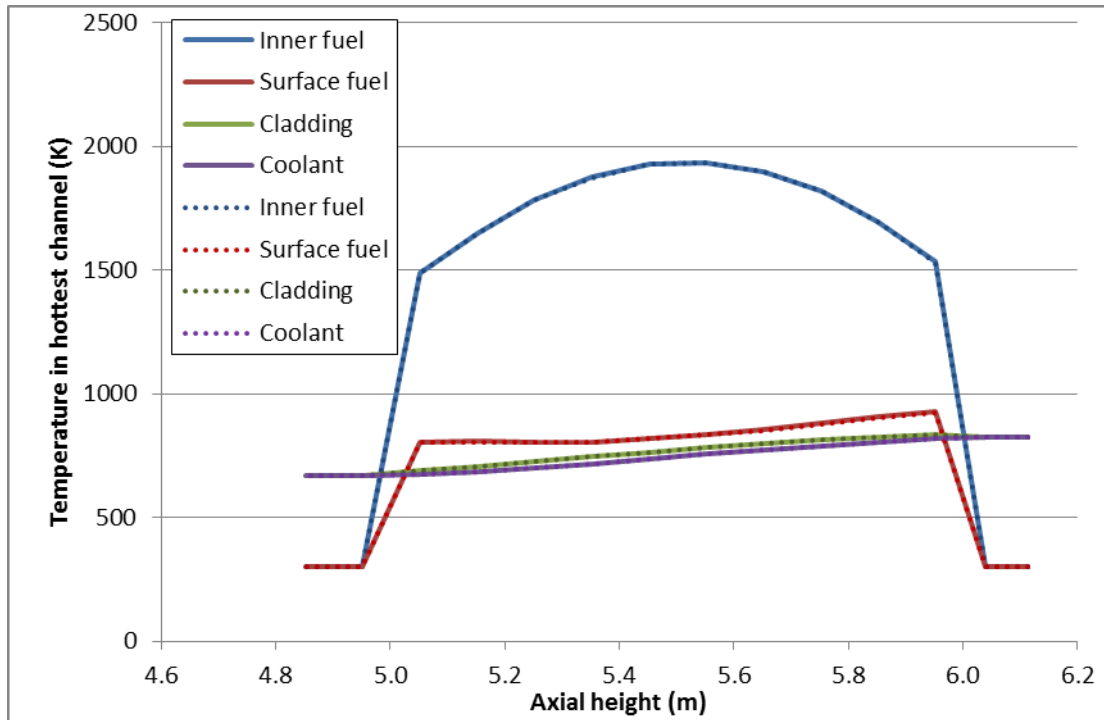

Figure F-5. Axial temperature distribution in the hottest channel, pellet type fuel. Dotted lines: Case 1b, full lines: Case 1a.

UTOP

For testing the model, a UTOP has been chosen, as in an over-power transient the impact of the porosity and thermal conductivity can be more directly observed with a ramp rate just representing an arbitrary parameter. The chosen ramp rate is artificial and has no mechanistic background.

A 50$ reactivity insertion in 1s is imposed to the core in both cases. The core behavior for this unprotected transient over power is analyzed for cases 1a and 1b. Figure F-6 shows the reactivity evolution in both cases during the imposed transient.
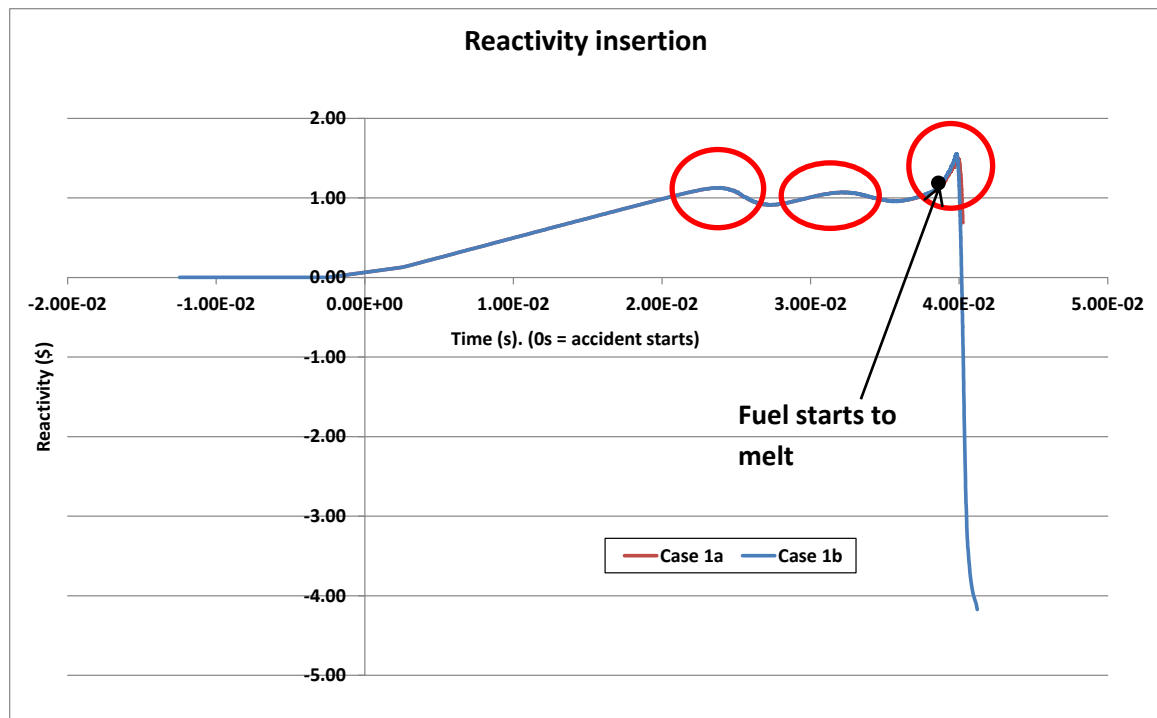

Figure F-6. Reactivity evolution in case of pellet fuel, during a UTOP of 50$/s.

From Figure F-6 it can be noted that a reactivity insertion of 1$ is performed in 20ms which confirms the UTOP of 50$/s. In the beginning of the accident, the reactivity follows the steep external reactivity ramp of 50$/s.

In the current case the reactivity reaches 1$ which means the reactor becomes prompt supercritical later on. The first power peak is then limited by the Doppler feedback and the power is reduced. In the following typical Doppler oscillations take place.

Since reactivity is permanently added to the core by the external power ramp of 50$/s, a second power peak is generated. Again the rise in fuel temperature causes the Doppler effect to counterbalance this power increase and leads the reactivity to drop. This time the reactivity decrease is not as steep as for the previous peak because of the Doppler feedback non-linearity. Fuel temperatures tend to stabilize to a value close to the melting point.

The continuing reactivity insertion leads the fuel to finally reach its melting temperature of 3002K. Cladding breaks up at the same time because the criterion is defined in this way by default in SIMMER-III. The coolant begins to vaporize in contact with the molten fuel and steel mixture. The positive sodium void coefficient leads then to a higher reactivity increase and triggers the last and

highest reactivity peak –Figure F-6. Fuel is discharged from the core region and leads to a steep reactivity decrease, eventually leading to reactor shutdown.
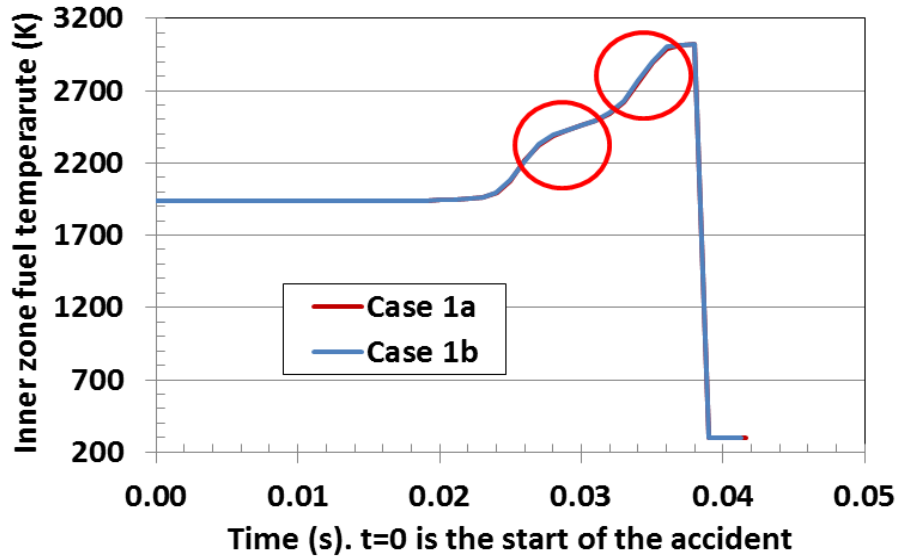

Figure F-7. Fuel inner temperature evolution in the hottest cell

NB: in SIMMER-III the solid temperature is set equal to a default value of 300.2 K in a cell and this values is shown in case the fuel is molten and has left the solid field. This explains the sudden temperature drop seen in Figure F-7.
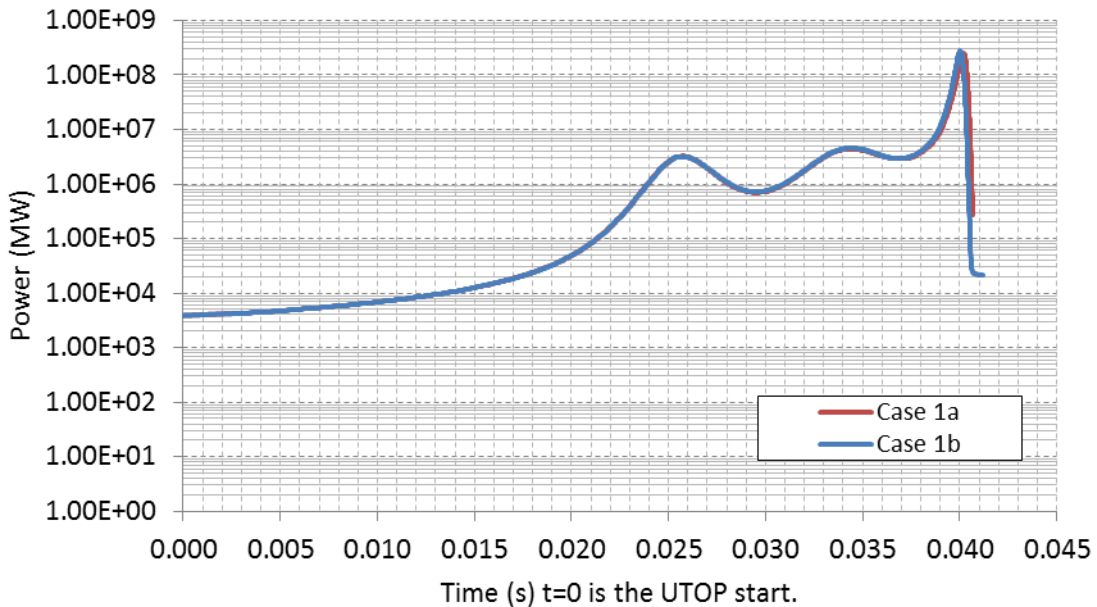
Figure F-8. Power evolution vs. time

The three power peaks observed in Figure F-8 correspond to the three reactivity peaks in Figure F-6. Even though the general core behavior is the same for both cases, a small discrepancy can be observed. For instance, the last reactivity swing in case 1a is smaller and delayed compared to case 1b –Figure F-9. This is due to the fact that the Doppler effect is larger in case 1a which delays a bit the fuel melting.

The last power peak in case 1a is delayed by 0.2ms, which is consistent with the phenomenon observed for reactivity. Snapshots of the accident evolution confirm this tendency as depicted in Figure F-10. In fact, the fuel melts to a higher extend in case 1b than in case 1a: 89% and 65% of the total fuel mass respectively 40ms after the accident starts. By the end of both calculations, all fuel is either molten or turned into particles.
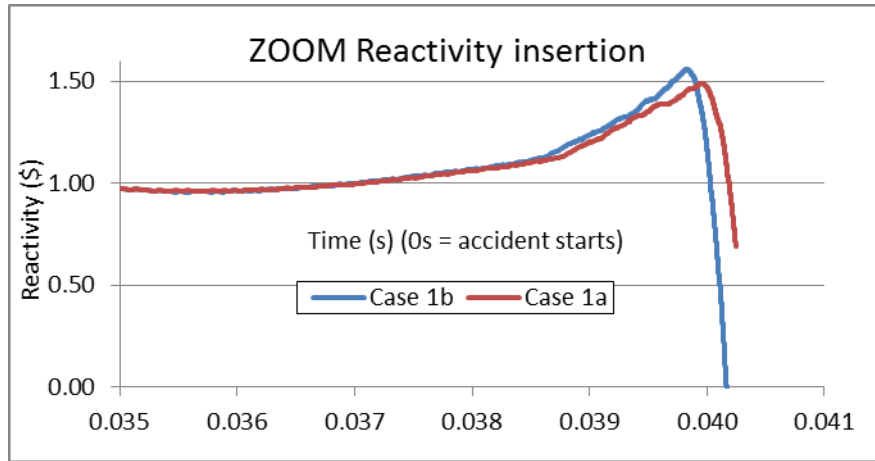

Figure F-9. Zoom on total reactivity evolution.
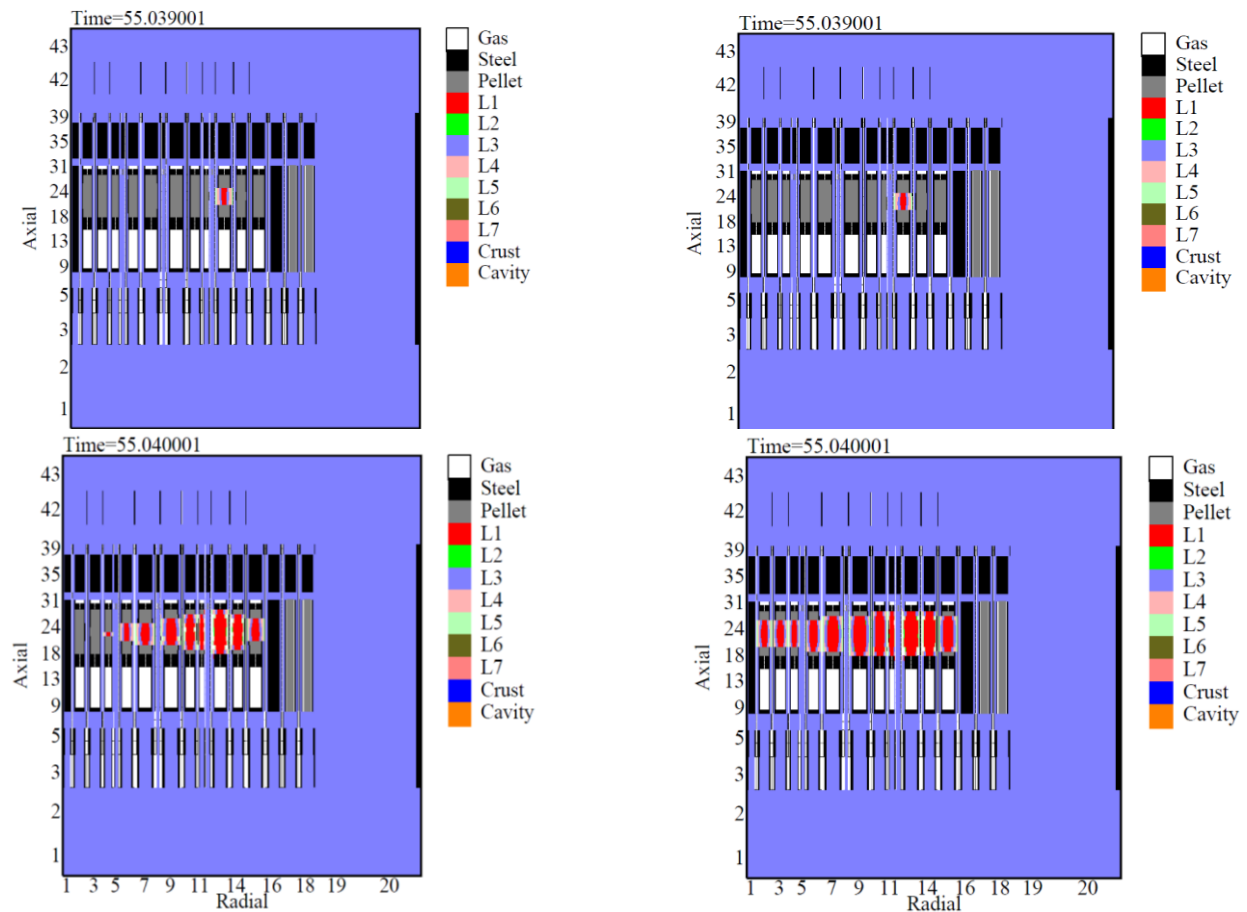
Figure F-10. Snapshots at 39 ms and 40 ms after the UTOP starts. Left column: case 1a, right column: case 1b. Legend: L1: liquid fuel, L2: liquid steel, L3 liquid sodium, L4: fuel particles, L5 steel particles, L6: control particles, L7: fuel chunks.

Conclusions

In case of pellet fuels, the small fuel porosity amount leads to similar thermal penetration length values. As the core behavior is the same in both cases, with and without taking into account the effect of porosity, and only 1.20% discrepancy can be noted for the thermal energy release during the accident, the initial SIMMER-III assumption to calculate thermal penetration lengths with fully dense material properties is validated.

<div style="text-align:center">

<u>Appendix G:</u>

Temperature distributions in the hottest ring of the CP-ESFR CONF2 core at beginning of life

</div>

Temperature distributions in the hottest ring of the CP-ESFR CONF2 core at beginning of life can be seen in Figure G-1 through Figure G-4.

Fresh sphere-pac and pellet fuel are considered. Distinction is made between non-restructured sphere-pac fuel and restructured sphere-pac fuel, representative of almost fresh fuel after some hours of irradiation.
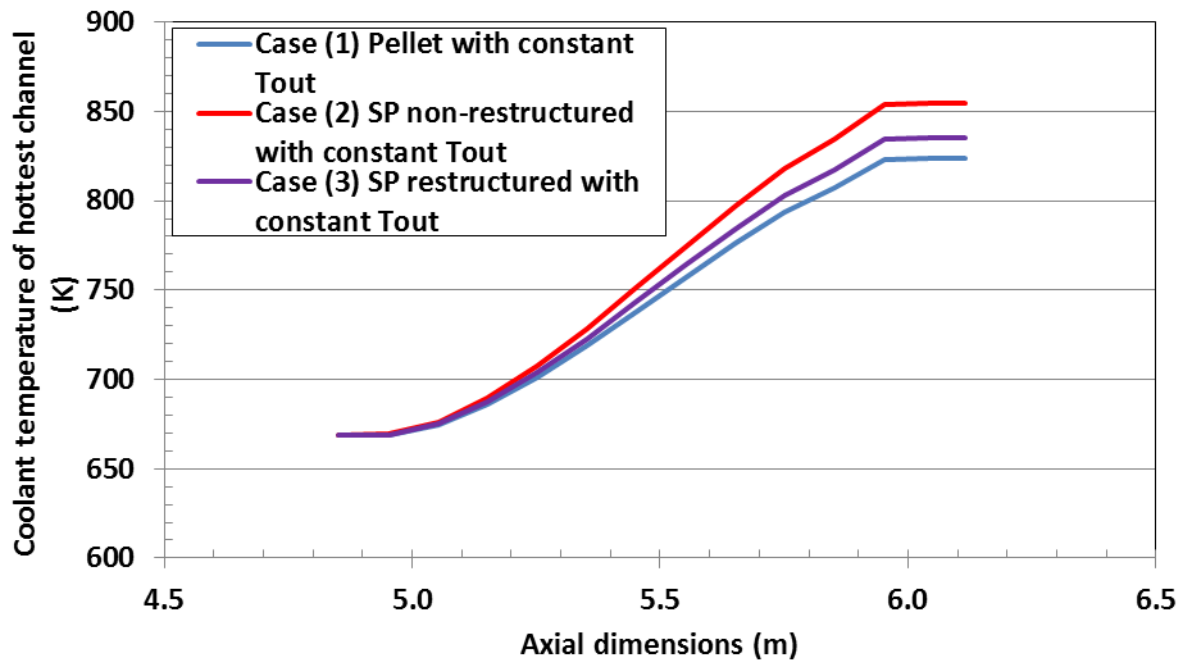
Figure G-1. Axial coolant temperature distribution in the hottest ring of the CP-ESFR CONF2 core at BOL.
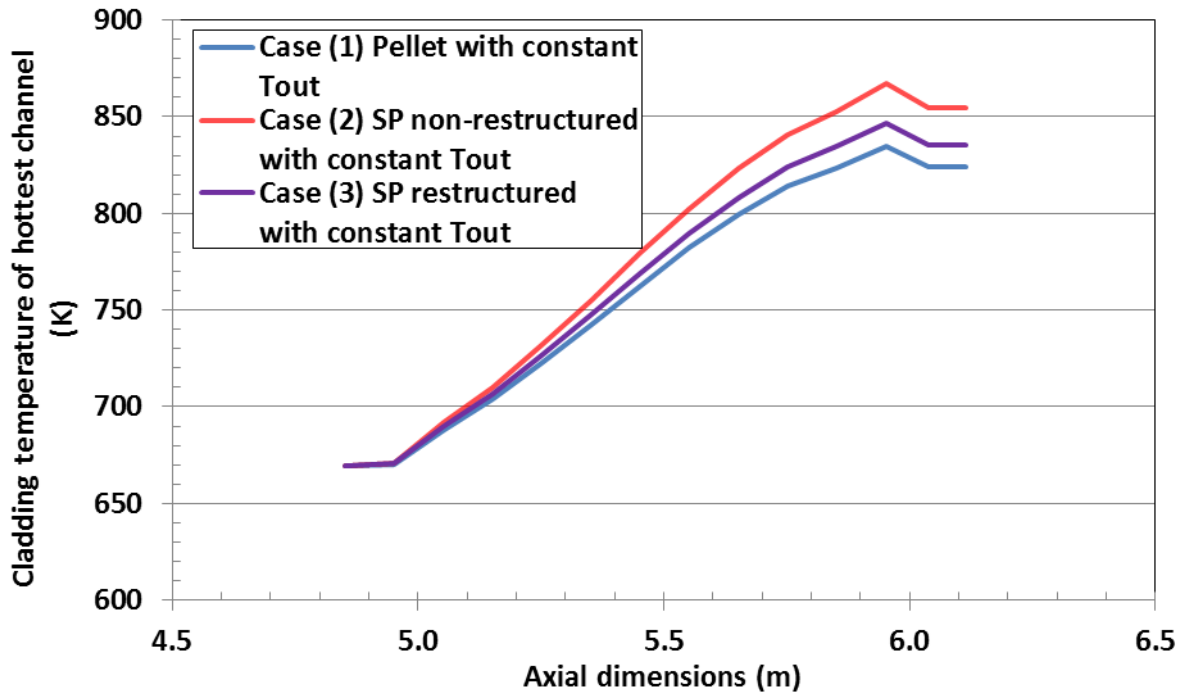
Figure G-2. Axial cladding temperature distribution in the hottest ring of the CP-ESFR CONF2 core at BOL.

Figure G-3. Axial distribution of the average fuel temperature in the hottest ring of the CP-ESFR CONF2 core at BOL.

Figure G-4. Axial distribution of the surface fuel temperature in the hottest ring of the CP-ESFR CONF2 core at BOL.

Appendix H:

Temperature distributions in the hottest ring of the CP-ESFR CONF2 core at equilibrium

Temperature distributions in the hottest ring of the CP-ESFR CONF2 core at equilibrium can be seen in Figure H-1 through Figure H-4. End of cycle 3 sphere-pac and pellet MOX fuel are considered.

Figure H-1. Axial distribution of the coolant temperature in the hottest ring of the CP-ESFR CONF2 core at equilibrium cycle.

Figure H-2. Axial distribution of the cladding temperature in the hottest ring of the CP-ESFR CONF2 core at equilibrium cycle.
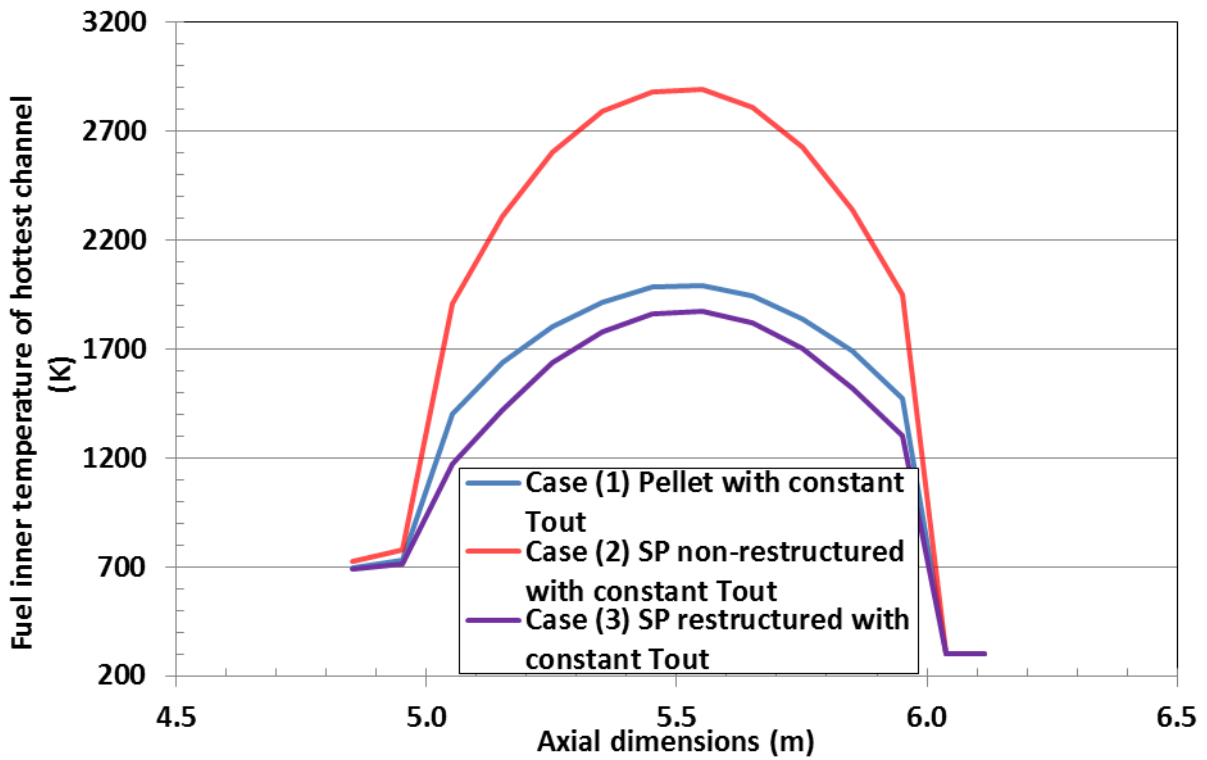
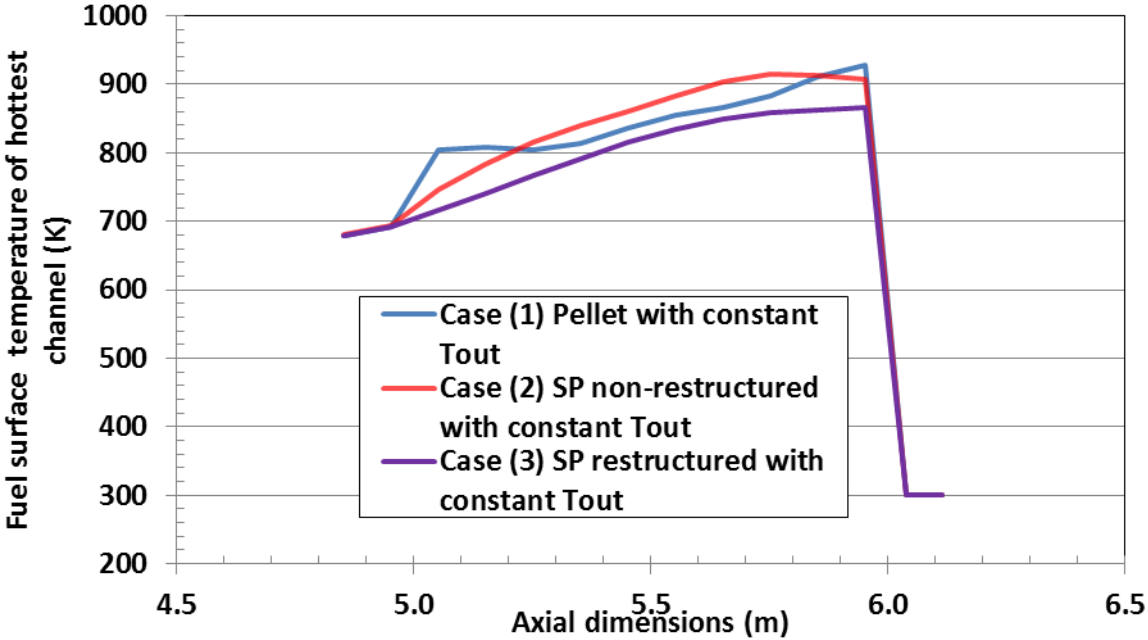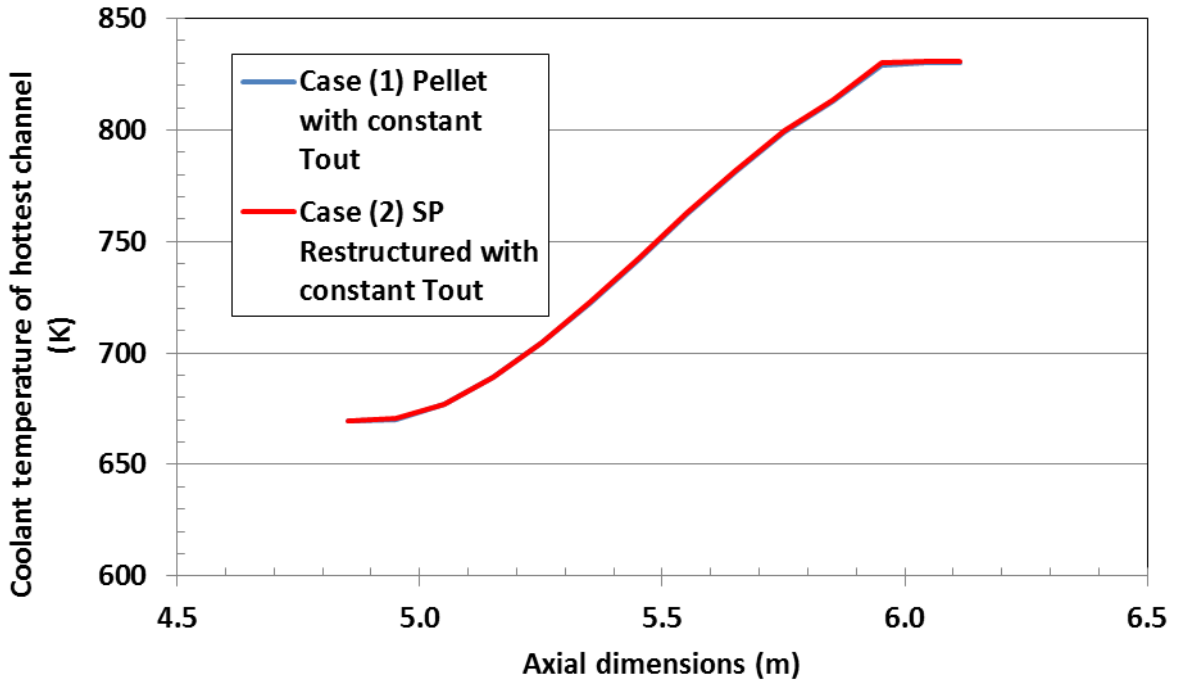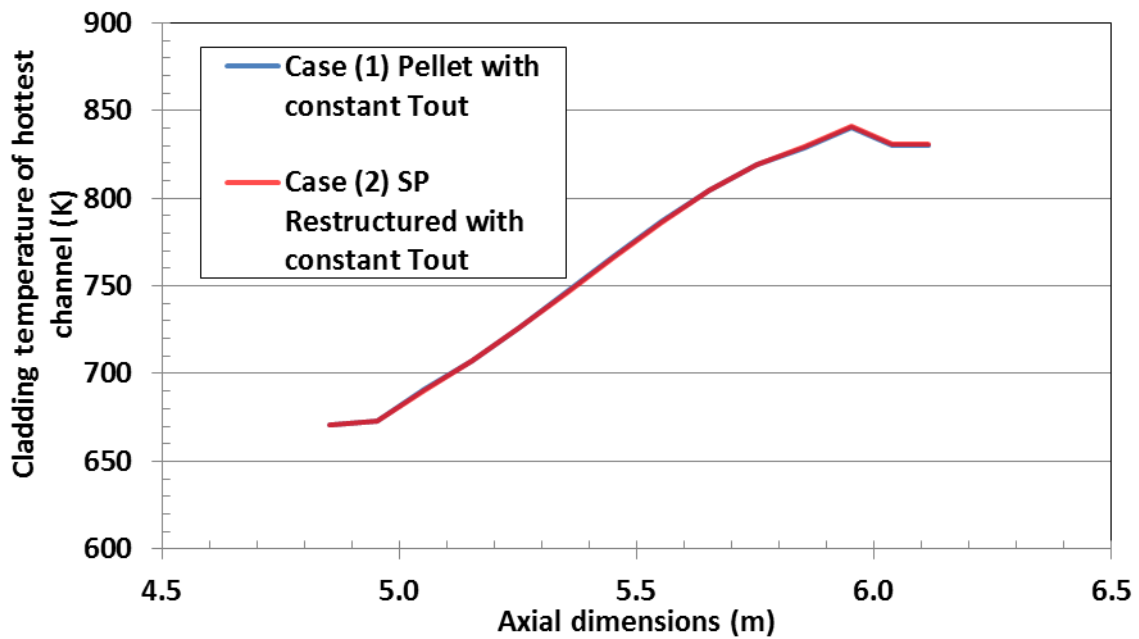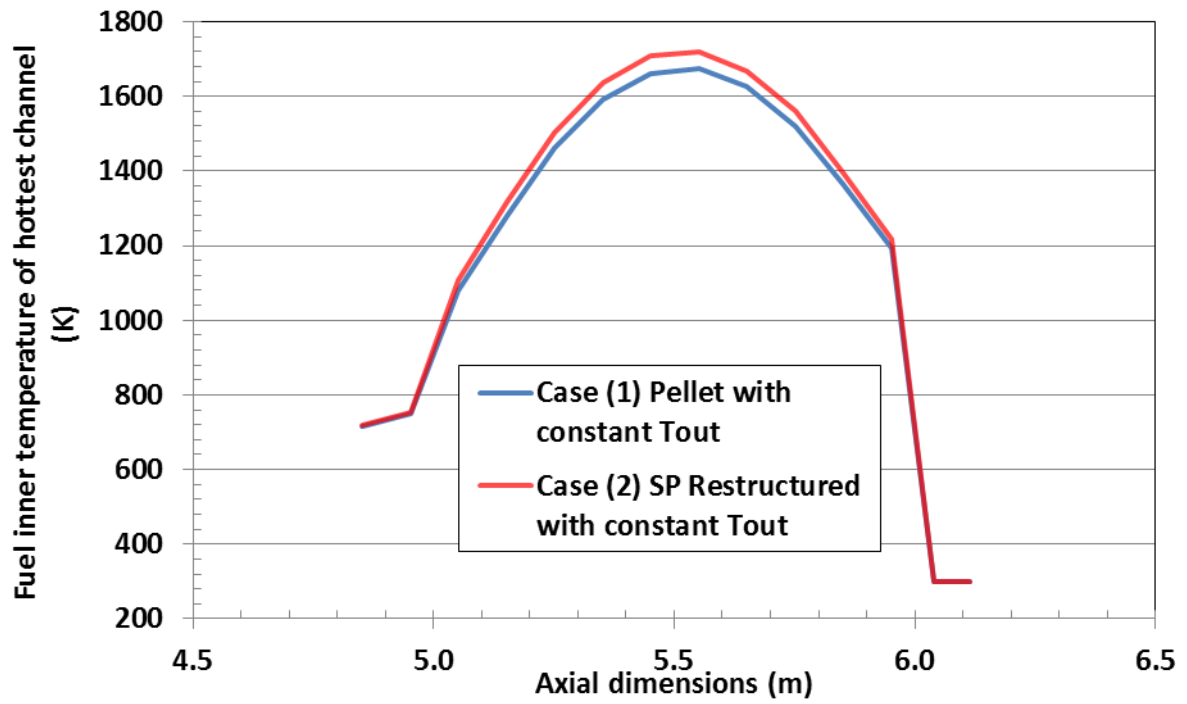**Figure H-3. Axial distribution of the average fuel temperature in the hottest ring of the CP-ESFR CONF2 core at equilibrium cycle.**
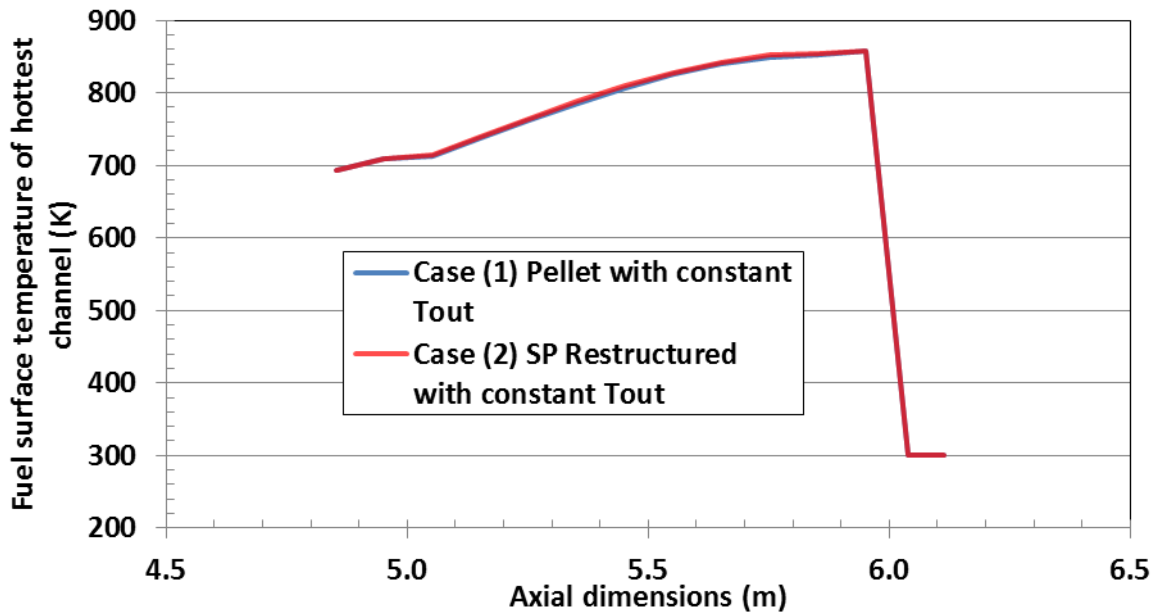

Figure H-4. Axial distribution of the fuel surface temperature in the hottest ring of the CP-ESFR CONF2 core at equilibrium cycle.

Appendix I:

Application of the DENSF method for core thermal expansion feedbacks in the EBR-II reactor

The Extended SIMMER version (S-III-v.E) developed at KIT [144; 165] for taking into account thermal expansion feedbacks has been applied to the analysis of the EBR-II SHRT-45R benchmark proposed by ANL. SHRT-45R is one of the transients carried out at the EBR-II facility that are considered within the Collaborative Research Project (CRP) launched by IAEA in 2012 about a Benchmark study on EBR-II Shutdown Heat Removal Tests [193–195].

The SHRT-45R represents an unprotected loss of flow transient (ULOF case). The 2D RZ SHRT-45R SIMMER model has been assessed at KIT following the benchmark specifications [164].

The SIMMER model has been neutronically characterized with respect to the ECCO-ERANOS model established for the neutronics benchmark part. Good results in terms of k-eff and reactivity feedbacks have been obtained [196].

The SIMMER beta effective value for metal ^{235}U enriched uranium fuel, specific of EBR-II, has been set up in agreement with a calculation performed with the 3D HEX-Z ECCO-ERANOS model using an extended version of the ERANOS code [197].

The EBR-II SIMMER model (see Figure I-1 and Figure I-2) has been adopted for testing the extended SIMMER version taking into account core thermal expansion feedbacks (DENSF method).

Results have been compared with the partner results, presented at the 3rd Research Coordination Meeting (RCM) on EBR-II in Bologna in 2015. For the analyses, the clad driven option has been considered. Irradiated compositions have been provided within the benchmark specifications where it has been assumed to have clad-fuel interaction conditions.

The evolution of the thermal power during the ULOF transient is shown in Figure I-3. This case corresponds to a SIMMER simulation in which the thermal expansion feedbacks (axial and radial) are treated assuming the conic expansion model (called in the following as CONIC), see chapter 6 section 6.4.1. In this case, the power evolution obtained by the SIMMER simulation is in reasonable agreement with the one of the project partners [196].

A case without thermal expansion feedbacks (named REF) and a case with cylindrical expansion model (called CYL) have also been considered. The thermal power evolution during the transient is shown in Figure I-4.

For this reactor, the case with cylindrical expansion allows to study the contribution of the axial expansion since the steel temperature of the lower grid does not change significantly during the transient and is fairly homogeneous in the diagrid. Therefore, for this specific case the radial expansion contribution (applying the cylindrical model) is practically negligible and only the axial expansion contribution is taken into account. In addition, due to the fact that the variation of the lower grid steel temperature during the transient is the same for the three cases (see Figure I-5), the separation of radial and axial reactivity contributions may be done in a first approximation by comparing the CYL and REF cases (providing the axial contribution – called as AX) and the CYL and CONIC cases (providing the radial contribution – called as RAD).
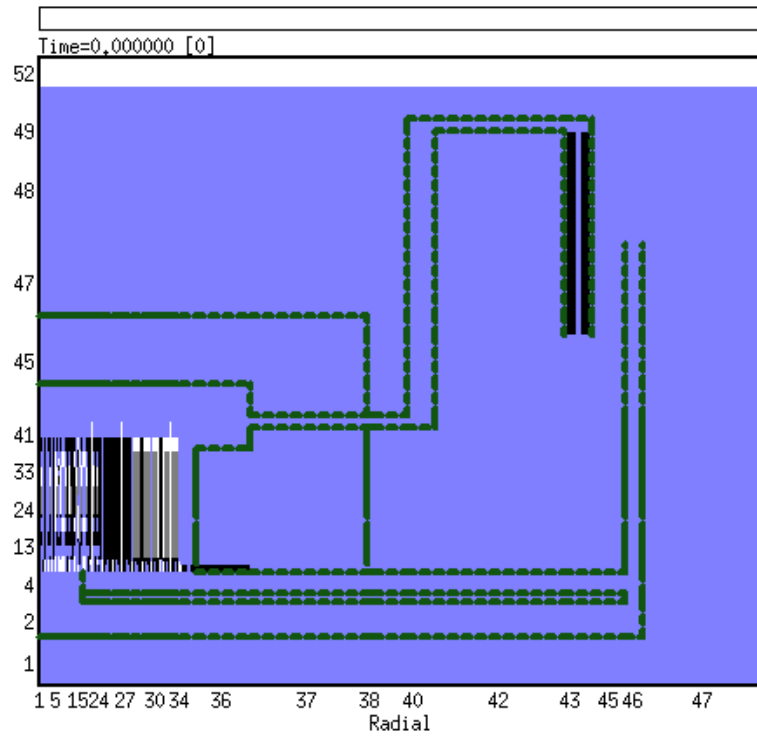
Figure I-1. EBR-II model: reactor vessel and components (core, inlet plena, upper plenum, Z-pipe, inlet pipes)
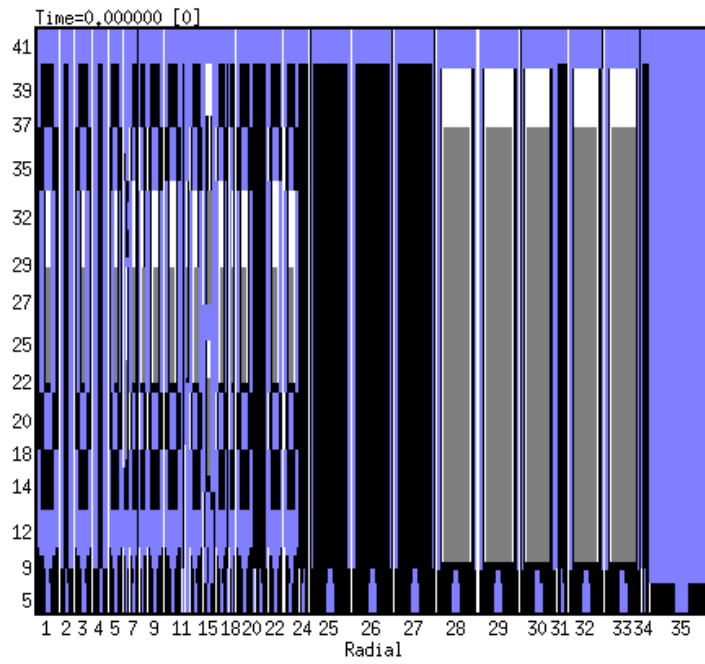
Figure I-2. EBR-II model: core zone
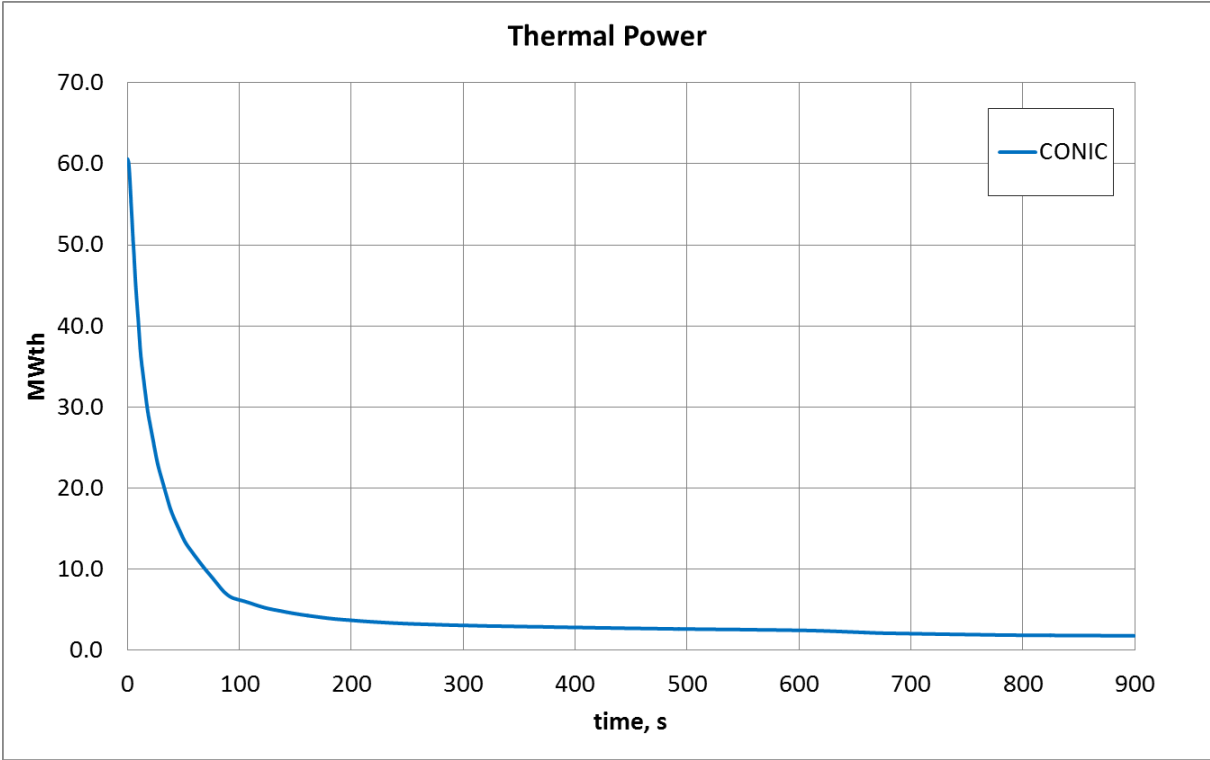
Figure I-3. EBR-II SIMMER results: thermal power versus time (CASE: CONIC)
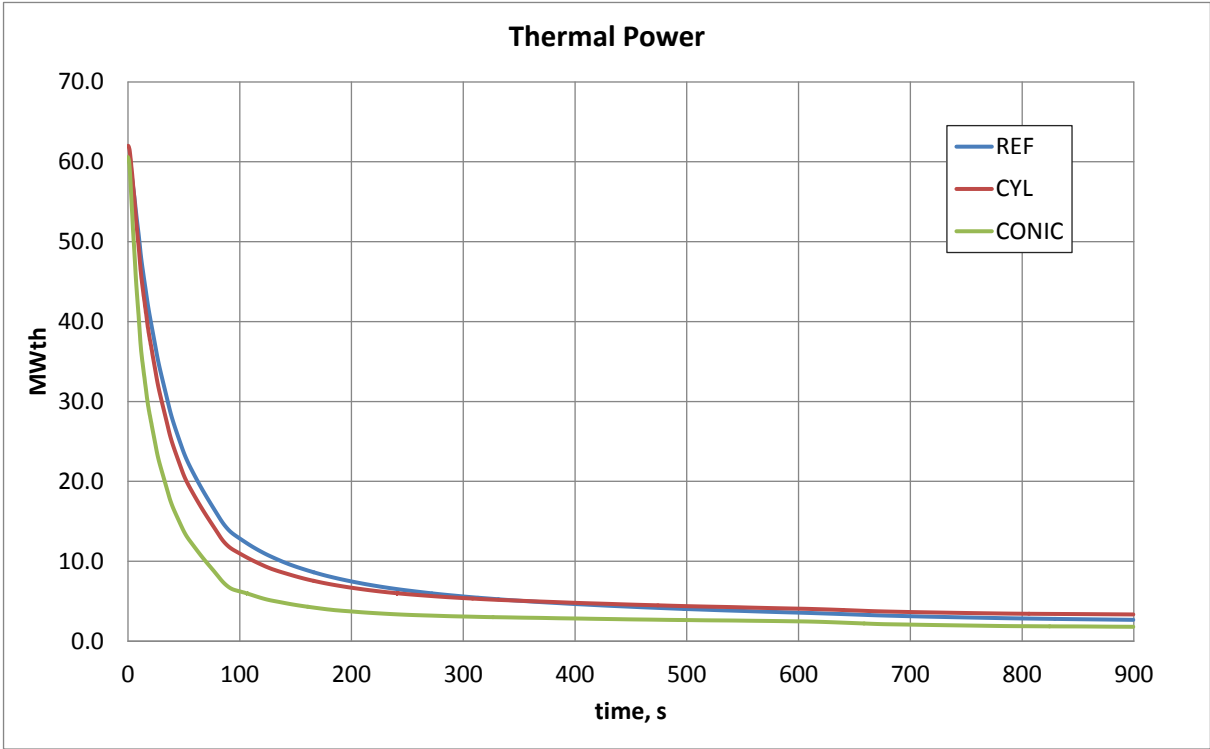
Figure I-4. EBR-II SIMMER results: thermal power versus time comparison three cases: REF, CYL and CONIC
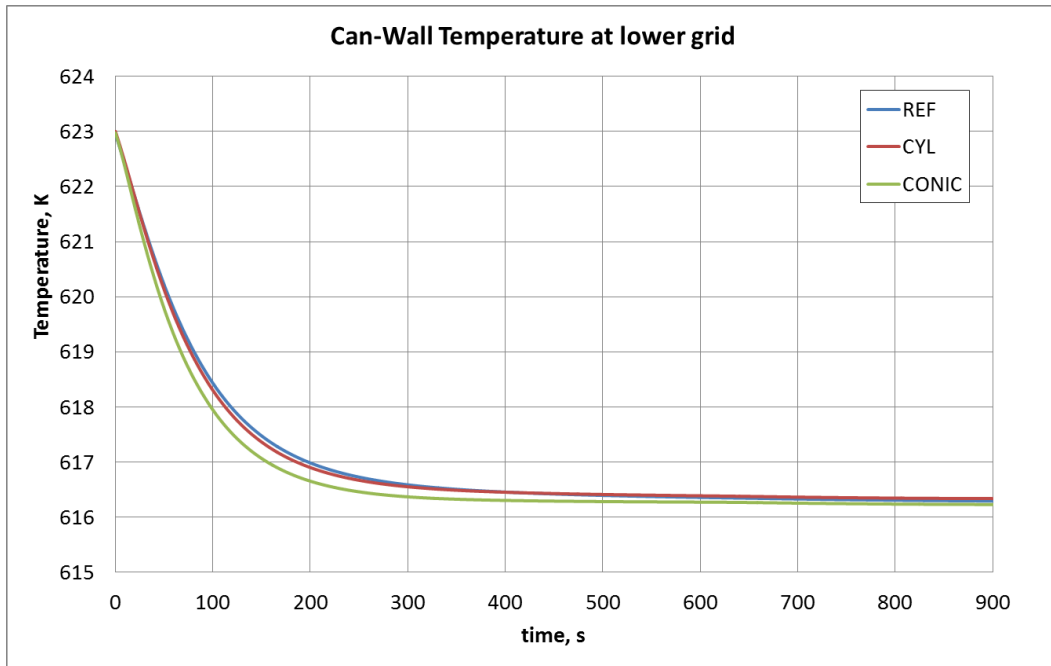
Figure I-5. EBR-II SIMMER results: steel temperature in lower grid: comparison of the three cases

The net reactivity determined by SIMMER for the three cases is shown in Figure I-6. In the REF case it includes Na density variation, Doppler and other material density variation feedback effects. In the CYL case it additionally includes the axial reactivity effect (as previously explained, Figure I-6) and in the CONIC case, in addition to the axial contribution it includes the radial expansion reactivity effect (approximation of flowering behavior). No detailed information about the EBR-II clamping system has been provided within the benchmark. Some approximation on the basis of the geometry description has been considered. The SIMMER results (CONIC and CYL model) are within the spread of data provided by the other partners of the project [196].
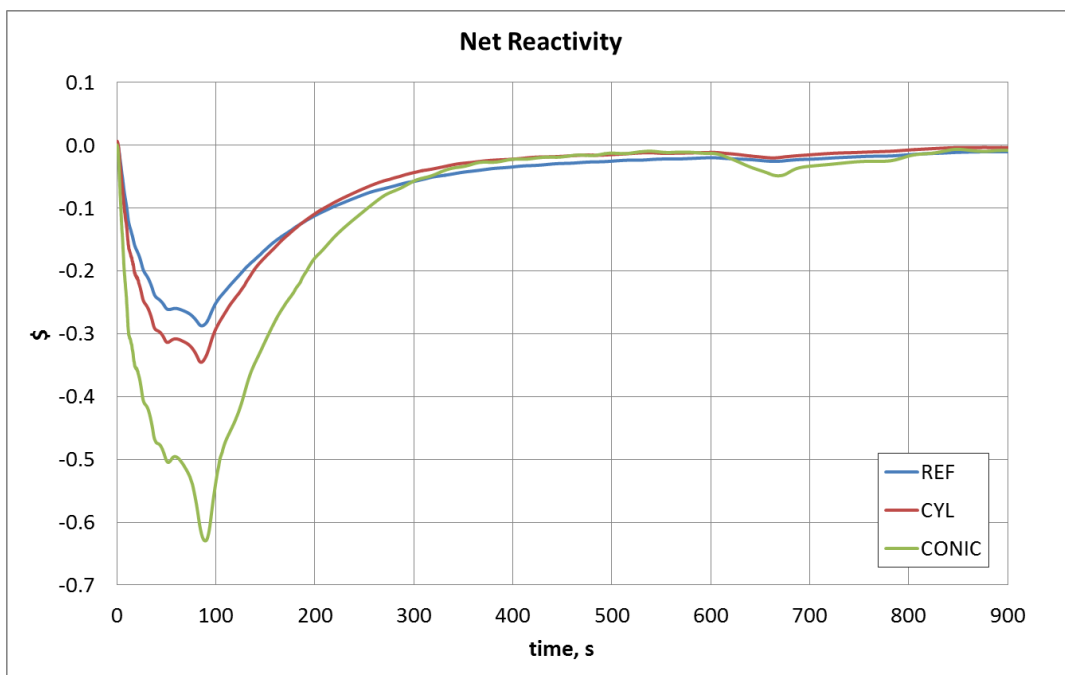
Figure I-6: EBR-II SIMMER results: net reactivity comparison of the three cases

The net reactivity of the REF case (Figure I-7) is in the range of values of the other participants [196].
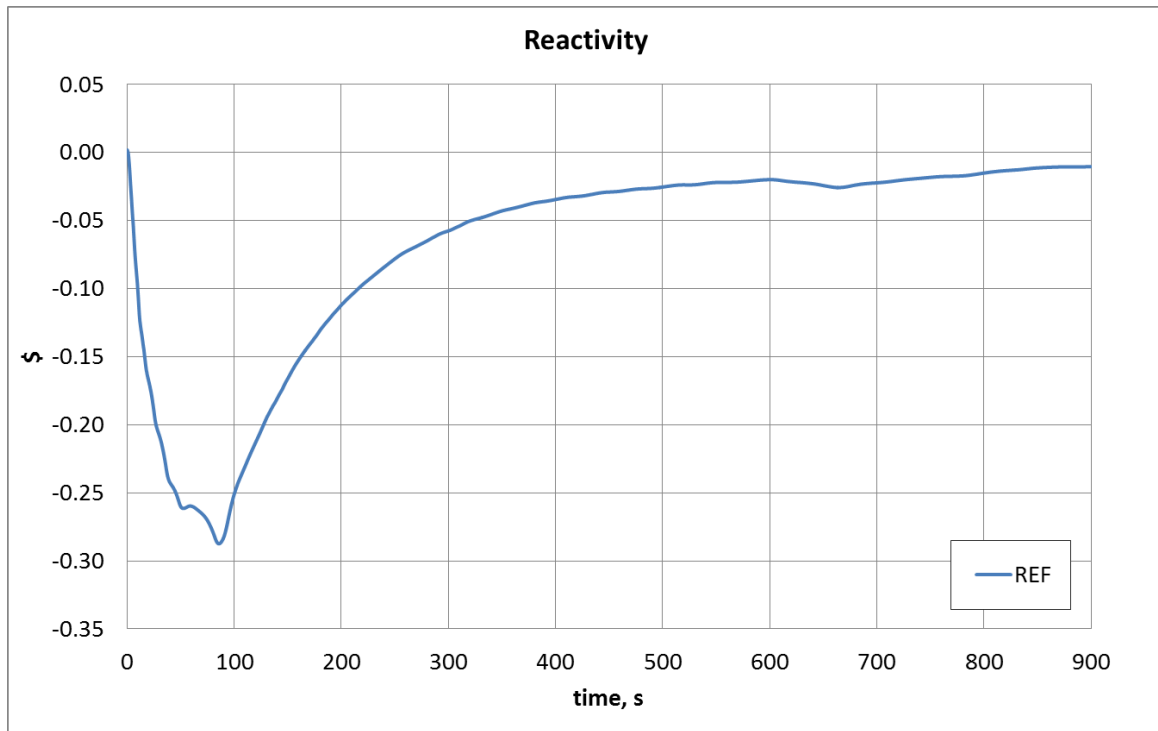
Figure I-7: EBR-II SIMMER results: net reactivity for REF case: namely corresponding to the contribution of Na density variation

The contribution of the axial thermal expansion reactivity feedback is calculated in a first approximation by the difference between the net reactivity for CYL model and the net reactivity for REF model. The behavior is shown in Figure I-8. The SIMMER results are in the range of the other participants [196].
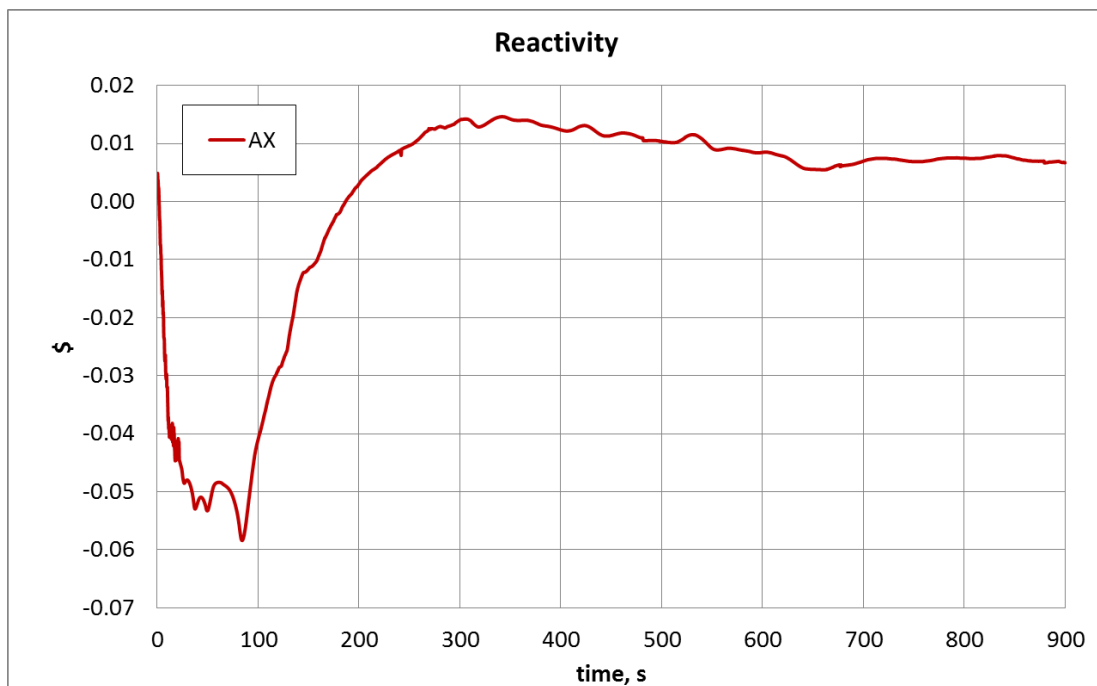
Figure I-8. EBR-II SIMMER results: axial reactivity effect (assumed in a first approximation as difference between CYL and REF cases)

The contribution of the radial thermal expansion reactivity feedback is calculated in a first approximation by the difference between the net reactivity for CONIC model and the net reactivity for CYL model. The behavior is shown in Figure I-9. SIMMER results are in good agreement with the results of other partners [196].
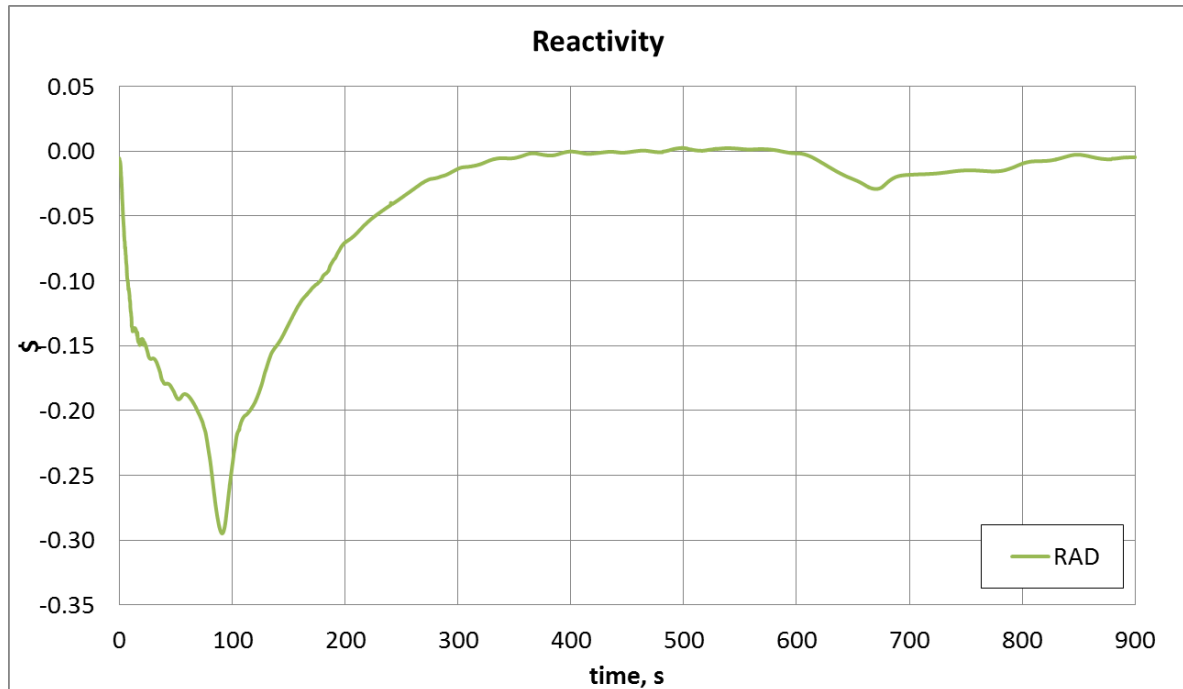
Figure I-9. EBR-II SIMMER results: radial reactivity effect (assuming in a first approximation as difference between CONIC and CYL cases)

Impact of the initial condition for the steel temperature

At the beginning of SIMMER calculations, the neutronics and thermodynamic part of SIMMER are out of balance because e.g. temperature distributions and coolant flow conditions are not specified in the input. Therefore, a so-called fixed power calculation is performed in order to reach a steady state. The steady state will depend on this input. However, as the DENSF factor is calculated at the start of the calculation, it depends on the input parameters. In order to test this effect, 4 cases have been compared:

Case 1: cylindrical expansion where the initial temperature of steel was set everywhere to 666.15 K (value larger than the steady state value of ca. 620K)

Case 2: identical to case 1 but setting the initial temperature of steel everywhere to 600 K (value lower than the steady state value ca. 620K)

Case 3: conic expansion setting the initial steel temperature everywhere to 666.15 K (value larger than the steady state value in the lower grid, ca. 620K, but lower than the steady state value at the upper constraint plate, ca. 750K)

Case 4: conic expansion setting the initial temperature of steel equal to 600 K in the lower part of the core, namely below the position of the upper constraints and equal to 720 K in the upper part of the core, namely above the upper constraint. The value is lower than steady state values of the lower grid, ca. 620K, and it is lower than the steady state value at the upper constraint plate, ca. 750K).

These cases have been compared both for fixed power calculations and during ULOF conditions. The ULOF results are slightly different (in terms of nominal values) with respect to the figures shown previously because the calculations were run with a different beta effective (almost half of the correct one). The beta effective taken in this case by default by SIMMER is typical of a MOX fuel and not of a U-metal fuel as appropriate for EBR-II.

CASE 1 and 2 are compared in Figure I-10 for the fixed power calculations. The two cases have a very different behavior which can be explained by the different temperature distribution. In case 1 a reactivity increase is observed due to a core shrinking (steel temperature in input is larger than the steady state value) while in case 2 the reactivity decreases due to an expansion of the core (steel temperature in input is lower than the steady state value). In terms of K-eff the two models are identical.

In order to check that there is not a large effect on the ULOF behavior, the net reactivity is shown in Figure I-11. The two different inputs led to an almost congruent behavior (small differences may be due to locally different distributions).

The fixed power calculations differ also for CASE 3 and 4 (Figure I-12). These differences disappear during the ULOF case (case 4 stopped but the initial behavior is the same). See Figure I-13 for the ULOF case.

The comparison has provided a first indication that the procedure implemented in SIMMER for taking into account core thermal expansion reactivity feedbacks [1,2] is independent of the input steel temperature specifications.

Figure I-10. EBR-II SIMMER results: Cylindrical model, comparison of different steel temperature in input specification (fixed power calculation)
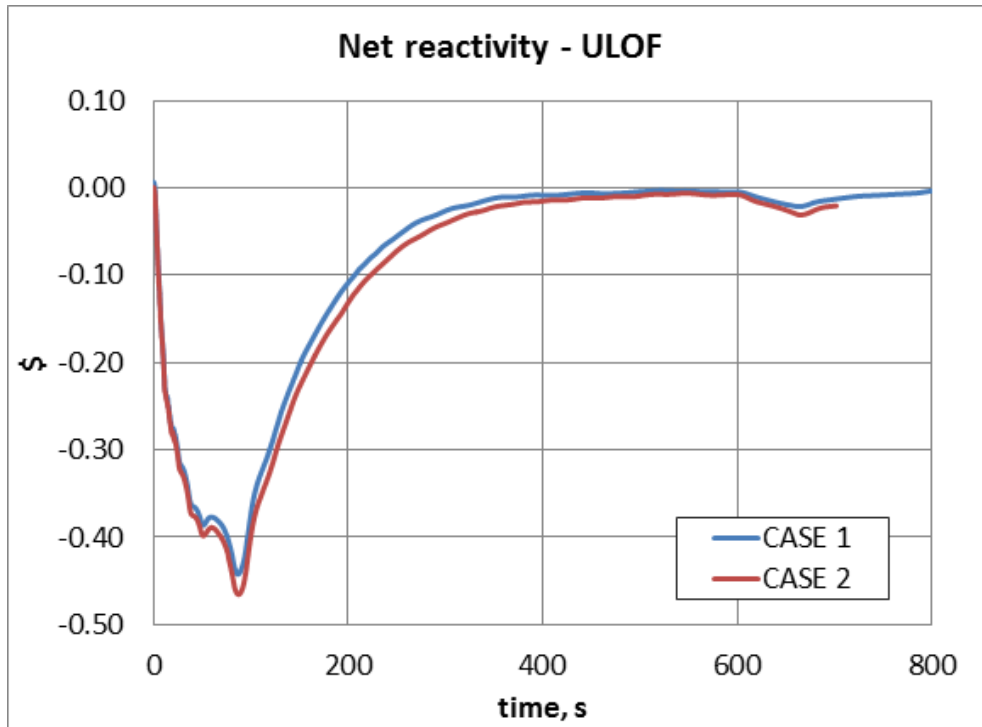
Figure I-11. EBR-II SIMMER results: Cylindrical model, comparison of different steel temperature in input specification (ULOF)
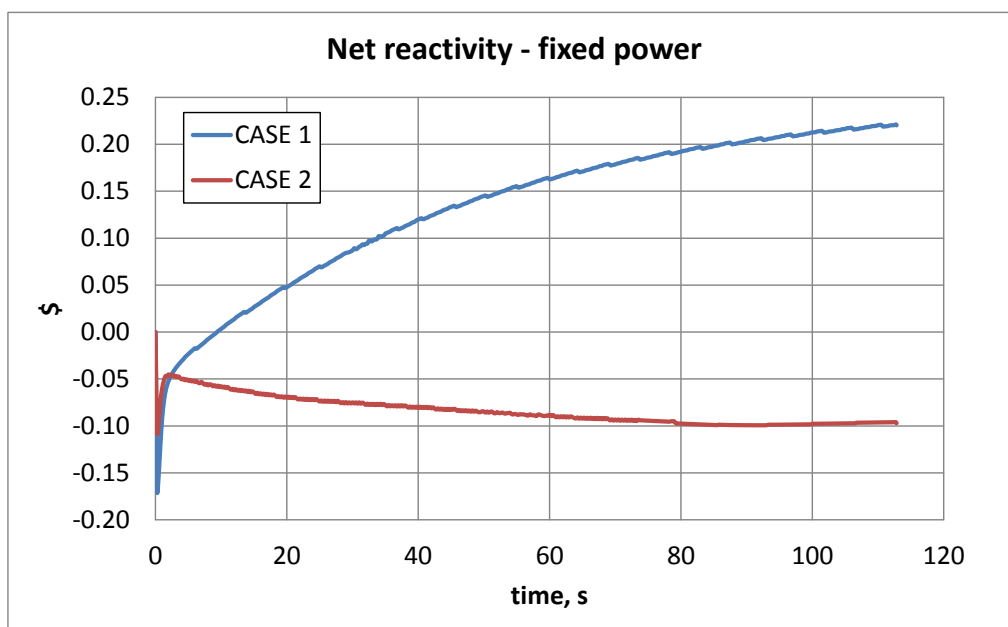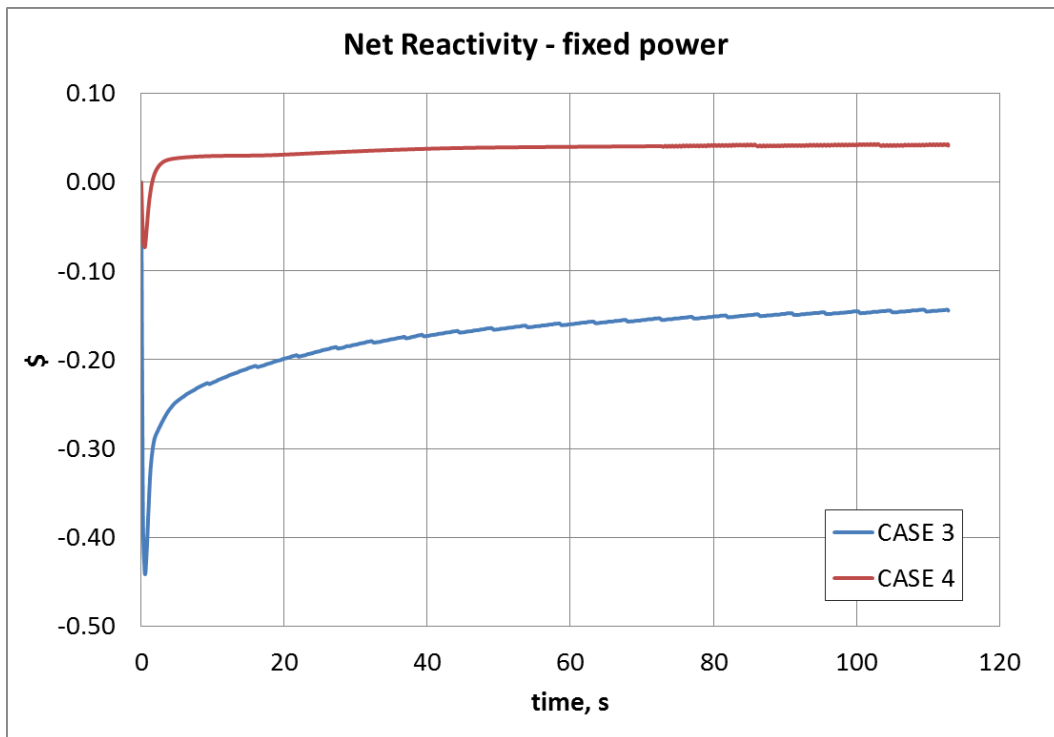

Figure I-12. EBR-II SIMMER results: Conic model, comparison of different steel temperatures in input specification (fixed power calculation)
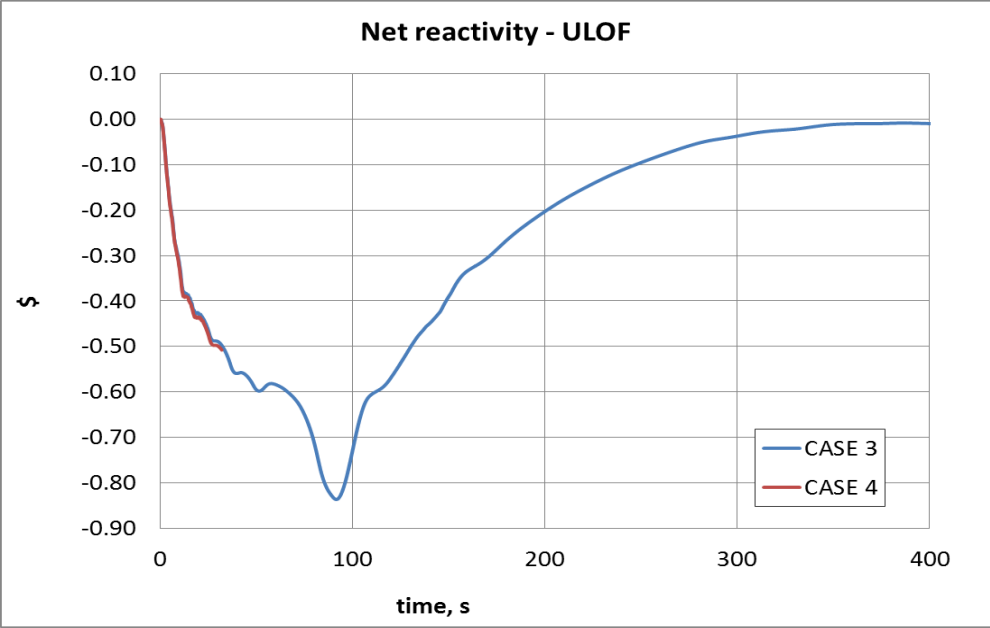
Figure I-13. EBR-II SIMMER results: Conic model, comparison of different steel temperature in input specification (ULOF)

APPENDIX I

Appendix J:
The equivalence principle

This appendix J aims at giving an additional explanation to the equivalence principle detailed in Chapter 6, section 6.5.1.

The equivalence principle stipulates that "*increasing all linear dimensions of <u>any</u> given reactor by a certain factor while simultaneously reducing all material densities by that same factor will result in <u>exactly</u> zero change to reactivity and flux distributions*" [161].

Consider an infinite medium and one energy group. The (infinite) multiplication constant k_∞ is expressed as Eq. J-1.:

$$k_\infty = \frac{\nu \Sigma_f}{\Sigma_a} \qquad \text{J-1}$$

Where ν is the number of neutrons produced per fission, Σ_f is the macroscopic fission cross-section in m^{-1}, Σ_a the macroscopic absorption cross-section in m^{-1}.

Consider a homogeneous expansion (i.e. same expansion for all materials) of α (i.e. a variation in the cross-sections of α). In this case the (infinite) multiplication constant can be expressed as Eq. J-2:

$$k_\infty = \frac{\nu \Sigma_f \alpha}{\Sigma_a \alpha} = \frac{\nu \Sigma_f}{\Sigma_a} \qquad \text{J-2}$$

Eq. K-2 demonstrates that there is no change in the infinite multiplication constant in case of an homogeneous expansion of α.

Now let's consider a finite medium and 1 energy group. The multiplication constant k_{eff} is expressed as Eq. J-3:

$$k_{eff} = k_\infty P_{NL} = k_\infty \frac{1}{1 + M^2 B_g^2} \propto \frac{1}{1 + \dfrac{1}{(\Sigma \cdot L)^2}} \qquad \text{J-3}$$

Where P_{NL} is the non-leakage probability, M^2 is the migration area in m^2, B_g^2 is the geometrical buckling in m^{-2}, L is a representative dimension in m.

If one wants to get the same multiplication constant for two configurations, e.g. one configuration and initially the same configuration but subjected then to a uniform isotropic expansion of α, it can be seen from Eq. J-3 that the neutron leakage probability has to be kept (since the infinite multiplication constant does not change during a uniform isotropic expansion as demonstrated in Eq. J-2). Hence, one can deduce that the product $\Sigma \cdot L$ has to be kept constant. This is exactly stipulated by the equivalence principle.

To illustrate this principle, consider the Working Horse core (details on this core can be found in Chapter 4) which has been submitted to a 2% homogeneous uniform isotropic expansion (i.e. the same expansion for all materials and in all directions, here radial and axial). The multiplication constant of this case is of 1.004174, see Figure J-1 (a). If the equivalence principle is now applied, one can consider the WH core in its initial dimensional configuration but with reduced cross-sections (by 4%) for all materials. Also in this case a multiplication factor of 1.004174 is obtained (Figure J-1 (b)), which illustrates well the equivalence principle.

(a)
k_{eff}= 1.004174

(b)
k_{eff}= 1.004174
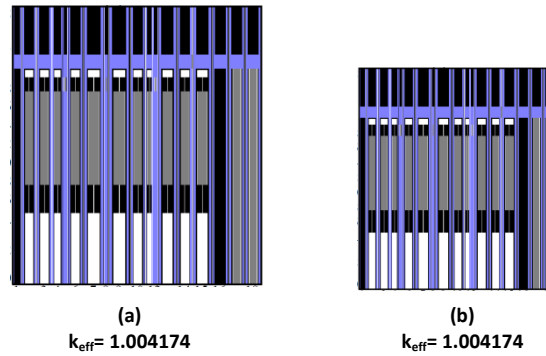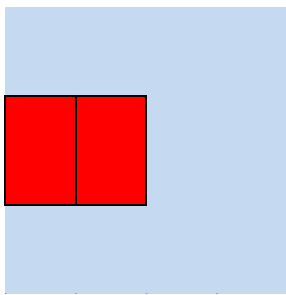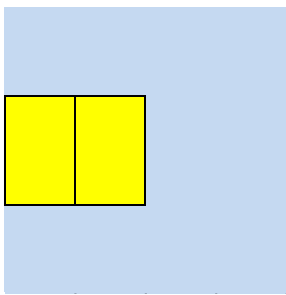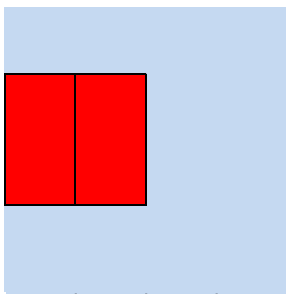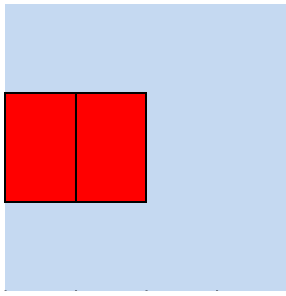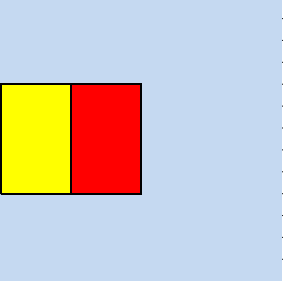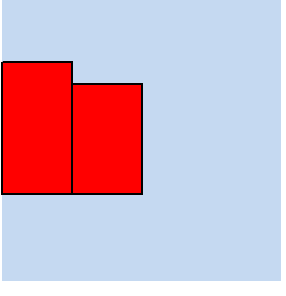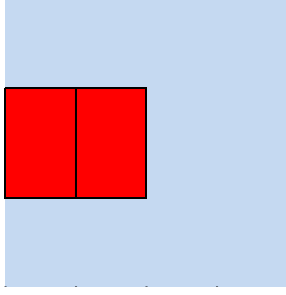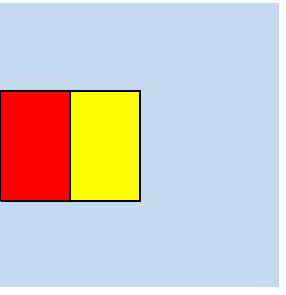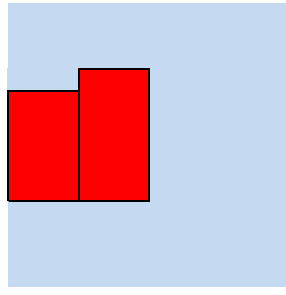
Figure J-1 Illustration of the equivalence principle in the Working Horse for a 2% homogeneous isotropic expansion of 2% (a) and ist equivalent configuration with original dimensions and modified (i.e. equivalent) cross-sections(b). Precision on k_{eff} is of 0.1 pcm.

Appendix K:
The DENSF approach

Appendix K aims at giving an additional explanation of the idea behind the DENSF factor detailed in Chapter 6. In this chapter, it has been demonstrated that one can treat any expansion as an axial expansion. The density effect related to this expansion can be treated by SIMMER based on the equivalence principle. The question is now how to treat the related axial dimensional (i.e. due to a dimension variation) effect.

Assume the global dimensional effect calculations have been performed for a 5% variation (the word global refers to the fact that in the whole reactor, all materials are subjected to the same variation). How to take into account the variations at different locations? The contributions of different nodes to the global effect are assumed to be proportional to their reactivity worth values. This is in line with the equivalence principle.

Table K-1. Cases considered for global or local variations of densities or dimensions. In red: original densities, in yellow: reduced densities.

For the next examples, the Working Horse core is considered (details on this core can be found in Chapter 4). In first approximation, the core has been subdivided into two zones for considering the expansion, as to know the inner and outer core zone.

At first, global density and dimensional effects are determined. Consider a global density variation of 5% in the two core zones (Case 1(b) in Table K-1). The related reactivity effect compared to the reference case (Case 1(a) in Table K-1) is of -873 pcm. Consider now a sole global axial dimensional variation of 5% (Case 1(c)) i.e. densities are unchanged compared to the reference core. The related reactivity effect compared to case 1(a) is of +625 pcm.

The next step consists in taking into account local variations. If we consider a local density variation of 5% in the first core zone only, the second core zone being unchanged as seen in Table K-1 (Case 2(b)), the related reactivity effect, compared to the reference case, is of -683 pcm. If one now wants to find out what the local dimensional variation effect in the first core zone would be, and if the assumption is made that the local dimensional variation is proportional to the local density variation in the first core zone, to the global density variation as well as to the global axial dimensional variation, one would obtain a reactivity variation of $-683 \cdot \dfrac{+625}{-873} = +489 \, pcm$. If now the actual case 2(c) is considered, where the axial dimensions of the first zone have been submitted to this variation of 5%, an effect of +509 pcm is obtained; hence a difference of -3.9% compared to the value obtained through the assumption of proportionality.

In the same way, one could consider a local density variation of 5% in the second core zone (case 3(b) in Table K-1), the related reactivity effect compared to the reference case is of -159 pcm. By assuming, as previously, the proportionality between a local dimensional variation effect and a local density variation effect, a global density variation effect and a global axial dimensional variation effect, the axial dimensional variation effect of 5% in the second core zone can be evaluated as $-159 \cdot \dfrac{+625}{-873} = +114 \, pcm$. If one considers the actual case 3(c) where the axial dimension of the second core zone has been modified via a variation of 5%, the reactivity effect is of 122 pcm, i.e. a relative difference of -6.6% compared to the evaluated effect. This relative difference is however within the uncertainty range of 10-15% for the current evaluation of reactivity feedbacks [198; 199].

In conclusion, the applicability of the proportionality assumption is demonstrated. This approach is exactly the one used in the DENSF coefficient approach (Chapter 6).

Appendix L:
Résumé détaillé de la thèse

L.1. Introduction

Mondialement, la demande en énergie n'a cessé de croitre les dernières décennies et génère le besoin d'un approvisionnement en énergie fiable et abordable. Avec la digitalisation du monde actuel, l'agence internationale pour l'énergie prévoit une croissance de 2.1% par an de la demande en électricité mondiale sur la période 2012-2040 [1]. Afin de répondre à cette demande tout en préservant le climat, un mix énergétique entre énergies fossiles, renouvelables et nucléaire doit être trouvé. Parmi les différentes sources d'énergie, le nucléaire fournit une électricité de base et compte parmi l'une des seules options à ne quasiment pas produire de CO_2. Cette énergie ne reçoit cependant pas toujours l'acceptation du public, notamment suite à l'accident de Fukushima Daiichi au Japon. Actuellement, 434 réacteurs nucléaires sont en opération et 76 nouveaux réacteurs sont en construction au niveau mondial. Ils représentent 332 GW de la capacité installée, produisant plus de 11% de l'électricité mondiale. Ces réacteurs sont tous des réacteurs à spectre thermique de génération 2 ou 3. Afin d'assurer une meilleure utilisation des ressources d'uranium et une gestion des déchets nucléaires, de nouveaux réacteurs dits de génération 4 sont actuellement à l'étude. Au sein du Forum International de Génération 4 [3], la recherche se focalise sur 6 principaux concepts de réacteurs nucléaires à savoir les réacteurs refroidis au plomb, au sodium, au gaz, à eau supercritique, à très haute température et à sels fondus. Tous ces réacteurs doivent démontrer leur durabilité, leur sûreté améliorée et leur résistance à la prolifération en plus d'être économiquement compétitifs [3]. Parmi ces six concepts, seuls les réacteurs à spectre rapide remplissent les critères de durabilité, l'un des concepts le plus avancé étant le réacteur à caloporteur sodium. Pour ce réacteur, des objectifs clés ont été définis parmi lesquels une amélioration de la sûreté intrinsèque ainsi que la prévention et la limitation des conséquences d'accidents graves à haut potentiel énergétique - et le développement de combustibles avancés - spécialement des combustibles contenant des actinides mineurs. Cette thèse s'insère dans cette problématique de sûreté améliorée et de réduction des déchets.

Ce travail contribue aux analyses de sûreté des réacteurs refroidis au sodium contenant des combustibles chargés en actinides mineurs. Le but de cette thèse est l'analyse de l'impact des combustibles sphere-pac innovants sur les performances de sûreté de ces réacteurs à la fois en conditions nominales et accidentelles. La thèse est effectuée dans le cadre du projet européen PELGRIMM (2012-2016) [11] qui vise à comparer les combustibles oxydes sous forme pastille ou sous forme sphere-pac en matière de fabrication, de comportement sous irradiation, et de modélisation lors d'accidents graves. Le cœur CONF2 [14; 9] issu du projet CP-ESFR (2009-2012) [6] a été choisi afin d'effectuer les analyses de sûreté. Ce cœur présente un effet de vidange sodium faiblement positif, et les différentes contre-réactions en jeu forment un équilibre délicat. Ce type de cœur est supposé présenter un meilleur comportement en transitoire. Par conséquent une modélisation améliorée de la phase d'initiation s'impose (spécifiquement pour le code SIMMER [73] développé à l'origine pour les cœurs largement dégradés).

Afin de répondre à cette problématique, deux voies de développement ont dû être suivies : la première vise à l'amélioration de la modélisation de la phase d'initiation avec le code SIMMER - le

point le plus urgent étant la prise en compte des effets de dilatation du cœur – la deuxième à prendre en compte les spécificités des combustibles sphere-pac.

Afin de comprendre le contexte dans lequel s'insère cette thèse, une explication introductive sur les systèmes de génération IV et sur leurs avantages en termes de réduction des déchets nucléaires et d'amélioration de l'utilisation du combustible est fournie au chapitre 2.

Lorsque l'on s'intéresse aux systèmes à spectre rapide, il convient de faire une analyse étendue de leur comportement de sûreté tant en conditions nominales qu'en conditions accidentelles, ces cœurs étant en effet dans une configuration qui n'est pas la plus réactive. L'approche de sûreté, les principes fondamentaux ainsi que les grandes familles d'accidents sont développés au chapitre 3.

Les cœurs à l'étude dans cette thèse sont détaillés au chapitre 4. Deux cœurs issus du précédent projet CP-ESFR [6; 187] sont analysés à savoir le cœur Working Horse (WH) et sa version optimisée le cœur CONF2.

Cette thèse étant axée sur les combustibles sphere-pac, une explication des différentes familles de combustibles s'est imposée. L'attention est ici portée principalement sur les combustibles oxydes sous deux formes spécifiques : la forme pastille traditionnelle et la forme sphere-pac. Le cycle combustible de ces deux combustibles est considéré dans le chapitre 5.

Le chapitre 6 traite d'une nouvelle extension de SIMMER pour la prise en compte des effets de dilatation du cœur. Ces effets sont particulièrement importants dans les cœurs à faible effet de vidange sodium, notamment en phase d'initiation de l'accident. Les codes SIMMER ne prennent pas en compte, à l'origine, les contre-réactions liées à la dilatation du cœur puisqu'ils ont été développés pour des cœurs largement dégradés, où ces effets étaient négligeables ou inexistants. Après avoir détaillé l'équation du transport et les différentes méthodes de résolution, avec une attention particulière pour la méthode quasi-statique sur laquelle repose le module neutronique de SIMMER, la physique de la dilatation du cœur ainsi que les différents modèles pour la prise en compte des effets neutroniques liés à cette dilatation sont détaillés. Deux modèles basés sur la théorie des perturbations du premier ordre et une troisième méthodologie basée sur la méthode directe y sont expliqués. Ce chapitre présente ensuite la validation des différentes hypothèses ainsi que de la procédure générale via l'analyse de cas tests. Enfin, l'amélioration des simulations de transitoires suite à cette nouvelle extension est démontrée dans le cas d'un accident de perte de débit primaire.

Le chapitre 7 traite de la modélisation des spécificités des combustibles sphere-pac pour le code SIMMER. Ces combustibles présentent en effet une conductivité thermique faible en début de vie, due à leur microstructure spécifique, comparé au combustible pastille de même densité. La conductivité thermique de ces combustibles s'améliore cependant rapidement sous irradiation sous l'effet de la restructuration liée aux gradients de température. De plus, le jeu pastille-gaine présent dans les aiguilles de combustibles pastille est inexistant dans les aiguilles de combustibles sphere-pac. Ce chapitre traite essentiellement de l'adaptation de la conductivité thermique des combustibles sphere-pac pour le code SIMMER. Une recherche bibliographique sur les différents modèles adaptables à la conductivité des combustibles sphere-pac y est proposée. Ces modèles étant trop détaillés pour le code SIMMER, qui utilise des corrélations fonctions de la température du combustible, il a fallu adapter les modèles les plus appropriés. Des corrélations pour un combustible neuf et pour un combustible irradié durant trois cycles sont développées pour les combustibles sphere-pac et pastilles.

Le chapitre 8 met l'accent sur l'analyse des résultats obtenus avec les extensions détaillées aux chapitres 6 et 7. Des analyses d'accidents de perte de débit primaire y sont proposées pour les cœurs WH et CONF2, contenant soit des aiguilles pastilles soit sphere-pac, en début de vie et après trois cycles d'irradiation, avec ou sans prise en compte des contre-réactions dues à la dilatation thermique du cœur. Les analyses des cœurs en début de vie mettent l'accent sur la différence fondamentale des conductivités thermiques des deux combustibles. Un cœur représentatif serait cependant un cœur à l'équilibre, où les combustibles sphere-pac auraient eu suffisamment de temps pour se restructurer. L'impact d'un ajout d'américium de 2% et 4% en masse sur les conclusions générales y est analysé.

Enfin, le chapitre 9 contient les conclusions principales et les perspectives de ce travail.

L.2. Les réacteurs à neutrons rapides : designs et missions

Les réacteurs à neutrons rapides présentent un avantage considérable non seulement pour une meilleure utilisation du combustible mais également pour le recyclage des combustibles irradiés. En effet, aujourd'hui, le combustible nucléaire irradié provenant des réacteurs à eau pressurisée (REP) contient, en sortie du réacteur, 95% d'uranium, ~1% de plutonium, ~4% de produits de fissions et ~0.1% d'actinides mineurs (américium, curium et neptunium) pour un taux d'irradiation d'environ 40 GWj/t [18; 10]. Ceci signifie que seuls quelques pourcents d'uranium sont effectivement utilisés dans les REP actuels.

En utilisant un mélange d'oxyde d'uranium et de plutonium (provenant des REPs) dans des réacteurs à spectre rapide, il est à la fois possible de recycler le plutonium, responsable de 90% de la radiotoxicité du combustible irradié, et d'atteindre une meilleure utilisation du combustible. La fission d'un atome de plutonium produit en effet suffisamment de neutrons pour à la fois maintenir la réaction en chaine et produire de nouveaux noyaux fissiles par capture sur l'uranium 238 [21]. Ainsi, la régénération devient possible en réacteur rapide.

Un spectre rapide entraine également une amélioration considérable du ratio fission sur absorption des actinides mineurs [26]. Il est par conséquent possible de réduire le volume et la radiotoxicité des déchets à entreposer en stockage géologique profond. Les réacteurs à neutrons rapides refroidis au sodium comptent parmi les concepts les plus avancés proposés dans le cadre du forum international de génération IV. Le caloporteur sodium est quasiment transparent aux neutrons et sa conductivité thermique élevée en fait un bon élément pour extraire la chaleur produite par fission nucléaire [36].

De par la composition de leur combustible, les réacteurs à neutrons rapides présentent des coefficients de sûreté différents de ceux des réacteurs thermiques ainsi qu'une fraction de neutrons retardés plus faibles. Parmi ces coefficients de sûreté on peut nommer l'effet Doppler, les coefficients liés aux effets de variations de concentration des différents matériaux (uniquement le sodium en cas nominal), et ceux liés aux effets de dilatation thermique. Il est à noter que, dans le cas général, une perte du caloporteur sodium induit un durcissement du spectre qui a pour effet une augmentation de la réaction en chaine. Durant la thèse, les accidents de pertes de caloporteur sont à l'étude.

L'ajout d'actinides mineurs dans le combustible des réacteur à neutrons rapides a un impact à la fois sur l'aval et l'amont du cycle combustible ainsi que sur les performances du cœur [49; 10]. Différents types de recyclages peuvent être effectués, notamment le recyclage homogène où les actinides mineurs sont insérés dans la zone nourricière ou le recyclage hétérogène où les actinides mineurs sont insérés dans des assemblages dédiées placés en périphérie du cœur (par exemple dans des couvertures centrales d'actinides mineurs CCAM).

En fonction du mode de recyclage choisi, les performances de transmutations, l'impact sur le cœur ainsi que les émissions de neutrons ou encore de chaleur résiduelle varient.

L.3. L'approche de sûreté pour les réacteurs à neutrons rapides refroidis au sodium

L'approche de sûreté repose sur trois objectifs fondamentaux i.e. un objectif de sûreté général, un objectif de protection contre les radiations et un objectif de sûreté technique [54]. Ainsi peuvent être définies deux principales lignes directrices pour les réacteurs à neutrons rapides refroidis au sodium : premièrement, les objectifs de sûreté définis dans le cadre européen pour la sûreté des nouvelles centrales nucléaires (et en particulier ceux pour l'EPR) constituent la base des lignes directrices pour les réacteurs à neutrons rapides refroidis au sodium, et deuxièmement, les objectifs doivent être atteints et leur réalisation doit être démontrée de manière robuste. Afin d'atteindre ces objectifs de sûreté, trois fonctions de sûreté doivent être remplies à savoir : le contrôle de la réactivité à tout moment et pour tout état du réacteur, le refroidissement du combustible en toute situation et temps, et le confinement de la matière radioactive.

Afin de garantir ces objectifs et fonctions de sûreté, deux grands principes doivent être suivis : l'approche multi-barrière et le principe de défense en profondeur. L'approche multi-barrière prévient et limite les rejets radioactifs hors de la centrale nucléaire. Elle dresse entre la matière radioactive et l'environnement quatre barrières qui sont la matrice combustible elle-même, la gaine, le circuit primaire et le bâtiment de confinement [181]. La défense en profondeur permet quant à elle de structurer et d'implémenter l'architecture de sûreté [51; 54]. Cette stratégie consiste tout d'abord à grouper les initiateurs d'incidents ou d'accidents en différentes catégories selon leur probabilité d'occurrence. Les conséquences radiologiques les plus élevées doivent être associées aux probabilités les plus basses. Elles sont évaluées via des analyses de sûreté, jugement technique et études probabilistes. Les conditions normales et anormales de la centrale dues à des transitoires anticipés sont groupées en quatre catégories et représentent les conditions d'accidents de dimensionnement [59]. Les accidents hors dimensionnement quant à eux sont des accidents de faible probabilité et correspondent à des accident dus à des ruptures multiples des barrières de sûreté [59]. Dans ces accidents hors-dimensionnement, on peut notamment citer les accidents graves qui sont des accidents postulés entrainant des dégradations sévères du cœur. L'un d'entre eux, à l'étude dans cette thèse, est l'accident de perte de débit primaire. Cet accident est en effet un accident global affectant la totalité du cœur couvrant les phénomènes les plus importants observables durant une dégradation sévère du cœur.

L.4. Designs spécifiques de réacteurs à neutrons rapides refroidis au sodium à l'étude

Plusieurs réacteurs à neutrons rapides refroidis au sodium ont été construits et exploités lors du siècle dernier. En France spécialement on peut mentionner les réacteurs Phénix et Superphénix dont on tient un vaste retour d'expérience [81]. Le design des RNR-Na a constamment évolué depuis leurs débuts, le but premier étant d'améliorer la prévention ainsi que la limitation des conséquences d'un accident grave. Dans le cadre du 7ème programme de recherche européen EURATOM, le projet CP-ESFR (2009-2012) [6; 187] a par exemple eu pour but d'optimiser les concepts de larges réacteurs à neutrons rapides refroidis au sodium, dans le but de démontrer la viabilité et d'évaluer les performances de ce type de réacteur en soutien au développement d'un réacteur européen à caloporteur sodium. Au début du projet, un cœur oxyde a notamment été étudié : le CP-ESFR Working Horse. Les analyses ont permis d'identifier les modifications nécessaires à l'amélioration du comportement de sûreté de ce réacteur à la fois en condition nominale et en condition accidentelle. L'un des axes de recherche était notamment la réduction de l'effet de vidange sodium, qui gouverne la phase d'initiation des accidents graves comme l'accident de perte de débit primaire (ULOF). Les conclusions tirées de cette étude ont donné naissance à un design de cœur à combustible oxyde optimisé: le cœur CONF2 [14]. Pour ce cœur, l'effet de vidange sodium a été considérablement réduit (par un facteur ~2.5, i.e. de +1211 pcm à +496 pcm en début de vie) notamment grâce à l'élargissement de la hauteur du plénum sodium ainsi que d'un ajout d'absorbant au-dessus de ce dernier pour empêcher la réflexion des neutrons vers le cœur [9]. Cet effet de vidange réduit permet de considérer l'introduction d'actinides mineurs dans le cœur. Ainsi des études de performances de transmutation ont été effectuées pour le cœur CONF2 et ses versions optimisées. L'introduction d'actinides mineurs dans le cœur CONF2 détériore les coefficients de sûreté (notamment l'effet de vidange et l'effet Doppler) ainsi que la fraction effective de neutrons retardés comme attendu. Le cœur CONF2 contenant 4% en masse d'américium dans le combustible en début de vie présente même des coefficients de sûreté similaires au cœur WH, annulant ainsi l'effet de l'élargissement du plénum sodium [9].

Ces deux cœurs, développés durant le projet CP-ESFR, servent de designs de référence pour les analyses de sûreté des combustibles sphere-pac présentés dans cette thèse.

L.5. Les combustibles nucléaires

Différents types de combustibles ont été développés depuis le début de la filière nucléaire. Les premiers combustibles étaient des combustibles métal. Dû à leur densité élevée de métaux lourds, leur processus de fabrication relativement simple ainsi que leur bonne conductivité thermique, ces combustibles présentaient tous les prérequis pour un gain de régénération élevé [96]. Ils ont cependant révélé une instabilité dimensionnelle sous irradiation due au gonflement et à la croissance sous l'effet du flux neutronique [94].

Les combustibles nitrures et carbures sont également des combustibles potentiels pour les réacteurs rapides. Le combustible privilégié reste cependant le combustible oxyde. Il profite en effet d'un large retour d'expérience de la filière thermique et a démontré sa résistance à l'irradiation [94]. La forme la plus répandue pour le combustible oxyde est la forme pastille mais des formes alternatives comme les combustibles sphere-pac sont étudiées. Dans les sections suivantes, ces deux combustibles sont détaillés.

L.5.1. Le combustible oxyde pastille

Le combustible pastille MOX peut être fabriqué via différents procédés. Traditionnellement il est fabriqué par voie métallurgique [25]. Les oxydes de plutonium et d'uranium sont mélangés dans les proportions requises via des étapes d'homogénéisation et de broyage, puis ce mélange est compacté sous forme de pastilles qui sont ensuite frittées. Cette étape est essentielle pour obtenir la densité souhaitée, habituellement de l'ordre de 85% à 95% de la densité théorique [101]. Une fois frittées, elles sont placées dans une gaine métallique pour former ce qu'on appelle les aiguilles qui sont ensuite remplies avec de l'hélium.

Les combustibles oxydes sont connus pour leur grande résistance sous irradiation. En effet, ce combustible ne présente que peu de gonflement par rapport aux combustibles nitrures par exemple (0.6% par at% de burnup contre 1.1-1.6%, [101]). De plus, le combustible oxyde peut être retraité sous forme aqueuse et ne nécessite donc pas de procédés électrométallurgiques comme la pyrolyse.

L'un des plus grands inconvénients du combustible oxyde est cependant sa conductivité thermique relativement faible, de l'ordre de 2-3 $W \cdot m^{-1} \cdot K^{-1}$ [94]. Cette propriété du matériau constitue un point essentiel pour la sûreté du combustible. Au vue de la faible conductivité thermique des oxydes, ces combustibles présentent généralement des températures élevées, donnant naissance à des processus thermiquement activés. L'un d'entre eux est la restructuration du combustible. Les températures et les gradients élevés provoquent un grossissement des grains et la formation de grains colonnaires par migration des porosités pour enfin former un trou central. La zone en périphérie de la pastille quant à elle reste quasiment inaffectée par ces changements. En parallèle à la restructuration, la composition locale de l'oxyde est sujette à des variations : les différents constituants du combustible migrent en effet le long des gradients de température [94]. Le jeu pastille gaine présent dès la fabrication tend lui aussi à se fermer sous irradiation suite à la dilatation et au gonflement de la pastille. Ces évolutions participent à une diminution de la température centrale de l'aiguille.

Les effets thermiques ne sont pas les seuls effets en jeu. La fission des atomes d'uranium et de plutonium engendre la formation de produits de fission, dont certains sont sous forme gazeuse. Ils engendrent un gonflement de la pastille. Les gaz de fission peuvent être relâchés et collectés dans les vases d'expansion [117]. Une conséquence du relâchement des produits de fission gazeux est leur éventuelle accumulation dans le jeu pastille gaine, ce qui peut entrainer une oxydation de la gaine. Le gonflement et la dilatation de la pastille peuvent quant à eux induire des contraintes mécaniques sur cette dernière. Celles-ci restent cependant relativement faibles pour les combustibles oxydes [94; 118].

Une fois le combustible oxyde irradié, il peut être retraité par voie aqueuse afin de récupérer le plutonium. Ce procédé nommé PUREX est notamment employé en France et en Grande Bretagne. Pour cela, le combustible irradié est refroidi quelques années pour atteindre une dose suffisamment faible afin de procéder au recyclage.

L.5.2. Le combustible oxyde sphere-pac

Lorsqu'il s'agit d'insérer des actinides mineurs dans le combustible oxyde, les formes TRISO, sphere-pac, ou vipac peuvent être préférables à la forme pastille. Seule la forme sphere-pac est considérée dans cette thèse. Les combustibles sphere-pac sont composés de sphères d'oxyde compactées par vibration dans le tube gaine[21] – Figure L-1. Ce concept est étudié dans le projet FP-7 PELGRIMM.

La motivation première pour l'utilisation du concept sphere-pac pour des combustibles contenant des actinides mineurs est la simplicité du processus de fabrication: il se déroule entièrement sous forme liquide ce qui évite la manipulation de poudres. Les risques de contamination ou d'ingestion en cas d'accident lors du processus de fabrication peuvent ainsi être réduits. Le processus de fabrication permet de produire des particules parfaitement sphériques. Leur taille peut être facilement contrôlée par adaptation de la taille de l'injecteur et aucun tamisage n'est requis. Une raison supplémentaire à l'utilisation du combustible sphere-pac pour la transmutation est son comportement sous irradiation : le volume de gaz entre les particules permet en effet une meilleure accommodation des gaz de fission et ainsi de réduire la pression sur la gaine [133].

(a)   (b)
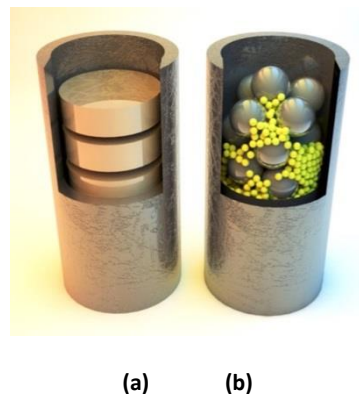
Figure L-1. Combustible pastille (a) et sphere-pac (b) [134].

Les combustibles sphere-pac présentent cependant une mauvaise conductivité thermique en début d'irradiation liée à leur microstructure spécifique : les points de contact entre les sphères sont étroits et peu nombreux, ne permettant pas un bon transfert de chaleur vers le caloporteur. La conductivité thermique se voit cependant améliorée durant l'irradiation puisque les combustibles sphere-pac se restructurent très rapidement sous l'effet des gradients de température élevés (la durée du processus est de l'ordre de quelques heures à quelques jours en fonction de la puissance du réacteur) [133].

---

[21] Plusieurs programmes d'irradiation de combustibles sphere-pac ont été conduits sous forme oxydes (et carbures). On peut notamment citer l'irradiation FUJI [133] ou encore l'irradiation SPHERE [134] actuellement en place dans le réacteur à haut flux aux Pays-Bas [143].

Les sphères qui composent les combustibles sphere-pac sont produites par un procédé sol-gel qui peut être interne ou externe. Ces deux procédés chimiques permettent de précipiter une solution de nitrate de métaux en un hydroxyde d'ammonium métal par ajout d'ammoniac. Pour le processus de gel interne, l'ammoniac est produit par décomposition chimique d'un précurseur, qui a été ajouté préalablement au mélange. Pour le processus de gel externe, l'hydroxyde d'ammonium est ajouté directement à la solution.

Une fois les microsphères de combustible produites, elles sont versées dans le tube gaine et compactées par vibration [131]. Deux techniques peuvent être utilisées pour cela : le remplissage parallèle (les sphères de différentes tailles sont versées simultanément dans le tube gaine) et le remplissage par infiltration (les sphères sont versées séparément, par ordre de taille décroissant). Cette dernière technique donne une distribution plus homogène de microsphères dans l'aiguille et permet d'obtenir des densités de tassement plus élevées, pouvant aller jusqu'à 95% de la densité théorique si plusieurs tailles de sphères sont utilisées lors du remplissage [131; 137].

La conductivité thermique relativement faible des combustibles sphere-pac induit une température centrale de l'aiguille plus élevée que dans le cas du combustible pastille de même densité et peut poser problème au niveau des marges de sûreté [131]. Cet effet est cependant rapidement réduit après le début de l'irradiation grâce à la large restructuration des combustibles sphere-pac : les pores dans la zone la plus chaude de l'aiguille migrent vers le centre et y forment un trou. La zone à proximité du trou ainsi formé est ensuite frittée sous l'effet des températures élevées et une zone de combustible très dense se forme. Une troisième zone peut être distinguée où le frittage est moins prononcé mais la microstructure initiale a disparue. Enfin, la zone périphérique du combustible garde la microstructure initiale (Figure L-2).

Suite aux températures et surfaces spécifiques globalement plus élevées, une proportion de produits de fission gazeux plus importante est relâchée dans le cas du combustible sphere-pac que dans le cas pastille. Les sphères composant le combustible sphere-pac peuvent néanmoins se déformer facilement et les volumes entre les sphères permettent d'accommoder les gaz de fission [138].

Zone II: Strongly sintered area
- Intermediate or final stage of sintering
- Original sphere structure not visible (similar to porous pellet)
- After 1 h temperatures typically >1400 ˚C (sphere diameter 70 µm and pressure 1bar)
- The zone proceeds toward the rim and lower temperatures with longer irradiation time, higher external load or smaller sphere size

Zone I: Center hole
- Emerges later in the life

Zone III: Transition zone
- Between fast and slow sintering areasing
- Moves outward and lower temperatures as irradiation proceeds
- On temperature scale, only 150-200 ˚C wide

Zone IV: Slow sintering
- Initial stage of sintering
- Original sphere structure visible
- Pores interconnected
- Temperature < 800 ˚C
- Irradiation creep dominates

Figure L-2. Schéma d'un combustible sphere-pac restructuré [138].

L.5.3. Conclusions

Une large variété de combustibles peut être utilisée pour les réacteurs à neutrons rapides. Tous présentent des avantages et des inconvénients en termes de fabrication, de comportement sous irradiation ou encore lors du recyclage du combustible usé. En Europe, le combustible oxyde reste le choix préférentiel dû au large retour d'expérience sur les réacteurs thermiques. Au sein du projet FP7-PELGRIMM, deux formes mécaniques sont étudiées : le combustible sphere-pac et le combustible pastille. Les procédés de fabrication, les performances sous irradiation ainsi que les propriétés fondamentales des combustibles sphere-pac doivent encore être étudiés en détail, de même que leur comportement en cas de transitoires accidentels. Dans ce cadre, les différents codes employés dans le projet FP7-PELGRIMM doivent être modifiés afin de prendre en compte les spécificités de ces combustibles.

L.6. Une méthodologie innovante pour simuler les effets de dilatation thermique du cœur dans les codes à cinétique spatiale

Ce chapitre détaille les modèles développés durant la thèse pour la prise en compte de la contre-réaction induite par la dilatation axiale et radiale du cœur pour des codes employant une cinétique spatiale et un maillage eulérien comme le code SIMMER. Cette contre-réaction n'était pas prise en compte dans SIMMER jusqu'à présent puisque ce code était développé pour des cœurs dans une configuration largement dégradée, où cette contre-réaction jouait un rôle négligeable. Cependant, si l'accident est simulé dès l'évènement initiateur avec le code SIMMER, il devient important de prendre en compte cette contre-réaction, spécialement pour les nouveaux design de cœurs de réacteurs présentant un effet de vidange sodium très faible, et un équilibre délicat entre les différentes contre-réactions.

L.6.1. La théorie du transport de neutrons

Cette partie détaille l'équation du transport de neutrons dépendante du temps et donne une explication aux différents termes composant l'équation. De même, l'équation régissant l'évolution temporelle des précurseurs de neutrons retardés y est décrite.

Le cas particulier de l'équation stationnaire est ensuite analysé et le concept de réacteur critique associé est introduit.

L.6.2. Méthodes de résolution de l'équation du transport de neutrons dépendante du temps

L'équation du transport dépendante du temps ne peut être résolue analytiquement sauf pour des cas très simplifiés. De manière générale, on résout l'équation numériquement en introduisant une discrétisation angulaire, spatiale, énergétique et temporelle.

Dans le code SIMMER, la variable angulaire est discrétisée via la méthode des ordonnées discrètes S_N qui utilise un set de directions discrètes associées à des poids. La composante spatiale est quant à elle discrétisée par une méthode de différences finies.

La variable énergie est ensuite discrétisée en groupes d'énergie. Pour chaque groupe d'énergie, les grandeurs représentatives, comme le flux et les sources, sont obtenues par intégration sur l'intervalle énergétique. Les sections efficaces multi-groupes sont quant à elles obtenues en gardant constants les taux de réactions. Ainsi, l'équation du transport peut être réécrite pour chaque groupe d'énergie.

Enfin, la variable temps est également discrétisée. Pour cela, différentes méthodes peuvent être appliquées.

On peut tout d'abord citer la méthode directe qui discrétise le temps par une méthode implicite. Cette méthode requiert cependant un temps de calcul important et pour des analyses de transitoires, des méthodes permettant l'utilisation d'un pas de temps plus grand lui sont généralement préférées, comme par exemple la méthode quasi-statique améliorée.

Celle-ci se base sur un principe de factorisation en espace et en temps avec une fonction de forme dépendante de l'espace et du temps et une fonction d'amplitude dépendant du temps seulement. Elle repose sur une séparation des fluctuations rapides et lentes du flux (par rapport au temps) : la fonction amplitude reflète le comportement rapide en temps alors que la fonction de forme varie lentement en fonction du temps. Deux échelles de temps sont alors considérées : une échelle de temps grossière sur laquelle on évalue la forme et une échelle de temps très fine sur laquelle on évalue l'amplitude. On considère donc un système couplé d'équations qui peut être résolu par méthode itérative.

La méthode adiabatique repose sur le même principe que la méthode quasi statique améliorée mais la fonction de forme est mise-à-jour durant le transitoire pour des pas de temps plus larges en résolvant une équation aux valeurs propres.

Enfin, la méthode de la cinétique point néglige toute dépendance temporelle du flux de forme (i.e. également dans l'équation du flux de forme) et le flux de forme initial est utilisé sur toute la durée du calcul. Cette dernière méthode est généralement appliquée dans les codes de calculs dédiés à l'analyse de la phase d'initiation de l'accident et permet de donner une idée de l'évolution de ce dernier.

La précision de la solution de l'équation du transport dépend des différentes méthodes et de la largeur des pas de temps utilisés.

L.6.3. La dilatation thermique du cœur de réacteur

Durant une situation accidentelle aussi bien que durant le fonctionnement nominal du réacteur, la température du cœur de réacteur est soumise à des variations qui impacteront ses dimensions et les densités des matériaux qui le composent. C'est ce qu'on appelle la dilatation thermique du cœur que l'on pourra sous-diviser en deux contributions : la dilatation radiale et la dilatation axiale.

La dilatation radiale du cœur est causée principalement par la dilatation du sommier qui a lieu lorsque la température en entrée du cœur varie. En plus du sommier, la dilatation de la grille supérieure peut également contribuer à la dilatation radiale du cœur. En effet, la dilatation thermique de ces deux éléments détermine la variation du pas entre les assemblages à différentes positions axiales, ce qui joue un rôle crucial sur la réactivité du cœur.

Lorsque ces structures voient leurs températures augmentées, le rayon du cœur est augmenté et la concentration du matériau fissile qui le compose est diminuée ce qui induit une augmentation des

fuites axiales. La contre-réaction est donc négative dans ce cas. Le fait d'avoir plus de caloporteur entre les assemblages combustibles ajoute de l'anti-réactivité.

Si, au contraire, les assemblages combustibles sont plus proches les uns des autres, i.e. on observe une compaction du cœur, les fuites axiales sont réduites et la contre-réaction sera positive.

La dilatation axiale du combustible quant à elle dépend de l'état du jeu combustible-gaine traditionnellement présent dans les aiguilles oxydes neuves et donc du taux d'irradiation. Si le jeu est ouvert, le combustible pourra se dilater librement. Si au contraire le jeu est fermé, la gaine retiendra le combustible et ralentira le processus de dilatation. La dilatation axiale de l'aiguille augmente la hauteur du cœur et par conséquent les fuites radiales. La contre-réaction sera donc négative.

Ces effets de dilatations de cœur sont d'autant plus importants sur les cœurs actuels présentant un équilibre délicat entre les différentes contre-réactions.

Pour modéliser ces effets de dilatations dans SIMMER, les coefficients d'expansion linéaires sont appliqués. Radialement, deux options ont été implémentées dans le code à savoir cylindrique ou conique. Dans le cas cylindrique, seule la dilatation radiale des cellules du sommier est considérée et calculée à partir des températures respectives. Toutes les cellules se trouvant au-dessus du sommier sont soumises à la même dilatation que celle du sommier. Dans le cas conique, la dilatation radiale des cellules de la grille supérieure est également considérée et les cellules se trouvant entre sommier et grille supérieure voient leurs dimensions radiales dilatées linéairement entre les deux.

Afin de calculer la dilatation axiale, la température du combustible ou de la gaine (selon que le jeu soit fermé ou ouvert) est considérée pour chaque cellule, en première approximation.

Une fois les dimensions radiales et axiales après dilatation de chaque cellule connues, les concentrations de chaque matériau sont calculées par conservation de la masse, sauf pour le caloporteur où la masse est augmentée (i.e. la densité macroscopique reste inchangée).

Les dimensions et les concentrations de chaque cellule après dilatation du cœur sont maintenant connues. SIMMER ne peut pas prendre directement en compte ces changements de dimensions puisqu'il emploie un maillage eulérien. Le modèle développé permet de garder ce maillage et de prendre en compte les effets dus à la dilatation via les concentrations seulement.

Les contre-réactions dues à la dilatation thermique du cœur sont calculées via la méthode des perturbations au premier ordre qui permet de traiter de façon indépendante les effets venant de chaque cellule et de superposer ces effets pour obtenir l'effet global. Cette hypothèse a donc dû être validée.

Les propriétés de linéarité et d'additivité des effets en réactivité liés à la dilatation thermique du cœur ont été testées pour une dilatation uniforme (i.e. même dilatation selon une direction) et non-uniforme. Pour cela, le code ERANOS a été utilisé [157]. Ce code est un code neutronique déterministe qui emploie la méthode des ordonnées discrètes en 2D et nodale en 3D. Un modèle simplifié du cœur ESFR a été utilisé pour cela. Les effets de linéarité et d'additivité ont été démontrés dans les cas uniformes et non-uniformes, en considérant une seule ou deux zones d'enrichissement, une dilatation du sodium différente ou encore 1, 11 ou 33 groupes d'énergies.

La méthodologie implémentée dans SIMMER durant la thèse repose sur une séparation de l'effet de dilatation en deux effets : un effet venant d'une dilatation homogène i.e. tous les matériaux, y compris le sodium, sont sujets à la même dilatation et un effet venant de la variation relative entre la dilatation des matériaux solides et du sodium. Afin de démontrer l'importance de simuler avec précision l'effet venant du sodium, le cœur simplifié a été analysé pour des dilatations uniformes et non-uniformes.

L.6.4. Une méthodologie innovante pour prendre en compte les contre-réactions dues à la dilatation du cœur pour les codes employant la cinétique spatiale.

La méthodologie développée pour tenir compte des effets en réactivité de dilatation du cœur repose sur le « principe d'équivalence ». Ce principe a été publié en 1959 [160] et a suscité un regain d'intérêt récemment [161]. Le principe permet de prendre en compte neutroniquement des effets de dimensions via des variations de sections efficaces (i.e. de concentrations).

Ce principe stipule que si l'on multiplie toutes les dimensions d'une configuration de cœur par un même facteur et que l'on divise simultanément toutes les sections efficaces par ce même facteur, la nouvelle configuration ainsi obtenue aura exactement le même état de réactivité que la configuration initiale i.e. aucun effet en réactivité n'est observé suite à cette manipulation.

Dans le cas d'une dilatation thermique uniforme et isotrope (i.e. même dilatation pour les toutes les dimensions dans toutes les directions), la nouvelle configuration pourra avoir les dimensions initiales avec des concentrations modifiées et refléter l'effet de la dilatation.

Dans le cas d'une dilatation uniforme non-isotrope (i.e. dilatations différentes pour les dimensions axiales que pour les dimensions radiales par exemple), il ne sera pas possible de revenir aux dimensions initiales tout en gardant l'effet en réactivité. Il faudra faire le choix de revenir sur la dimension axiale ou radiale et utiliser une étape supplémentaire pour prendre en compte la totalité de l'effet de dilatation.
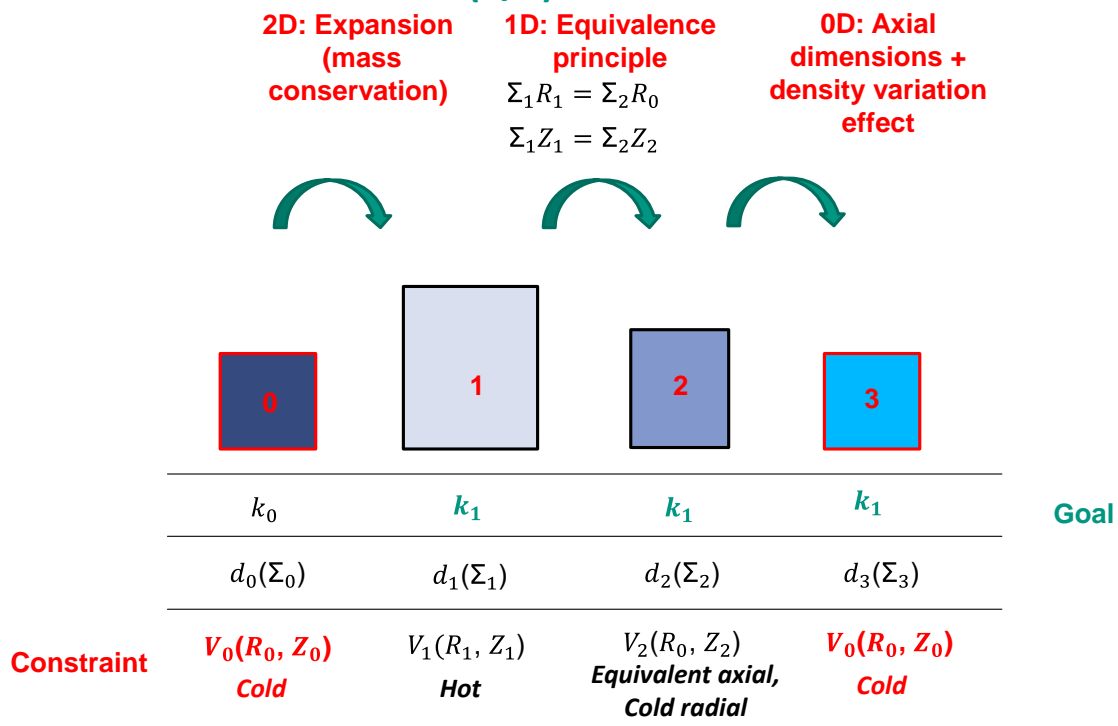
2D: Expansion (mass conservation)

1D: Equivalence principle
$$\Sigma_1 R_1 = \Sigma_2 R_0$$
$$\Sigma_1 Z_1 = \Sigma_2 Z_2$$

0D: Axial dimensions + density variation effect

	0	1	2	3	
	k_0	k_1	k_1	k_1	Goal
	$d_0(\Sigma_0)$	$d_1(\Sigma_1)$	$d_2(\Sigma_2)$	$d_3(\Sigma_3)$	
Constraint	$V_0(R_0, Z_0)$ *Cold*	$V_1(R_1, Z_1)$ *Hot*	$V_2(R_0, Z_2)$ *Equivalent axial, Cold radial*	$V_0(R_0, Z_0)$ *Cold*	

Figure L-3. Méthodologie DENSF pour la prise en compte des contre-réactions dues à la dilatation thermique du cœur.

Une comparaison entre les cas réellement dilatés et la configuration équivalente (i.e. obtenue en appliquant le principe d'équivalence) est proposée. Les calculs montrent que, dans les deux cas, l'effet en réactivité dû à la dilatation thermique du cœur diffère de seulement 5% pour différentes dilatations homogènes uniformes isotropes. Dans le cas de dilatations non-uniformes, par exemple dans différentes zones du cœur d'enrichissement homogène, un écart de 2% est observé.

Il est démontré dans cette thèse que la méthodologie basée sur le principe d'équivalence est applicable pour des cas proches de dilatations uniformes, i.e. dans les mêmes conditions que celles des codes comme CATHARE. Pour des configurations plus complexes, la méthode nécessite d'être améliorée.

En se basant sur le principe d'équivalence, une première méthode a été améliorée. Elle consiste à appliquer le principe d'équivalence dans un premier temps et un coefficient global de concentration (DENSF) pour traiter l'effet de dilatations non-uniformes dans un second temps Figure L-3. Ce coefficient est calculé initialement et appliqué durant le calcul de transitoire.

La méthodologie consiste à traiter les dilatations thermiques via des variations de sections efficaces (i.e. de concentrations) uniquement. Elle permet ainsi d'employer le maillage eulérien de SIMMER tout en ayant la capacité de refléter les effets de la dilatation du cœur.

La première étape consiste à calculer théoriquement les variations de dimensions et de concentrations liées à la dilatation thermique. Puis, le principe d'équivalence est appliqué et l'on retrouve, dans le cas général, une dilatation uniforme axiale uniquement (le choix de revenir sur une dilatation axiale seulement est arbitraire) avec des concentrations que l'on appellera concentrations équivalentes. Une troisième étape est ensuite introduite afin de pouvoir revenir axialement sur les dimensions initiales. Pour cela, un facteur de concentration est calculé et défini comme étant le ratio entre a) l'effet en réactivité dû à une variation de x% de la dimension axiale de tout le réseau obtenu

par calcul direct et b) l'effet en réactivité dû à la variation de concentration de x% obtenue par un calcul en théorie des perturbations du premier ordre. Les concentrations équivalentes sont alors modifiées par un facteur tenant compte du facteur de concentration [144].

Cette méthodologie a été validée pour le cœur CP-ESFR WH dans le cas de dilatations homogènes uniformes isotropes et non-isotropes, après avoir confirmé l'indépendance de l'effet Doppler et de vidange de l'effet en dilatation et vice versa. Les résultats montrent un accord entre le cas réellement dilaté et le cas où la méthodologie a été appliquée avec une erreur relative de l'ordre de 11%, ce qui reste dans l'intervalle d'incertitudes pour les effets en réactivité [198; 199]. La composante non-homogène de l'effet de la dilatation (i.e. due au caloporteur qui n'est en général pas soumis à la même dilatation que les matériaux solides) est prise en compte directement dans le calcul du flux de forme. Les résultats pour les cas de dilatations non-homogènes avec ce traitement du sodium correspondent aux cas réellement dilatés avec une incertitude relative de l'ordre de ~15%.

La méthode précédente a à nouveau été améliorée via l'introduction de facteurs de concentration fonctions de la composante radiale. En effet, dans un cœur de réacteur, on observe une distribution radiale de puissance et par conséquent un poids différent pour les contributions provenant des différents anneaux de combustible à l'effet de dilatation total. Les résultats dans le cas de de dilatations uniformes sont concluants.

Dans le cas de dilatations non-uniformes, l'écart relatif entre les cas utilisant le modèle développé et les calculs de référence augmente et une troisième méthodologie basée sur la méthode directe a été testée avec le code de calcul ERANOS. Les résultats sont prometteurs [165].

Enfin, la méthodologie DENSF a été testée pour les calculs transitoires. Le cœur CP-ESFR WH a été simulé pour un accident de perte de débit primaire. Deux cas de dilatation axiale ont été considérés à savoir une dilatation due à la dilatation de la gaine ou du combustible. Les calculs démontrent un délai dans la progression de l'accident et une réduction du pic de puissance comparé aux cas ne prenant pas en compte cette contre-réaction. Le modèle a également été testé et validé avec succès dans le cadre d'un benchmark international (IAEA-CRP) sur le cœur EBR-II [200] .

L.6.5. Conclusions

Suite aux développements effectués durant cette thèse, le code SIMMER a la capacité de simuler la phase d'initiation d'un accident avec plus de précision. Le code peut maintenant tenir compte des contre-réactions provenant de la dilatation du cœur qui sont de haute importance en début d'accident dans les cœurs à faible effet de vidange comme le cœur CONF2.

L.7. Une nouvelle caractéristique du code SIMMER-III : les combustibles sphere-pac innovants.

L'une des différences les plus prononcées entre les combustibles oxyde pastilles et sphere-pac est leur conductivité thermique respective. Cette propriété influence directement le transfert thermique vers le caloporteur. Une recherche bibliographique sur les différents modèles de conductivité possiblement adaptables au combustible sphere-pac s'est imposée. On peut citer le modèle de conductivité de Philipponneau pour les combustibles pastilles MOX [173], le modèle de Schulz pour les matériaux poreux [175], le modèle de Hall et Martin pour les lits de poudres [176], le modèle de Maxwell pour les matériaux composites [180] ou encore celui de Godbee pour les poudres [179]. Une comparaison de ces différents modèles a révélé que ceux de Schulz [175] et de Hall et Martin [176] sont les plus adaptés à la simulation de la conductivité thermique des combustibles sphere-pac (Figure L-4).
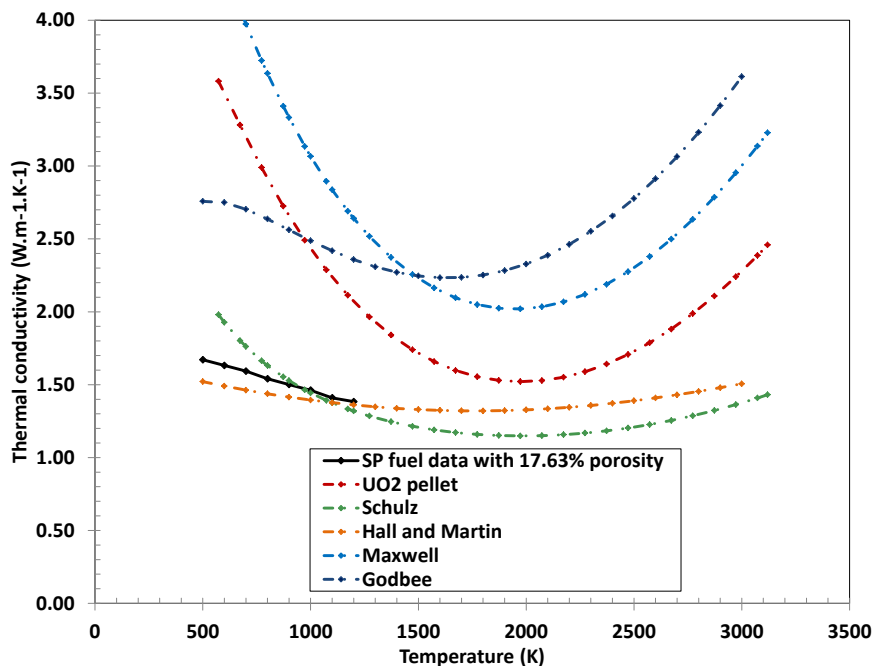

Figure L-4. Conductivité thermique de combustible sphere-pac (SP) UO₂ (2 fractions de sphères de 1200 µm et 35 µm en diamètre, 0% de striction, 1 bar de pression d'Hélium) pour différentes corrélations et comparaison avec les données tirées de [181].

Une fois les modèles les plus adéquats déterminés, les corrélations à implémenter dans SIMMER ont été établies. Pour cela, on a différencié l'état du combustible en début de vie, et son état après trois cycles d'irradiation. Ces états diffèrent d'autant plus que le combustible sphere-pac est soumis à une large restructuration durant les premières heures ou jours en réacteur.

Pour le combustible neuf, trois cas ont été considérés (Figure L-5) : l'aiguille de combustible pastille du CP-ESFR, l'aiguille de combustible sphere-pac et un troisième cas avec une aiguille composée de pastilles, de même densité de remplissage de la gaine que le combustible sphere-pac, ne présentant ni jeu pastille-gaine ni trou central. La comparaison des deux premiers cas nous informe sur l'impact

à la fois de la géométrie interne de l'aiguille et de la conductivité thermique. La comparaison des deux derniers cas révèle l'impact de la différence entre les conductivités thermiques uniquement.

| (a) | (b) | (c) |

Hole + gap
Fuel porosity 5%
Smear porosity 11.20%

No hole + no gap
Smear porosity 16.59%
Porosity for conductivity calculation 17.63%

No hole + no gap
Smear porosity 16.59%
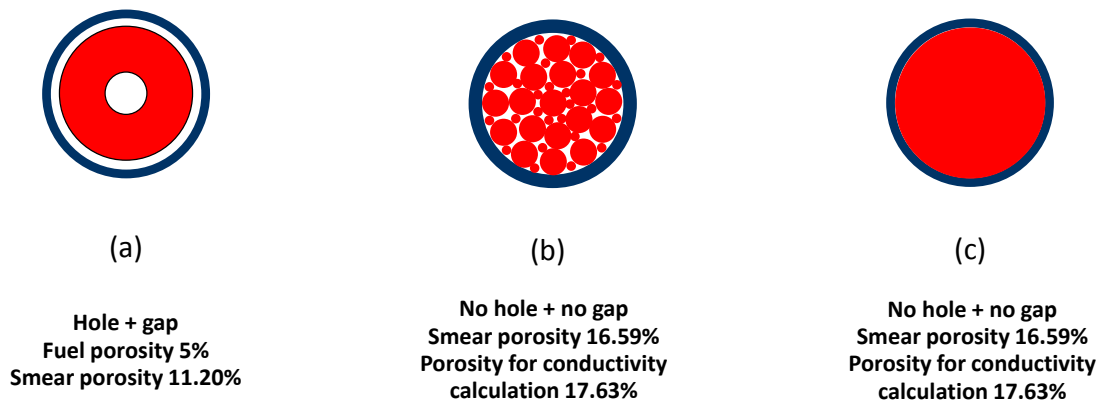**Porosity for conductivity calculation 17.63%**

Figure L-5. Cas considérés pour le CP-ESFR en début de vie : (a) design d'aiguille standard (b) aiguille de combustible sphere-pac non-restructuré (c) aiguille de combustible pastille pleine.

Pour le combustible irradié durant trois cycles, deux cas ont été considérés (Figure L-6). Leurs propriétés sont décrites dans le Tableau 1.
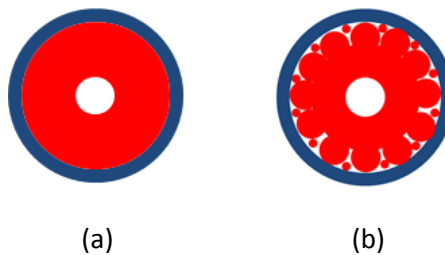

| (a) | (b) |

Figure L-6. Aiguille de combustible pastille après trois cycles d'irradiation (a) Aiguille de combustible sphere-pac après trois cycles d'irradiation (b)

Tableau 1. Propriétés des combustibles pastilles et sphere-pac MOX du CP-ESFR après trois cycles d'irradiation.

	Standard MOX pellet pin	Restructured MOX sphere-pac pin
Fuel smear porosity (*%*)	16.59	16.59
Fuel porosity and other characteristics	Fuel porosity 7.5%	2 fuel zones: restructured and non-restructured
		2 sphere diameters: 1200 µm or 35 µm
		Restructured zone porosity 7.5%
Central hole diameter (*mm*)	3.05	2.92 (30% of cladding inner diameter)
Burnup (*at%*)	6	6
Oxygen over metal ratio	2	2
Gap state	Closed gap	No gap

Les corrélations de conductivité thermique en début de vie et après trois cycles d'irradiation pour les deux types de combustibles ont été établies et sont représentées en Figure L-7.

Une étude sur l'importance de l'inclusion de la porosité dans la détermination de la longueur de pénétration thermique a également était conduite. Les résultats ne sont que peu impactés même dans le cas des combustibles sphere-pac, présentant une porosité élevée en comparaison au combustible pastille (16.59% au lieu de 5%).
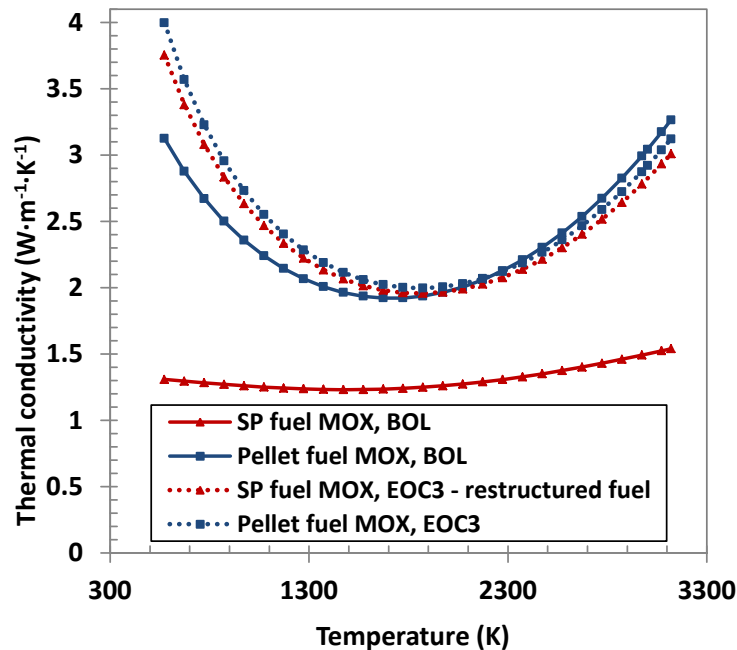

Figure L-7. Conductivités thermiques utilisées pour les combustibles sphere-pac (SP) et pastille MOX dans le cas du CP-ESFR, en début de vie (BOL) et après trois cycles d'irradiation (EOC3).

L.8. Analyses de sûreté avec le code SIMMER-III

Durant le projet CP-ESFR, le cœur WH a été dûment analysé avec des aiguilles pastilles [9]. Le cœur CONF2 quant à lui n'a pas profité d'une analyse de sûreté étendue. Une première étape a donc été l'analyse de ce dernier chargé avec des aiguilles pastilles afin de démontrer l'effet de l'élargissement du plénum sodium sur l'évolution de l'accident. Une deuxième étape a consisté à analyser les cœurs chargés avec des combustibles sphere-pac afin de les comparer aux cœurs chargés avec du combustible pastille. Pour cela, des études à l'état nominal ont été effectuées dans un premier temps, suivies dans un deuxième temps d'analyses d'accidents de débit primaire.

L.8.1. Modélisation

La modélisation des cœurs CP-ESFR WH et CONF2 avec le code SIMMER-III est rappelée dans cette section ainsi que les principales différences entre les deux cœurs. La modélisation 2D considérée est RZ.

L.8.2. Conditions nominales

Le cœur WH a été analysé pour les cas décrits en Figure L-5 et en Figure L-6. En début de vie, comme attendu, les températures moyennes dans les aiguilles sphere-pac sont plus élevées que dans les aiguilles pastilles du fait de leur conductivité thermique plus faible (Figure L-8). On observera une fonte du combustible dans au moins trois anneaux de combustibles dans le cas des aiguilles sphere-pac à l'état nominal.

Après trois cycles d'irradiation, le combustible a eu suffisamment de temps pour se restructurer et les distributions de températures sont très similaires dans le cœur pastille et le cœur sphere-pac. Ceci était attendu de par les conductivités thermiques très similaires à ce stade de l'irradiation. Les températures maximales restent largement en deçà des limites à la fonte (marge de 1380 K).
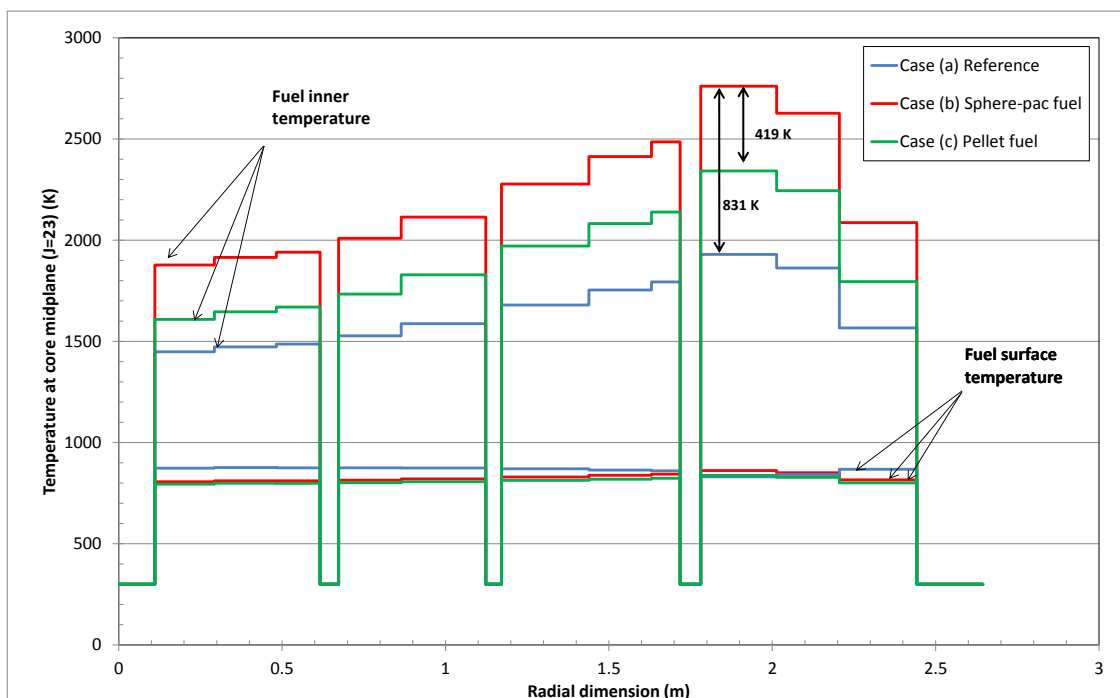

Figure L-8. Distribution radiale de température dans le cœur CP-ESFR WH en début de vie pour différents combustibles.

Le cœur CONF2 montre une distribution de température semblable au cœur WH et amène à des conclusions similaires.

A partir de ces états nominaux, une étude sur les accidents de perte de débit primaire a été conduite.

L.8.3. Simulation d'un accident de perte de débit primaire

Le but de cette étude est de démontrer des éventuelles différences dans le comportement des combustibles sphere-pac et pastilles en situation accidentelle afin de déterminer les besoins en modélisation pour ces combustibles. Ainsi, dans un premier temps, les calculs sont effectués sans prendre en compte la contre-réaction venant de la dilatation thermique du cœur (approche conservative).

Le cœur WH montre une fonte totale du cœur, que ce soit avec des aiguilles sphere-pac ou pastilles (Figure L-9). L'analyse du cœur WH chargé en combustible sphere-pac sert de base pour la compréhension des différences comportementales avec le combustible pastille. Le cœur CONF2 i.e. la version améliorée du cœur WH étant le cœur à l'étude dans le projet FP-7 PELGRIMM, le même accident de perte de débit primaire est analysé pour ce cœur.
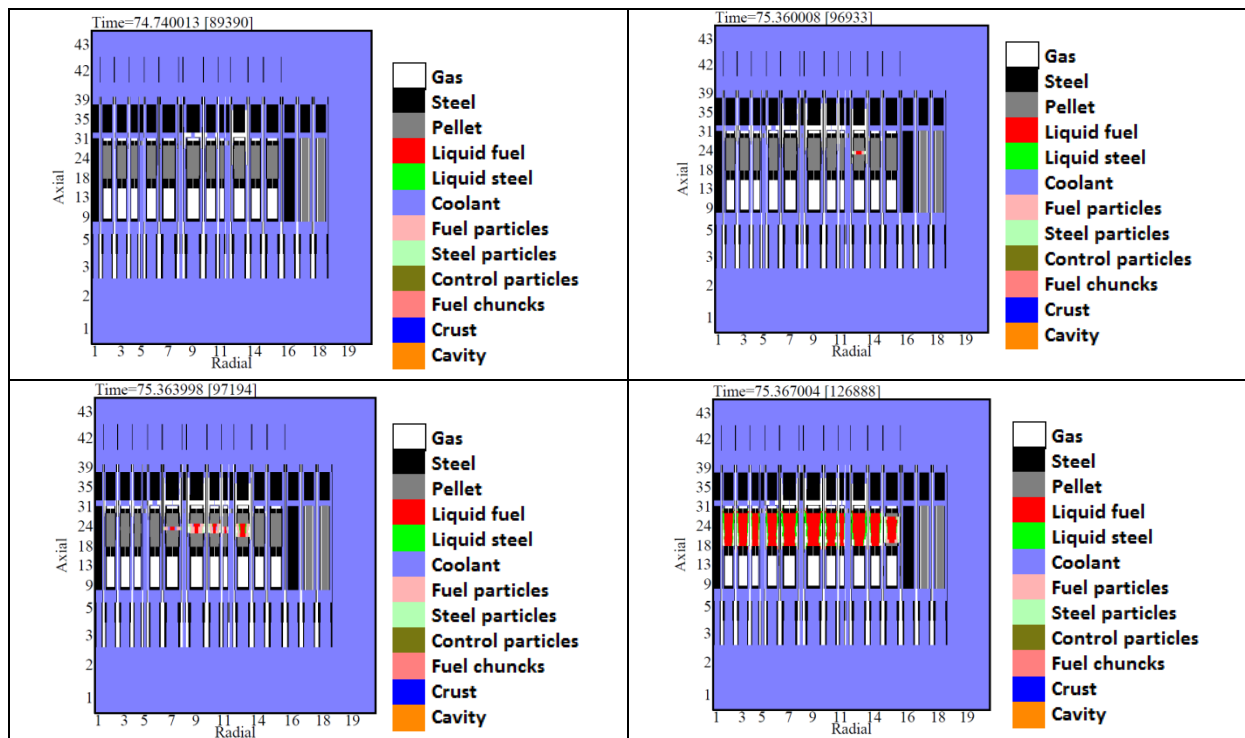

Figure L-9. Distributions des différents matériaux durant un accident de perte de débit primaire dans le cœur WH à l'équilibre (après trois cycles d'irradiation).

En premier lieu, le cœur CONF2 chargé en combustible pastille est analysé afin de démontrer l'amélioration du comportement de sûreté du cœur dû à l'élargissement du plénum sodium. En début de vie, l'effet de vidange sodium étendu est en effet de +496 pcm pour le cœur CONF2 au lieu de +1211 pcm pour le cœur WH. La Figure L-11 décrit l'évolution de la puissance nominale normalisée et de la réactivité durant cet accident de perte de débit primaire. La criticité prompte n'est jamais atteinte pour ce cœur.

La distribution de matériaux durant l'accident peut être observée en Figure L-10. Le caloporteur commence à vaporiser dans les anneaux les plus chauds en zone externe du cœur (le profil de

puissance du cœur est très piqué dans la zone de cœur externe). Le vide sodium dans le plénum induit alors une première baisse de réactivité qui contre l'effet de vide sodium du cœur fissile. L'effet de vidange étant globalement positif, un pic de réactivité et de puissance est observé et les aiguilles se rompent (la rupture de la gaine en étant la cause). Une quantité limitée mais suffisante de combustible est alors éjectée de la zone fissile du cœur par entrainement vapeur et amène le cœur à un état largement sous-critique (-16 \$). On observe même un remplissage de certaines zones. L'évolution à long terme de l'accident dépend de l'évacuation de la puissance résiduelle. Etant donné que le combustible reste en grande partie dans la zone fissile, des re-criticités ne sont pas à exclure en cas de fonte progressive du cœur sous l'effet de la puissance résiduelle. Ces effets de fonte sont cependant longs et des compactions rapides induisant des rampes de réactivité importantes sont moins probables.

L'analyse du cœur CONF2 chargé avec du combustible sphere-pac non–restructuré montre une évolution similaire. Les aiguilles se rompent cependant 9 s plus tôt que dans le cas pastille car localement le combustible est déjà fondu à l'état nominal.
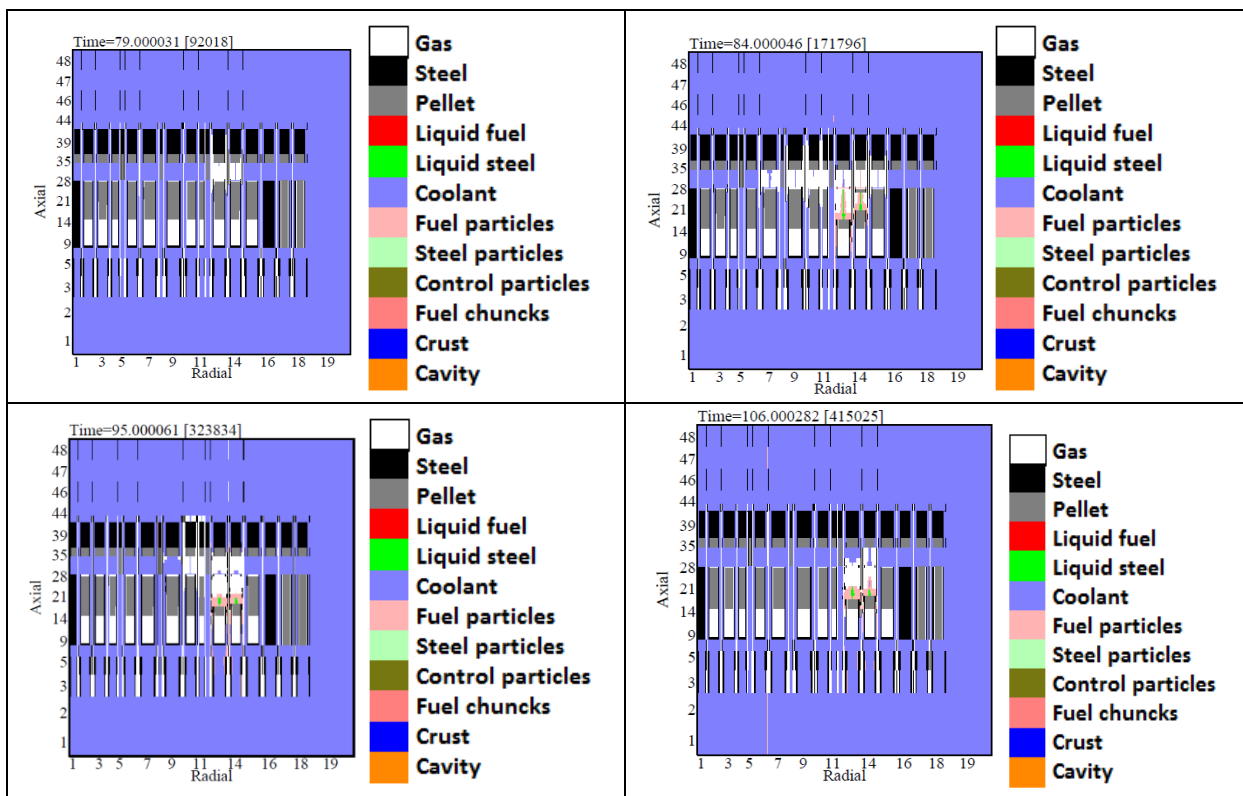

Figure L-10. Distributions de matériaux durant un accident de perte de débit primaire dans le cœur CONF2 pastille en début de vie.
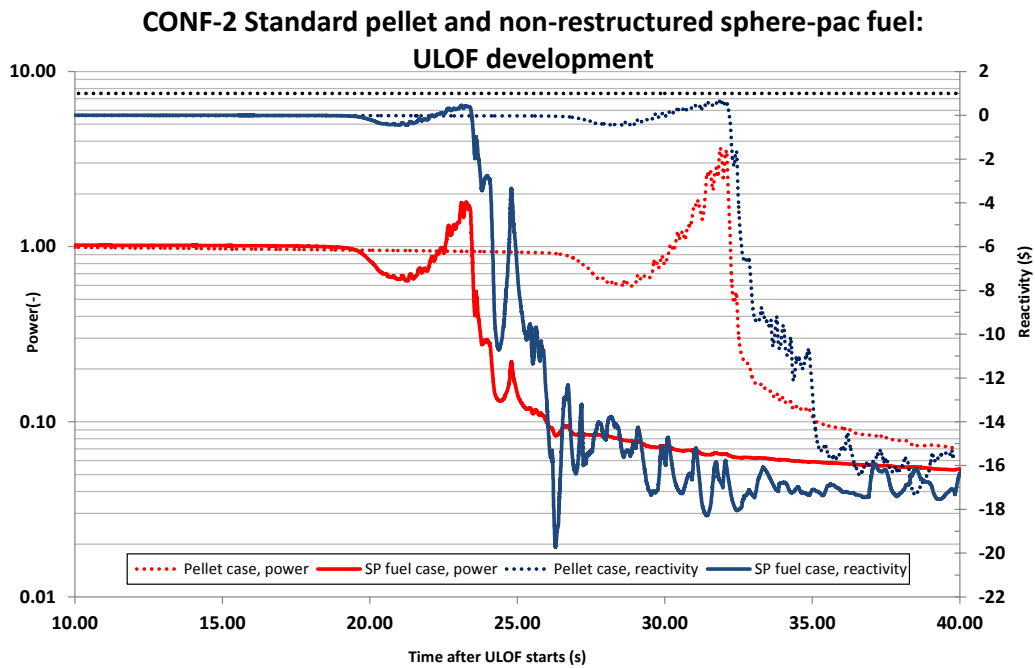
Figure L-11. Evolution de la réactivité et de la puissance normalisée durant un accident de perte de débit primaire dans le cœur CONF2 en début de vie, contenant soit des aiguilles pastilles (pointillés) soit des aiguilles sphere-pac (traits pleins).

Une comparaison du cœur CONF2 chargé avec du combustible sphere-pac restructuré est montrée en Figure L-12. Le pic de puissance dans le cas du cœur CONF2 avec un combustible restructuré est au plus bas à cause de la conductivité thermique élevée et de l'existence du trou central. La rupture de la gaine entraine une redistribution du combustible – à l'état de particules – vers la partie basse du cœur. Une quantité plus faible de combustible est éjectée du cœur comparé au cas du combustible non-restructuré et par conséquent l'état final du cœur est moins sous-critique (-8 $ au lieu de -16$).
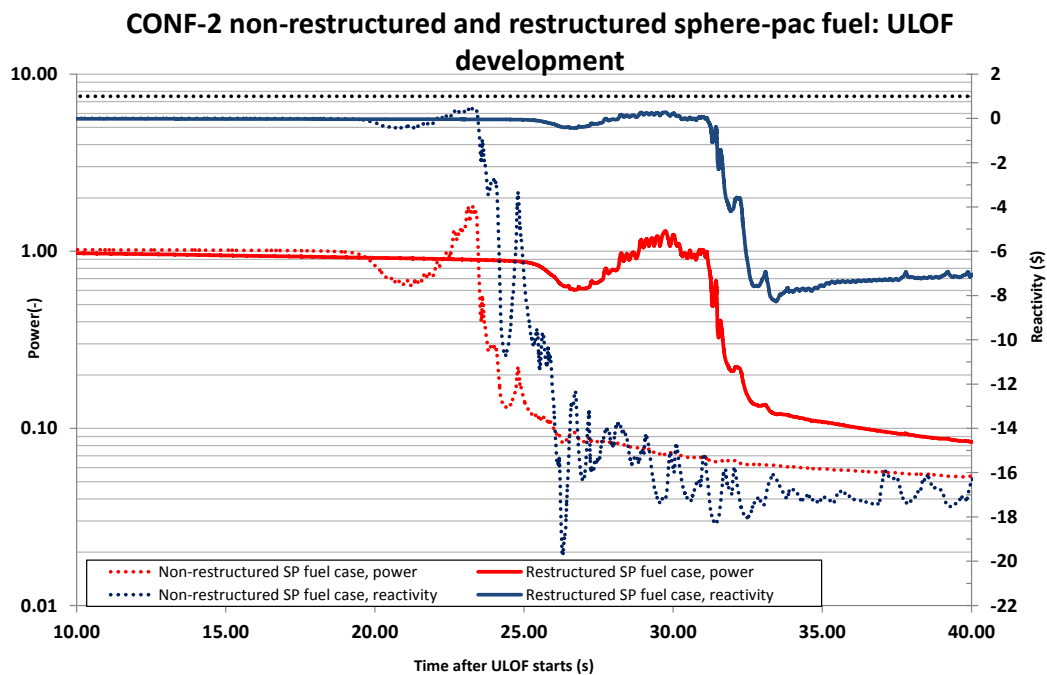

Figure L-12. Evolution de puissance et de réactivité durant un accident de perte de débit primaire dans le cas du cœur CONF2 en début de vie contenant du combustible sphere-pac restructuré (traits pleins) ou non restructuré (pointillés).

En conclusion, toutes les simulations convergent vers un transitoire très doux en comparaison au transitoire observé dans le cœur WH, démontrant ainsi l'efficacité du plénum sodium pour limiter la propagation de l'accident. De même, les simulations démontrent que l'utilisation du combustible sphere-pac à la place du combustible pastille ne présente pas de problème d'un point de vue de la sûreté.

Dans le cas du cœur CONF2 à l'équilibre, contenant du combustible irradié durant trois cycles, les analyses démontrent un comportement similaire pour les deux combustibles, dû à la conductivité thermique très similaire - Figure L-13.
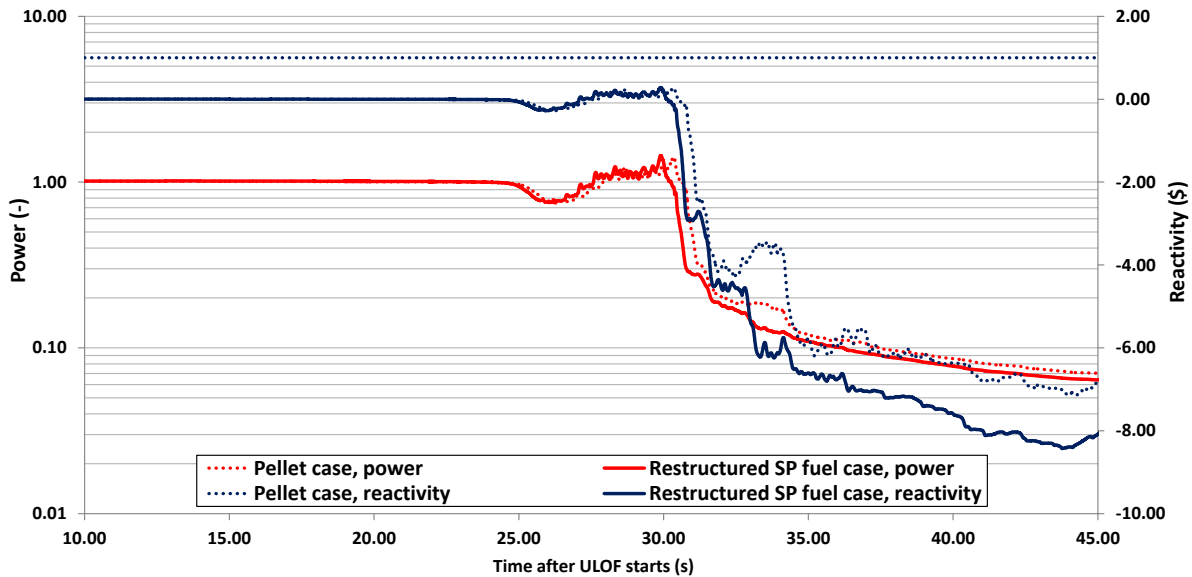

Figure L-13. Evolution de puissance et de réactivité durant un accident de perte de débit primaire dans le cœur CONF2 à l'équilibre chargé avec du combustible pastille (pointillés) ou sphere-pac restructuré (traits pleins) irradié durant trois cycles.

L.8.4. Impact d'un ajout d'actinides mineurs dans le combustible sur l'évolution de l'accident.

Les combustibles sphere-pac sont une bonne alternative au combustible pastille lorsqu'il s'agit d'insérer des actinides mineurs – notamment l'américium - dans le combustible, en grande partie grâce à la simplicité de leur processus de fabrication (entièrement sous forme liquide ce qui évite la manipulation de poudres) et de leur comportement sous irradiation (le volume de gaz entre les sphères permet en effet une meilleure accommodation des gaz de fission et ainsi une réduction de la pression sur la gaine). Il est donc naturel, une fois les analyses sur le combustible sphere-pac MOX terminées, d'analyser un cœur contenant du combustible MOX dans lequel on a ajouté de façon homogène de l'américium.

Cet ajout détériore davantage les coefficients de sûreté et l'effet de vidange sodium étendu du plénum est à nouveau augmenté, atteignant des valeurs proches de celles du cœur WH (en début de vie) avec 4% en masse. De même, l'effet Doppler est réduit en valeur absolue.

La Figure L-14 montre l'évolution de la puissance et de la réactivité lors d'un accident de perte de débit primaire dans le cœur CONF2 chargé avec du combustible sphere-pac irradié durant trois cycles, contenant initialement 0%, 2% ou 4% en masse d'américium dans la zone nourricière.

On peut y observer que, plus la teneur en américium est élevée, plus l'excursion de puissance a lieu tôt et est prononcée, ce qui est en lien avec la détérioration des coefficients de sûreté.

Dans le cas d'une teneur en américium de 2% en masse initialement, le transitoire est relativement moins énergétique. Cependant, les contre-réactions positives prévalent et le cœur atteint un état critique prompt avec un pic de puissance 3000 fois supérieur à la puissance nominale. Ceci peut notamment être expliqué par l'effet de vidange sodium largement positif (+1290 pcm). Il est intéressant de noter qu'à aucun moment le combustible fond.

Dans le cas d'une teneur de 4% en masse d'américium en début de vie, le cœur subit une excursion de puissance critique prompte, entrainant la dégradation du cœur et une fusion complète du combustible – Figure L-15. On peut conclure que l'effet de vidange sodium accru et la réduction de l'effet Doppler contrebalancent largement l'effet du plénum sodium et la quantité de combustible éjectée de la zone fissile est insuffisante pour mettre fin à l'accident.

Il a par conséquent était démontré que le comportement de sûreté prometteur du cœur CONF2 est uniquement valable en début de vie. Sous l'effet de l'irradiation et sous l'effet d'un ajout d'actinides mineurs, un accident de fusion du cœur n'est pas à exclure et des optimisations supplémentaires du design du cœur sont nécessaires.
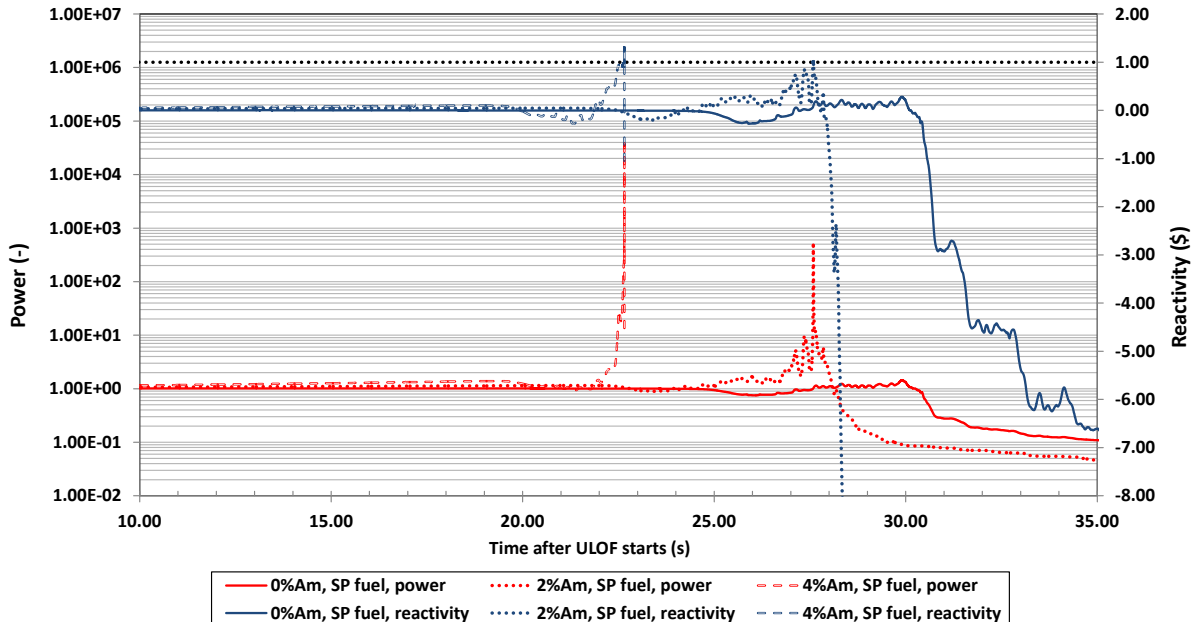

Figure L-14. Evolution de puissance et de réactivité durant un accident de perte de débit primaire dans le cœur CONF2 à l'équilibre. Combustible sphere-pac restructuré, avec une teneur en américium de 0%, 2% ou 4% en masse en début de vie.
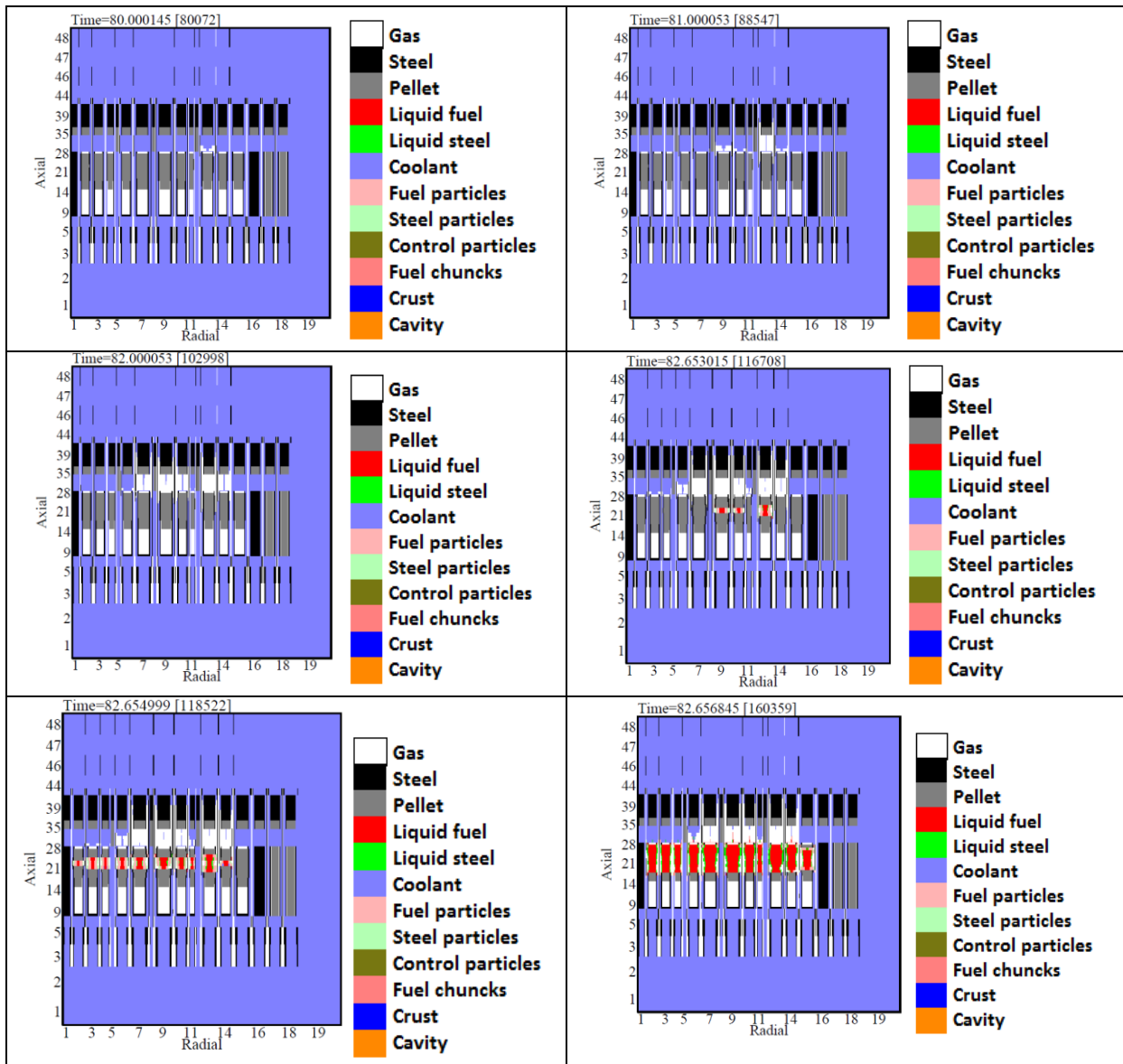
Figure L-15. Distribution de matériaux durant un accident de perte de débit primaire dans le cœur CONF2 à l'équilibre, contenant du combustible sphere-pac restructuré d'une teneur initiale en américium de 4% en masse.

L.8.5. Impact du modèle d'expansion thermique sur les simulations

Afin d'identifier l'effet du modèle d'expansion développé durant la thèse, le cœur CONF2 contenant du combustible sphere-pac est analysé en début de vie en considérant ou non le modèle d'expansion. Axialement, l'hypothèse a été faite que la gaine est responsable de la dilatation étant donné qu'il n'existe pas de jeu pastille-gaine pour ce type de combustible. Radialement, le mode cylindrique a été choisi i.e. le sommier est responsable de la dilatation radiale du cœur. Comme attendu, le suivi de la puissance et de la réactivité démontre un délai de 1 s pour la vaporisation du sodium, de 2 s sur la fonte du combustible et enfin de 2.6 s sur l'excursion de puissance (Figure L-16). Il est à mentionner que la contre-réaction due à la dilatation thermique du cœur serait encore plus prononcée dans le cas d'une expansion purement combustible.
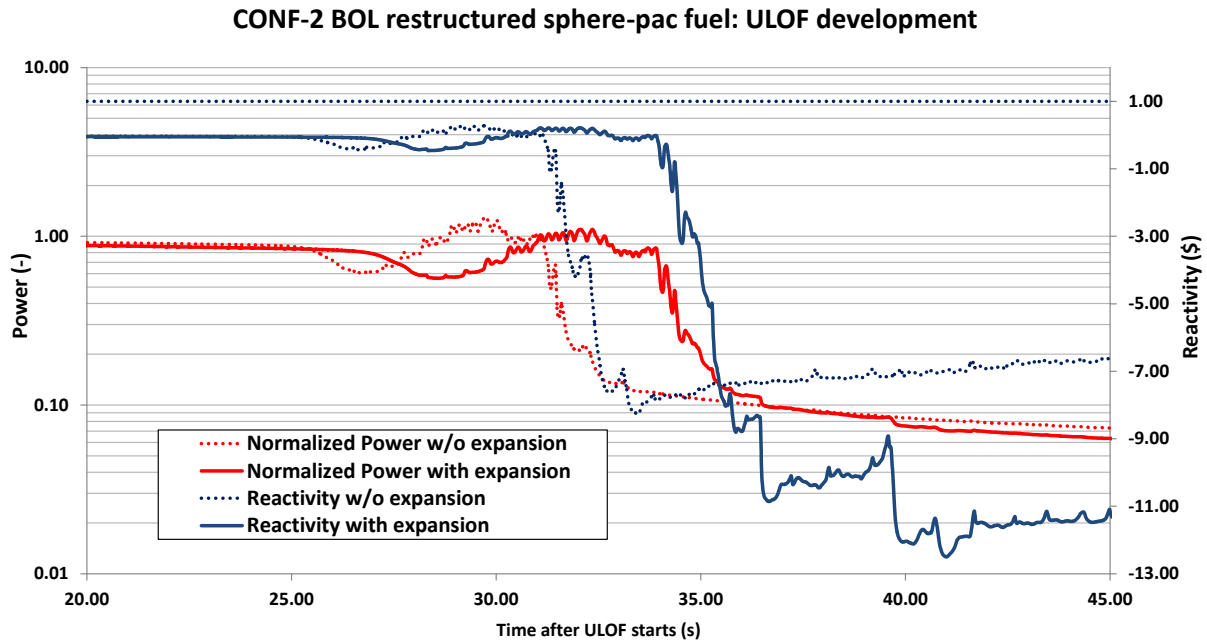
Figure L-16. Evolution de puissance et de réactivité durant un accident de perte de débit primaire dans le cœur CONF2 en début de vie, contenant du combustible restructuré avec ou sans la prise en compte des contre-réactions provenant de la dilatation thermique du cœur.

L.9. Conclusions générales

L'énergie nucléaire réunit tous les prérequis pour jouer un rôle substantiel dans l'approvisionnement énergétique mondial pour les prochaines décennies, sous conditions d'une utilisation durable des ressources et d'une gestion des déchets nucléaires. Les concepts de réacteurs rapides, spécialement les réacteurs à neutrons rapides refroidis au sodium, comptent parmi les options les plus prometteuses pour répondre à ces exigences. Ces cœurs n'étant pas dans leur configuration la plus réactive à l'état nominal, une analyse détaillée de sûreté tant en condition nominale qu'en condition accidentelle s'impose.

Ce travail de thèse s'insère dans ce contexte et a pour but d'évaluer l'impact des combustibles sphere-pac innovants sur les performances de sûreté des réacteurs à neutrons rapides refroidis au sodium. Afin de répondre à cette problématique, deux voies de développement ont été suivies, à savoir une amélioration de la modélisation de la phase primaire d'un transitoire accidentel d'une part et une prise en compte des spécificités des combustibles sphere-pac d'autre part.

Pour des cœurs à faible effet de vidange, les contre-réactions dues à la dilatation thermique du cœur jouent un rôle essentiel dans l'équilibre neutronique. Ces contre-réactions n'étaient jusqu'à présent pas incluses dans le code de calcul SIMMER, développé à l'origine pour des cœurs en configuration largement dégradée où leurs effets étaient négligeables.

Afin de prendre en compte ces effets pour des codes de calculs employant une méthode de cinétique spatiale et un maillage eulérien comme le code SIMMER, une méthodologie a été développée au

cours de cette thèse. Cette dernière permet de prendre en compte des effets de dilatation du cœur via des variations de concentrations uniquement. Tout d'abord, les dimensions dilatées sont calculées. Puis, les concentrations après dilatation sont calculées pour chaque cellule du maillage de dynamique des fluides sur la base du principe de conservation de la masse, excepté pour le caloporteur pour lequel la concentration est conservée. L'effet en réactivité lié à la dilatation axiale et radiale du cœur est ensuite sous-divisé en deux effets :

(1) L'effet lié à une variation de concentrations et de dimensions identique pour tous les matériaux à un endroit donné (i.e. dilatation homogène)
(2) L'effet de la variation relative de la concentration du sodium par rapport aux concentrations des autres matériaux.

Le premier effet est calculé en employant un principe d'équivalence étendu qui se base sur le principe d'équivalence (qui est exact) avec une hypothèse supplémentaire qui considère que l'effet total lié à la dilatation du cœur est la somme des effets des différentes sous-régions (considérés indépendants).

Le deuxième effet est pris en compte dans SIMMER directement lors du calcul des sections efficaces.

La méthodologie a conduit au développement de trois modèles. Le premier se base sur la théorie des perturbations du premier ordre et sur un coefficient de concentration global. Il permet de prédire avec précision les effets de dilatations uniformes, isotropes ou anisotropes et sert de base pour le second modèle. Ce dernier utilise des coefficients de concentrations dépendant de la position radiale de la cellule à considérer. Ces deux modèles prédisent l'effet en réactivité lié à une dilatation uniforme avec une erreur relative de 11% par rapport aux calculs de référence. Certaines limitations dans le cas de dilatations non-uniformes ont été mises en lumière et le développement d'un troisième modèle a été entrepris. Ce dernier a été testé avec le code de calcul ERANOS et donne des résultats concluants par rapport aux calculs de référence (erreur relative de l'ordre de 3%).

La deuxième partie de ce travail a consisté à prendre en compte les spécificités des combustibles sphere-pac dans le code de calcul SIMMER, notamment la conductivité thermique. En effet, celle-ci est soumise à de larges variations sous irradiation, dues notamment à la microstructure de ces combustibles. Une recherche bibliographique étendue a permis de déterminer les modèles de conductivités thermiques les plus appropriés pour modéliser celle des combustibles sphere-pac. Des corrélations ont été établies pour des combustibles sphere-pac en début de vie et après restructuration (après trois cycles d'irradiation) ainsi que pour des combustibles pastilles.

Des analyses de sûreté ont ensuite étaient conduites pour les cœurs CP-ESFR WH et CONF2 chargés avec du combustible pastille ou du combustible sphere-pac. La structure du cœur WH a été conservée puisque des combustibles sphere-pac avec la densité requise peuvent être fabriqués, selon la littérature. Les études ont d'abord été effectuées pour des combustibles sphere-pac neufs. Ce choix est dû au fait que la conductivité thermique à ce stade est faible et peut conduire à des températures centrales de l'aiguille élevées. Les analyses démontrent en effet qu'une procédure spécifique au démarrage du réacteur est requise pour les combustibles sphere-pac afin de leur donner suffisamment de temps pour se restructurer et améliorer leur conductivité thermique. Un accident de perte de débit primaire dans ce cœur à l'équilibre entraine une dégradation sévère du cœur avec une fusion totale du combustible, tant dans le cas pastille que dans le cas sphere-pac.

Le cœur CONF2 a ensuite été analysé. Ce cœur n'a pas bénéficié d'une analyse de sûreté poussée dans le projet CP-ESFR. Une première étape a donc été l'analyse de ce cœur chargé avec du combustible pastille afin de démontrer l'effet de l'élargissement du plénum sodium sur l'évolution de l'accident de perte de débit primaire, notamment en début de vie (l'effet de vidange sodium étendu est en effet réduit d'un facteur 2.4 par rapport au cœur WH). Les résultats confirment l'action atténuante du plénum sodium élargi : la vidange du plénum insère suffisamment d'anti-réactivité pour pouvoir contrebalancer les effets en réactivité positifs. La puissance reste relativement faible durant le transitoire permettant un retour de sodium liquide dans les assemblages combustibles et le processus de dégradation reste limité. Après un premier pic de puissance relativement faible, aucune recriticité n'est observée et la suite de l'accident dépend uniquement de la capacité à évacuer la chaleur produite par puissance résiduelle.

Le cœur CONF2 a ensuite été étudié lorsque le combustible pastille est remplacé par du combustible sphere-pac. Les analyses ont d'abord été effectuées pour un cœur chargé avec du combustible neuf, en considérant un cas de combustible non-restructuré et un autre de combustible restructuré. Les résultats confirment que dans le cas du combustible sphere-pac neuf non-restructuré, les températures excèdent localement la température de fusion du combustible, dans les zones à haute puissance. Dans les deux cas, le plénum sodium prévient un scénario dans lequel des recriticités multiples seraient observées.

Pour le cœur CONF2 à l'équilibre contenant du combustible irradié, le comportement de sûreté est significativement détérioré du fait de la détérioration des coefficients de sûreté, notamment l'effet de vidange et spécialement lorsque de l'américium est ajouté au combustible. Des effets de vidange supplémentaires sont causés par un blow-out des produits de fission et de l'hélium. Les améliorations observées en début de vie ne sont plus d'actualité dans le cœur à l'équilibre et ce dernier subit un transitoire sévère avec une dégradation et une fusion complète du cœur.

Le modèle neutronique développé durant la thèse a été utilisé par la suite afin d'améliorer les analyses de sûreté et démontre un délai et une atténuation du potentiel énergétique de l'accident.

Les découvertes clés suite à l'évaluation du comportement de sûreté du cœur CONF2 chargé avec du combustible sphere-pac sont donc les suivantes :

- Les combustibles sphere-pac peuvent être insérés dans un réacteur à neutrons rapides refroidi au sodium sans impacter significativement le design du cœur ou son comportement de sûreté
- Une procédure spécifique de démarrage d'un réacteur chargé avec du combustible sphere-pac est nécessaire pour éviter une fusion du combustible à l'état nominal. Concrètement, cette phase de démarrage devrait se dérouler à une puissance inférieure à la puissance nominale afin d'observer une restructuration du combustible (durée de quelques heures/jours).
- Les analyses du transitoire accidentel de perte de débit primaire ne démontrent aucun changement significatif dans le scénario accidentel lorsqu'un réacteur est chargé avec du combustible sphere-pac.
- L'élargissement du plénum sodium améliore significativement le comportement accidentel du cœur. Cet avantage est cependant perdu avec l'irradiation ou avec un ajout supplémentaire d'américium dans le cœur.

Ces analyses de sûreté ont permis d'identifier les points nécessitants une modélisation améliorée et des informations expérimentales supplémentaires. Des travaux futurs devront prendre en compte le comportement cinétique détaillé dû au relâchement des produits de fission et de l'Hélium en opération et lors de scénarios accidentels. Des données expérimentales ou encore des évaluations techniques de données seront nécessaires pour comprendre le comportement du combustible sphere-pac en conditions transitoires et sous haute contrainte thermique. De même, une modélisation précise du comportement de l'anneau non-restructuré du combustible sphere-pac en cas de rupture de gaine sera nécessaire.